

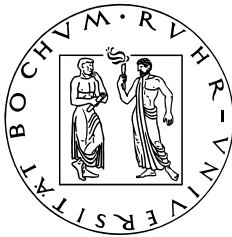
Study of  $B \rightarrow D_s^{(*)+} X$  and  
 $B^0 \rightarrow D_s^{(*)+} D^{*-}$  Decays with  
the  $B_{\text{A}}B_{\text{A}}\text{R}$  Detector

Dissertation

zur Erlangung des Grades eines  
Doktors der Naturwissenschaften

der

Fakultät für Physik und Astronomie  
Institut für Experimentalphysik I  
der Ruhr-Universität Bochum



vorgelegt von Serguei Ganjour  
geb. in Gomel

Bochum, im März 2002



# ABSTRACT

Precise measurements of  $D_s^+$  and  $D_s^{*+}$  meson production from  $B$  mesons and  $q\bar{q}$  continuum events near the  $\Upsilon(4S)$  resonance are presented in this thesis. Using the *BABAR* data recorded in 1999 and 2000 of  $20.8\text{ fb}^{-1}$  on-resonance and  $2.6\text{ fb}^{-1}$  off-resonance, we have measured the inclusive branching fractions  $\mathcal{B}(B \rightarrow D_s^+ X) = (10.93 \pm 0.19 \pm 0.58 \pm 2.73)\%$  and  $\mathcal{B}(B \rightarrow D_s^{*+} X) = (7.9 \pm 0.8 \pm 0.7 \pm 2.0)\%$ , where the first error is statistical, the second is the systematic error, and the third is the error due to the  $D_s^+ \rightarrow \phi\pi^+$  branching fraction uncertainty. The branching fractions  $\Sigma\mathcal{B}(B \rightarrow D_s^{(*)+} \bar{D}^{(*)}) = (5.07 \pm 0.14 \pm 0.30 \pm 1.27)\%$  and  $\Sigma\mathcal{B}(B \rightarrow D_s^{*+} \bar{D}^{(*)}) = (4.1 \pm 0.2 \pm 0.4 \pm 1.0)\%$  have been determined from the fit of the measured  $D_s^{(*)+}$  momentum spectra.

The study of different fragmentation functions was done for the  $D_s^{(*)+}$  momentum spectrum produced from  $q\bar{q}$  continuum events. Their production cross sections at center-of-mass energies about 40 MeV below the  $\Upsilon(4S)$  mass  $\sigma(e^+e^- \rightarrow D_s^\pm X) \times \mathcal{B}(D_s^\pm \rightarrow \phi\pi^\pm) = 7.55 \pm 0.20 \pm 0.34\text{ pb}$  and  $\sigma(e^+e^- \rightarrow D_s^{*\pm} X) \times \mathcal{B}(D_s^\pm \rightarrow \phi\pi^\pm) = 5.8 \pm 0.7 \pm 0.5\text{ pb}$  has been determined.

Employing a partial reconstruction technique, the branching fractions of the  $B^0 \rightarrow D_s^{(*)+} D^{*-}$  decays have been determined.  $(1.03 \pm 0.14 \pm 0.14 \pm 0.26)\%$  and  $(1.97 \pm 0.15 \pm 0.28 \pm 0.49)\%$  have been measured for the  $B^0 \rightarrow D_s^+ D^{*-}$  and  $B^0 \rightarrow D_s^{*+} D^{*-}$  channels, respectively, using  $D_s^+$  mesons identified in the three decay modes such as  $D_s^+ \rightarrow \phi\pi^+$ ,  $\bar{K}^{*0} K^+$ ,  $\bar{K}^0 K^+$ . From the angular analysis of  $B^0 \rightarrow D_s^{*+} D^{*-}$  the fraction of longitudinal polarization is determined to be  $(51.9 \pm 5.0 \pm 2.8)\%$ . It is in good agreement with the theoretical prediction assuming factorization.



# Contents

<b>1</b>	<b>Introduction</b>	<b>1</b>
<b>2</b>	<b>Quark Mixing and <math>CP</math> Violation</b>	<b>5</b>
2.1	Conservation of Symmetries . . . . .	5
2.2	$CP$ Violation in the $K^0$ System . . . . .	7
2.3	$B^0 - \overline{B}^0$ System . . . . .	10
2.4	$CP$ Violation in the Standard Model . . . . .	15
2.5	$CP$ Violation Measurements in the $B^0$ System . . . . .	19
2.6	Observation of $CP$ Violation in the $B^0$ System . . . . .	23
<b>3</b>	<b>The BABAR Experiment</b>	<b>27</b>
3.1	The PEP-II $e^+e^-$ asymmetric $B$ Factory . . . . .	27
3.2	The BABAR detector . . . . .	30
3.2.1	The Silicon Vertex Tracker (SVT) . . . . .	31
3.2.2	The Drift Chamber (DCH) . . . . .	32
3.2.3	The Detector of Internally Reflected Cherenkov light (DIRC) .	34
3.2.4	The Electromagnetic Calorimeter (EMC) . . . . .	36
3.2.5	The Instrumented Flux Return (IFR) . . . . .	38
<b>4</b>	<b>Hadronic <math>B</math> Physics with the BABAR detector</b>	<b>41</b>
4.1	Heavy-Quark Expansion . . . . .	41
4.2	Factorization . . . . .	43

4.2.1	The $B \rightarrow D_s^{(*)+} \bar{D}^{(*)}$ Decays . . . . .	43
4.2.2	The $B \rightarrow D_s^{(*)+} X_q$ Inclusive Rates . . . . .	46
4.3	Charm Production Rate from $B$ Decays . . . . .	49
4.4	Motivation. . . . .	50
4.5	Reconstruction of $B$ Mesons . . . . .	53
4.5.1	Full Reconstruction . . . . .	53
4.5.2	Partial Reconstruction . . . . .	54
<b>5</b>	<b><math>D_s^{(*)+}</math> Signal Extraction</b>	<b>57</b>
5.1	Data Set . . . . .	57
5.2	Event Preselection . . . . .	58
5.2.1	Selection of Tracks and Neutrals . . . . .	58
5.2.2	Particle Identification . . . . .	59
5.2.3	$D_s^+$ Skims from Multihadron Events . . . . .	60
5.3	$D_s^{(*)+}$ Reconstruction . . . . .	61
5.3.1	$D_s^+$ Signal Selection . . . . .	61
5.3.2	$D_s^{*+}$ Signal Selection . . . . .	64
<b>6</b>	<b>The <math>B \rightarrow D_s^{(*)+} X</math> Decays</b>	<b>69</b>
6.1	$D_s^+$ Momentum Spectrum . . . . .	69
6.2	$D_s^{*+}$ Momentum Spectrum . . . . .	76
6.3	$B \rightarrow D_s^{(*)+} X$ Branching Fraction . . . . .	85
6.4	$D_s^{(*)+}$ production from $q\bar{q}$ continuum . . . . .	88
6.4.1	Cross Sections . . . . .	88
6.4.2	Fragmentation Functions . . . . .	88
6.5	The Systematic Errors . . . . .	92
6.5.1	Tracking Efficiency . . . . .	92
6.5.2	Neutral Efficiency . . . . .	93
6.5.3	Particle Identification . . . . .	94

6.5.4	$\pi^0$ Overlap . . . . .	95
6.5.5	Signal Shape . . . . .	96
6.5.6	Background Subtraction . . . . .	97
6.5.7	Momentum Smearing . . . . .	98
6.6	Fits to $D_s^{(*)+}$ Momentum Spectra . . . . .	102
6.6.1	Components of Momentum Spectrum . . . . .	102
6.6.2	Fit and Systematic Errors . . . . .	104
6.7	$D_s^+$ and $D^+$ Mass Difference . . . . .	109
6.8	Summary . . . . .	111
<b>7</b>	<b>The <math>B^0 \rightarrow D_s^{(*)+} D^{*-}</math> Decays</b>	<b>113</b>
7.1	Signal Extraction . . . . .	113
7.2	Background Study . . . . .	116
7.2.1	Peaking Backgrounds . . . . .	116
7.2.2	Non-Peaking Background . . . . .	118
7.2.3	Monte Carlo Simulation of the Backgrounds . . . . .	119
7.3	The $B^0 \rightarrow D_s^{(*)+} D^{*-}$ Decay Rates . . . . .	126
7.4	Systematic Errors . . . . .	128
7.5	Polarization Measurement . . . . .	130
7.5.1	$B^0 \rightarrow D_s^{*+} D^{*-}$ Angular Distributions . . . . .	130
7.5.2	Extracting Angular Distributions . . . . .	132
7.5.3	Result and Systematic Errors . . . . .	134
7.6	Prospect for the $D_s^+ \rightarrow \phi \pi^+$ Branching Fraction Measurement . . .	137
7.7	Summary . . . . .	138
<b>8</b>	<b>Comparison with Theory and Other Experiments</b>	<b>139</b>
<b>9</b>	<b>Conclusion</b>	<b>143</b>





# Chapter 1

## Introduction

The decays of  $B$  mesons into final states involving  $D_s^{(*)+}$  mesons provide the opportunity to study the production mechanism of  $c\bar{s}$  quark pairs \*. Although several mechanisms can lead to  $D_s^{(*)+}$  production in  $B$  decays, the dominant mechanism [1] is expected to be due to external  $W^+ \rightarrow c\bar{s}$  emission. The precise knowledge of this production rate is interesting with respect to continuing theoretical difficulties [2] to account simultaneously for semileptonic branching fraction and inclusive charm production in  $B$  decays. Indeed, it has been pointed out [3] that an enhanced  $B$  decay rate to charm would help explain the small semileptonic rate.

In addition,  $D_s^{(*)+}$  mesons can be produced from  $q\bar{q}$  continuum events in  $e^+e^-$  annihilation. The process of fragmentation followed by the formation of hadrons can only be calculated using phenomenological models, since it is non-perturbative. Two features of hadron production which can be experimentally measured, are the relative production of states with different spins, e.g.  $D_s^+$  ( $J^P = 0^-$ ) and  $D_s^{*+}$  ( $J^P = 1^-$ ), and the hadron momentum spectrum. The ratio of vector to pseudoscalar production rates is of particular interest for testing such models. Decays into  $D_s^+$  and  $D_s^{*+}$  mesons are well suited to measure this quantity because the  $c\bar{s}$  states with  $L=1$  ( $D_s^{**}$ ) have not been observed to decay to either  $D_s^+$  or  $D_s^{*+}$ .

The factorization assumption, which seems to describe well the processes with relatively low  $q^2 \simeq M_\pi^2, M_\rho^2$ , has not been checked with sufficient accuracy for processes with relatively high  $q^2 \simeq M_{D_s^{(*)+}}^2$  yet. The precise knowledge of the branching fractions for the exclusive decay modes involving  $D_s^{(*)+}$  mesons provides such a test. The factorization assumes no final state interactions between the quarks of two final state mesons. Factorization has been verified experimentally in some  $B$  decays, such as

---

\*Unless otherwise noted, reference in this work to a specific decay channel or state also implies the charge conjugated decay or state. The notation  $D_s^{(*)+}$  means either  $D_s^+$  or  $D_s^{*+}$ .  $B \rightarrow D_s^{(*)+} \bar{D}^{(*)}$  is a general representation of any of the modes with  $c\bar{s}$  and  $\bar{c}q$  states including their  $L=0$  excited states.  $B \rightarrow D_s^{(*)+} X$  includes also  $\bar{B} \rightarrow D_s^{(*)+} X$ .

$D^*\pi$ ,  $D^*\rho$ ,  $D^*\rho'$  for which both the branching fraction and the polarization have been predicted successfully. However, it is possible that this assumption is not applicable in the case where a heavy quark is emitted, such as in the decays  $B \rightarrow D_s^{(*)+} \bar{D}^{(*)}$ .

This thesis presents the results of measurement of  $B \rightarrow D_s^{(*)+} X$  branching fractions and of the corresponding momentum spectra. The extraction of the sum of the  $B \rightarrow D_s^{(*)+} \bar{D}^{(*)}$  two-body decays is performed from a fit to the momentum spectra. The measurements of the fragmentation functions of  $c$  quarks, which describe the hadronization process, are obtained from the  $D_s^{(*)+}$  momentum spectra from continuum events. The production cross sections for  $D_s^{(*)+}$  from continuum events are reported as well.

Measurements of the branching fractions of the two decay modes  $B^0 \rightarrow D_s^{(*)+} D^{*-}$  using a partial reconstruction technique is also measured using these events. The measurement of the  $D_s^{*+}$  polarization in the decay mode  $B^0 \rightarrow D_s^{*+} D^{*-}$  is obtained from an angular analysis.

This analysis is based on the 1999-2000 *BABAR* data sample. It represents an integrated luminosity of  $20.8 \text{ fb}^{-1}$  collected at the  $\Upsilon(4S)$  resonance mass corresponding to  $22.7 \times 10^6$  produced  $B\bar{B}$  pairs. In addition, data recorded at an energy about 40 MeV below the  $\Upsilon(4S)$  mass with an integrated luminosity of  $2.6 \text{ fb}^{-1}$  is also incorporated in the analysis.

The dissertation consists of the following sections:

- **Chapter 2** provides an overview of the  $CP$  violation phenomena. The various observations related to the neutral kaon decays are discussed in Section 2.2. The general formalism describing a system of a neutral particle and its antiparticle and the implications of  $CP$  non conservation are derived in Section 2.3. It is shown how the mass generation mechanism in the framework of the Standard Model leads to the quark mixing and  $CP$  violation phenomena. It is also discussed how the relevant measurements can constrain the magnitude of  $CP$  violation and the various possibilities for observing this effect are summarized. The observation of  $CP$  violation in neutral  $B$  decays with the *BABAR* detector is discussed in Section 2.6.
- **Chapter 3** describes the PEP-II asymmetric  $B$ -Factory and the *BABAR* detector. Section 3.1 gives a summary of the machine performance and the recorded luminosity. The detector subsystems are discussed in Section 3.2.
- **Chapter 4** gives an overview of the mathematical formalism used to describe both exclusive and inclusive  $B \rightarrow D_s^{(*)+} X$  decays. The predictions of the Heavy Quark Expansion (HQE) for the  $D$  meson mass spectrum are given in Section 4.1. The commonly used factorization approach for the description of the processes  $b \rightarrow c\bar{c}s$  is presented in Section 4.2. The formulas for the decay rates

of  $B \rightarrow D_s^{(*)+} \bar{D}^{(*)}$  and the predicted inclusive rates of  $D_s^+$  and  $D_s^{*+}$  from  $B$  meson decays are given. Section 4.3 discusses the “problem of small observed decay rates for the semileptonic  $B$  decays” and shows how it is connected to charm production rate. After the motivation for the presented analysis (Section 4.4) the methods used for the  $B$  meson reconstruction (full and partial reconstruction) are discussed in Section 4.5.

- **Chapter 5** describes the  $D_s^{(*)+}$  event selection procedure. The data sample used in the analysis is presented in Section 5.1. Section 5.2 addresses the  $D_s^{(*)+}$  preselection from multihadron events (skim production) as well as the criteria for charged and neutral particles selection and identification used for the  $D_s^{(*)+}$  reconstruction. The  $D_s^+$  and  $D_s^{*+}$  signal extraction with  $D_s^+$  decaying to  $D_s^+ \rightarrow \phi\pi^+$ ,  $D_s^+ \rightarrow \bar{K}^{*0}K^+$ ,  $D_s^+ \rightarrow \bar{K}^0K^+$ ,  $D_s^+ \rightarrow \phi\rho^+$  is presented in Section 5.3
- **Chapter 6** is devoted to the description of the measurement of the  $D_s^+$  and  $D_s^{*+}$  production from  $B$  decays and continuum  $e^+e^-$  annihilation. The extraction of the  $D_s^{(*)+}$  momentum spectra from  $B$  decays using the  $D_s^+ \rightarrow \phi\pi^+$  decay mode is reported in Sections 6.1, 6.2. The branching fractions are summarized in Section 6.3. Section 6.4 describes the studies of the various fragmentation functions used for the parametrization of hadronization processes from the continuum. The cross sections of the  $D_s^{(*)+}$  meson production from  $q\bar{q}$  continuum events are reported as well. The various sources for the systematic errors are studied in Section 6.5. The fit procedure to the  $D_s^{(*)+}$  momentum spectra is described in Section 6.6. The result for the  $m(D_s^+) - m(D^+)$  mass difference is reported in Section 6.7.
- **Chapter 7** describes the studies of the two exclusive two-body decay modes  $B^0 \rightarrow D_s^+ D^{*-}$  and  $B^0 \rightarrow D_s^{*+} D^{*-}$  using a partial reconstruction technique. The  $B$  signal extraction using the  $D_s^+$  decay modes ( $D_s^+ \rightarrow \phi\pi^+$ ,  $D_s^+ \rightarrow \bar{K}^{*0}K^+$ ,  $D_s^+ \rightarrow \bar{K}^0K^+$ ) is presented in Section 7.1. The decay rates and the polarization measurement are described in Sections 7.3, 7.5, respectively. Section 7.4 addresses the study of the systematic errors.
- **Chapter 8** gives a comparison of the results with the data from other experiments and the theoretical predictions.



## Chapter 2

# Quark Mixing and $CP$ Violation

The violation of  $CP$  symmetry is a fundamental property of the nature which plays a key role in the understanding of the evolution of the universe. Since neither its origin nor its magnitude are yet well established, it deserves particular studies. There are many lectures and reviews on this phenomenon. As an example, lectures in which the  $CP$  violation mechanism is described can be found in [4].

The requirement of the conservation of various symmetries greatly simplifies the elaboration of the physical theories. The conservation of energy, momentum and spin involves invariance principles of the physical law under continuous transformations such as translation in time, space or rotation, respectively. An other category of conservation laws, for example conservation of electric, baryonic and leptonic charge and strong isospin is associated with the dynamics of the processes. They act on abstract spaces such as phases or isospin and also involve continuous transformations.

The category of the discrete transformations which are also connected with the dynamics of the interaction plays a special role. These transformations are *charge conjugation, parity and time reversal*.

### 2.1 Conservation of Symmetries

For a particle described by the wave function  $\psi(\vec{p}, \vec{s})$  where  $\vec{p}$  and  $\vec{s}$  denote its momentum and spin, the action of the charge conjugation is to change the particle into its antiparticle without modifying  $\vec{p}$  and  $\vec{s}$ . Thus the transformation of charge conjugation  $C$  can be expressed as

$$C|\psi(\vec{p}, \vec{s})\rangle = \eta_C |\bar{\psi}(\vec{p}, \vec{s})\rangle \quad (2.1)$$

where  $\eta_C$  is a phase factor. The antiparticle ( $\bar{\psi}$ ) is defined by changing the sign of all the charges associated to the particle (electric, baryonic, leptonic...).

The parity transformation  $P$  changes the space vector  $\vec{r}$  into  $-\vec{r}$ . This means that the momentum  $\vec{p}$  becomes  $-\vec{p}$ , while orbital momentum remains unchanged ( $\vec{L} = \vec{r} \times \vec{p}$ ). Hence

$$P|\psi(\vec{p}, \vec{s})\rangle = \eta_P|\psi(-\vec{p}, \vec{s})\rangle \quad (2.2)$$

where  $\eta_P$  is a phase factor.

Under time reversal transformation  $T$ ,  $t$  is changed to  $-t$  and therefore  $\vec{p}$  is modified into  $-\vec{p}$ . Moreover the wave function is also replaced by its complex conjugate due to the fact that it should satisfy the Schrödinger equation. Thus

$$T|\psi(\vec{p}, \vec{s})\rangle = \eta_T^s|\psi^*(-\vec{p}, -\vec{s})\rangle \quad (2.3)$$

where  $\eta_T^s$  is a phase factor depending on the spin.

The conservation of  $C$  parity in the strong interactions is verified by comparing the angular distributions for the charged pions, for example in the reaction  $p\bar{p} \rightarrow \pi^+\pi^-\pi^0$ . Although it is technically difficult, it was shown that  $C$  parity is conserved at the percent level. It is easier to check the conservation of  $C$  parity in electromagnetic processes. For example the reaction  $e^+e^- \rightarrow \mu^+\mu^-\pi^0$  is forbidden if  $C$  is conserved. Since this decay is not observed, one can set an upper limit at  $5 \times 10^{-6}$ .

The reaction  $p + F^{19} \rightarrow Ne^{20*} \rightarrow O^{16} + \alpha$  is forbidden if Parity is conserved. No such reaction is observed, which allows one to make very precise tests of Parity conservation in strong interactions. This leads to an upper limit of the order of  $10^{-12}$ .

The comparison of the process  $a+b \rightarrow c+d$  with its time reversed process  $c+d \rightarrow a+b$  shows an upper limit for  $T$  violation at the level of  $4 \times 10^{-3}$ .

Thus Charge Conjugation and Parity are conserved in the strong and electromagnetic interaction within experimental errors. However, it is important to note that  $C$  has to be violated at some time, because the world is made of matter. The weak interactions play a very special role in this context. The pion decays  $\pi^+ \rightarrow \mu^+\nu$  and  $\pi^- \rightarrow \mu^-\bar{\nu}$  are governed by weak interaction since a neutrino is involved. The measurement of the muon helicity via the angular distributions of its decay products shows that both Charge Conjugation and Parity are violated in a maximal way. However, the  $CP$  transformation where  $C$  and  $P$  are applied consequently, seems to be conserved.

Based on a very general hypothesis it can be shown that  $CPT$  is conserved in field theories [5], leading to very important consequences. For example, the lifetimes and masses of a particle and its antiparticle are equal. The experimental measurement of the mass difference for a particle and its antiparticle demonstrates the conservation of the  $CPT$  symmetry. As an illustration, some experimental mass differences are given:

$$|m_{e^+} - m_{e^-}| \leq 0.02 \text{ eV}, \quad |m_p - m_{\bar{p}}| \leq 1 \text{ eV}, \quad |m_K - m_{\bar{K}}| \leq 3.6 \cdot 10^{-10} \text{ eV} \quad (2.4)$$

## 2.2 $CP$ Violation in the $K^0$ System

In the early 50ties the discovery of two new particles, the  $\Lambda$ - Baryon and the  $K^0$ - Meson was accompanied by the observation of a “strange” phenomenon. In  $\pi^-p$  collisions at low energy, the neutral  $K^0$  mesons are produced in association with  $\Lambda$ 's, while the production of its antiparticle  $\overline{K}^0$  is associated with antibaryon  $\overline{\Lambda}$ , for example  $\pi^- + p \rightarrow \Lambda + K^0$ . In addition, both  $\Lambda$  and  $K^0$  have very long lifetime. The lifetime of  $\Lambda$  is of order of  $2.6 \times 10^{-10}s$  which is  $10^{14}$  times higher than that one of the  $\Delta$ - Baryon.

In order to explain this phenomena, Gell-mann proposed to introduce a new quantum number called Strangeness  $S$  associated with the kaon system. The Strangeness must be conserved in strong and electromagnetic interactions ( $\Delta S = 0$ ). Thus,  $\overline{K}^0$  and  $\Lambda$  have  $S = +1$ , while  $K^0$  and  $\overline{\Lambda}$  have  $S = -1$ . Furthermore, one can predict that  $K^0$  and  $\overline{K}^0$  have to be mixed [6] since they have a common final state  $\pi^+\pi^-$ . Thus, if a  $K^0$  propagate in space, it can oscillate into  $\overline{K}^0$  and visa versa via virtual intermediate states, e.g.,

$$K^0 \rightarrow \pi^+\pi^- \rightarrow \overline{K}^0 \quad (2.5)$$

where for these decays are  $|\Delta S| = 1$ . Consequently, the suggestion was made that  $K^0$  and  $\overline{K}^0$  are not the physical states, but instead are superpositions of the mass eigenstates  $K_1$  and  $K_2$ .

$$|K_1\rangle = \frac{|K^0\rangle + |\overline{K}^0\rangle}{\sqrt{2}}, \quad |K_2\rangle = \frac{|K^0\rangle - |\overline{K}^0\rangle}{\sqrt{2}} \quad (2.6)$$

By this definition it is easy to verify that  $K_1$  and  $K_2$  are  $CP$  eigenstates using the convention  $CP|K^0\rangle = |\overline{K}^0\rangle$

$$CP|K_1\rangle = +|K_1\rangle, \quad CP|K_2\rangle = -|K_2\rangle \quad (2.7)$$

Now let us investigate how the physical states  $K_1$  and  $K_2$  are coupled to  $\pi^+\pi^-$ . Since the  $\pi^+\pi^-$  system has the  $CP$  parity  $+1$  due to Bose symmetry, only the decay  $K_1 \rightarrow \pi^+\pi^-$  is allowed if  $CP$  is conserved in weak interactions. For  $K_2$  only three body decays such as  $\pi^+\pi^-\pi^0$  will occur. This final state, however, is strongly suppressed due to limited phase space, therefore the lifetime of  $K_2$  is much longer than the one of  $K_1$ . It was observed

$$\tau_S = (0.8927 \pm 0.0009) \times 10^{-10}s, \tau_L = (5.17 \pm 0.04) \times 10^{-8}s \quad (2.8)$$

where the indices  $S$  and  $L$  commonly denote the short-lived  $K_S$  and long-lived  $K_L$  mass eigenstates, respectively.

Since the wave functions must be solutions of the Schrödinger equation, they can be written as

$$|K_1(t)\rangle = e^{-(\Gamma_1/2 + im_1)t}|K_1\rangle, \quad |K_2(t)\rangle = e^{-(\Gamma_2/2 + im_2)t}|K_2\rangle \quad (2.9)$$

where  $\Gamma_1$ ,  $m_1$  and  $\Gamma_2$ ,  $m_2$  are the widths and masses of  $K_1$  and  $K_2$ , respectively. Therefore, using Eq. 2.6 one can write

$$|K^0(t)\rangle = \frac{e^{-(\Gamma_1/2+im_1)t}|K_1\rangle + e^{-(\Gamma_2/2+im_2)t}|K_2\rangle}{\sqrt{2}}. \quad (2.10)$$

A similar equation holds for  $|\overline{K}^0(t)\rangle$ . Thus, the probability for the transition  $K^0 \rightarrow f$  is

$$I(K^0) = |\langle f|T|K^0(t)\rangle|^2 = \frac{1}{2}e^{-\Gamma_1 t} |\langle f|T|K_1\rangle|^2 + \frac{1}{2}e^{-\Gamma_2 t} |\langle f|T|K_2\rangle|^2 + e^{-\frac{\Gamma_1+\Gamma_2}{2}t} \cos(\Delta m t - \Delta\phi) |\langle f|T|K_1\rangle \langle f|T|K_2\rangle^*| \quad (2.11)$$

where  $\Delta m = m_2 - m_1$  and  $|\Delta\phi|$  is the strong phase difference  $\phi_2 - \phi_1$  in the final state. It is easy to show that a similar formula is obtained for the  $\overline{K}^0 \rightarrow \overline{f}$  transition with the exception of the interference term, which has the opposite sign. Using Eq. 2.11 one can conclude that only the transition  $\langle f|T|K_2\rangle$  remains for  $t \gg \hbar/\Gamma_1$ . It is very fortunate that  $K_1$  and  $K_2$  have so different lifetimes. It allows one to obtain pure  $K_2$  beams, and therefore one can verify whether **CP** is conserved by searching for the forbidden  $K_2 \rightarrow \pi^+\pi^-$  decay. This transition was observed [7], establishing that **CP** is violated very slightly, ( $\sim 2 \times 10^{-3}$ ) in the  $K^0$  decays. Using this finding, the equivalence between the **CP** eigenstates and mass eigenstates has to be reconsidered. One has to write

$$|K_S\rangle = \frac{|K_1\rangle + \epsilon_K |K_2\rangle}{\sqrt{1 + |\epsilon_K|^2}}, \quad |K_L\rangle = \frac{|K_2\rangle + \epsilon_K |K_1\rangle}{\sqrt{1 + |\epsilon_K|^2}} \quad (2.12)$$

where  $\epsilon_K$  is a complex coefficient describing the strength of **CP** violation. Here  $K_S$  and  $K_L$  are the observed physical states. The present value for  $\epsilon_K$  is  $|\epsilon_K| = (2.271 \pm 0.017) \times 10^{-3}$  [8].

A measurements of **CP** symmetry in decays of the  $K^0$  particles can be carried out either with a pure  $K_L$  state or a coherent superposition of  $K_S$  and  $K_L$  states.

#### A Pure $K_L$ State

The first measurement is based on the comparison of the decay rates  $K_L \rightarrow f$  with its **CP**-conjugate one. Using semileptonic decays of  $K_L$ , one can compare the rate of positively charged leptons to the rate of negatively charged ones and define the asymmetry

$$\delta(l) = \frac{\Gamma(K_L \rightarrow l^+\nu_l\pi^-) - \Gamma(K_L \rightarrow l^-\nu_l\pi^+)}{\Gamma(K_L \rightarrow l^+\nu_l\pi^-) + \Gamma(K_L \rightarrow l^-\nu_l\pi^+)} \quad (2.13)$$

One can show that  $\delta(l)$  is connected to  $\epsilon_K$  by the equation

$$\delta(l) = \frac{2\text{Re}\epsilon_K}{1 + |\epsilon_K|^2} \quad (2.14)$$



The other method implies a measurement of the  $K_L$  decay rate to a  $CP$ -forbidden final state. It can be shown that the ratio of the decay amplitudes

$$\eta = \frac{A(K_L \rightarrow \pi\pi)}{A(K_S \rightarrow \pi\pi)} = \frac{(1 + \epsilon_K) \langle \pi\pi | K^0 \rangle - (1 - \epsilon_K) \langle \pi\pi | \bar{K}^0 \rangle}{(1 + \epsilon_K) \langle \pi\pi | K^0 \rangle + (1 - \epsilon_K) \langle \pi\pi | \bar{K}^0 \rangle} \quad (2.15)$$

leads to  $|\eta| = |\epsilon_K|$ . It was proposed in [9] that the origin of  $CP$  violation in  $K^0$  system might be related to a new interaction called “Superweak”, which allows transitions with  $\Delta S = 2$ . It can be demonstrated [4] that if  $CP$  is only violated via the mixing mechanism then

$$\eta^{+-} = \frac{A(K_L \rightarrow \pi^+\pi^-)}{A(K_S \rightarrow \pi^+\pi^-)} = \frac{A(K_L \rightarrow \pi^0\pi^0)}{A(K_S \rightarrow \pi^0\pi^0)} = \eta^{00} \quad (2.16)$$

However, the most recent measurements of  $\eta^{00}/\eta^{+-} = 0.99098 \pm 0.00161$  [10, 11] show that this ratio differs from unity. As a consequence, it is now established that  $CP$  is also violated in the decay mechanism. Hence the superweak model is ruled out and the origin of  $CP$  violation can be attributed to the weak interactions.

#### *Coherent Superposition of $K_S$ and $K_L$ States*

Complementary to the method using pure  $K_L$  beams it is possible to measure  $CP$  violation by studying the interference between the  $K_S$  and  $K_L$  components of a “ $K^0$ ” beam: the presence of  $K_S$  and  $K_L$  leads to the regeneration phenomenon.

1. From a “ $K^0$ ” beam propagating in vacuum over a long distance, only the  $K_L$  component remains. If the  $K_L$ -beam traverses a thin foil of material then one obtains the superposition

$$|K_L \rangle \rightarrow |K_L \rangle + r |K_S \rangle, \quad (2.17)$$

because the elastic cross section is different for  $K^0$  and  $\bar{K}^0$ .

2. One could use  $K^0$  and/or  $\bar{K}^0$  beams directly since they are already a superposition of  $K_S$  and  $K_L$ . For example, a  $K^0$  beam can be obtained using the annihilation process  $p\bar{p} \rightarrow K^-\pi^+K^0$  where the flavor of the neutral kaon can be deduced from the sign of the charged kaon.

Assuming  $CPT$  conservation and writing

$$\frac{A(K_L \rightarrow \pi\pi)}{A(K_S \rightarrow \pi\pi)} = |\eta| e^{i\Delta\phi} \quad (2.18)$$

one can extract  $|\eta|$  and  $\Delta\phi$  fitting the interference term, in which these parameters appear.

It is important to point out the method involving the measurement of a time dependent asymmetry using neutral kaons. By definition the time dependent asymmetry is

$$A_{\pi\pi}(t) = \frac{\text{Rate}(\overline{K}^0(t) \rightarrow \pi^+\pi^-) - \text{Rate}(K^0(t) \rightarrow \pi^+\pi^-)}{\text{Rate}(\overline{K}^0(t) \rightarrow \pi^+\pi^-) + \text{Rate}(K^0(t) \rightarrow \pi^+\pi^-)} \quad (2.19)$$

By introducing *CP* violation, it can be shown using Eq.2.11

$$A_{\pi\pi}(t) = 2\text{Re}\epsilon_K - \frac{2|\eta^{+-}|e^{\left(\frac{\Gamma_S - \Gamma_L}{2}\right)t} \cos(\Delta m_K t - \Delta\phi^{+-})}{1 + |\eta^{+-}|^2 e^{(\Gamma_S - \Gamma_L)t}} \quad (2.20)$$

This asymmetry has been measured and the value  $|\eta^{+-}| = (2.254 \pm 0.024 \pm 0.024) \times 10^{-3}$  is obtained [12]

### 2.3 $B^0 - \overline{B}^0$ System

Like the kaons, which have an associated quantum number S, the neutral particle systems called the  $D^0$  and  $B^0$  mesons, have their own quantum numbers C (charm) and B (beauty), respectively. There are two systems of neutral  $B$  mesons involving  $b$  quarks:  $B_d$  mesons consist of  $\bar{b}$ -type antiquarks and one  $d$ -quark.  $B_s$  mesons made of one  $\bar{b}$  and one  $s$ . Let us describe the  $B^0 - \overline{B}^0$  system with a formalism which can be transferred to any other system composed of a neutral particle and its antiparticle. As shown in Section 2.2, the  $K^0$  and  $\overline{K}^0$  are not physical states. Therefore, the arbitrary state

$$\psi = a|B^0\rangle + b|\overline{B}^0\rangle \quad (2.21)$$

has to satisfy the Schrödinger equation

$$i\frac{d}{dt} \begin{pmatrix} a \\ b \end{pmatrix} = H \begin{pmatrix} a \\ b \end{pmatrix} = \left(M - i\frac{\Gamma}{2}\right) \begin{pmatrix} a \\ b \end{pmatrix}. \quad (2.22)$$

$M$  and  $\Gamma$  are  $2 \times 2$  Hermitian matrices, called dispersive and absorptive parts of the transition amplitude from  $B^0$  and  $\overline{B}^0$ , respectively. The off-diagonal elements in these matrices are important for the discussion of *CP* violation. One can demonstrate [4], that due to *CPT* invariance  $H_{11} = H_{22}$  and  $H_{12} = H_{21}^*$ . The off-diagonal elements in these matrices, are particularly important in the discussion of *CP* violation. Requiring conservation of *CP* symmetry one obtains:

$$\begin{aligned} M_{11} &= M_{22} \text{ and } \Gamma_{11} = \Gamma_{22} \\ M_{12} &= M_{21} \text{ and } \Gamma_{12} = \Gamma_{21} \text{ with } M_{12} \text{ and } \Gamma_{12} \text{ real} \end{aligned} \quad (2.23)$$

In order to obtain the mass eigenstates, the matrix  $H$  has to be diagonalized. According to the treatment of the kaons, the eigenstates  $|B_S\rangle$  and  $|B_L\rangle$  can be written as

$$|B_S\rangle = p|B^0\rangle + q|\overline{B}^0\rangle, \quad |B_L\rangle = p|B^0\rangle - q|\overline{B}^0\rangle. \quad (2.24)$$

The complex coefficients  $p$  and  $q$  obey the normalization condition  $|q|^2 + |p|^2 = 1$ . The eigenstates have well defined masses and widths

$$\begin{aligned} M_S &= M_{11} + \text{Re}\sqrt{\left(M_{12} - \frac{i}{2}\Gamma_{12}\right)\left(M_{12}^* - \frac{i}{2}\Gamma_{12}^*\right)} \\ M_L &= M_{11} - \text{Re}\sqrt{\left(M_{12} - \frac{i}{2}\Gamma_{12}\right)\left(M_{12}^* - \frac{i}{2}\Gamma_{12}^*\right)} \\ \Gamma_S &= \Gamma_{11} - 2\text{Im}\sqrt{\left(M_{12} - \frac{i}{2}\Gamma_{12}\right)\left(M_{12}^* - \frac{i}{2}\Gamma_{12}^*\right)} \\ \Gamma_L &= \Gamma_{11} + 2\text{Im}\sqrt{\left(M_{12} - \frac{i}{2}\Gamma_{12}\right)\left(M_{12}^* - \frac{i}{2}\Gamma_{12}^*\right)} \end{aligned} \quad (2.25)$$

and hence

$$\begin{aligned} \Delta m &= M_L - M_S = -2\text{Re}\sqrt{\left(M_{12} - \frac{i}{2}\Gamma_{12}\right)\left(M_{12}^* - \frac{i}{2}\Gamma_{12}^*\right)} \\ \Delta\Gamma &= \Gamma_L - \Gamma_S = 4\text{Im}\sqrt{\left(M_{12} - \frac{i}{2}\Gamma_{12}\right)\left(M_{12}^* - \frac{i}{2}\Gamma_{12}^*\right)} \end{aligned} \quad (2.26)$$

The ratio  $q/p$  can be expressed in the terms of the  $M$ ,  $\Gamma$ - matrix elements:

$$\frac{q}{p} = \sqrt{\frac{M_{12}^* - \frac{i}{2}\Gamma_{12}^*}{M_{12} - \frac{i}{2}\Gamma_{12}}} \quad (2.27)$$

Since  $M_{12}$  and  $\Gamma_{12}$  are real (Eq. 2.23), if  $CP$  conservation applies, one obtains  $p/q = 1$ . Thus,  $CP$  eigenstates are

$$|B_S\rangle = \frac{|B^0\rangle + |\overline{B}^0\rangle}{\sqrt{2}} \equiv |B_+\rangle, \quad |B_L\rangle = \frac{|B^0\rangle - |\overline{B}^0\rangle}{\sqrt{2}} \equiv |B_-\rangle. \quad (2.28)$$

This would mean an ideal mixing of  $B^0$  and  $\overline{B}^0$  governed by the parameter  $x$  defined as

$$x = \frac{\Delta m}{\left(\frac{\Gamma_S + \Gamma_L}{2}\right)} = \frac{2M_{12}}{\Gamma(B^0 \rightarrow X)} \quad (2.29)$$

This parameter was measured for the  $B_d^0$  system by the experiments running on the  $\Upsilon(4S)$  resonance (*ARGUS* and *CLEO*):  $x_d = 0.708 \pm 0.080$ . Using the total width of  $B_d^0$  mesons, as derived from the lifetime measurement ( $\tau = (1.56 \pm 0.04) \times 10^{-12} \text{s}$ ), one obtains  $\Delta m_{B_d} \simeq 3.0 \cdot 10^{-4} \text{eV}$ . This quantity can be also measured directly from the observation of the period of oscillation between  $B_d^0$  and  $\overline{B}_d^0$ .

If the  $CP$  symmetry is not conserved, the physically observed states are

$$|B_S\rangle = \frac{|B_+\rangle + \epsilon|B_-\rangle}{\sqrt{1+|\epsilon|^2}}, \quad |B_L\rangle = \frac{|B_-\rangle + \epsilon|B_+\rangle}{\sqrt{1+|\epsilon|^2}}. \quad (2.30)$$

where the complex parameter  $\epsilon = \frac{p-q}{p+q}$  is \*

$$\epsilon = \frac{p-q}{p+q} = \frac{ReM_{12} - \frac{i}{2}Re\Gamma_{12} - \sqrt{(M_{12} - \frac{i}{2}\Gamma_{12})(M_{12}^* - \frac{i}{2}\Gamma_{12}^*)}}{iImM_{12} + \frac{1}{2}Im\Gamma_{12}} \quad (2.32)$$

Starting with the time dependent equations for the physical states

$$|B_S(t)\rangle = e^{-(\Gamma_S/2 + im_S)t}|B_S(0)\rangle, \quad |B_L(t)\rangle = e^{-(\Gamma_L/2 + im_L)t}|B_L(0)\rangle \quad (2.33)$$

let us examine the time evolution of  $B^0$  and  $\overline{B}^0$ , once they are created. Using Eqs. 2.28, 2.30, 2.33 one obtains

$$|B^0(t)\rangle = \frac{1}{2}e^{-(im + \frac{\Gamma}{2})t} \left[ (e^{(\frac{\Delta\Gamma}{4} + i\frac{\Delta m}{2})t} e^{-(\frac{\Delta\Gamma}{4} + i\frac{\Delta m}{2})t})|B^0\rangle + (e^{(\frac{\Delta\Gamma}{4} + i\frac{\Delta m}{2})t} - e^{-(\frac{\Delta\Gamma}{4} + i\frac{\Delta m}{2})t})\left|\frac{q}{p}\right|e^{2i\Phi_M}|\overline{B}^0\rangle \right] \quad (2.34)$$

$$|\overline{B}^0(t)\rangle = \frac{1}{2}e^{-(im + \frac{\Gamma}{2})t} \left[ (e^{(\frac{\Delta\Gamma}{4} + i\frac{\Delta m}{2})t} + e^{-(\frac{\Delta\Gamma}{4} + i\frac{\Delta m}{2})t})|\overline{B}^0\rangle + (e^{(\frac{\Delta\Gamma}{4} + i\frac{\Delta m}{2})t} - e^{-(\frac{\Delta\Gamma}{4} + i\frac{\Delta m}{2})t})\left|\frac{p}{q}\right|e^{-2i\Phi_M}|B^0\rangle \right] \quad (2.35)$$

Here, the following notations have been used:

$$\Gamma = \frac{\Gamma_S + \Gamma_L}{2}, \quad \Delta\Gamma = \Gamma_L - \Gamma_S, \quad m = \frac{m_S + m_L}{2}, \quad \Delta m = m_L - m_S. \quad (2.36)$$

Taking into account that the Standard Model predicts  $\Delta\Gamma \ll \Delta m$  for  $B_d^0$  mesons, one can compute the probability of the transition  $B^0 \rightarrow f$ :

$$\begin{aligned} | \langle f|T|B^0(t)\rangle |^2 &= e^{-\Gamma t} \left[ \cos^2 \frac{\Delta m t}{2} | \langle f|T|B^0\rangle |^2 \right. \\ &\quad + \sin^2 \frac{\Delta m t}{2} \left| \frac{q}{p} \right|^2 | \langle f|T|\overline{B}^0\rangle |^2 \\ &\quad - \frac{i}{2} \left| \frac{q}{p} \right| \sin \Delta m t e^{-2i\Phi_M} \langle f|T|B^0\rangle \langle f|T|\overline{B}^0\rangle^* \\ &\quad \left. + \frac{i}{2} \left| \frac{q}{p} \right| \sin \Delta m t e^{2i\Phi_M} \langle f|T|\overline{B}^0\rangle \langle f|T|B^0\rangle^* \right]. \end{aligned} \quad (2.37)$$

---

\*It is interesting to note, since the parameter  $|\epsilon_K|$  in the  $K^0$  system is small, this expression for  $\epsilon_K$  can be simplified:

$$\epsilon_K \simeq \frac{iImM_{12} + \frac{1}{2}Im\Gamma_{12}}{2ReM_{12} - iRe\Gamma_{12}} \simeq \frac{iImM_{12} + \frac{1}{2}Im\Gamma_{12}}{\Delta m - \frac{i}{2}\Delta\Gamma}. \quad (2.31)$$

Using the phase convention which imposes  $\Gamma_{12}$  to be real, one can obtain the value of the phase of  $\epsilon_K$  from the measured  $\Delta m_K$  and  $\Delta\Gamma_K$  [8]:  $\phi_{\epsilon_K} \simeq 43.5^\circ$ .

The time evolution for the initial  $\overline{B}^0$  can be obtained in a similar way:

$$\begin{aligned}
| \langle f | T | \overline{B}^0(t) \rangle |^2 = & e^{-\Gamma t} [\cos^2 \frac{\Delta m t}{2} | \langle f | T | \overline{B}^0 \rangle |^2 \\
& + \sin^2 \frac{\Delta m t}{2} |\frac{p}{q}|^2 | \langle f | T | B^0 \rangle |^2 \\
& + \frac{i}{2} |\frac{p}{q}| \sin \Delta m t e^{-2i\Phi_M} \langle f | T | B^0 \rangle \langle f | T | \overline{B}^0 \rangle^* \\
& - \frac{i}{2} |\frac{p}{q}| \sin \Delta m t e^{2i\Phi_M} \langle f | T | B^0 \rangle^* \langle f | T | \overline{B}^0 \rangle].
\end{aligned} \tag{2.38}$$

Equations identical to Eqs. 2.37, 2.38 can be found for the final state  $|\overline{f}\rangle \equiv CP|f\rangle$ . Thus, the comparison of all these transition probabilities may exhibit  $CP$  violation.

It is very important to note, that generation of  $CP$  non conservation can be elaborated without involving any particular theory. The  $CP$  violation effects can be classified in the following three *model independent* ways:

The flavor specific final state

The final state  $f$  can only originate from the flavor of the initial  $B^0$ , i.e. it is possible to determine unambiguously the nature of the  $B$ .

1.  $CP$  violation is observed, if

$$B \rightarrow f \neq \overline{B} \rightarrow \overline{f}$$

If no oscillation has occurred ( $B^0(t) = B^0(0)$ ) and if  $Pr(B^0(t) \rightarrow f) \neq Pr(\overline{B}^0(t) \rightarrow \overline{f})$ , then  $| \langle f | T | B^0 \rangle |^2 \neq | \langle \overline{f} | T | \overline{B}^0 \rangle |^2$ . This time independent measurement would demonstrate the so called *direct CP violation*. One should note that the charged mesons can be used as well. An example of this method revealing  $CP$  non conservation is the comparison of the branching ratio of  $B^+ \rightarrow K^+ \rho^0$  and  $B^- \rightarrow K^- \rho^0$

2.  $CP$  violation due to the  $B^0 - \overline{B}^0$  mixing is observed if

$$B^0 \rightarrow \overline{B}^0 \neq \overline{B}^0 \rightarrow B^0.$$

Let us note that this asymmetry is also an indication of  $T$  violation. In this case, one can write the asymmetry as

$$A = \frac{Pr(\overline{B}^0(t) \rightarrow f) - Pr(B^0(t) \rightarrow \overline{f})}{Pr(\overline{B}^0(t) \rightarrow f) + Pr(B^0(t) \rightarrow \overline{f})} = \frac{|\frac{p}{q}|^2 - |\frac{q}{p}|^2}{|\frac{p}{q}|^2 + |\frac{q}{p}|^2} \simeq \frac{4Re\epsilon_B}{1 + |\epsilon_B|^2} \tag{2.39}$$

The measurement of the time dependence in  $B^0 \overline{B}^0 \rightarrow l^+ l^- + X$  and  $B^0 \overline{B}^0 \rightarrow l^- l^+ + X$  can be used to observe this type of  $CP$  asymmetry.

Non flavor specific final states

Here the final states are produced from both  $B^0$  and  $\overline{B}^0$ .

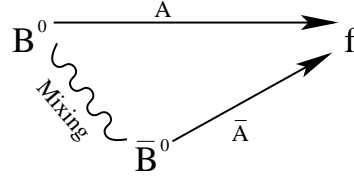
$$B^0 \rightarrow f, \quad \overline{B}^0 \rightarrow f$$

The condition above holds for several final states, but particularly for  $CP$  eigenstates:

$$CP|f_{CP}\rangle = \eta_{CP}|f_{CP}\rangle,$$

where  $\eta_{CP}$  is the  $CP$  parity of the final state ( $\eta_{CP} = \pm 1$ ).

3. In this case,  $CP$  violation can be observed by interplay between mixing and decays, e.g.:



Taking into account the  $CP$  violating phase in the decay, one has:

$$e^{-i\Phi_D} \langle f_{CP}|T|B^0\rangle \rightarrow \eta_{CP} e^{i\Phi_D} \langle f_{CP}|T|\overline{B}^0\rangle. \quad (2.40)$$

Here the phase  $\Phi_D$  is originating from the decay process. From Eqs. 2.37, 2.38, assuming the Standard Model prediction  $|\frac{q}{p}| \simeq 1$ , one gets:

$$\begin{aligned} Pr(B^0(t) \rightarrow f_{CP}) &= |\langle f_{CP}|T|B^0\rangle|^2 e^{-\Gamma t} [1 - \eta_{CP} \sin 2(\Phi_M + \Phi_D) \sin \Delta m t] \\ Pr(\overline{B}^0(t) \rightarrow f_{CP}) &= |\langle f_{CP}|T|\overline{B}^0\rangle|^2 e^{-\Gamma t} [1 + \eta_{CP} \sin 2(\Phi_M + \Phi_D) \sin \Delta m t] \end{aligned} \quad (2.41)$$

Here we assume

$$|\langle f_{CP}|T|B^0\rangle| = |\langle f_{CP}|T|\overline{B}^0\rangle| \quad (2.42)$$

Thus, the time dependence asymmetry  $As(t)$  can be expressed as

$$As(t) = \frac{Pr(\overline{B}^0(t) \rightarrow f_{CP}) - Pr(B^0(t) \rightarrow f_{CP})}{Pr(\overline{B}^0(t) \rightarrow f_{CP}) + Pr(B^0(t) \rightarrow f_{CP})} = -\eta_{CP} \sin 2(\Phi_M + \Phi_D) \sin \Delta m t. \quad (2.43)$$

Note that Eq. 2.42 is not always correct, as other terms arise in the presence of direct  $CP$  violation. An example of this time dependent asymmetry measurement is the “Gold Plated” mode  $B^0 \rightarrow J/\psi K_s^0$ .

## 2.4 *CP Violation in the Standard Model*

Non conservation of *CP* symmetry has been introduced in the Standard Model (SM) in 1973 [13], by requiring three massless families of quark and lepton doublets

$$\begin{pmatrix} u \\ d \\ \nu_e \\ e \end{pmatrix} \quad \begin{pmatrix} c \\ s \\ \nu_\mu \\ \mu \end{pmatrix} \quad \begin{pmatrix} t \\ b \\ \nu_\tau \\ \tau \end{pmatrix} \quad (2.44)$$

Amongst other things, the remarkable success of the Standard Model is demonstrated by the fact, that the measured mass of the *t* quark ( $m_t = 173.2 \pm 5.2 \text{ GeV}/c^2$  [8]) is consistent with the SM prediction derived from the measured mass ratio of the *Z* and *W* bosons. The introduction of the spontaneous  $SU(2) \times U(1)$  symmetry breaking by the Higgs mechanism [14] allows one to generate the mass of each fermion through a Yukawa type coupling. Its interaction Lagrangian can be written as

$$\mathcal{L}_{Yukawa} = - \left( \bar{\mathbf{u}}'_L \mathbf{m} \mathbf{u}'_R + \bar{\mathbf{d}}'_L \tilde{\mathbf{m}} \mathbf{d}'_R + h.c. \right) \left( 1 + \frac{\Phi_0}{v} \right), \quad (2.45)$$

where  $\Phi_0$  is the scalar field of the neutral Higgs and  $v$  is its value in the new vacuum. The quark fields  $\mathbf{u}'_{L,R}$  and  $\mathbf{d}'_{L,R}$  are vectors in flavor space for the left- and right-handed up- and down-type quarks, respectively,

$$\bar{\mathbf{u}}'_{L,R} = \frac{1 \mp \gamma_5}{2} \begin{pmatrix} u' \\ c' \\ t' \end{pmatrix}, \quad \bar{\mathbf{d}}'_{L,R} = \frac{1 \mp \gamma_5}{2} \begin{pmatrix} d' \\ s' \\ b' \end{pmatrix}, \quad (2.46)$$

$\mathbf{m}$  and  $\tilde{\mathbf{m}}$  are  $3 \times 3$  matrices of arbitrary complex numbers. Since  $\mathbf{m}$  and  $\tilde{\mathbf{m}}$  are not diagonal, one needs to define the *physical* fermion fields  $\mathbf{u}_{L,R} = V_{L,R} \mathbf{u}'_{L,R}$  and  $\mathbf{d}_{L,R} = \tilde{V}_{L,R} \mathbf{d}'_{L,R}$ , where  $V_{L,R}$  and  $\tilde{V}_{L,R}$  are unitary matrices. The mass matrices in Eq. 2.45 are diagonalized in terms of these new fields with  $\mathbf{m}_D = V_L \mathbf{m} V_R^\dagger$  and  $\tilde{\mathbf{m}}_D = \tilde{V}_L \tilde{\mathbf{m}} \tilde{V}_R^\dagger$ . The coupling to the charged  $W^\pm$  introduces the mixing between families, while the observed absence of the flavor changing neutral currents means that the coupling of the physics quarks to the neutral *Z* preserves the flavor. Thus, the interaction Lagrangian for the charged coupling is

$$\mathcal{L} = \frac{g}{\sqrt{2}} \left( \bar{\mathbf{u}}_L \gamma^\mu W_\mu^+ \mathbf{V} \mathbf{d}_L + \bar{\mathbf{d}}_L \gamma^\mu W_\mu^- \mathbf{V}^\dagger \mathbf{u}_L \right) \quad (2.47)$$

where  $\mathbf{V} = V_L \tilde{V}_L^\dagger$  is a unitary matrix called Cabibbo-Kobayashi-Maskawa (CKM) or quark-mixing matrix:

$$V = \begin{pmatrix} V_{ud} & V_{us} & V_{ub} \\ V_{cd} & V_{cs} & V_{cb} \\ V_{td} & V_{ts} & V_{tb} \end{pmatrix}. \quad (2.48)$$

The elements of the CKM matrix are related to the mass of the fermions. There were several attempts to explain this connection, but none is able to describe the experimental data. Since there exists no obvious way to deduce the values of these elements from theory, it is necessary to measure them in order to verify the predictions.

Let us see how the CKM matrix can be constructed and what are its properties. Being unitary this matrix can be constructed from a product of rotation matrices. The general expression of  $V$  can be deduced from  $n(n-1)/2$  mixing angles and  $(n-1)(n-2)/2$  phases, where  $n$  is the number of fermion families. It is interesting to note, that only with more than two families the elements of CKM matrix can be complex. Therefore only in this case  $CP$  violation can be generated through the interference of two diagrams involving different matrix elements. In particular, three mixing angles and a single phase are the *fundamental parameters* of the theory with three families. There exist many different parameterizations. The parameterization frequently used [8] is

$$V = \begin{pmatrix} C_{12}C_{13} & S_{12}C_{13} & S_{13}e^{-i\delta} \\ -S_{12}C_{23} - C_{12}S_{23}S_{13}e^{i\delta} & C_{12}C_{23} - S_{12}S_{23}S_{13}e^{i\delta} & S_{23}C_{13} \\ S_{12}S_{23} - C_{12}S_{23}S_{13}e^{i\delta} & -C_{12}S_{23} - S_{12}C_{23}S_{13}e^{i\delta} & C_{23}C_{13} \end{pmatrix} \quad (2.49)$$

where  $C_{ij} = \cos \theta_{ij}$  and  $S_{ij} = \sin \theta_{ij}$ . The unitarity of the CKM matrix leads to various relations among its elements. In particular, three of them are very useful for understanding the prediction of the SM for  $CP$  violation in different decays. They are

$$V_{ud}V_{us}^* + V_{cd}V_{cs}^* + V_{td}V_{ts}^* = 0 \quad (2.50)$$

$$V_{us}V_{ub}^* + V_{cs}V_{cb}^* + V_{ts}V_{tb}^* = 0 \quad (2.51)$$

$$V_{ud}V_{ub}^* + V_{cd}V_{cb}^* + V_{td}V_{tb}^* = 0 \quad (2.52)$$

Since these three relations imply the sum of three complex quantities to be equal zero, each of them can be geometrically presented in the complex plane as a triangle. Knowing the experimental values for the various  $|V_{ij}|$  one can easily demonstrate that only Eq. 2.52 has 3 sides of the same order. This triangle is commonly called the “Unitarity Triangle”. For the first two triangles, one side is much shorter than the others two. Therefore one can intuitively understand why  $CP$  violation is small



in  $K$  decays (Eq. 2.50).  $CP$  violation in  $B$  system is related to the third triangle. Fig 2.1 shows the rescaled Unitarity Triangle derived from Eq. 2.52 choosing a phase convention with  $|V_{cd}V_{cb}^*|$  being real and dividing the length of all sides by  $|V_{cd}V_{cb}^*|$ . Thus, two vertices of the triangle are fixed at  $(0,0)$  and  $(1,0)$  while the remaining vertex is placed at  $(\rho, \eta)$ .

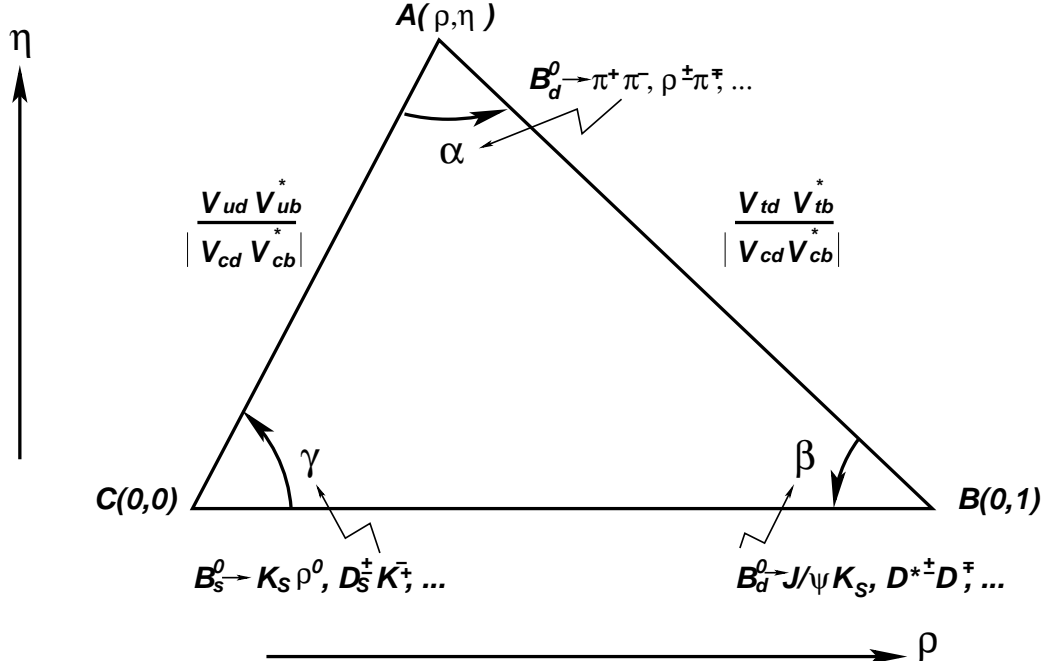


Figure 2.1: The unitarity triangle. Some  $B$  decay modes, which allow one to measure the angles are shown.

Another, (approximate) parameterization of the CKM matrix was proposed by Wolfenstein [15] with parameters  $(\lambda, A, \rho, \eta)$ :

$$V = \begin{pmatrix} 1 - \frac{\lambda^2}{2} & \lambda & A\lambda^3(\rho + i\eta) \\ -\lambda & 1 - \frac{\lambda^2}{2} & A\lambda^2 \\ A\lambda^3(1 - \rho - i\eta) & -A\lambda^2 & 1 \end{pmatrix} + \mathcal{O}(\lambda^4), \quad (2.53)$$

where  $\eta$  carries the  $CP$  violating phase information and  $\lambda = \sin \theta_C$ . The angle  $\theta_C$  is the Cabibbo angle ( $\lambda = 0.2205 \pm 0.0018$ ). This approximation is at the order of  $\lambda^3$ , which is good enough at the present experimental sensitivity.

From the present measurements of the CKM matrix elements and using the unitarity constraints, one can narrow some of the ranges and put constraints on the top mixing.

The numerical values of these elements obtained in such a way ([8]) are

$$V = \begin{pmatrix} 0.9755 \pm 0.0007 & 0.2205 \pm 0.0018 & 0.0026 \text{ to } 0.0038 \\ 0.2205 \pm 0.0018 & 0.9745 \pm 0.0008 & 0.0395 \pm 0.0020 \\ 0.0062 \text{ to } 0.0104 & 0.0395 \pm 0.0020 & 0.9993 \pm 0.0001 \end{pmatrix} \quad (2.54)$$

In order to estimate the feasibility to measure the three angles, it is useful for experimentalists to know what might be their potential values. Using the present experimental results, the region of the  $(\rho, \eta)$ -point can be constrained in the imaginary plane. The following experimental results define the region of the apex of the unitarity triangle:

- **CP violation in the neutral  $K^0$  system**

In the framework of the Standard Model the parameter  $\epsilon_K$  (Section 2.2) can be expressed as function of the  $\eta$ - and  $\rho$ - parameters:

$$|\epsilon_K| = CB_K V_{cb}^2 \eta \left[ [\eta_3 f_3(y_t) - \eta_1] y_c + \eta_2 y_t f_2(y_t) V_{cb}^2 (1 - \rho) \right] \quad (2.55)$$

Here are  $C = \frac{G_F^2 m_W^2 \lambda^2 m_K f_K^2}{6\pi^2 \sqrt{2} \Delta m_K} = (1.86 \pm 0.04) \times 10^3$ ,  $\eta_1 = 1.32 \pm 0.22$ ,  $\eta_2 = 0.57 \pm 0.01$  and  $\eta_3 = 0.47 \pm 0.04$  are the constants accounting for QCD correction factors [16], the functions  $f_2(y_i)$  and  $f_3(y_i)$  are [17]

$$f_2(y_t) = 1 - \frac{3}{4} \frac{y_t(1+y_t)}{(1-y_t)^2} \left[ 1 + \frac{2y_t}{1-y_t^2} \ln(y_t) \right]$$

$$f_3(y_t) = \ln \frac{y_t}{y_c} - \frac{3}{4} \frac{y_t}{1-y_t} \left[ 1 + \frac{y_t}{1-y_t} \ln(y_t) \right]$$

with  $y_i = \frac{m_i^2}{m_W^2}$ ,  $i = c, t$ . Using the present experimental data we can constrain the position of the apex in the  $\rho - \eta$  plane by the following equation:

$$\eta = \frac{1.32}{1 + 3.24(1 - \rho)} \times [1 \pm \underbrace{0.14}_{V_{cb}} \pm \underbrace{0.16}_{B_K} \pm \underbrace{0.05}_{m_t}] \quad (2.56)$$

- **$B_q^0 - \overline{B}_q^0$  mixing.**

Measurement of  $\Delta m_{B_d}$

The parameter  $x_d$  quantifying the mixing can be calculated in the framework of the Standard Model:

$$\Delta m_{B_d} = \frac{G_F^2}{6\pi^2} m_{B_d} m_t^2 f_2(y_t) f_B^2 B_B \eta_{QCD} |V_{td}^* V_{td}|^2 \quad (2.57)$$

where  $\eta_{QCD} = 0.55$ . The Wolfenstein parameterization for the CKM parameters gives  $|V_{td}^* V_{ts}|^2 = A^2 \lambda^6 [(1 - \rho)^2 + \eta^2]$ . Using the world average  $\Delta m_d = 0.489 \pm 0.009 \hbar ps^{-1}$  and a conservative range for  $\sqrt{B_{B^0}} f_{B^0} = 207 \pm 50 \text{ MeV}$ , one finds that the apex of the unitarity triangle has to lie in a circle described by equation:

$$\sqrt{(1 - \rho)^2 + \eta^2} = 0.95 \pm 0.24 \quad (2.58)$$

#### Measurement of $B_s^0 - \overline{B}_s^0$ oscillation

The large theoretical uncertainty on the value of  $\sqrt{B_{B_q}} f_{B_q}$  can be reduced including the measurement of  $\Delta m_{B_s}$ .

$$\frac{\Delta m_{B_s}}{\Delta m_{B_d}} = \frac{m_{B_s^0}}{m_{B_d^0}} \underbrace{\frac{B_{B_s^0} f_{B_s^0}^2}{B_{B_d^0} f_{B_d^0}^2}}_{\xi_s^2} \left| \frac{V_{ts}}{V_{td}} \right|^2 = \xi_s^2 \frac{1}{\lambda^2} \frac{1}{(1 - \rho)^2 + \eta^2} \quad (2.59)$$

where the ratio  $\xi_s = 1.14 \pm 0.08$  is slightly different from unity due to SU(3) breaking. Using the combination of the experimental results  $\Delta m_{B_s} > 14.6 \hbar ps^{-1}$ , one derives the equation

$$\sqrt{(1 - \rho)^2 + \eta^2} < 1.03 \quad (2.60)$$

#### • $|V_{ub}|$ and $|V_{cb}|$

Combining the inclusive and exclusive measurement of  $V_{ub}$  and  $V_{cb}$  [8] one derives

$$0.27 < \frac{|V_{ub}|}{\lambda |V_{cb}|} = \sqrt{\rho^2 + \eta^2} < 0.45 \quad (2.61)$$

Fig 2.2 illustrates the allowed region of  $(\rho, \eta)$  defined from the present experimental constraints (Eqs 2.56, 2.58, 2.60, 2.61). Thus, the predicted values for the unitarity angles are:

$$-0.6 \leq \sin 2\alpha \leq 0.9, \quad 0.45 \leq \sin 2\beta \leq 0.82, \quad -0.60 \leq \sin 2\gamma \leq 1 \quad (2.62)$$

## 2.5 *CP Violation Measurements in the $B^0$ System*

The most extensive study of the  $B$  meson decays up to date has been performed at  $e^+e^-$  colliders operating at the center-of-mass energy of about 10.6 GeV, corresponding to the  $\Upsilon(4S)$  resonance. Although the cross section ( $\sigma(e^+e^- \rightarrow \Upsilon(4S)) = 1.1 \text{ nb}$ ) (Fig 2.3) is not so large, it is the cleanest source of  $B\overline{B}$  pairs ( $\sim 50\%$   $B^+B^-$  and  $\sim 50\%$   $B^0\overline{B}^0$ ). It is also important to say, that no other particles are produced which allows one to get a good tagging efficiency. The main background is essentially due

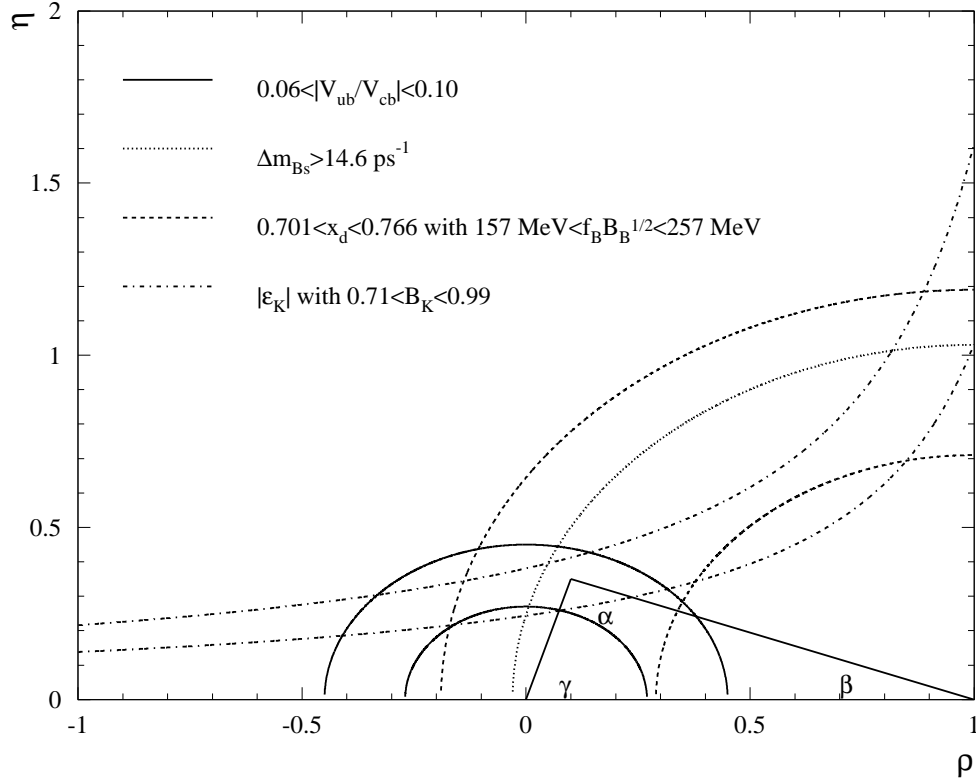
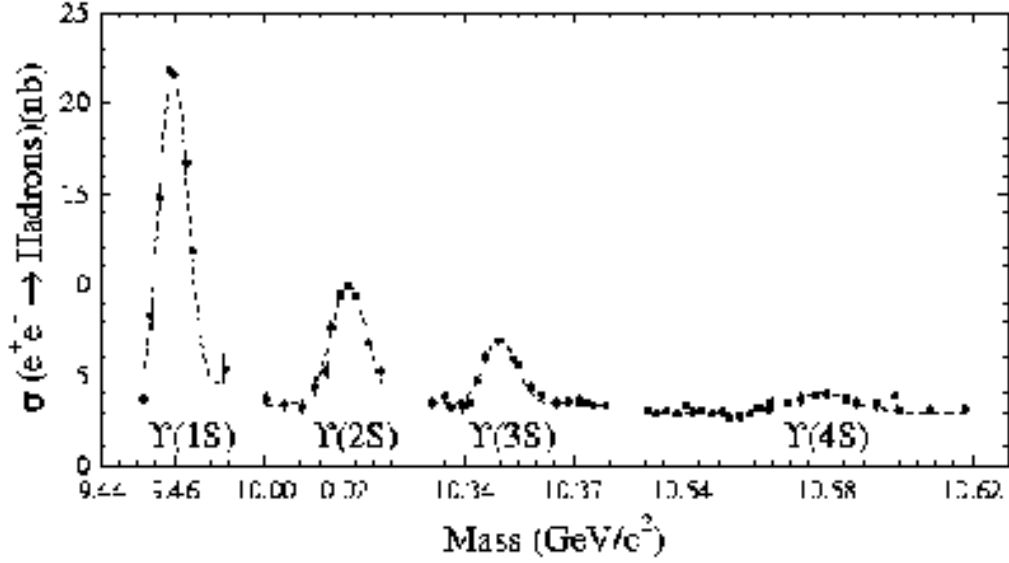


Figure 2.2: Experimental constraints of the unitarity triangle before observation of  $CP$  violation in the  $B^0$  system.

to  $q\bar{q}$  continuum events. As we will see later (Section 4.5.1) using the fact that  $B$  mesons are produced almost at rest and continuum events have a jet-like shape, this background can be significantly reduced.

In  $e^+e^-$  collisions at the  $\Upsilon(4S)$  energy (The quantum numbers of this resonance are  $J^{PC} = 1^{--}$ )  $B\bar{B}$  pairs are produced in a coherent  $L = 1$  state. For the neutral  $B$ 's that means, that at any time there is always exactly one  $B^0$  and one  $\bar{B}^0$  until one of them decays. Thus, only at that time the nature of the second meson ( $B^0$  or  $\bar{B}^0$ ) is defined. However, if one of the particles decays, the other continues to evolve, and therefore events with two  $B^0$  or two  $\bar{B}^0$  decays may happen. Thus, one should consider the  $B\bar{B}$  system as a whole instead of individual  $B$  mesons. Since the wave function of the  $B\bar{B}$  pair is antisymmetric

$$\frac{|B(t_1)\bar{B}(t_2) - |\bar{B}(t_1)B(t_2)|}{\sqrt{2}} > 0 \quad (2.63)$$

Figure 2.3: Hadronic cross section in the  $\Upsilon$  region.

Eqs. 2.37, 2.38 read as

$$\begin{aligned}
 Pr(\overline{B}^0(t_1)_{tag}, B(t_2) \rightarrow f) = & e^{-\Gamma(t_1+t_2)} [\cos^2 \frac{\Delta m \Delta t}{2} | \langle f|T|B^0 \rangle |^2 \\
 & + \sin^2 \frac{\Delta m \Delta t}{2} | \frac{q}{p} |^2 | \langle f|T|\overline{B}^0 \rangle |^2 \\
 & - \frac{i}{2} | \frac{q}{p} | \sin \Delta m \Delta t e^{-2i\Phi_M} \langle f|T|B^0 \rangle \langle f|T|\overline{B}^0 \rangle^* \\
 & + \frac{i}{2} | \frac{q}{p} | \sin \Delta m \Delta t e^{2i\Phi_M} \langle f|T|B^0 \rangle^* \langle f|T|\overline{B}^0 \rangle ].
 \end{aligned} \tag{2.64}$$

$$\begin{aligned}
 Pr(B^0(t_1)_{tag}, B(t_2) \rightarrow f) = & e^{-\Gamma(t_1+t_2)} [\cos^2 \frac{\Delta m \Delta t}{2} | \langle f|T|\overline{B}^0 \rangle |^2 \\
 & + \sin^2 \frac{\Delta m \Delta t}{2} | \frac{p}{q} |^2 | \langle f|T|B^0 \rangle |^2 \\
 & + \frac{i}{2} | \frac{p}{q} | \sin \Delta m \Delta t e^{-2i\Phi_M} \langle f|T|B^0 \rangle \langle f|T|\overline{B}^0 \rangle^* \\
 & - \frac{i}{2} | \frac{p}{q} | \sin \Delta m \Delta t e^{2i\Phi_M} \langle f|T|B^0 \rangle^* \langle f|T|\overline{B}^0 \rangle ].
 \end{aligned} \tag{2.65}$$

As it can be seen, this probability is governed by the time between the two decays, i.e. the reference time,  $t_0$ , is not the  $\Upsilon(4S)$  decay time anymore, but the time at which one of the  $B$  mesons is identified. The consequence of this is that it is mandatory to measure  $\Delta t$  if one wants to use the interplay of  $B$  decays and  $B^0 - \overline{B}^0$  mixing for  $CP$  violation search. If  $\Delta t$  is not measured and one needs to integrate the time dependence, the  $\sin \Delta m \Delta t$  vanishes. This fact can be easily demonstrated for  $B \rightarrow f_{CP}$ , for which

the transition probability is

$$Pr\left(\overset{(-)}{B^0}(t_1)_{tag}, B(t_2) \rightarrow f_{CP}\right) \propto e^{-\frac{\Delta t}{\tau}} \left[1 + \overset{(-)}{\eta_{CP}} \sin 2\Phi \sin \Delta m_B \Delta t\right] \quad (2.66)$$

Therefore, for the asymmetry as defined in Eq. 2.42, one obtains

$$A_{CP}(\Delta t) == -\eta_{CP} \sin 2\Phi \sin(\Delta m \Delta t). \quad (2.67)$$

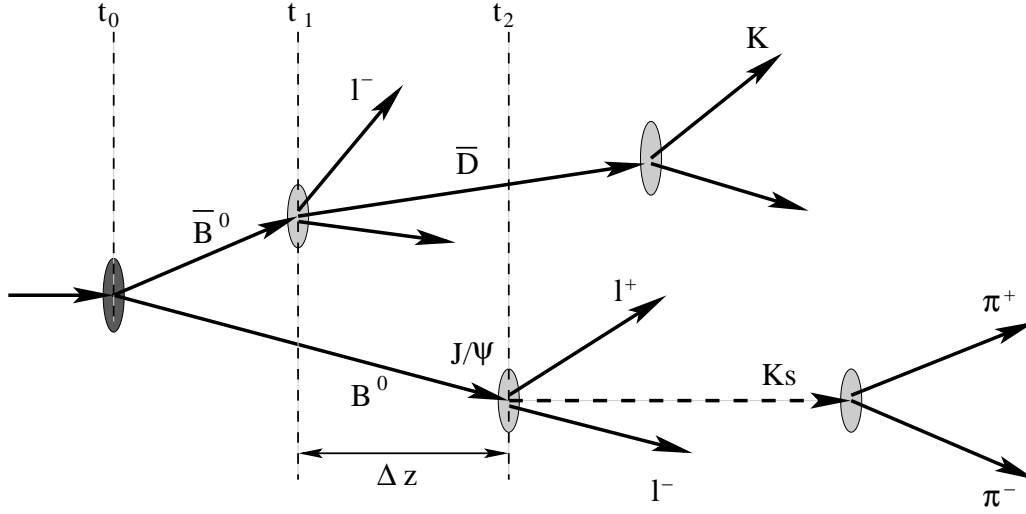


Figure 2.4: A schematic view of an interaction with asymmetric beam energy.

The time between two  $B$  decays has to be measured as the flight distance of the  $B$  meson using  $L = \beta\gamma ct$ . As it was mentioned above,  $B$  mesons originate almost at rest ( $P_B \simeq 300 \text{ MeV}$ ) in the  $\Upsilon(4S)$  center of mass. Therefore the average distance between two  $B$  decay vertices is about  $50\mu\text{m}$ , which is the same order of magnitude as the resolution obtained with the present detector technology and is limited by the multiple scattering. Now let us assume that the  $\Upsilon(4S)$  resonance is produced with a boost  $\beta\gamma$ . Fig 2.4 shows how a typical  $B\bar{B}$  event may look like. The distance  $\Delta z$  can be expressed as

$$\Delta z = \beta\gamma c\tau \left[ \frac{t_2 - t_1}{\tau} \right] + \gamma\beta_{cm} c\tau \cos \theta_B^* \left[ \frac{t_2 + t_1}{\tau} \right], \quad (2.68)$$

where  $\beta\gamma$  is the boost of the  $\Upsilon(4S)$ ,  $c\tau$  is the average flight distance of a  $B$  meson and  $\beta_{cm}$  is its velocity in the  $\Upsilon(4S)$  center of mass ( $\beta_{cm} \simeq 0.07$ ),  $\theta_B^*$  is the angle between  $B$  meson produced in the  $\Upsilon(4S)$  rest frame with respect to the beam direction. For most studies the last term in Eq. 2.68 can be neglected. Thus, assuming  $\beta\gamma \simeq 0.56$ , one obtains  $\beta\gamma c\tau \approx 250\mu\text{m}$ , which is measurable with today's technique.

Besides the measurement of  $\Delta z$  the flavor of the  $B^0$  at time  $t = t_0$  has to be determined. There are several techniques for **tagging** the initial flavor of a  $B$  meson. They are based on the determination of the charge of the  $b$  quark. The most useful methods are tagging using leptons and kaons.

- The Lepton Tagging

The charge of the  $b$  quark in the decays  $b \rightarrow cl\nu$  can be deduced by the charge of the lepton. Since the total inclusive branching fraction ( $\mathcal{B}(B \rightarrow X_c e \nu_e) + \mathcal{B}(B \rightarrow X_c \mu \nu_\mu)$ ) is about 20%, this is very attractive.

- The Kaon Tagging

In the direct cascade  $b \rightarrow c \rightarrow s$ , the charge of the  $s$  quark is the same as the charge of  $b$ , and therefore, if the  $s$  quark produces a charged kaon, its charge should have the same sign as the charge of the initial  $b$ .

## 2.6 Observation of $CP$ Violation in the $B^0$ System

The observation of  $CP$  violation in the  $B^0$  system has been recently reported by the BABAR collaboration [18]. The complete data sample collected in 1999-2001, which consists of 32 million produced  $B\bar{B}$  pairs, has been used to fully reconstruct a sample of neutral  $B$  mesons decaying into  $CP$  eigenstates such as  $f = J/\psi K_S^0$ ,  $\psi(2S)K_S^0$ ,  $J/\psi K_L^0$ ,  $\chi_{c1}K_S^0$  and  $J/\psi K^{*0}(K^{*0} \rightarrow K_S^0 \pi^0)$  ( $B_{CP}$ )<sup>†</sup>.

In the Standard Model, for the decays  $b \rightarrow c\bar{c}s$ , the time dependent decay asymmetry is given by (Eq. 2.67)

$$A_{CP}(\Delta t) = -\eta_{CP} \sin 2\beta \sin(\Delta m_{B^0} \Delta t). \quad (2.69)$$

where  $\eta_{CP}$  is the  $CP$ -eigenvalue of the state  $f$  and  $\beta \equiv \Phi = \arg(-V_{cd}V_{cb}^*/V_{td}V_{tb}^*)$  is the  $CP$  violating phase in the unitarity triangle.  $\eta_{CP} = -1$  for  $J/\psi K_S^0$ ,  $\psi(2S)K_S^0$  and  $\chi_{c1}K_S^0$  and  $+1$  for  $J/\psi K_L^0$ . Fig 2.5 shows the resulting beam-energy substituted mass  $m_{ES} = \sqrt{(E_{beam}^{cm})^2 - (p_B^{cm})^2}$  distribution for  $B_{CP}$  candidates with  $K_S^0$  in the final state ( $\eta_{CP} = -1$ ) and the difference  $\Delta E$  between the energy of the candidates containing a  $K_L^0$  ( $\eta_{CP} = +1$ ) and the beam-energy in the center-of-mass (Section 4.5.1).

As shown in Sec.2.5, the measurement of  $CP$  asymmetry requires determination of  $\Delta t = t_{CP} - t_{tag}$ . It is also important to determine the fraction of events  $w$ , in which the tag assignment is incorrect. A potential mistag reduces the observed  $CP$  asymmetry by a factor  $(1 - 2w)$ . Two other  $B$  samples are necessary for the determination of the mistag fraction, one for the determination of  $\Delta t$  resolution ( $B_{flav}$  sample) and another

---

<sup>†</sup>  $J/\psi K^{*0}(K^{*0} \rightarrow K_S^0 \pi^0)$  state is not a pure  $CP$  eigenstate. Therefore, one needs to do the angular analysis to define the fraction of  $CP$ -odd eigenstate [19].

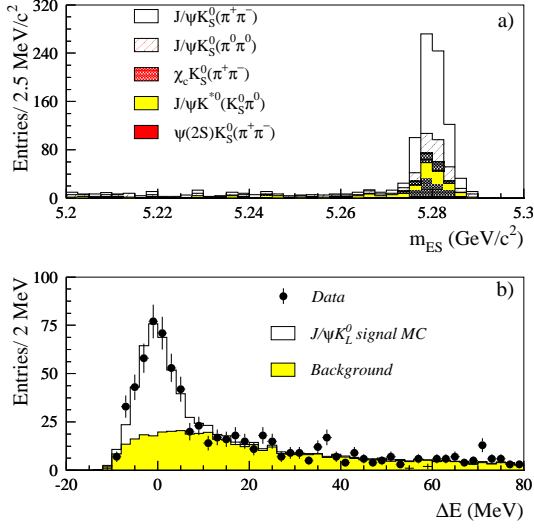


Figure 2.5: a) Distribution of  $M_{ES}$  for  $B_{CP}$  candidates having a  $K_S^0$  in the final state ( $\eta_{CP} = -1$ ); b) distribution of  $\Delta E$  for  $J/\psi K_L^0$  candidates ( $\eta_{CP} = +1$ ).

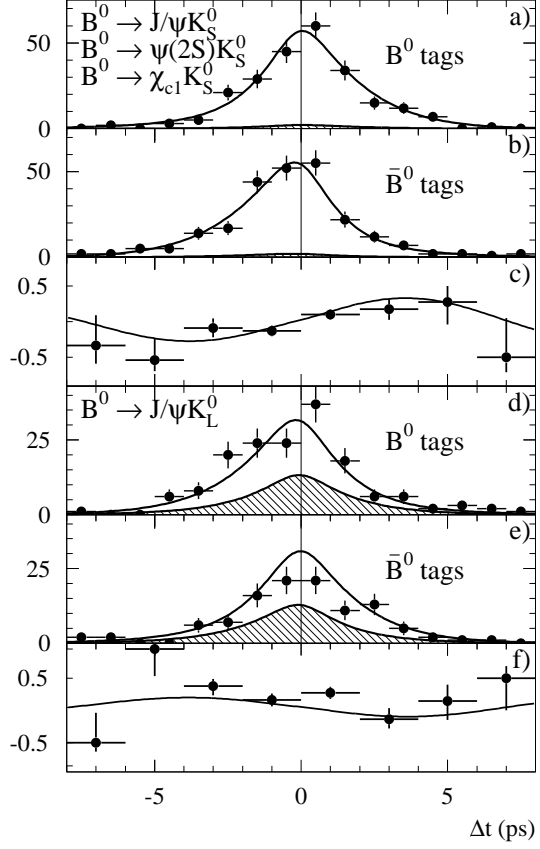


Figure 2.6: The time dependent asymmetry. Number of candidates having a  $K_S^0$  in the final state ( $\eta_{CP} = -1$ ) in the signal region a) with a  $B^0$  tag  $N_{B^0}$  and b) with a  $\bar{B}^0$  tag  $N_{\bar{B}^0}$  and c) the asymmetry as a function of  $\Delta t$ . The plots d)-f) present the corresponding information for  $J/\psi K_L^0$  mode ( $\eta_{CP} = +1$ ).

one for validation studies. The  $B_{flav}$  sample consists of the channels  $D^{(*)-}h^+(h^+ = \pi^+, \rho^+, a_1^+)$  and  $J/\psi K^{*0}(K^{*0} \rightarrow K^+\pi^-)$ . The control sample for validation studies consists of charged  $B$  mesons decaying to the final states  $J/\psi K^+$ ,  $\psi(2S)K^+$ ,  $\chi_{c1}K^+$  and  $\bar{D}^{(*)0}\pi^+$ .

The second  $B$  of the produced  $B\bar{B}$  state is used for flavor tagging. Each event is assigned one of four exclusive tagging categories. The Lepton and Kaon categories contain events with high momentum leptons or with kaons. The two other categories are based on neural network algorithms whose tagging power originates primarily from soft pion detection of  $D^{*+}$  decays and from recovering unidentified primary leptons.



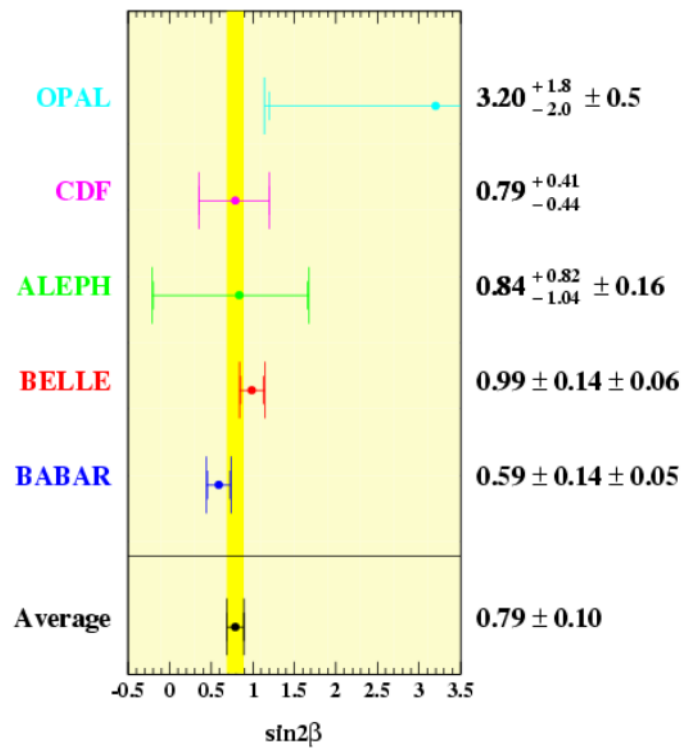
The number of tagged events for the  $B_{CP}$  sample was 801, with an average purity of about 80%, while the  $B_{flav}$  and control  $B$  charged samples contain 7591 and 6814 tagged events, respectively.

The time difference  $\Delta t$  between the two  $B$  vertices is determined from  $\Delta z = z_{CP} - z_{tag}$  including an event-by-event correction for the direction of the  $B$  with respect to the  $z$  direction in the  $\Upsilon(4S)$  rest frame (Eq. 2.68). The tagging vertex is defined by fitting the tracks not coming from the  $B_{CP}$  or  $B_{flav}$  candidate to a common vertex. The achieved  $\Delta z$  resolution is reproduced by 2 Gaussians of  $100\mu m$  and  $190\mu m$ . The narrow Gaussian represents about 70% of the events.

Fig 2.6 shows the number of  $B_{CP}$  candidates and  $A_{CP}$  as a function of  $\Delta t$  overlaid with the likelihood fit result for  $\eta_{CP} = -1$  and  $\eta_{CP} = +1$  samples. The combined fit to the  $CP$  modes and the flavor decay modes gives

$$\sin 2\beta = 0.59 \pm 0.14(\text{stat}) \pm 0.05(\text{syst}) \quad (2.70)$$

For the control sample of charged  $B$   $\sin 2\beta = 0.03 \pm 0.04$  was found, which is well consistent with zero. The measured value of  $\sin 2\beta$  establishes  $CP$  violation in  $B$  decays at the  $4.1\sigma$  level. The probability of obtaining this result in absence of  $CP$  violation is less than  $3 \cdot 10^{-5}$ . This result is consistent with the range implied by the present experimental constraints (Eq. 2.62). Fig. 2.7 shows graphically the existing  $\sin 2\beta$  measurements from all experiments. The world average number is also presented on this plot.

Figure 2.7: Graphical displays of existing  $\sin 2\beta$  measurements.

## Chapter 3

# The $B_A B_{AR}$ Experiment

The primary goal of the *BABAR* experiment is a systematic study of the  $CP$  violation in the decays of  $B$  mesons. As it was pointed out in sec 2.5, the  $\Upsilon(4S)$  resonance is a very good source for studying  $B$  mesons. Due to a limited phase space, the  $B$  mesons from  $\Upsilon(4S) \rightarrow B\bar{B}$  decay are produced almost at rest in the center of mass frame. The asymmetry in the beam energies allows one to boost the  $B$  mesons with a significant momentum in the laboratory frame. This enables the measurement of the time-dependent  $CP$  asymmetry in the decays of neutral  $B$  mesons.

Since  $CP$  violating effects in  $B$  system are expected to be large, a relatively small sample of the event allows one to perform significant measurement. Unfortunately, the decay channels which are interesting for the  $CP$  violation, have very small branching fractions (of the order of  $10^{-4}$ ). Therefore, a large sample of  $B$ 's (about  $10^7$ ) is necessary to perform these measurements. Thus, the accelerator luminosity must be a few  $10^{33} \text{ cm}^{-2} \text{ sec}^{-1}$ .

### 3.1 The PEP-II $e^+e^-$ asymmetric $B$ Factory

The accelerator complex PEP-II/*BABAR* is located at the Stanford Linear Accelerator Center (SLAC). PEP-II [20] is an  $e^+e^-$  storage ring system designed to produce a luminosity of at least  $3 \times 10^{33} \text{ cm}^{-2} \text{ sec}^{-1}$ , and operates at a center of mass energy corresponding to the  $\Upsilon(4S)$  resonance at  $\sqrt{s} = 10.58 \text{ GeV}$ . The asymmetric energies of 9 GeV for the electron and of 3.1 GeV for the positron beam provide a boost in the laboratory frame of  $\beta\gamma=0.56$ . Such collisions produce  $B$  mesons with two decay vertices separated by about  $\beta\gamma c\tau=250 \mu\text{m}$ .

PEP-II consists of a High Energy Ring (HER) for electrons and a Low Energy Ring (LER) for positrons as it is shown in Fig. 3.1. The HER replaces the old PEP machine,

while LER is put on the top of HER. Table 3.1 shows the PEP-II designed parameters and the average obtained during the first year operation. The designed number of particles per bunch is  $2.1 \times 10^{10}$  for the electrons and  $5.9 \times 10^{10}$  for the positrons.

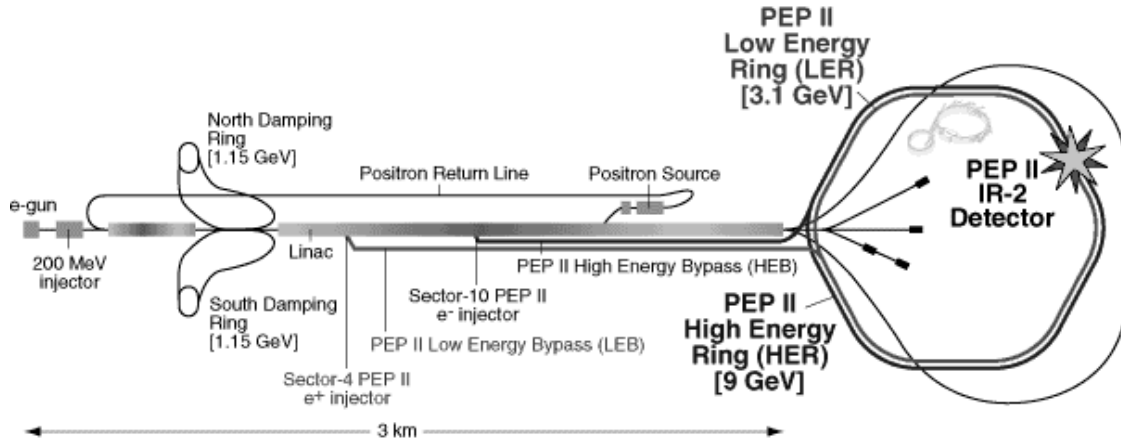


Figure 3.1: The PEP-II/*BABAR* accelerator complex.

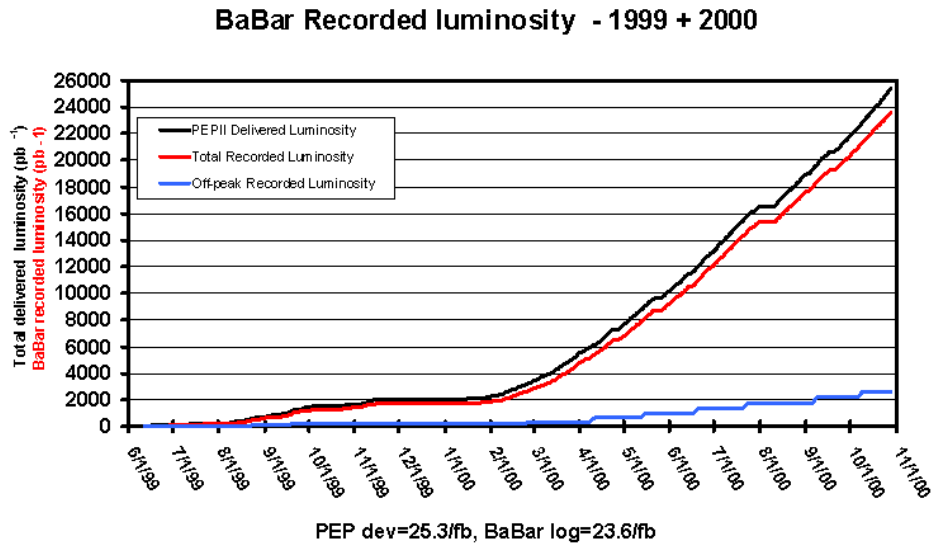


Figure 3.2: The PEP-II/*BABAR* integrated luminosity in 1999-2000.

The most crucial parameters for the *BABAR* detector are the luminosity, the energies and the sizes and position of the beams. Bhabha scattering is used for the online fast monitoring of the luminosity, while the more accurate offline measurement of the

Parameters	Design	Average
Energy HER/LER (GeV)	9.0/3.1	9.0/3.1
Current HER/LER (A)	0.75/2.15	0.7/1.3
Number of bunches	1658	553-829
Bunch spacing (ns)	4.2	6.3-10.5
$\sigma_x$ ( $\mu\text{m}$ )	110	120
$\sigma_y$ ( $\mu\text{m}$ )	3.3	5.6
$\sigma_z$ (mm)	9	9
Luminosity ( $10^{33} \text{ cm}^2 \text{ s}^{-1}$ )	3	2.5
Luminosity ( $\text{pb}^{-1}/\text{day}$ )	135	120

Table 3.1: PEP-II parameters. Values are given for the design and average during the first year of operation. The notations HER and LER means the high energy  $e^-$  and low energy  $e^+$  ring, respectively.  $\sigma_x$ ,  $\sigma_y$  and  $\sigma_z$  refer to the horizontal, vertical and longitudinal rms of the bunches.

luminosity is performed mainly using processes like  $e^+e^-$  and  $\mu^+\mu^-$ . The systematic uncertainty of the relative changes of the luminosity is about 0.5% while the absolute value of the luminosity has a systematic error about 1.5%. A data sample of  $1 \text{ fb}^{-1}$  provides a statistical error at the 1% level.

The accuracy of the relative setting of the beam energies is about 1 MeV. The beam energy is calculated from the average deviation of the accelerating frequency from the central value and the total magnetic bending strength. The accuracy for the absolute value is estimated to be about 5-10 MeV. The ratio of the  $B\bar{B}$  hadronic events to the number of lepton pairs monitoring is used to ensure that the data are taken at the  $\Upsilon(4S)$  resonance. A 2.5% variation of this value near the peak corresponds to a 2 MeV change in the center of mass energy.

The sizes and position of the beams which play an important role in all time-dependent measurements are defined online and offline continuously by analyzing the well measured two-track events.

Although most of data are taken at the  $\Upsilon(4S)$  resonance energy (“on-resonance”), about 12% are recorded about 40 MeV below the  $\Upsilon(4S)$  mass (“off-resonance”), which is necessary for studying the non-resonant background. Fig. 3.2 shows the integrated luminosity delivered by PEP-II and recorded by the *BABAR* detector in 1999-2000. The recorded off-resonance data are shown as well.

## 3.2 The BABAR detector

The BABAR detector (Fig. 3.3) [22] measures the charged particles by a combination of a five-layer (double-sided) silicon vertex tracker (SVT), which provides the measurements of the impact parameters and the track angles, and of a 40-layer central drift chamber (DCH) used for the measurements of the track momentum and its energy loss. The tracking system is embedded in a 1.5 T solenoidal field produced by a superconducting magnetic coil and provides good momentum resolution. The DCH is surrounded by the Detector of Internally Reflected Cherenkov Light (DIRC). It consists of 12 sectors of quartz bars read out by a matrix of about 11000 photo-tubes arranged on the internal surface of a water tank. The electromagnetic showers are measured by the Electromagnetic Calorimeter (EMC) composed of CsI(Tl) crystals. The Instrumented Flux Return (IFR) with resistive plate chambers provides the identification of the muons and neutral hadrons. Charged hadrons are identified using the ionization energy loss ( $dE/dx$ ) measured in the DCH and SVT, and the Cherenkov radiation detected in the DIRC.

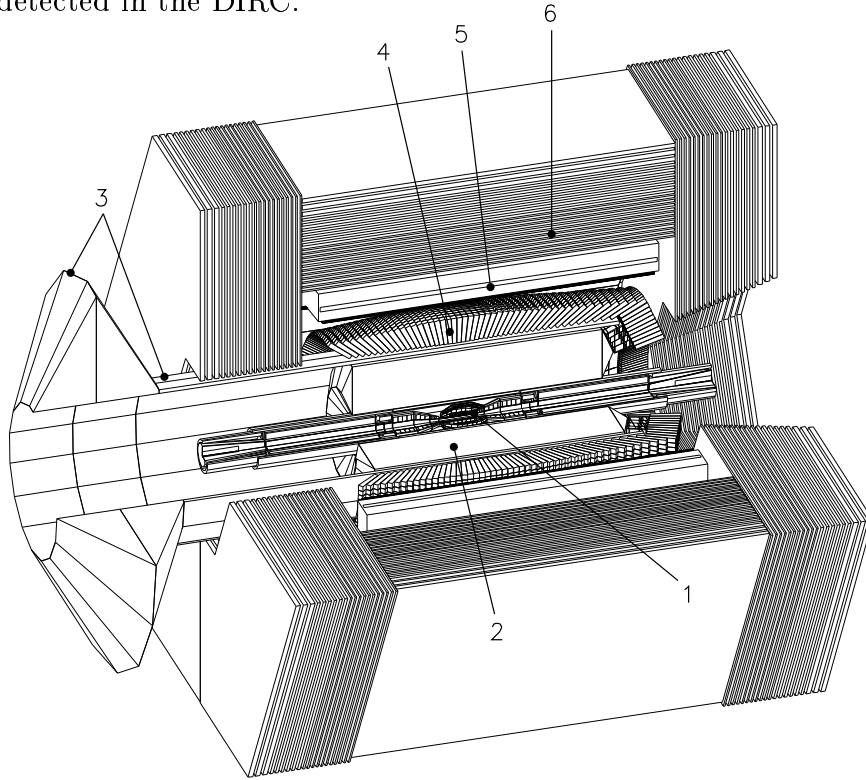


Figure 3.3: The BABAR Detector. 1. Silicon Vertex Tracker (SVT), 2. Drift Chamber (DCH), 3. Particle Identification Subsystem (DIRC–Detector of Internally Reflected Cherenkov Light), 4. Electromagnetic Calorimeter (EMC), 5. Magnet, 6. Instrumented Flux Return (IFR).

### 3.2.1 The Silicon Vertex Tracker (SVT)

The Silicon Vertex Tracker (SVT) provides the required vertex resolution for the measurement of the  $CP$  violation and other decay-time-dependence measurements. In addition, when the charged particles have a low transverse momentum ( $p_T < 120 \text{ MeV}/c$ ) and cannot be measured by the central drift chamber, the SVT is capable to act as an independent tracker.

Fig. 3.4 shows a schematic view of the SVT. Its design has been studied in order to minimize the multiple scattering. It takes into account the physical constraints imposed by the PEP-II geometry, such as the presence of the permanent magnets nearby the interaction point, which are necessary to separate the beams shortly after the interaction point. The polar angle acceptance  $\theta$  is  $-0.87 < \cos \theta_{lab} < 0.96$  ( $-0.95 < \cos \theta_{cm} < 0.87$ ) and is limited by the beamline elements. A detailed description of the SVT and its components can be found in Ref. [23].

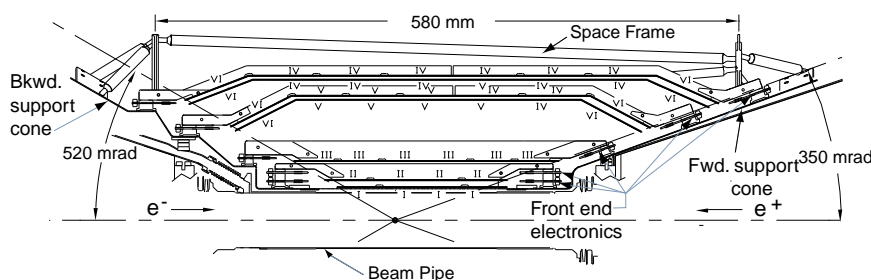


Figure 3.4: Schematic view of SVT.

The SVT consists of five double-sided layers of the silicon detectors assembled on carbon fiber support cones. The first three layers provide the tracking resolution while the last two are necessary to measure the low momentum tracks independently from the drift chamber information. The modules are read out by a special low-noise radiation-hard chip mounted on a passive circuit. The single hit resolution in azimuthal and longitudinal planes is shown in Fig. 3.5. The achieved average hit reconstruction efficiency is above 98%. The SVT precision determines the impact parameter resolution for the measurement of high transverse momentum tracks, where the distance between two vertices is reconstructed with a resolution of about  $50 \mu\text{m}$ . Two  $B$  decay vertices are separated with a typical accuracy of  $110 \mu\text{m}$ .

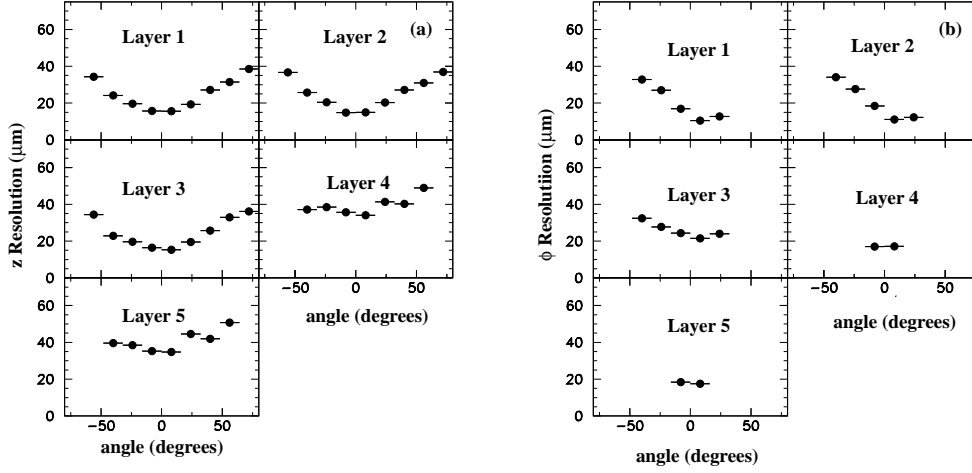


Figure 3.5: The SVT resolution in  $z$ (left) and  $\phi$ (right) coordinates in microns as a function of the angle of incidence of the tracks.

### 3.2.2 The Drift Chamber (DCH)

The main purpose of the Drift Chamber (DCH) is the precise and efficient measurement of charge particle parameters such as momenta and angles, with transverse momenta  $p_T$  above about 120 MeV/c. The DCH complements the information about the impact parameter and the direction of the track measured by the SVT. The reconstruction of decay vertices, for example  $K_S^0$ , outside of the SVT requires, in addition to the transverse momenta and position, the measurement of the longitudinal position with an accuracy of about 1 mm. The DCH has also to provide the particle identification at relatively low momenta by measuring the ionization loss ( $dE/dx$ ) and has to supply information for the charge particle trigger.

Fig. 3.6 shows a schematic view of the DCH. It has an outer radius of 80.9 cm and a length of 280 cm. The interaction point is shifted by 36.7 cm relatively to the center of the chamber, in order to improve the forward acceptance, given the asymmetric boost for the  $\Upsilon(4S)$  events. The acceptance of the DCH covers the polar angle  $-0.92 < \cos \theta_{lab} < 0.96$ . 40 layers of small hexagonal cells provide spatial and amplitude measurements. Each hexagonal cell consists of a  $20 \mu\text{m}$  rhenium-tungsten sense wire operating nominally in the range 1900–1960 V. It is surrounded by 6 cathode wires. The longitudinal position is measured by placing the wires in 24 layers at a small angle with respect to the  $z$ -axis.

The Drift Chamber provides an average single point resolution of  $125 \mu\text{m}$ . Fig. 3.7 shows the single cell resolution as a function of the drift distance, obtained from an ensemble of charged tracks (operation at 1960 V). The design of the drift chamber





for the different types of particles is shown in Fig. 3.8. The mean  $dE/dx$  resolution of 7% provides a  $\pi/K$  separation up to 700 MeV/c.

Each four layers are grouped in one superlayer with the same orientation for sense and field wires within a given superlayer. This structure allows one to perform a fast local segment finding as the first step in pattern recognition. The information from all superlayers is included in the Level-1 trigger track finding, while only the axial superlayers are involved in the Level-1 trigger  $p_T$  determination.

The tracking system consisting of the central drift chamber and the vertex tracker is arranged inside a magnetic field of 1.5 T produced by a superconducting magnet. It provides a typical momentum resolution of

$$\delta p_T/p_T = (0.13 \pm 0.01)\% \cdot p_T + (0.45 \pm 0.03)\%, \quad (3.1)$$

where  $p_T$  is given in GeV/c.

### 3.2.3 The Detector of Internally Reflected Cherenkov light (DIRC)

As shown in Section 2.5, the study of  $CP$  violation requires the ability to tag the flavor of one of the  $B$  mesons and to fully reconstruct the second  $B$  decay. The maximal momenta of the kaons used for the tagging of  $B$  via decay cascade  $b \rightarrow c \rightarrow s$  are about 2 GeV/c. In contrast, the pions and kaons from the rare two-body decays  $B^0 \rightarrow \pi^+\pi^-$ ,  $K^+\pi^-$  have momenta between 1.7 and 4.2 GeV/c.

The *Detector of Internally Reflected Cherenkov light* (DIRC) [24] is the principal particle identification system of the BABAR detector. Fig. 3.9 shows the basic principle of the DIRC. Charged particles, produced at the interaction point inside the detector, traverse the quartz bars in which Cherenkov radiation is produced. The angle of this radiation ( $\theta_c$ ) with respect to the incident particles is a measure of the velocity of these particles ( $v$ ) from the equation  $\cos\theta_c = 1/n\beta$  ( $\beta = v/c$ ,  $v$  - velocity of the particle,  $c$ -velocity of light,  $n=1.473$  - mean refractive index of the quartz radiator). The Cherenkov photons propagate along the rectilinear bars by total internal reflection, preserving the angular information and exiting outside the detector into a large pure water tank, called the standoff box. Using the position of the photo-tube and the arrival time of the signals, the DIRC is a three-dimensional imaging device. Since the tracking system provides the track position and the angles, the measured photon propagation angles are used to determine the Cherenkov angle. The arrival time of the signal can be also related to the propagation angles and provides an additional constraint, which is very useful to avoid ambiguities in the signal association due to high background rates.

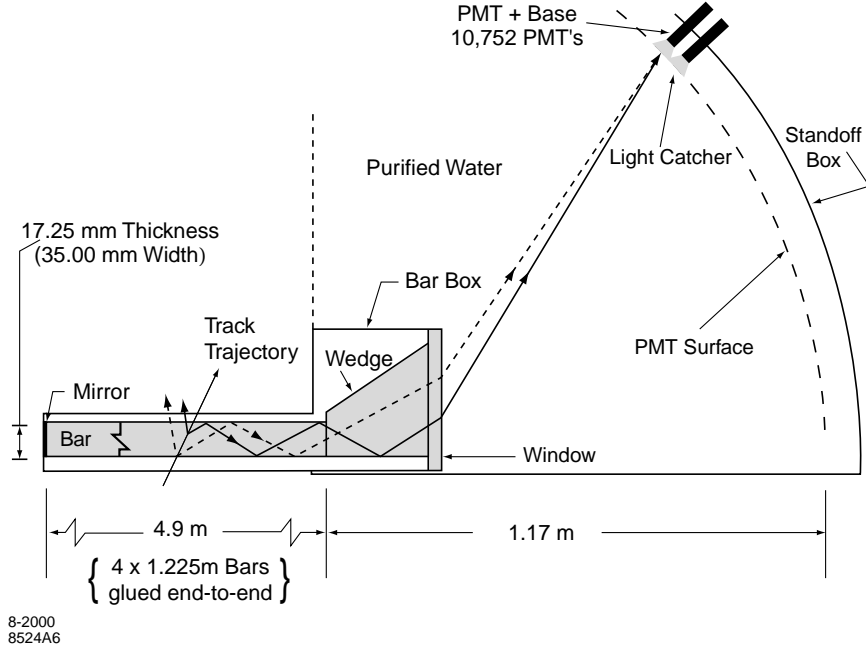


Figure 3.9: Schematic view of DIRC quartz radiator bar and the photon detection region.

The DIRC consists of quartz bars inside the detector and of the standoff box, supporting photomultipliers outside the detector at the backward end. The bars are supported by a mechanical structure which is attached to the barrel iron via special structural elements. The water tank is composed of a cylinder, a cone and 12 cylindrical sections. 10752 photomultipliers are mounted on the sectors placed at about 1.17 meters from the exit point to permit a precise measurement of the angle for each photon. The standoff box is arranged inside a special low magnetic field volume ([25]) which diminishes the value of the fringe fields from the main solenoid.

A single photon angular resolution of about 10.2 mrad with an average of 30 photons per track corresponds to about 2.8 mrad for the Cherenkov angle. With a timing precision of 1.7 ns the separation between charged kaons and pions is approximately three standard deviation at 3.5 GeV/ $c$ .

The selection efficiency and misidentification for kinematically identified kaon and pion tracks from the  $D^{*+} \rightarrow D^0 \pi^+$ ,  $D^0 \rightarrow K^- \pi^+$  sample are shown in Figs. 3.10, 3.11 as a function of track momentum.

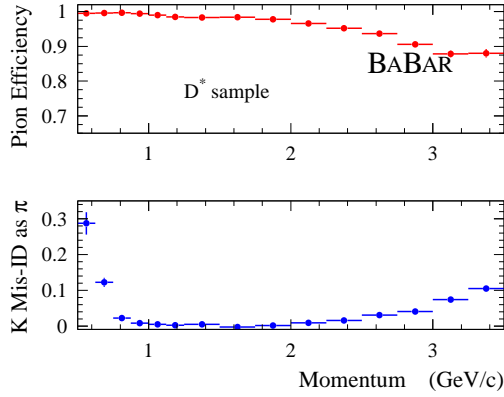


Figure 3.10: The efficiency and misidentification for pion tracks

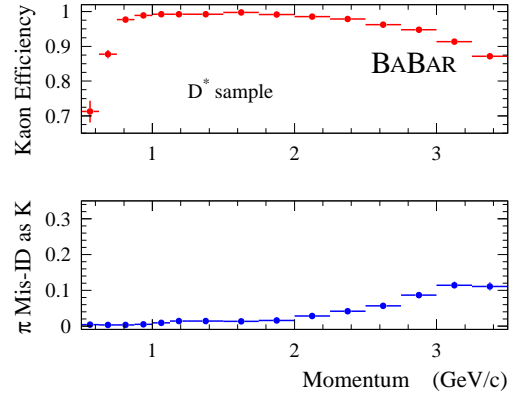


Figure 3.11: The efficiency and misidentification for kaon tracks

### 3.2.4 The Electromagnetic Calorimeter (EMC)

The Electromagnetic Calorimeter (EMC) provides the measurement of electromagnetic showers with high efficiency and good energy and angular resolution. The energy range from 20 MeV to 9 GeV covered by EMC is required to detect the photons from  $\pi^0$  and  $\eta$  as well as from radiative and electromagnetic processes. The QED processes, like  $e^+e^- \rightarrow e^+e^- (\gamma)$  and  $e^+e^- \rightarrow e^+e^-$ , used for the calibration and luminosity measurements sets the high limit, while the capability to reconstruct the  $B$  mesons in modes containing multiple  $\pi^0$  and  $\eta$  with high efficiency set the low limit.

The Electromagnetic Calorimeter (EMC) (Fig. 3.12) covers polar angles of  $-0.78 < \cos \theta_{lab} < 0.96$ . It contains 6580 CsI crystals doped with thallium iodide at about 1000 ppm. Each crystal has the shape of a trapezoidal pyramid. The crystals range from 16 to 17.5 radiation lengths in thickness. The front faces are typically  $\sim 5$  cm in each dimension.

Each crystal is wrapped with a diffuse reflective material (TYVEK) and housed in a thin eggcrate-like carbon fiber composite mechanical structure. There are 280 such modules in the barrel (7 types, 40 of each type) and 20 identical endcap modules. The crystals are read out with two independent PIN photodiodes ( $2 \text{ cm}^2$  area) glued to their rear faces. Dual-range preamplifiers are arranged directly behind the photodiodes in a shielded housing, that also provides a thermal path for heat removal. Shielded ribbon cables carry analog signals to the end flanges of the barrel and the back plate of the endcap, where additional amplification and digitizing electronics are mounted providing a total of four overlapping linear ranges.

The energy resolution is measured directly with a radioactive source at low energies and with electrons from Bhabha scattering at high energies, yielding resolutions of

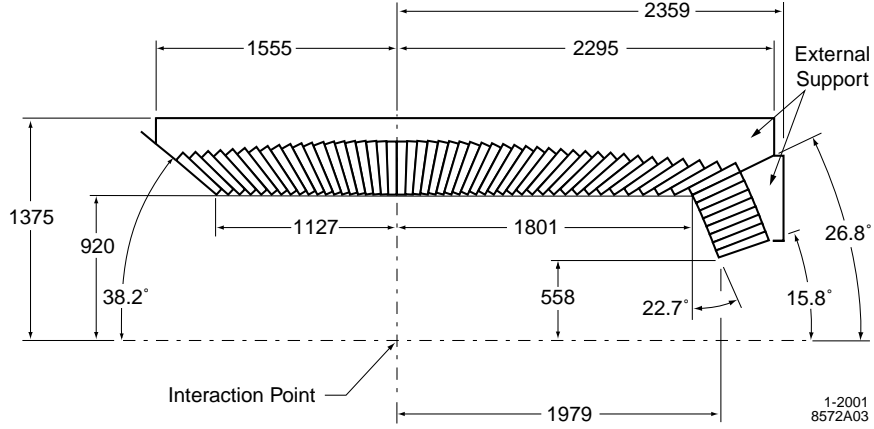


Figure 3.12: Schematic view of EMC.

$\sigma(E)/E = 5.0 \pm 0.8\%$  at 6.13 MeV and  $\sigma(E)/E = 1.9 \pm 0.07\%$  at 7.5 GeV, respectively. The energy resolution can also be inferred from the observed mass resolutions for the  $\pi^0$  (Fig. 3.14) and  $\eta$ , which are measured to be around 7 MeV and 16 MeV, respectively.

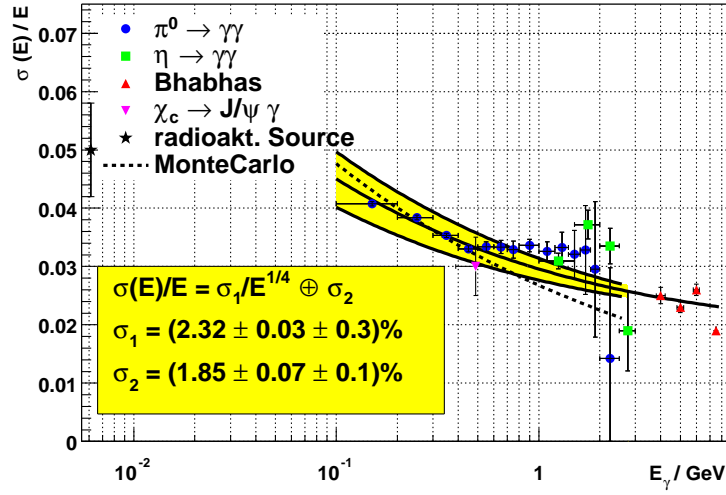


Figure 3.13: The EMC energy resolution as a function of energy, as determined from the observed width of  $\pi^0$  and  $\eta$  decays to two photons of equal energy and from Bhabha electrons. The shaded band is the best fit to the  $\pi^0$ ,  $\eta$ , and Bhabha data. Also shown is the energy resolution of the 6.13 MeV photons from the radioactive source and from the photons of the transition  $\chi_{c1} \rightarrow J/\psi \gamma$ .

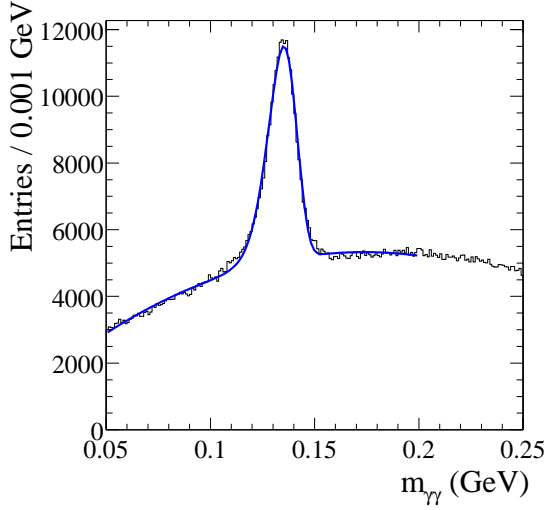


Figure 3.14: Two gamma invariant mass distribution showing the  $\pi^0 \rightarrow \gamma\gamma$  decay.

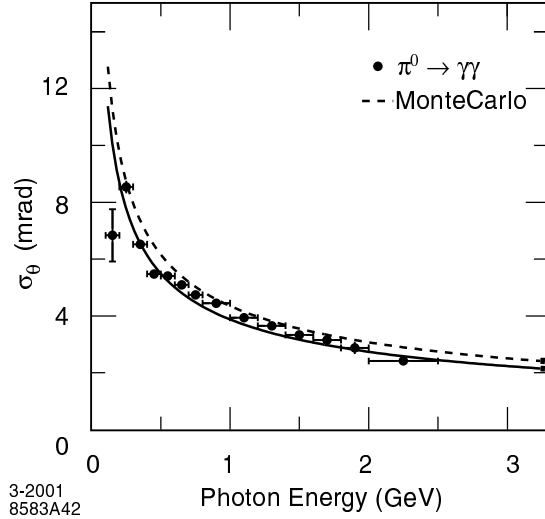


Figure 3.15: The EMC angular resolution as a function of energy.

Fig. 3.13 shows the energy resolution extracted from a variety of data as a function of energy. A fit to the  $\pi^0$ ,  $\eta$ , and Bhabha energy resolution measurements, assuming an energy dependence of the form:

$$\sigma(E)/E = \sigma_1(E/\text{GeV})^{-1/4} \oplus \sigma_2, \quad (3.2)$$

gives  $\sigma_1 = (2.32 \pm 0.30)\%$  and  $\sigma_2 = (1.85 \pm 0.12)\%$ .

The  $\pi^0$  and  $\eta$  data are also used to measure the angular resolution of the calorimeter. It is found to vary between about 12 mrad at low energies and 3 mrad at high energies (Fig. 3.15), described by an energy dependence according to:

$$\sigma_{\theta,\phi} = \sigma_1(E/\text{GeV})^{-1/2} + \sigma_2, \quad (3.3)$$

with  $\sigma_1 = (3.87 \pm 0.07)$  mrad and  $\sigma_2 = (0.00 \pm 0.04)$  mrad.

The calorimeter is also used for the separation of hadrons from electrons, and in conjunction with the IFR for muon- and  $K_L$ - identification; its performance in these areas is described in section 3.2.5.

### 3.2.5 The Instrumented Flux Return (IFR)

The primary aim of the Instrumented Flux Return (IFR) is to identify muons with high efficiency and purity, and to detect neutral hadrons, mainly  $K_L^0$  in a wide momentum and angle range. It plays a major role in tagging the flavor of neutral  $B$

mesons via semileptonic decays, in reconstructing the vector mesons, mainly  $J/\psi$  and in studying rare decays of  $B$  and  $D$  mesons involving leptons. The  $K_L^0$  reconstruction is of special importance for the study of exclusive  $B$  decays into  $CP$  eigenstates.

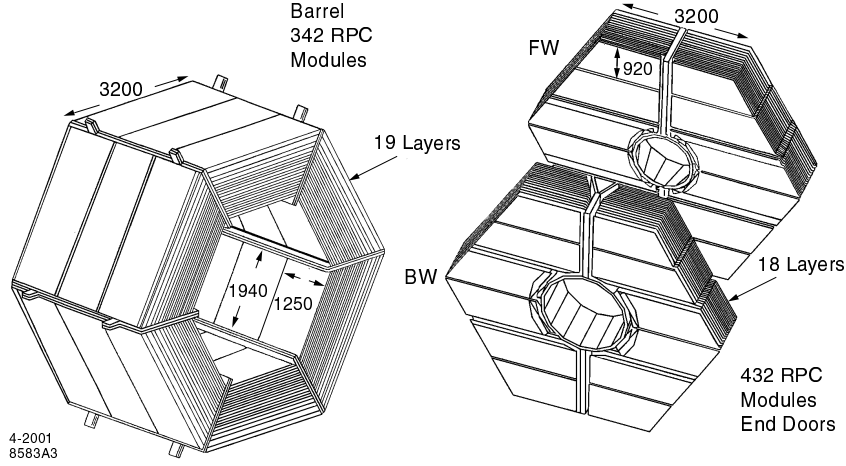


Figure 3.16: Schematic view of IFR resistive plate chambers.

Single gap resistive plate chambers (RPCs) with two-coordinate readout are embedded in the steel flux return system of the magnet, which acts as a muon filter and hadron absorber (Fig. 3.16). The barrel is segmented into 19 RPC layers and the endcap into 18 layers with increasing thickness from 2 cm for the inner ones to 10 cm for the outer plates. Two extra layers of RPCs are installed between the EMC and the solenoid cryostat to detect the particles escaping from the EMC.

$K_L^0$  and other neutral hadrons interact in the steel of the IFR and can be identified as clusters which are not associated with charged tracks. Monte Carlo simulation shows that approximately 65% of  $K_L^0$  with momentum above 1 GeV/c produce a cluster in the cylindrical RPC's, or a cluster with hits in two or more planar RPC layers. Unassociated clusters which have an angular separation less than 0.3 rad, are combined into a composite cluster. The direction of the neutral hadron is defined from the event vertex and the centroid of the neutral cluster. No information on the energy of the cluster can be obtained. Since a significant part of hadrons interact before reaching the IFR, the information from the EMC and the cylindrical RPC is combined in order to perform the matching of the clusters.

Selecting the multihadron events with reconstructed  $J/\psi$  decay, the angular difference between the missing momentum and the direction of the nearest neutral hadron cluster can be determined. Fig. 3.17 shows a clean peak, which demonstrates that the missing momentum can be associated with a neutral hadron, assumed to be a  $K_L^0$ . Its efficiency increases approximately linearly with momentum. It varies between 20% and 40% in the momentum range from 1 GeV/c to 4 GeV/c.

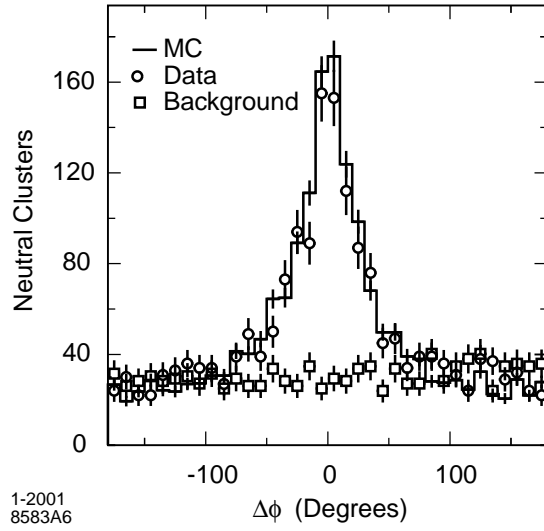


Figure 3.17: The difference between the direction of the reconstructed neutral hadron cluster and the missing transverse momentum.

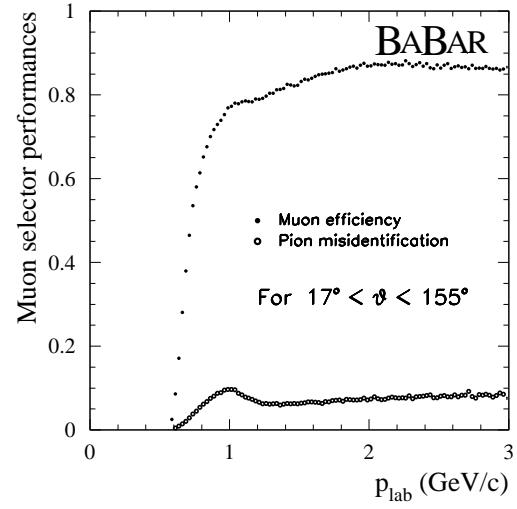


Figure 3.18: The muon efficiency and pion misidentification as a function of a track momentum.

Fig 3.18 shows the muon efficiency and the pion misidentification as a function of a track momentum.



## Chapter 4

# Hadronic $B$ Physics with the $B_{\text{A}}B_{\text{AR}}$ detector

Besides the study of  $CP$  violation in  $B$  decays, many others very interesting topics involving  $B$  physics can be investigated at  $B$  factories. One of the goals in  $B$  decays is to probe and understand physics at very short distances. In addition, it is hoped that a precise measurement of  $CP$  violation, rare decays and flavor changing processes may provide important insights into “new” physics beyond the Standard Model.

In this chapter the theoretical techniques used for studying  $B$  mesons are described. In particular, the theoretical issues connected to the  $b \rightarrow c\bar{c}s$  transitions and their contribution to the understanding of the production of  $D_s^{(*)+}$  mesons are discussed.

### 4.1 Heavy-Quark Expansion

There are several appropriate theoretical methods for describing  $B$  meson decays to the  $D_s^{(*)+}$  and  $D^{(*)}$ . They include effective field theories such as the Heavy-Quark Expansion (HQE) and Chiral Perturbation Theory (ChPT). Effective field theories derive their predictions by an expansion of a small parameter. A ratio of mass scales is considered at a particular limit or special kinematics.

The basic idea of effective field theories is that only certain degrees of freedom are important to describe the system. In particular, the intermediate states with high virtuality may be removed from the theory, since kinematical considerations restrict the momenta of the external particles and subsequently, restrict effectively the momenta of the virtual particles as well. This absence may be compensated by introducing “effective” interactions between the remaining degrees of freedom.

Both HQE and ChPT are derived from formal limits of QCD in which the theory exhibits useful symmetries. In the case of HQE, this limit is  $m_c, m_b \rightarrow \infty$ , where the

“spin-flavor” symmetry gives a variety of predictions for heavy hadron spectroscopy. For ChPT, the limit  $m_u, m_d, m_s \rightarrow 0$  leads to predictions for the emission and absorption of the soft pions. It is important to say, that in both cases the quark masses are either larger or smaller compared to the scale of nonperturbative QCD, typically hundreds of MeV. Unfortunately, the use of HQE and ChPT is restricted to a small number of processes involving certain initial and final states.

The consideration of the physics characterized by virtualities  $\mu \simeq m_b$  is different from that a virtual  $W$  in weak decays, besides it is still a case that  $\alpha_s(m_b)/\pi \simeq 0.1 \ll 1$ . This happens because the  $b$ -quark is real. Let us consider a hadron  $H_Q$  composed of a heavy quark  $Q$  and “light degrees of freedom” consisting of quarks, antiquarks and gluons, in the limit  $m_Q \rightarrow \infty$ . In this limit, the light degrees of freedom do not allow to probe the scale  $\lambda_Q \sim 1/m_Q$ , since the typical momentum exchanged between the light degrees of freedom and heavy quark is of order  $\Lambda_{QCD} \ll m_Q$ . Thus,  $Q$  acts as a static source of the electric and chromoelectric field.

The fact that the interaction of the light degrees of freedom with the heavy quark does not depend on  $m_Q$ , leads to the presence of the **spectrum of excitations**. These excitations determine the spectrum of heavy hadrons  $H_Q$  with the splitting  $\Delta_i \sim \Lambda_{QCD}$ . Consequently, the light degrees of freedom appear exactly in the same states in the mesons  $B_i$  and  $D_i$  ( $i = d, s$ ) with an offset  $B_i - D_i = m_b - m_c$ .

The spin quantum number of the heavy quark of  $S_Q = 1/2$  leads to a chromomagnetic moment  $\mu_Q \propto g/2m_Q$ , which is  $\mu_Q \rightarrow 0$  if  $m_Q \rightarrow \infty$ . Therefore, the interaction between the spin of the heavy quark and light degrees of freedom is insensitive to  $S_Q$  (whether it is  $S_Q^z = 1/2$  or  $S_Q^z = -1/2$ ). Hence each energy level of the  $B$  and  $D$  mesons is actually doubled, one for every spin projection.

Supposing the light degrees of freedom have an orbital angular momentum  $\vec{L}$ . Combined with the heavy quark spin  $\vec{S}_Q$ , the physical hadron states with the angular momentum

$$j = |L \pm \frac{1}{2}| \quad (4.1)$$

can be produced. This yields two states if  $L \neq 0$ . Thus the chromomagnetic interactions split the states for a given  $L$  but different  $j$ . Since “hyperfine” splitting is proportional to the heavy quark magnetic moment  $\mu_Q$ , it can be demonstrated ([26]) that

$$m_{B^*}^2 - m_B^2 = m_{D^*}^2 - m_D^2, \quad (4.2)$$

which is a nonperturbative prediction of the heavy-quark symmetry. Taking into account the correction of order  $\Lambda_{QCD}(1/m_c - 1/m_b) \sim 0.1 \text{ GeV}^2$ , the above prediction is well confirmed, since  $m_{B^*}^2 - m_B^2 = 0.49 \text{ GeV}^2$  and  $m_{D^*}^2 - m_D^2 = 0.55 \text{ GeV}^2$  experimental prove.

Besides the two narrow states  $D_1(2420)$  and  $D_2^*(2460)$  which have already been observed [8], the heavy-quark symmetry predicts two broad states with  $L = 1$  and

respectively  $j = 1/2$  and  $j = 3/2$ . A recent study of the charmed meson spectroscopy, for  $D$  mesons performed by CLEO [27] shows evidence for one of these states, which is interpreted as  $D_1^0(j = 1/2)$ .

## 4.2 Factorization

### 4.2.1 The $B \rightarrow D_s^{(*)+} \bar{D}^{(*)}$ Decays

The factorization model assumes that the amplitude of the decay is described as a product of two independent currents parameterized in terms of Lorentz invariant form factors. In other words, the matrix element factorizes

$$\langle M_1(p'), M_2(q) | j^\mu A_\mu | \bar{B}(p) \rangle = \langle M_1(p') | j^\mu | \bar{B}(p) \rangle \times \langle 0 | A_\mu | M_2(q) \rangle \quad (4.3)$$

The value of the form factor is given for the minimum or maximum value of the transferred momentum,  $q^2 = 0$  or  $q^2 = q_{max}^2$ , and then extrapolated to an intermediate value using different phenomenological models. For example, Bauer, Stech and Wirbel (BSW) ([28]) use a simple pole form while other calculations ([29, 30, 31]) use form factors motivated by Heavy-Quark Effective Theory (HQET) ([32]).

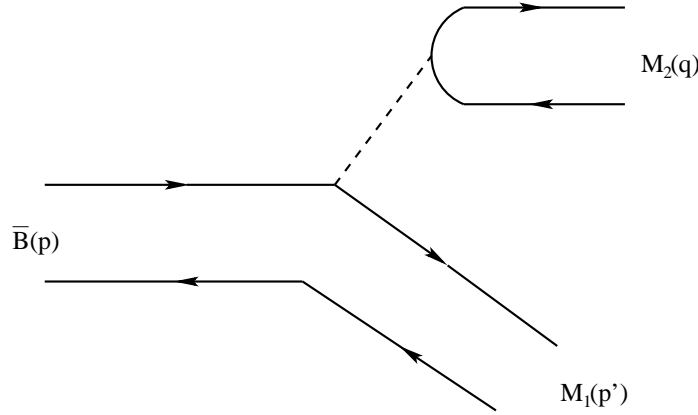


Figure 4.1: Diagram shows a two-body decay of  $B$  mesons.

A  $B$  meson (containing  $\bar{b}$  quark) decays to a meson  $M_1$  (containing  $\bar{c}$  quark) and the weak current which produces the meson  $M_2$  (Fig. 4.1). The decay constant is involved in the matrix element of the axial-vector or vector current between  $M_2$  and vacuum:

$$\langle 0 | A_\mu | P(q) \rangle = i q_\mu f_P \quad (4.4)$$

for a pseudoscalar meson  $P$  with the four-momentum  $q$  and

$$\langle 0 | V_\mu | V(q, \epsilon) \rangle = \epsilon_\mu M_V f_V \quad (4.5)$$

for a vector meson  $V$  with the four-momentum  $q$  and the polarization vector  $\epsilon_\mu$ . In the limit that the mass of the heavy quark is infinitely large, the recoil of the light quark does not change the velocity of the heavy quark. In this picture, the QCD interactions of the light quark are not perturbed by the transition of one heavy quark to another. In the heavy-quark limit both  $f_P$  and  $f_V$  are derived from the nonrelativistic quark-model:

$$f_P^2 = f_V^2 = 12|\psi(0)|^2/M \quad (4.6)$$

where  $\psi(0)$  is the wave function of the light antiquark and the heavy quark at the origin, and  $M$  is the mass of the heavy meson. An important consequence of this theory is that all heavy meson decays are governed by one single form factor.

Let us consider that  $M_1$  is the meson  $D$  or  $D^*$ , while meson  $M_2$  is either  $\pi$ ,  $\rho$ ,  $D_s^+$ ,  $D_s^{*+}$ ,  $D$  or  $D^*$ . Assuming factorization (Eq. 4.3) and the matrix elements Eqs. 4.4, 4.5, the decay amplitude of the transition  $B^0 \rightarrow D^- P$  is given by the product

$$\langle D^- | j^\mu | B^0 \rangle |_{q^2=m_P^2} \times i q_\mu f_P. \quad (4.7)$$

For the corresponding decay to a vector meson,  $B^0 \rightarrow D^- V$ , the amplitude is

$$\langle D^- | j^\mu | B^0 \rangle |_{q^2=m_V^2} \times \epsilon_\mu M_V f_V. \quad (4.8)$$

The matrix element for  $B \rightarrow D^{(*)}$  transition can be expressed via the universal form factor  $\xi(w^2)$ , known as Isgur-Wise function:

$$\langle D(v') | V^\mu | B(v) \rangle = \sqrt{m_c m_b} \xi(w^2) (v + v')^\mu \quad (4.9)$$

where  $v$  and  $v'$  are the four-velocities,  $v = p/m_B$  and  $v' = p'/m_D$ , and  $w = v - v'$  with

$$w^2 = \frac{q^2 - q_{max}^2}{m_B m_D} = \frac{q^2 - (m_B - m_D)^2}{m_B m_D} \quad (4.10)$$

It is important to note that the matrix element for  $B \rightarrow D^{(*)}$  transition as a function of  $q^2$  can be extracted from semileptonic  $B$  decay. We take  $m_b = m_B = 5.28 \text{ GeV}/c^2$  and  $m_c$  equal to the spin-weighted average of  $D$  and  $D^*$  masses,  $m_c = m_D = 1.97 \text{ GeV}/c^2$ . The following expression is derived by Rosner [29] for the decay rate of a  $B$  meson to a pseudoscalar and a  $D$ :

$$\Gamma(B^0 \rightarrow D^- P^+) = \frac{G_F^2}{32\pi} m_B^3 |\xi(w_p^2)|^2 \Lambda f_p^2 |V_{cb} V_{ij}|^2 (1 - \sqrt{\zeta})^2 \lambda^{1/2}(1, \zeta, y_p) \frac{[(1 + \sqrt{\zeta})^2 - y_p]^2}{4\sqrt{\zeta}} \quad (4.11)$$

where  $\Lambda$  are QCD corrections,  $\zeta = m_D^2/m_B^2$ ,  $y_{p,v} = m_{p,v}^2/m_B^2$ ,  $\lambda(a, b, c) = a^2 + b^2 + c^2 - 2ab - 2ac - 2bc$ . The rates for the decays involving one or two vector mesons in the final state can be expressed by similar expressions:

$$\Gamma(B^0 \rightarrow D^- V^+) = \frac{G_F^2}{32\pi} m_B^3 |\xi(w_v^2)|^2 \Lambda f_v^2 |V_{cb} V_{ij}|^2 (1 + \sqrt{\zeta})^2 \lambda^{3/2}(1, \zeta, y_v) \frac{1}{4\sqrt{\zeta}} \quad (4.12)$$

$$\Gamma(B^0 \rightarrow D^{*-} P^+) = \frac{G_F^2}{32\pi} m_B^3 |\xi(w_p^2)|^2 \Lambda f_p^2 |V_{cb} V_{ij}|^2 (1 + \sqrt{\zeta})^2 \lambda^{3/2}(1, \zeta, y_p) \frac{1}{4\sqrt{\zeta}} \quad (4.13)$$

$$\Gamma(B^0 \rightarrow D^{*-} V^+) = \frac{G_F^2}{32\pi} m_B^3 |\xi(w_v^2)|^2 \Lambda f_v^2 |V_{cb} V_{ij}|^2 N(\zeta, y_v) \lambda^{1/2}(1, \zeta, y_v) \frac{(1 + \sqrt{\zeta})^2 - y_v}{4\sqrt{\zeta}} \quad (4.14)$$

where

$$N(\zeta, y_v) = (1 - \sqrt{\zeta})^2 [(1 + \sqrt{\zeta})^2 - y_v] + 4y_v(1 + \zeta - y_v)$$

In decays involving only one vector meson, the vector meson is necessarily longitudinally polarized with respect to the decay axis. When the  $B$  meson decays into two vector mesons, different polarizations are possible: either both are longitudinal ( $\Gamma_L$ ), or both are transverse with polarization vectors parallel( $\parallel$ ) or perpendicular ( $\perp$ ) to each other. The fraction of the longitudinal polarization is

$$\frac{\Gamma_L}{\Gamma} = (1 - \sqrt{\zeta})^2 [(1 + \sqrt{\zeta})^2 - y_v] / N(\zeta, y_v) \quad (4.15)$$

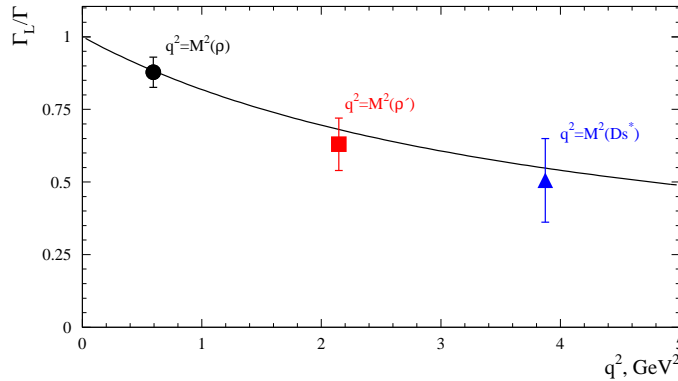


Figure 4.2: Factorization prediction for the fraction of the longitudinal polarization for the decays involving two vector mesons as a function of  $q^2$ . The experimental results for  $B \rightarrow D^* \rho$ ,  $B \rightarrow D^* \rho'$  and  $B \rightarrow D^* D_s^{*+}$  are shown too.

Fig 4.2 shows this dependence as a function of  $q^2$ .

There are several proposals for an analytical expression of the Isgur-Wise function. Rosner [29] suggested

$$\xi(w^2) = \frac{1}{1 - w^2/w_0^2} \quad (4.16)$$

while Mannel, Roberts and Ryzak [30] use the parameterization

$$\xi(w^2) = \exp\{kw^2\}. \quad (4.17)$$

$\frac{\Gamma(B \rightarrow D_s^{*+} D)}{\Gamma(B \rightarrow D_s^+ D^*)}$	$\frac{\Gamma(B \rightarrow D_s^+ D)}{\Gamma(B \rightarrow D_s^+ D^*)}$	$\frac{\Gamma(B \rightarrow D_s^{*+} D^*)}{\Gamma(B \rightarrow D_s^{*+} D)}$
$1.1 \left( \frac{f_{D_s^*}}{f_{D_s}} \right)^2$	1.5	2.5

Table 4.1: Factorization model predictions for the relative branching fractions of  $B \rightarrow D_s^{(*)+} \bar{D}^{(*)}$ . Average values for the different form factor parameterization are displayed.

The calculation of the Isgur-Wise function proposed by Neubert and Rieckert [31] includes the leading mass corrections in the heavy quark limit. It leads to

$$\xi(w^2) = \frac{1}{1 - w^2/4} \exp\left\{\beta \frac{w^2}{4 - w^2}\right\}. \quad (4.18)$$

In all three expressions, there is a free parameter ( $w_0$ ,  $k$ , or  $\beta$ ), which can be extracted using experimental data, for example the measurement of semileptonic  $B$  decays. The simultaneous fit of the ratios  $\mathcal{B}(B \rightarrow D l \nu)/\mathcal{B}(B^0 \rightarrow \pi^+ D^{(*)-})$ ,  $\mathcal{B}(B \rightarrow D^* l \nu)/\mathcal{B}(B^0 \rightarrow \pi^+ D^{(*)-})$  and the polarization variable  $\alpha = 2\Gamma_L/\Gamma_T - 1$  gives the following values for these parameters [56]:

$$w_0 = 1.17 \pm 0.20, \quad k = 0.49 \pm 0.12, \quad \beta = 1.53 \pm 0.63 \quad (4.19)$$

Table 4.1 shows the predicted relative branching fractions for the  $B \rightarrow D_s^{(*)+} \bar{D}^{(*)}$  decay modes using the factorization approach.

As will be shown below, the ratio

$$\frac{\Gamma(B^0 \rightarrow D_s^+ D^-)}{\Gamma(B^0 \rightarrow \pi^+ D^-)} = \frac{f_{D_s^+}^2}{f_\pi^2} \cdot \frac{|V_{cs}|^2}{|V_{ud}|^2} \cdot \frac{|\xi(w_{D_s^+}^2)|^2}{|\xi(w_{\pi^+}^2)|^2} \cdot \frac{\lambda^{1/2}(1, \zeta, y_{D_s^+})}{\lambda^{1/2}(1, \zeta, y_{\pi^+})} \cdot \frac{[(1 + \sqrt{\zeta})^2 - y_{D_s^+}]^2}{[(1 + \sqrt{\zeta})^2 - y_{\pi^+}]^2} \quad (4.20)$$

might be useful for the extraction of the decay constants.

#### 4.2.2 The $B \rightarrow D_s^{(*)+} X_q$ Inclusive Rates

The spectator quark model allows one to obtain the inclusive decay rate of a  $B$  meson to a  $D_s^+$  by writing

$$\Gamma(B \rightarrow D_s^+ X_q) \simeq \Gamma(\bar{b} \rightarrow D_s^+ \bar{q}) + \Gamma(\bar{b} \rightarrow D_s^{*+} \bar{q}), \quad (4.21)$$

where  $q$  is an outgoing quark as shown in Fig. 4.4. As mentioned in the introduction, decays of the higher excited states (lowest P wave) of  $c\bar{s}$  ( $D_s^{**}$ ) do not lead to a  $D_s^+$

meson since their main decays are to  $D^{(*)}K$ . Using the factorization approach Eq. 4.3 one can write the effective matrix element for the weak decay  $\bar{b} \rightarrow D_s^{(*)+} \bar{q}$  as

$$\langle D_s^{(*)+} \bar{q} | \mathcal{H}_{eff} | \bar{b} \rangle = \frac{G_F}{\sqrt{2}} a_1 V_{qb}^* V_{cs} \langle \bar{q} | J^\mu | \bar{b} \rangle \langle 0 | A_\mu(V_\mu) | D_s^{(*)+} \rangle. \quad (4.22)$$

Here, the parameter  $a_1$  is

$$a_1 = c_1 + \frac{c_2}{N_c}. \quad (4.23)$$

Since factorization is so far consistent with the experimental data,  $|a_1| = 1.00 \pm 0.06$  has been extracted using a combined fit of several measured modes in exclusive decays where only type 1 diagrams are involved. The Wilson coefficients in the equation above are [33]

$$c_1 = \frac{c_+ + c_-}{2}, \text{ and } c_2 = \frac{c_+ - c_-}{2}, \quad c_\pm = \left( \frac{\alpha_s(\mu)}{\alpha(m_W)} \right)^{d_\pm} \quad (4.24)$$

where  $d_+ = -6/23$  and  $d_- = 12/23$ .

The rate of the inclusive  $\bar{b} \rightarrow D_s^+ \bar{q}$  is calculated using the Eqs. 4.4, 4.5 for the emission of a pseudoscalar or vector meson. One finds [34]

$$\Gamma^{(0)}(\bar{b} \rightarrow D_s^+ \bar{q}) = \frac{G_F^2}{8\pi} a_1^2 |V_{qb}^* V_{cs}|^2 f_{D_s^+}^2 \frac{(m_b^2 - m_q^2)^2}{m_b^2} \left( 1 - \frac{m_{D_s^+}^2 (m_b^2 + m_q^2)}{(m_b^2 - m_q^2)^2} \right) p_{D_s^+} \quad (4.25)$$

where  $p_{D_s^+} = \sqrt{(m_b^2 - (m_{D_s^+} + m_q)^2)(m_b^2 - (m_{D_s^+} - m_q)^2)}/2m_b$  is the momentum of the  $D_s^+$  meson in the  $b$  rest frame. Here, the notation  $\Gamma^{(0)}$  is used for the width without including the radiative corrections. By replacing  $f_{D_s^+}$  and  $m_{D_s^+}$  with  $f_{D_s^{*+}}$  and  $m_{D_s^{*+}}$ , respectively, a similar formula is obtained for  $\Gamma^{(0)}(\bar{b} \rightarrow D_s^{*+}(\lambda = 0) \bar{q})$  where  $D_s^{*+}$  is longitudinally polarized. For the transverse polarization one can find

$$\Gamma^{(0)}(\bar{b} \rightarrow D_s^{*+}(\lambda = \pm 1) \bar{q}) = \frac{G_F^2}{4\pi} a_1^2 |V_{qb}^* V_{cs}|^2 f_{D_s^{*+}}^2 m_{D_s^{*+}} \frac{m_b^2 + m_q^2}{m_b^2} \left( 1 - \frac{m_{D_s^{*+}}^2}{(m_b^2 + m_q^2)^2} \right) p_{D_s^{*+}} \quad (4.26)$$

Using  $m_{D_s^{*+}}^2 \ll m_b^2$  and  $m_q^2 \ll m_b^2$ , it can be deduced

$$\frac{\Gamma_T}{\Gamma_L} = \frac{\Gamma^{(0)}(\bar{b} \rightarrow D_s^{*+}(\lambda = \pm 1) \bar{q})}{\Gamma^{(0)}(\bar{b} \rightarrow D_s^{*+}(\lambda = 0) \bar{q})} \simeq \frac{2m_{D_s^{*+}}^2}{m_b^2 - 4m_q^2} \quad (4.27)$$

Thus, the expected order of magnitude of the ratio  $\Gamma_T/\Gamma_L$  is about 1/2 and 1/3 for  $\bar{b} \rightarrow D_s^{*+} \bar{c}$  and  $\bar{b} \rightarrow D_s^{*+} \bar{u}$  transitions, respectively (using  $m_b = 4.85 \text{ GeV}/c^2$  and  $m_c = 1.45 \text{ GeV}/c^2$ ). Adding both longitudinal and transverse polarization, one obtains

$$\Gamma^{(0)}(\bar{b} \rightarrow D_s^{*+} \bar{q}) = \frac{G_F^2}{8\pi} a_1^2 |V_{qb}^* V_{cs}|^2 f_{D_s^{*+}}^2 \frac{(m_b^2 - m_q^2)^2}{m_b^2} \left( 1 + \frac{m_{D_s^{*+}}^2 (m_b^2 + m_q^2 - 2m_{D_s^{*+}}^2)}{(m_b^2 - m_q^2)^2} \right) p_{D_s^{*+}} \quad (4.28)$$

The radiative corrections to  $\bar{b} \rightarrow D_s^+ \bar{q}$  at order  $\alpha_s$  are computed in [35], and

$$\Gamma(\bar{b} \rightarrow D_s^{(*)+} \bar{q}) = \Gamma^{(0)}(\bar{b} \rightarrow D_s^{(*)+} \bar{q}) \left[ 1 + \frac{4}{3} \frac{\alpha_s}{\pi} \eta^*(\xi_{D_s^{(*)+}}, r_q) \right] \quad (4.29)$$

is obtained, where  $\xi = q^2/m_b^2$  and  $r_q = m_q/m_b$ . The functions  $\eta^{(*)}(\xi_{D_s^{(*)+}}, r_q)$  are slowly varying with  $r$  and  $\xi$  and in the limit  $\xi \rightarrow 0$ ,  $r_q \rightarrow 0$  they can be approximated like

$$\eta(0, 0) = \eta^{(*)}(0, 0) = \frac{5}{4} - \frac{\pi^2}{3} \quad (4.30)$$

The following numerical values are used in Ref. [35] to derive the expected branching fractions:

- Quark masses:

$$m_b^2 = 4.85 \text{ GeV}/c^2, \quad m_c = 1.45 \text{ GeV}/c^2, \quad m_u \simeq 0. \quad (4.31)$$

- The decay constants:

$$f_{D_s^+} = 230 \text{ MeV}, \quad f_{D_s^{*+}} = 280 \text{ MeV}. \quad (4.32)$$

- The radiative corrections for  $q = c$  with the  $\alpha_s(m_b) = 0.2$ :

$$\begin{aligned} \frac{4}{3} \frac{\alpha_s}{\pi} \eta(\xi_{D_s^+}, r_c) &= -0.095 \\ \frac{4}{3} \frac{\alpha_s}{\pi} \eta^*(\xi_{D_s^{*+}}, r_c) &= -0.108 \end{aligned} \quad (4.33)$$

- $\tau_B = 1.6 \text{ ps}$ , and  $|V_{cb}| = 0.04$

Including QCD correction, the  $D_s^+$  branching fraction from  $B$  decays (Eq. 4.21) is calculated like

$$\mathcal{B}(B \rightarrow D_s^+ X_c) \simeq 8\% \quad (4.34)$$

where the corresponding terms for the  $D_s^+$  and  $D_s^{*+}$  production are

$$\mathcal{B}(\bar{b} \rightarrow D_s^+ \bar{c}) \simeq 2.6\%, \quad \text{and} \quad \mathcal{B}(\bar{b} \rightarrow D_s^{*+} \bar{c}) \simeq 5.4\%, \quad (4.35)$$

respectively. The calculated branching fraction Eq. 4.34 is consistent with the world average value  $(10.0 \pm 2.5)\%$  given in [8]. The  $D_s^+ \rightarrow \phi \pi^+$  branching fraction uncertainty [8] is the common and the dominant error for all measurements. Therefore, the ratio of the vector to pseudoscalar production rates looks very attractive since it cancels out this quantity.



### 4.3 Charm Production Rate from $B$ Decays

The inclusive semileptonic branching fraction is defined as

$$\mathcal{B}_{SL} = \frac{\Gamma(\bar{B} \rightarrow X e^- \bar{\nu}_e)}{\sum_l \Gamma(\bar{B} \rightarrow X l^- \bar{\nu}_e) + \Gamma_{\text{had}} + \Gamma_{\text{rare}}} \quad (4.36)$$

where  $\Gamma_{\text{had}}$  and  $\Gamma_{\text{rare}}$  are the partial widths of hadronic and rare final states.

The semileptonic branching fractions are measured to be smaller than 11% [36], while the theoretical predictions show that it is very difficult to obtain a value for  $\mathcal{B}_{SL}$  below 12.5% [2]. Indeed, the branching fractions  $\mathcal{B}(b \rightarrow cl\nu)$  and  $\mathcal{B}(b \rightarrow c\bar{c}s)$  are correlated and depend both on  $m_c/m_b$  and  $\mu/m_b$  [3], it is difficult to account them simultaneously. Here  $\mu$  is the scale factor needed for renormalization of the coupling constant  $\alpha_s(\mu)$  and Wilson coefficients  $c_{\pm}(\mu)$  used in non-leptonic decay rates.

Several attempts have been carried out to scrutinize this problem. It has been suggested that the higher order perturbative QCD corrections may significantly increase the rate  $b \rightarrow c\bar{c}s$ , thereby decreasing  $\mathcal{B}_{SL}$  [37]. Therefore, one can measure  $n_c$ , the average number of charm (or anti-charm) quarks per  $B$  decay and regard this problem as the joint problem of  $\mathcal{B}_{SL}$  and  $n_c$ .

The quantity  $n_c$  is difficult to determine experimentally, since one has to identify and measure all final states which contain one or more charm quarks. The yields of  $D^0$ ,  $D^+$ ,  $D_s^+$  and  $J/\psi$  are relatively easy to determine, while the contribution from the other charmonium states and from charmed baryons are more difficult to measure. Summarizing all relevant measurements for this quantity [38], the values are

$$n_c = 1.12 \pm 0.05, \text{ and } n_c^Z = 1.22 \pm 0.08, \quad (4.37)$$

where the notation  $n_c^Z$  refers to the ALEPH measurement [39].

Most measurements of  $\mathcal{B}_{SL}$  at the  $\Upsilon(4S)$  are averaged over the  $\bar{B}^0$  and  $B^-$ , because only the lepton is identified in order to maximize the detection efficiency. Averaging the measurements from CLEO and ARGUS [36]

$$\mathcal{B}_{SL} = (10.23 \pm 0.39)\% \quad (4.38)$$

is obtained. For comparison  $\mathcal{B}_{SL}^Z$ , which is the semileptonic branching fraction for the  $b$ -hadron mixture produced in  $Z^0$  decays, was measured by the LEP experiments [40]. This is

$$\mathcal{B}_{SL}^Z = (10.95 \pm 0.32)\%. \quad (4.39)$$

At the  $Z^0$ , the  $B_s$  and  $b$  baryons are included in the samples as well. Since  $b$  baryon lifetimes are typically shorter than those of  $B$  mesons, one can assume that semileptonic rates are very similar.

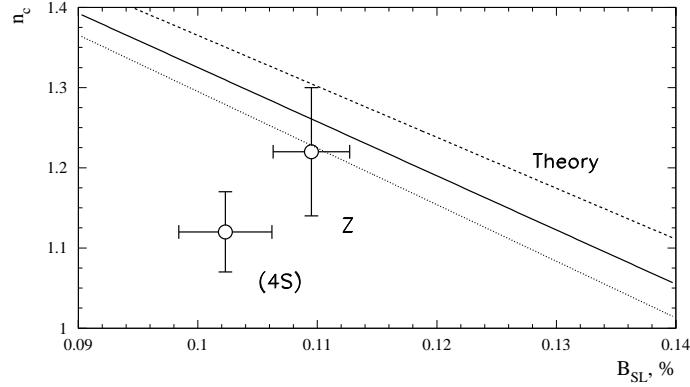


Figure 4.3: Comparison of  $n_c$  versus  $B_{SL}$  for measurements at the  $\Upsilon(4S)$  and the  $Z$  with theoretical prediction from Ref. [41].

Fig. 4.3 shows the theoretical summary given in [41] with the points  $(B_{SL}, n_c)$  and  $(B_{SL}^Z, n_c^Z)$  overlaid. Since it is difficult to state whether there is or not a problem in explaining the measured value of  $B_{SL}$  within the present experimental and theoretical uncertainties, it is important to continue this study in both theoretical and experimental analysis until the problem is resolved.

## 4.4 Motivation.

As mentioned the decay of  $B$  mesons into final states involving a  $D_s^{(*)+}$  provides the opportunity to study the production mechanism of  $c\bar{s}$  quark pairs. Although several Feynman diagrams can lead to  $D_s^{(*)+}$  mesons in  $B$  decays, the spectator diagram (Fig. 4.4) is expected to dominate. Fig. 4.5 shows many alternative diagrams. The precise knowledge of this production rate might help to explain some of the theoretical difficulties in accounting simultaneously for the charm inclusive  $B$  decay rate and the semileptonic branching fraction of the  $B$  meson. It has been pointed out in the previous section, that the charm rate from  $B$  decays may be large. This would help to the understanding of small observed value for the inclusive semileptonic rate. The measurement of the  $D_s^{(*)+}$  momentum spectra allows one to determine the fractions of two-body and multi-body decay modes, which help understanding the  $b \rightarrow c\bar{c}s$  transitions.

In addition,  $D_s^{(*)+}$  mesons can be produced from  $q\bar{q}$  continuum events in  $e^+e^-$  annihilation. The process of fragmentation, formation of hadrons, can only be calculated using phenomenological models, since this process is non-perturbative. The ratio of vector to pseudoscalar production rates is of particular interest for testing such mod-

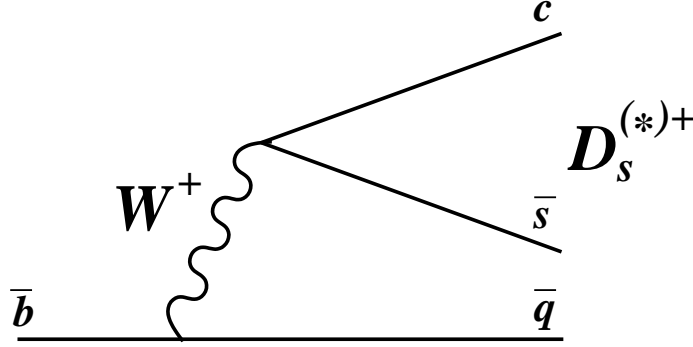


Figure 4.4: The main spectator diagram leading to the production of  $D_s^{(*)+}$  mesons in  $B$  decays.

els. The  $D_s^+$  system is well suited to measure this quantity because the  $c\bar{s}$  states with  $L=1$  have not been observed to decay to  $D_s^+$  or  $D_s^{*+}$ .

Finally, the measurement of the rate and momentum spectrum of  $D_s^+$  meson produced in  $B$  decays beyond the kinematical limit for the process  $B \rightarrow D_s^{*+} X_c$  is sensitive to  $b \rightarrow u$  transitions. Despite the fact that purely hadronic final states are more difficult to understand theoretically, one may use these decays to extract  $V_{ub}/V_{cb}$  [34].

Indeed, relatively large branching fraction makes these decay modes an ideal sample for studying the systematic errors of the double-charm  $B$  decays reconstruction. As shown in Section 4.2, the theoretical framework describing weak decays of heavy flavor mesons assumes the factorization hypothesis, which describes well semileptonic decays and non leptonic modes with relatively low  $q^2$ . For example,  $B \rightarrow D^*\pi$ ,  $D^*\rho$  branching fractions and polarization for  $D^*\rho$  are well described by this approach.

The  $B \rightarrow D_s^{(*)+} \bar{D}^{(*)}$  decay modes are well suited either to test further factorization for final states with two heavy quarks or to extract the values of the decay constants  $f_{D_s^{(*)}}$  if factorization is assumed. This transition can only occur via  $c\bar{s}$  quarks pair coupling with a  $W$  boson emitted externally in  $b \rightarrow cW$  transition. In terms of the BSW model these decays are pure  $a_1$  transition, since they can not be produced by color suppressed diagrams. The width of  $B \rightarrow \bar{D}^{(*)} D_s^{(*)+}$  decay can be written as

$$\Gamma(B \rightarrow \bar{D}^{(*)} D_s^{(*)+}) = K G_F^2 |V_{cb} V_{cs}^*|^2 (a_1^{c\bar{s}})^2 f_{D_s^{(*)}}^2 \xi^2(w_{D_s^{(*)}}^2) \quad (4.40)$$

where  $K$  is some kinematic factor which can be calculated using Eqs.4.11-4.14, and  $a_1$  as a QCD factor [29]. Some theoretical and experimental uncertainties cancel out for the ratio:

$$\frac{\Gamma(B \rightarrow \bar{D}^{(*)} D_s^{(*)+})}{d\Gamma(B \rightarrow \bar{D}^* l^+ \nu)/dq^2|_{q^2=m_{D_s^{(*)}}^2}} = k (a_1^{c\bar{s}})^2 f_{D_s^{(*)}}^2 |V_{cs}|^2 \quad (4.41)$$

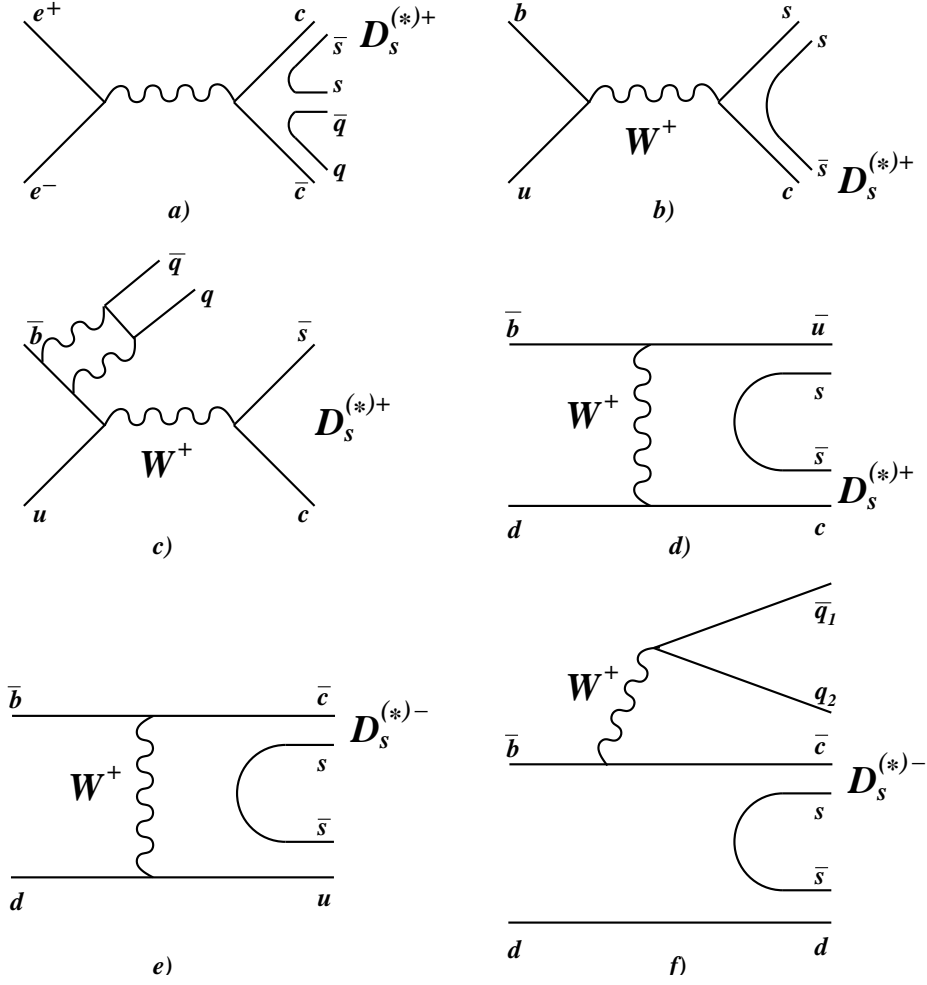


Figure 4.5: Additional diagrams leading to the production of  $D_s^{(*)+}$  mesons from the  $c\bar{c}$  continuum or from  $B$  decays.

The decay constants can also be obtained by measuring the ratio  $\mathcal{B}(B \rightarrow \bar{D}^{(*)} D_s^{(*)+}) / \mathcal{B}(B^0 \rightarrow \pi^+ / \rho^+ D^{(*)-})$  (Eq. 4.20) and if one assumes a parameterization of the form factor, for example as given in Eqs. 4.16-4.18. It is important to note, that only neutral decay modes can be used for this approach, since the corresponding charged  $B$  decay modes can be produced either via internal or external  $W$  emission.

In the following, we discuss the measurements made with the *BABAR* detector both concerning the inclusive  $D_s^{(*)+}$  production rates, the momentum spectra in  $B$  decays as well as the branching fractions of the some specific two-body  $B$  decay modes involving a  $D_s^{(*)+}$  meson. The latter measurements are made using a partial reconstruction technique.

## 4.5 Reconstruction of $B$ Mesons

Two methods of the  $B$  meson reconstruction are used in *BABAR*. The first method implies the full reconstruction of the decay mode. This allows one to obtain a very clean  $B$  sample using beam energy constrain which significantly improves the  $B$  mass resolution. The second method uses the partial reconstruction technique, where only the  $D_s^{(*)+}$  meson is reconstructed fully. This method improves the reconstruction efficiency, although an ambiguity relative to the  $B$  direction increases the combinatorial background.

### 4.5.1 Full Reconstruction

Due to phase space, the  $B$  mesons produced from  $\Upsilon(4S) \rightarrow B\bar{B}$  decay are almost at rest in the center-of-mass frame. However, the asymmetry of the beam energies causes a boost of the  $B$  mesons in the laboratory frame.

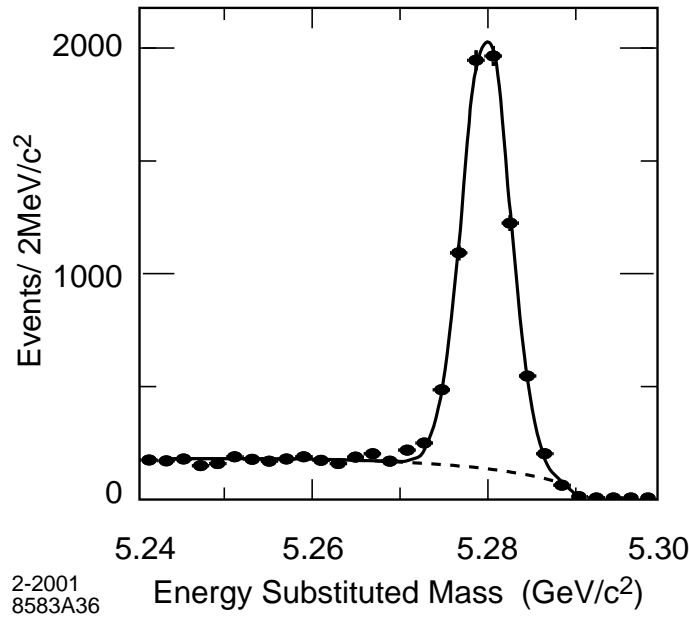


Figure 4.6: The  $M_{ES}$  distribution for the reconstructed  $B$  mesons.

For background rejection, two almost uncorrelated kinematic variables, are used. The difference between the energy of the reconstructed  $B$  meson and the beam energy in the center-of-mass frame:

$$\Delta E = E_B^* - E_{beam}^* \quad (4.42)$$

$\Delta E$  is insensitive to the boost and peaks at zero for  $e^+e^- \rightarrow B\bar{B}$  events. The signal can be fitted with a Gaussian on the top of the background which is usually a linear function. The second parameter is the beam-energy substituted mass

$$M_{ES} = \sqrt{E_{beam}^{*2} - p_B^{*2}} \quad (4.43)$$

where  $p_B^*$  is the  $B$  momentum in the center-of-mass. This variable has a typical resolution of about 2.5-3 MeV which is about 10 times more accurate than the invariant mass computed by a simple sum of the 4-momentum of the measured decay products. The background shape in  $M_{ES}$  is described by an ARGUS function [42]

$$B = \alpha y \sqrt{1 - y^2} \exp(s_f(1 - y^2)), \quad (4.44)$$

where  $y = M_{ES}/E_{beam}^*$ .

### 4.5.2 Partial Reconstruction

Examples of the modes, which can be reconstructed partially are  $B \rightarrow D^{*-}X$ , where  $X = \pi^+, \rho^+, a_1, D^{(*)}, D_s^{(*)+}$ . No attempt is made to reconstruct the  $D^0$  from  $D^{*-} \rightarrow \bar{D}^0\pi_s^-$  decays. Let us consider the method of the partial reconstruction based on  $B^0 \rightarrow D_s^{(*)+}D^{*-}$  decay modes since they are connected with the analysis being presented in this document.

A soft pion from  $D^{*-}$  decay is combined with the fully reconstructed  $D_s^{(*)+}$  where the total  $D_s^{(*)+} - \pi$  charge is 0. Assuming that the origin of the  $D_s^{(*)+} - \pi$  pair is a  $B^0$  meson, the missing invariant mass is derived. This mass should be the  $D^0$  mass if the hypothesis is correct. More explicitly, the following equations hold:

$$\mathbf{P}_B^0 = \mathbf{P}_{D_s^{(*)+}} + \mathbf{P}_D^* \quad (4.45)$$

$$\mathbf{P}_B^0 = \mathbf{P}_{D_s^{(*)+}} + \mathbf{P}_\pi + \mathbf{P}_X \quad (4.46)$$

Here,  $\mathbf{P}$  are the 4-vectors and  $X$  is the missing particle.

In the  $\Upsilon(4S)$  frame, the  $B$  meson are monoenergetics. Therefore, assuming that the decay is two-body like as in Eq.4.45, it is straightforward to calculate the angle of the  $B$  direction relative to the  $D_s^{(*)+}$ .

$$\cos \theta_B^0 = \frac{E_{D_s^{(*)+}} - \gamma_B^0 E_{D_s^{(*)+}}^*}{\beta_B^0 \gamma_B^0 p_{D_s^{(*)+}}^*} \quad (4.47)$$

where  $\gamma_B^0 = E_B^0/m_B^0$ ,  $\beta_B^0 = p_B^0/E_B^0$  and the  $*$  indicates the value in the  $\Upsilon(4S)$  rest frame.

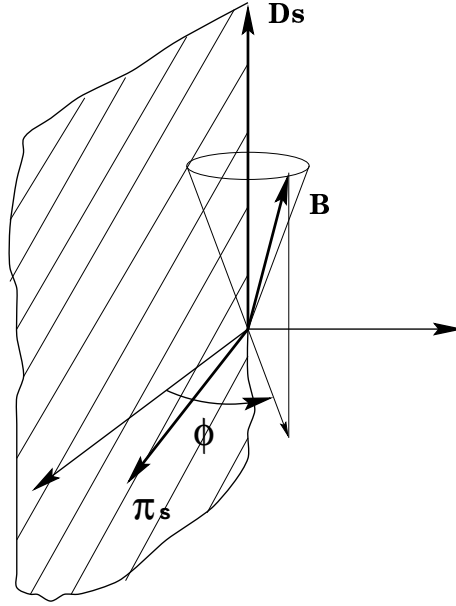


Figure 4.7: Definition of the  $B$  cone angle  $\theta_B$  and arbitrary angle  $\phi$ .

At this point, the angle  $\phi$  around the  $D_s^{(*)+}$  is degenerated as we have no means of determining it without any further assumption. A possibility is to postulate  $X = D^0$ . In that case, one can solve the equations 4.45 and 4.46 and extract the angle  $\phi$  with a 4-fold ambiguity. It was decided not to do so as one prefers to deduce the missing mass and use this variable to determine the background by studying both side bands and wrong sign combination as well as Monte Carlo as will be shown later. However to derive the missing mass  $m_X$ , one needs to fix arbitrary the angle  $\phi$ . To that end, we use the convention where the direction of the  $B^0$  meson lies in the plane  $\{\vec{p}_\pi, \vec{p}_{D_s^{(*)+}}\}$ .





# Chapter 5

## $D_s^{(*)+}$ Signal Extraction

### 5.1 Data Set

Multihadron events produced in  $e^+e^-$  annihilation at the PEP-II collider (SLAC) were collected with the *BABAR* detector and have been used in the present analysis. An integrated luminosity of  $20.8 \text{ fb}^{-1}$  was recorded in 1999 and 2000 corresponding to about 22.7 million  $B\bar{B}$  pairs at the  $\Upsilon(4S)$  resonance (“on-resonance”) and  $2.6 \text{ fb}^{-1}$  at an energy about 40 MeV below the  $\Upsilon(4S)$  mass (“off-resonance”).

A  $B$ -counting technique (described in [43]) is used to determine the number of  $\Upsilon(4S)$  mesons produced in *BABAR*. This method selects hadronic events in both the on-resonance and off-resonance data samples. It compares the ratio of hadronic events to muon pairs between the on- and off-resonance runs and attributes the excess observed in on-resonance data to  $\Upsilon(4S)$  production. Thus, the number of observed  $\Upsilon(4S)$  mesons can be obtained as

$$N_{\Upsilon} = N_{mh} - N_{\mu\mu} R_{off} k. \quad (5.1)$$

Here  $N_{mh}$  is the number of hadron events satisfying the selection criteria in the on-resonance sample,  $N_{\mu\mu}$  is the number of muon pairs selected in the on-resonance sample,  $R_{off} = N_{mh}^{off}/N_{\mu\mu}^{off}$  is the ratio of hadronic events to muon pairs in the off-resonance sample,  $k$  is a factor close to unity used to account for the variation of the cross sections and efficiencies at the different center-of-mass energies. The total number  $N_{\Upsilon}^0$  of  $\Upsilon(4S)$  produced in the data set is derived from the observed number  $N_{\Upsilon}$  after correcting for the  $B\bar{B}$  event selection efficiency  $\epsilon_{B\bar{B}}$ :

$$N_{\Upsilon}^0 = N_{\Upsilon} / \epsilon_{B\bar{B}} \quad (5.2)$$

In the period 1999-2000, the *BABAR* detector had several improvements concerning the subdetectors and the reconstruction software. The most crucial ones relate to

	ON resonance	OFF resonance
	1900 V	
Luminosity	11289.639 pb <sup>-1</sup>	1253.366 pb <sup>-1</sup>
$N_{B\bar{B}}$	12076676.6±193702.1	
ON/OFF ratio	9.013±0.012	
	1960 V	
Luminosity	9534.189 pb <sup>-1</sup>	1360.607 pb <sup>-1</sup>
$N_{B\bar{B}}$	10626687.7±170497.8	
ON/OFF ratio	7.138±0.009	
	Total	
Luminosity	20823.827 pb <sup>-1</sup>	2613.972 pb <sup>-1</sup>
$N_{B\bar{B}}$	22703364.3±363727.3	
ON/OFF ratio	8.039±0.008	

Table 5.1: Luminosity, number of  $B\bar{B}$  events  $N_{B\bar{B}}$  and the ratio on to off resonance data sets for the different voltages on the drift chamber

the tracking system, and in particular the drift chamber. As it will be discussed in Section 6.5, the efficiency of the track finding algorithm is different for two data subsets since different values of the high voltage were used in the drift chamber. Table 5.1 shows the integrated luminosity, the number of  $B\bar{B}$  events and the ratio of on- to off-resonance data sets obtained with the  $B$ -counting procedure for the two voltages. One sees that a luminosity of 11.29 fb<sup>-1</sup> was collected at 1900 V, while 9.53 fb<sup>-1</sup> was recorded at 1960 V. The systematic errors due to the tracking efficiency will be studied separately in both samples.

## 5.2 Event Preselection

### 5.2.1 Selection of Tracks and Neutrals

Charged tracks are required to originate from within  $\pm 10$  cm of the interaction point along the beam direction and  $\pm 1.5$  cm in the transverse plane. Each track should be

reconstructed with at least 12 hits in the drift chamber. The list of this kind of tracks in the event has a special name “GoodTracksLoose” (*GTL*). The requirement on the number of hit implies a minimum transverse momentum of about 120 MeV/ $c$ .

As mentioned in Section 3.2.1, the low momentum tracks can be reconstructed independently from the drift chamber information. Thanks to the 5 layers of the SVT, charge tracks having a momentum higher than about 50 MeV/ $c$  can be measured. This is important in order to reconstruct the decay  $D^{*+} \rightarrow D^0 \pi^+$  where the bachelor pion is very soft. A list of tracks where no hits in the drift chamber is created and is called “GoodTracksVeryLoose” (*GTVL*).

The present analysis uses the “GoodTracksLoose” list to form the  $D_s^+$  candidates. The soft pion candidates for the reconstruction of  $B^0 \rightarrow D_s^{(*)+} D^{*-}$  modes are taken from the “GoodTracksVeryLoose” list.

A photon candidate is defined as a localized energy maximum in the calorimeter acceptance. It must be isolated from any other photon candidate or track and have a lateral energy profile consistent with a photon shower. The set of such photons in the event forms the “GoodPhotonDefault” list, which is used as “single photons” to reconstruct the  $D_s^{*+} \rightarrow D_s^+ \gamma$  candidates.

## 5.2.2 Particle Identification

In order to reconstruct  $D_s^+$  meson, particle identification is necessary to obtain sufficiently clean samples. To this end, both the energy loss ( $dE/dx$ ) in the drift chamber and the vertex detector and the information from the DIRC are used to identify at least one of the kaons produced in the  $D_s^+$  decay. The kaon selector (*PidKaonSimpleSelector*), which is used, produces two lists of identified kaons: a loose list, *KSimpleLoose* and a tight one, *KSimpleTight*. The selection is based on the likelihoods given by each detector. We define a relative likelihood for each track consisting of the ratio of likelihood for the pion and the kaon mass hypothesis  $L_\pi/L_K$ . If this ratio is less than 1 for at least one of the considered subsystems, it is accepted as a loose kaon.

The DIRC is used both in the positive identification mode and the veto mode for selecting kaons. Tracks with momentum  $p > 0.7$  GeV/ $c$  and a number of expected photon for pion  $N_{exp}^\pi > 10$  are considered. If the number of measured photons is  $N_{pe} > 5$ , one requires  $N_{pe} < N_{exp}^\pi - 3\sqrt{N_{exp}^\pi}$ . For  $N_{pe} < 5$ , the track is considered as a kaon if  $N_{exp}^\pi > 15$ . For the tight criteria, a total likelihood is defined as the product of the likelihoods of each subsystem. The track is tagged as a tight kaon if the ratio of the total likelihood  $L_\pi^{tot}/L_K^{tot}$  is less than unity.

### 5.2.3 $D_s^+$ Skims from Multihadron Events

The first step of preselection is to filter out the multihadron events from all recorded events. The main goals of this selection are the following:

- good discrimination of beam gas and varying beam conditions,
- minor sensitivity of the final result to small variation in the selection,
- high efficiency to maximize the statistics,
- rejection of non  $B\bar{B}$  events, especially Bhabha and tau pairs.

The requirement of at least three “GoodTracksLoose” in the event achieves essentially this purpose.

Different selection criteria for the reconstructed mesons are used to optimize the total errors. For example, the statistical significance is the most crucial parameter for the study of rare  $B$  decays for  $V_{ub}$  measurements, while most inclusive studies are not limited by statistics, as the systematics become the dominant factor in the total errors. The two main goals of the skims and tag bits are to minimize the processing time needed for analysis on the one hand and satisfy all possible requirements of the different analyses on the other hand. The skims include four decay modes of the  $D_s^+$  mesons:  $D_s^+ \rightarrow \phi\pi^+$ ,  $D_s^+ \rightarrow \bar{K}^{*0}K^+$ ,  $D_s^+ \rightarrow \bar{K}^0K^+$ ,  $D_s^+ \rightarrow \phi\rho^+$ . These modes offer a good combination for the branching ratios, detection efficiency and signal to background ratio. The subsequent decays  $\phi \rightarrow K^+K^-$ ,  $\bar{K}^{*0} \rightarrow K^-\pi^+$ ,  $K_s^0 \rightarrow \pi^+\pi^-$ , and  $\rho^+ \rightarrow \pi^+\pi^0$  are used.

Three criteria based on *particle identification, track quality and momentum* are taken into account to produce the skims. Only tracks which are not identified as very tight pions (KMicroNotAPion) are accepted as kaons to form  $D_s^+$  candidates. At least one of the three tracks forming a  $D_s^+$  meson has to be reconstructed as “GoodTracksLoose”. In order to include the Cabibbo suppressed  $D^+$  decay, the reconstructed invariant of the  $D_s^+$  candidate is required to be within  $\pm 160 \text{ MeV}/c^2$  of the nominal  $D_s^+$  mass. The mass of the  $\phi$ ,  $K^{*0}$ ,  $K_s^0$ , and  $\rho^+$  candidates has to lie within  $\pm 5\sigma$  of their observed widths.

Two  $D_s^+$  skims are produced: one includes only the  $D_s^+ \rightarrow \phi\pi^+$  mode with no momentum cut (DsToPhiPi), while the second one contains all four modes  $D_s^+ \rightarrow \phi\pi^+$ ,  $D_s^+ \rightarrow \bar{K}^{*0}K^+$ ,  $D_s^+ \rightarrow \bar{K}^0K^+$ ,  $D_s^+ \rightarrow \phi\rho^+$  where the momentum of the candidate in the center-of-mass has to be greater than  $1.3 \text{ GeV}/c$  (InclDs). Table 5.2 shows the rates of these skims and the reconstruction efficiencies for the four  $D_s^+$  modes. These efficiencies are obtained from the Monte Carlo simulation using generated  $B^0 \rightarrow D_s^{(*)+}D^{*-}$  decays where the  $D_s^+$  momentum is in the range  $1.3$  to  $2 \text{ GeV}/c$  in the  $\Upsilon(4S)$  center-of-mass.

	Efficiency	Rate
DsToPhiPi	53%	1.86%
InclDs	48%	5.35%
$D_s^+ \rightarrow \phi\pi^+$	53%	
$D_s^+ \rightarrow \overline{K}^{*0}K^+$	78%	
$D_s^+ \rightarrow \overline{K}^0K^+$	48%	
$D_s^+ \rightarrow \phi\rho^+$	24%	

Table 5.2: The skim rates and efficiencies for the four  $D_s^+$  decay modes.

### 5.3 $D_s^{(*)+}$ Reconstruction

Although the four modes  $D_s^+ \rightarrow \phi\pi^+$ ,  $D_s^+ \rightarrow \overline{K}^{*0}K^+$ ,  $D_s^+ \rightarrow \overline{K}^0K^+$ ,  $D_s^+ \rightarrow \phi\rho^+$  are used, it will be demonstrated later, that the  $D_s^+ \rightarrow \phi\pi^+$  mode offers the best combination of the branching fraction, detection efficiency and signal purity. Therefore, it is used to study the inclusive  $D_s^+$  and  $D_s^{*+}$  production from  $B$  decays and  $q\bar{q}$  continuum, as it is very important for this study to measure the momentum spectrum at very low values where the combinatorial background is high. In addition to  $D_s^+ \rightarrow \phi\pi^+$ , the other modes can be included to perform the measurement of the branching fractions of  $B^0 \rightarrow D_s^{(*)+}D^{*-}$  as it helps to improve the statistical significance. It is possible because the reconstruction of the exclusive  $B$  channels with a partial reconstruction is not so sensitive to the purity of  $D_s^+$ , and the minimum momentum of the  $D_s^+$  produced in these  $B$  meson decays is about 1.3 GeV/c, which improves significantly the purity.

#### 5.3.1 $D_s^+$ Signal Selection

- $D_s^+ \rightarrow \phi\pi^+$

Three charge tracks coming from a common vertex are combined to form a  $D_s^+$  candidate. Two opposite charged tracks have to be identified as kaons using the tight list for one of them and the loose list for the other. The  $K^+K^-$  invariant mass must be within 8 MeV of the  $\phi$  nominal mass. In this particular decay, the  $\phi$  meson is polarized longitudinally and therefore the angular distribution of the kaons has a  $\cos^2\theta_H$  dependence. The angle  $\theta_H$  is the angle between the  $K^+$  (or the  $K^-$ ) in the  $\phi$  rest frame with respect to the  $\phi$  direction in the  $D_s^+$  rest

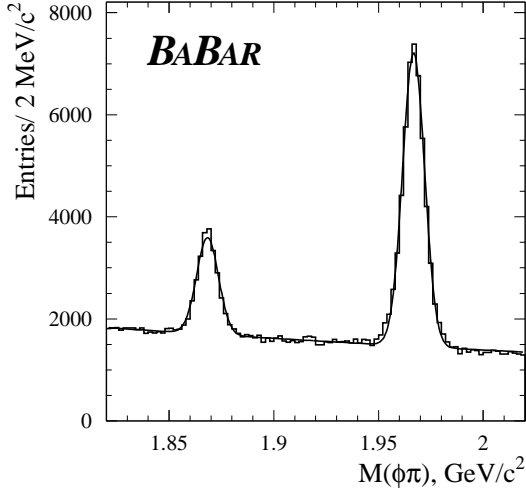


Figure 5.1: The  $\phi\pi^+$  invariant mass spectrum from the InclDs skim

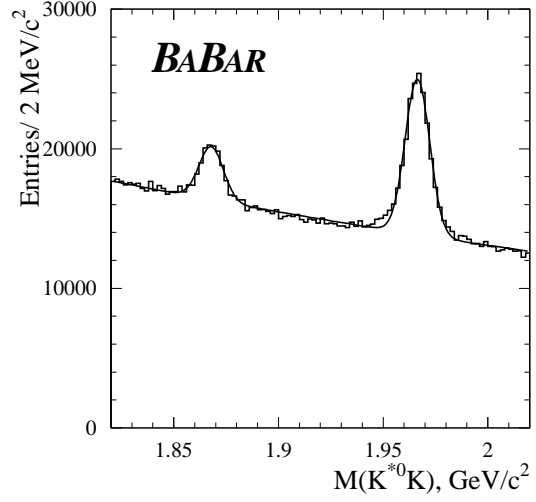


Figure 5.2: The  $\bar{K}^{*0}K^+$  invariant mass spectrum from the InclDs skim.

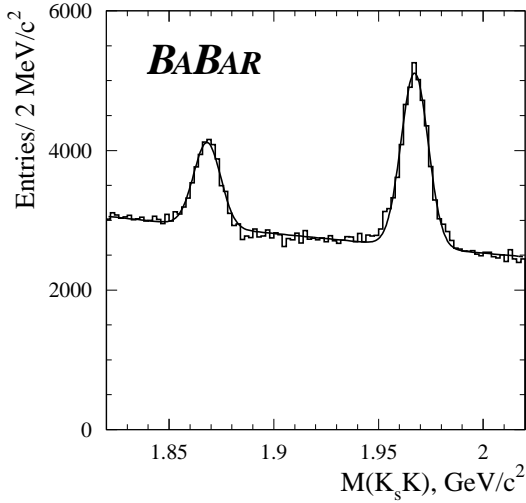


Figure 5.3: The  $K_s^0 K^+$  invariant mass spectrum from the InclDs skim.

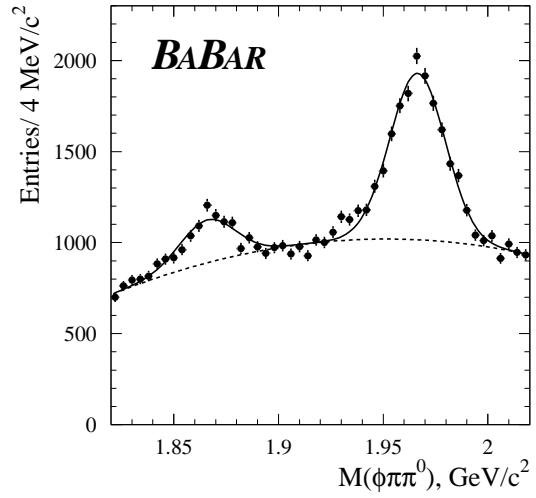


Figure 5.4: The  $\phi\pi^+\pi^0$  invariant mass spectrum from the InclDs skim.

frame. This feature is useful to improve the signal over background ratio as this distribution is more or less flat for the background. We require  $|\cos\theta_H| > 0.3$ , keeping thus 97% of the signal. Fig.5.1 shows the  $\phi\pi$  invariant mass distribution after applying the above cuts. In addition to the  $D_s^+$  peak, a lower mass peak corresponding to the Cabibbo-suppressed decay mode  $D^+ \rightarrow \phi\pi^+$  is observed.

The fit function is a single Gaussian for each peak with their width constrained to be equal on top of an exponential background.

- $D_s^+ \rightarrow \bar{K}^{*0} K^+$

Here the  $\bar{K}^{*0} \rightarrow K^- \pi^+$  invariant mass must be within 65 MeV of the nominal value. This wider window leads to a fraction of combinatorial background much larger than for the former case. To reduce this background at a reasonable level, we require the helicity angle  $|\cos \theta_H| > 0.3$ . In addition, there is a serious physical background coming from  $D^+ \rightarrow \bar{K}^{*0} \pi^+$  and  $D^+ \rightarrow \bar{K}^0 \pi^+$  decays. Indeed, when one of the pions is misidentified, the reconstructed mass for such decays tends to peak around the  $D_s^+$  mass. In order to eliminate these reflections, we require the tight identification criteria for the bachelor kaon while the loose criterium is applied to the other kaon. Fig.5.2 shows the reconstructed  $\bar{K}^{*0} K$  invariant mass. The same fit function as for  $\phi \pi^+$  mass spectrum has been used.

- $D_s^+ \rightarrow \bar{K}^0 K^+$

The  $\pi^+ \pi^-$  invariant mass for  $\bar{K}_s \rightarrow \pi^+ \pi^-$  must be within 15 MeV of the nominal mass and the bachelor kaon is identified using the tight criteria. To improve the purity of the reconstructed  $K_s$ , we determine the angle between the  $K_s$  direction and the direction defined by its decay vertex and the primary vertex of the event. The distribution of this angle is expected to peaked at  $\cos \alpha = 1$  for the signal. We require  $\cos \alpha > 0.98$  to reject the combinatorics background while no signal is lost. The  $K_s K$  invariant mass distribution is shown in Fig.5.3 where the same fit function as for  $\phi \pi^+$  mass spectrum has been used.

- $D_s^+ \rightarrow \phi \rho^+$

For this mode, the  $\phi$  is reconstructed using two opposite charged tracks both identified as tight kaons. A third track is added to the  $\phi$  and all tracks are fitted to a common vertex.  $\pi^0$  candidates are then combined to the pion to form the  $\rho^+$  meson. Each  $\pi^0$  is reconstructed using the photons with an energy greater than 50 MeV in the laboratory frame. A  $\pi^0$  is selected if the invariant  $\gamma\gamma$  mass is within 20 MeV/c<sup>2</sup> of its nominal value and if its energy in the  $\Upsilon(4S)$  rest frame is  $E^* > 0.5$  GeV. Fig.5.4 shows the  $\phi \pi \pi^0$  invariant mass distribution for  $0.6 < M_{\pi^+ \pi^0} < 0.94$ , corresponding to the  $\rho^+$  mass window. The signal is fitted with a single Gaussian for each peak ( $D_s^+$  and  $D^+$ ) with their width constrained to be equal. The background is modelled by a third order polynomial. The significant larger width of the signal comparing with the other channels is due to the energy resolution of the photons.

The selection criteria and the fit parameters obtained for data and Monte Carlo are summarized in Table 5.3. The efficiency, invariant mass and momentum resolution

	$D_s^+ \rightarrow \phi\pi^+$	$D_s^+ \rightarrow \bar{K}^{*0}K^+$	$D_s^+ \rightarrow \bar{K}^0K^+$	$D_s^+ \rightarrow \phi\rho^+$
$\frac{\mathcal{B}}{\mathcal{B}(D_s^+ \rightarrow \phi\pi^+)}$	1	$0.95 \pm 0.10$	$1.01 \pm 0.25$	$1.86 \pm 0.48$
Cuts	$\mathcal{P}(\chi^2)_{D_s^+} > 0.01$ $1.011 < M_\phi < 1.026$ $p^* > 1.3 \text{ GeV}/c$ $ \cos\theta_H  > 0.3$	$\mathcal{P}(\chi^2)_{D_s^+} > 0.01$ $0.825 < M_{K^*} < 0.965$ $p^* > 1.3 \text{ GeV}/c$ $ \cos\theta_H  > 0.3$	$\mathcal{P}(\chi^2)_{D_s^+} > 0.01$ $0.485 < M_{K_s} < 0.51$ $p^* > 1.3 \text{ GeV}/c$ $\cos\alpha > 0.98$	$\mathcal{P}(\chi^2)_{KK\pi} > 0.01$ $1.011 < M_\phi < 1.026$ $p^* > 2.5 \text{ GeV}/c$ $0.115 < M_{\pi^0} < 0.150$ $0.6 < M_{\pi\pi^0} < 0.94$ $E_{\pi^0}^* > 0.5 \text{ GeV}$
# events	$37699 \pm 249$	$81973 \pm 599$	$20165 \pm 288$	$7572 \pm 235$
$\sigma$ , MeV	$5.23 \pm 0.04$	$5.97 \pm 0.04$	$6.46 \pm 0.10$	$13.2 \pm 0.4$
Monte Carlo				
$\epsilon$ , %	$39.0 \pm 2.0$	$53.7 \pm 1.8$	$36.1 \pm 1.4$	$10.5 \pm 1.1$
$\sigma$ , MeV	$4.2 \pm 0.1$	$5.2 \pm 0.2$	$4.7 \pm 0.2$	$10.6 \pm 1.3$
$\Delta p^*$ , MeV/c	$5.9 \pm 0.3$	$6.1 \pm 0.2$	$5.9 \pm 0.3$	$9.2 \pm 0.4$

Table 5.3: Selection criteria, fit parameters and efficiencies for  $D_s^+ \rightarrow \phi\pi^+$ ,  $D_s^+ \rightarrow \bar{K}^{*0}K^+$ ,  $D_s^+ \rightarrow \bar{K}^0K^+$  and  $D_s^+ \rightarrow \phi\rho^+$  decay modes. The data from the InclDs skim are analyzed.

obtained from the Monte Carlo using the two-body  $B^0 \rightarrow D_s^{(*)+}D^{*-}$  signal events are presented in the same table. The detail study of these parameters with generic events as a function of momentum will be shown below.

As one can see, the measured mass resolution is about 30% larger than the Monte Carlo (Table 5.3). The  $D_s^+$  momentum resolution for the different reconstructed modes is shown in Fig. 5.5 and summarized in Table 5.3.

### 5.3.2 $D_s^{*+}$ Signal Selection

$D_s^{*+}$  mesons are reconstructed using the decay  $D_s^{*+} \rightarrow D_s^+\gamma$  with the subsequent decays  $D_s^+ \rightarrow \phi\pi^+$ ,  $D_s^+ \rightarrow \bar{K}^{*0}K^+$  and  $D_s^+ \rightarrow \bar{K}^0K^+$ .  $D_s^+$  candidates are selected by requiring the  $D_s^+$  invariant mass to be within 2.5 standard deviations ( $\sigma$ ) of the fitted peak value. These  $D_s^+$  are then combined with photon candidates in the event. The



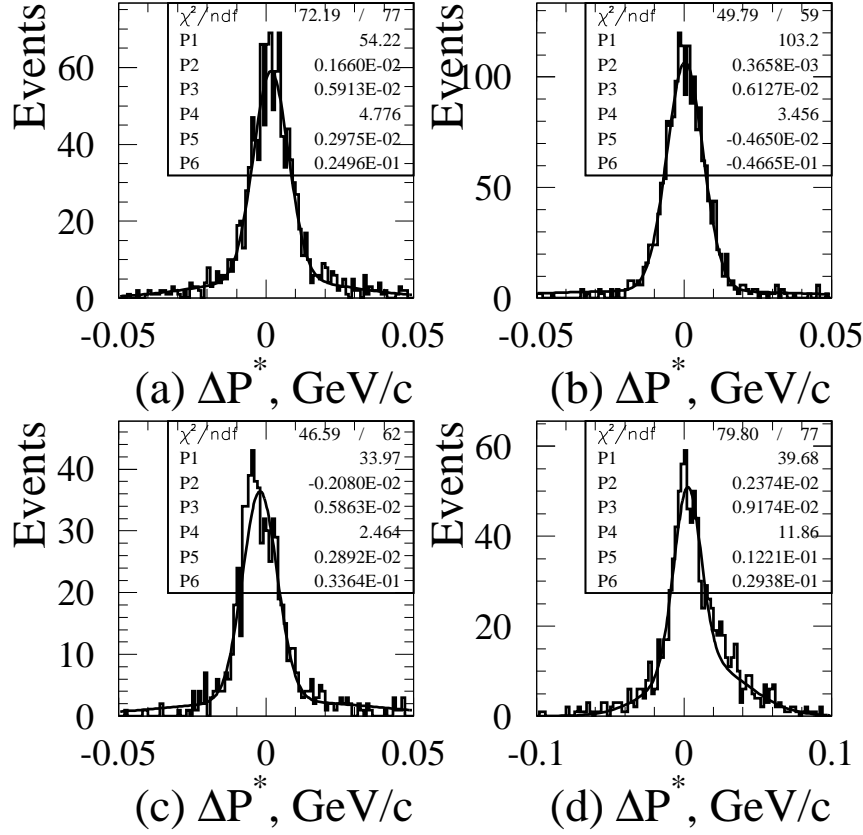


Figure 5.5:  $D_s^+$  momentum resolution from SP3 Monte Carlo. (a) -  $D_s^+ \rightarrow \phi \pi^+$ , (b) -  $D_s^+ \rightarrow \bar{K}^{*0} K^+$ , (c) -  $D_s^+ \rightarrow \bar{K}^0 K^+$ , (d) -  $D_s^+ \rightarrow \phi \rho^+$

photon candidates are defined in the following way.

- $E_\gamma > 50$  MeV, where  $E_\gamma$  is the photon energy in the laboratory frame.
- $E_\gamma^* > 110$  MeV, where  $E_\gamma^*$  is the photon energy in the  $\Upsilon(4S)$  center-of-mass.
- When combined with any other photon in the event, the photon candidate should not form a  $\pi^0$ , defined by a total center-of-mass energy  $E_{\gamma\gamma}^* > 200$  MeV and an invariant mass  $115 < M_{\gamma\gamma} < 155$  MeV/ $c^2$ .

The distributions of the mass difference  $\Delta M = M(D_s^+ \gamma) - M(D_s^+)$  are shown for the different  $D_s^+$  decay modes in the Fig.5.6,5.7,5.8,5.9.

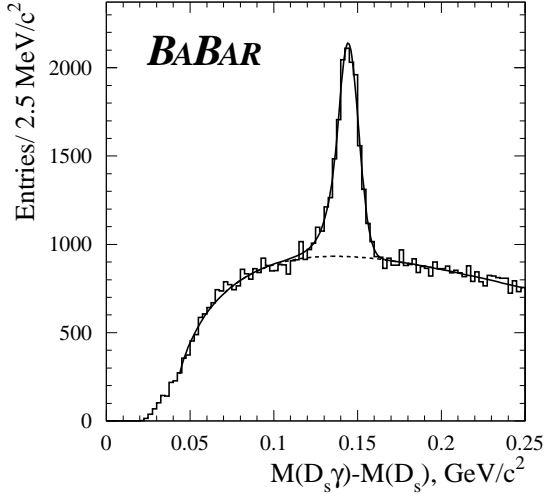


Figure 5.6: Distribution of the  $\Delta M = M_{D_s\gamma} - M_{D_s}$  with  $D_s^+$  identified in  $D_s^+ \rightarrow \phi\pi^+$  mode from the InclDs skim. The fit function is a Crystal Ball function for the signal plus a threshold function.

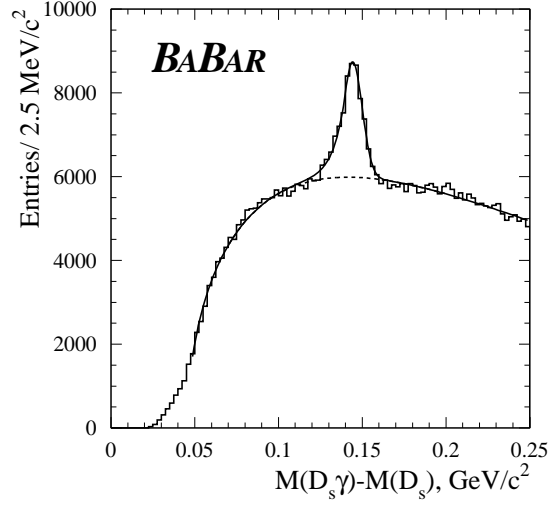


Figure 5.7: Distribution of the  $\Delta M = M_{D_s\gamma} - M_{D_s}$  with  $D_s^+$  identified in  $D_s^+ \rightarrow \bar{K}^{*0}K^+$  mode from the InclDs skim. The fit function is a Crystal Ball function for the signal plus a threshold function.

The  $\Delta M$  distribution of the signal is fitted with an asymmetric function  $f(x)$  (Crystal Ball function [44]) to account for energy leakage and calorimeter shower shape fluctuations.

$$f(x) = N \cdot \begin{cases} \exp\left(-\frac{(x-\bar{x})^2}{2\sigma^2}\right) & ; (x - \bar{x})/\sigma > \alpha \\ A \times (B - \frac{x-\bar{x}}{\sigma})^{-n} & ; (x - \bar{x})/\sigma \leq \alpha \end{cases} \quad (5.3)$$

where  $A \equiv \left(\frac{n}{|\alpha|}\right)^n \times \exp(-|\alpha|^2/2)$  and  $B \equiv \frac{n}{|\alpha|} - |\alpha|$ .  $N$  is a normalization factor,  $\bar{x}$  and  $\sigma$  are the peak position and width of the Gaussian portion of the function,  $\alpha$  is the point at which the function changes to the power function and  $n$  is the exponent of the power function.  $A$  and  $B$  are defined so that the function and its first derivative are continuous at  $\alpha$ . For the background, a threshold function

$$f(\Delta M) = p_1(\Delta M - p_2)^{p_3} e^{p_4(\Delta M - p_2)} \quad (5.4)$$

is used, where the four parameters  $p_i$  are left free in the fit. A clear peak with  $17891 \pm 217$   $D_s^{*+}$  events at  $\Delta M = 144.4 \pm 0.1$  MeV/ $c^2$  is observed for the sum of three  $D_s^+$  modes. The number of the signal events is counted by integrating the signal function after background subtraction.

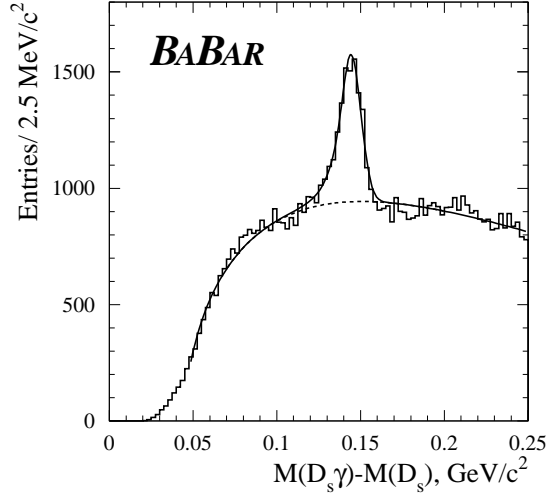


Figure 5.8: Distribution of the  $\Delta M = M_{D_s \gamma} - M_{D_s}$  with  $D_s^+$  identified in  $D_s^+ \rightarrow \bar{K}^0 K^+$  mode from the InclDs skim. The fit function is a Crystal Ball function for the signal plus a threshold function.

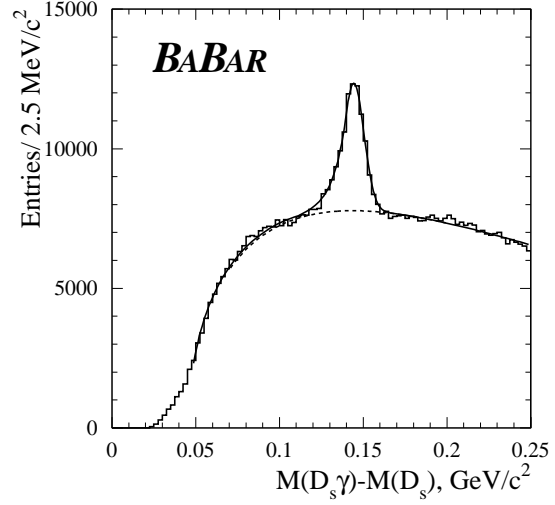


Figure 5.9: Distribution of the  $\Delta M = M_{D_s \gamma} - M_{D_s}$  with  $D_s^+$  identified in  $D_s^+ \rightarrow \phi \pi^+$ ,  $D_s^+ \rightarrow \bar{K}^{*0} K^+$  and  $D_s^+ \rightarrow \bar{K}^0 K^+$  modes from the InclDs skim.

The efficiency and invariant mass resolution obtained with Monte Carlo using the two-body  $B^0 \rightarrow D_s^{(*)+} D^{*-}$  signal events are shown in Table 5.4. The detail studies of the fit parameters will be described in section 6.2 using generated  $B\bar{B}$  and  $q\bar{q}$  events as a function of momentum. The  $\Delta M$  resolution is slightly higher in the data than in the Monte Carlo simulation. For the selection criteria described above, the average reconstruction efficiency is  $14.9 \pm 0.7\%$ .

	$D_s^+ \rightarrow \phi\pi^+$	$D_s^+ \rightarrow \bar{K}^{*0}K^+$	$D_s^+ \rightarrow \bar{K}^0K^+$	Sum
$N_{\text{ev}}$ $\Delta M$ , MeV/ $c^2$ $\sigma$ , MeV	Data			
	$4115 \pm 99$	$8830 \pm 230$	$2148 \pm 131$	$17891 \pm 217$
	$144.4 \pm 0.2$	$144.4 \pm 0.2$	$144.3 \pm 0.6$	$144.4 \pm 0.1$
	$6.21 \pm 0.18$	$5.64 \pm 0.17$	$5.90 \pm 0.06$	$6.09 \pm 0.04$
$\sigma$ , MeV $\epsilon$ , %	Monte Carlo			
	$5.3 \pm 0.4$	$6.0 \pm 0.5$	$7.0 \pm 0.9$	$5.7 \pm 0.3$
	$14.5 \pm 1.0$	$16.8 \pm 1.1$	$14.2 \pm 1.3$	$14.9 \pm 0.7$

Table 5.4: The fit results for  $\Delta M = M(D_s^+\gamma) - M(D_s^+)$  mass spectrum. The  $D_s^+$  mesons are identified in  $D_s^+ \rightarrow \bar{K}^0K^+$ ,  $D_s^+ \rightarrow \bar{K}^{*0}K^+$ ,  $D_s^+ \rightarrow \bar{K}^0K^+$  modes. The data from the InclDs skim are analysed.

## Chapter 6

# The $B \rightarrow D_s^{(*)+} X$ Decays

### 6.1 $D_s^+$ Momentum Spectrum

As shown in the previous section the mode  $D_s^+ \rightarrow \phi\pi^+$  with the subsequent decay  $\phi \rightarrow K^+K^-$  is the best match of branching fraction, detection efficiency, and signal to background ratio and therefore allows one to study the full  $D_s^+$  momentum spectrum. The events preselected with the DsToPhiPi skim are used to study the  $D_s^+$  and  $D_s^{*+}$  production in  $B$  meson decays as well as from continuum  $e^+e^-$  annihilation. The  $\phi\pi^+$  invariant mass distribution obtained from the preselected sample is shown in Fig. 6.1. The  $D_s^+$  signal includes  $47801 \pm 304$  events and has an average mass resolution of  $5.23 \pm 0.04$  MeV.

The momentum spectrum of  $D_s^+$  mesons in the center-of-mass frame is extracted by fitting the  $\phi\pi$  invariant mass distribution in 24 windows of momentum. Each window is 200 MeV/ $c$  wide, which is much larger than the momentum resolution of about 6 MeV (Section 5.3.1). Each of  $D_s^+$  and  $D^+$  peak is fitted using a single Gaussian. However, both peaks are fitted simultaneously constraining the width of the Gaussians to the same value. The combinatorial background is accounted for by an exponential function. As there are many more events in the on-resonance data sample, the number of  $D_s^+$  in the off-resonance data is extracted using the same fit function where the values of the Gaussian parameters ( $M_{D^+}$ ,  $M_{D_s^+}$  and  $\sigma$ ) were fixed to those obtained from the on-resonance data. The  $\phi\pi^+$  invariant mass distributions corresponding to the different  $D_s^+$  momentum windows in the  $\Upsilon(4S)$  rest frame are shown in Figs. 6.3,6.4 for the on-resonance data sample, while Figs. 6.5,6.6 show those obtained with the off-resonance data sample.

Fig.6.7 shows the variation of the  $D_s^+$  mass versus its momentum. Since the reconstruction of the tracks is not perfect, one observes a dependence of the fitted  $D_s^+$  mass as a function of the  $D_s^+$  momentum in the  $\Upsilon(4S)$  center-of-mass. This effect

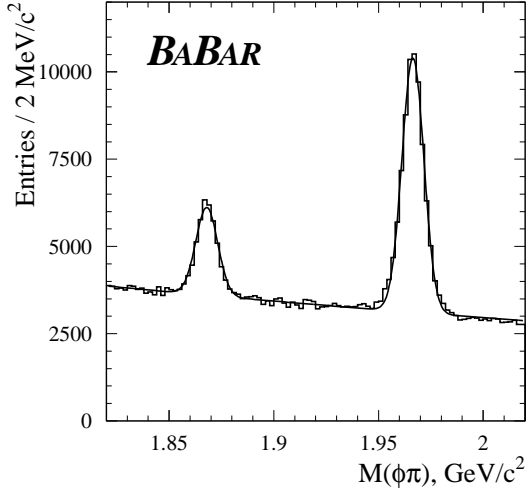


Figure 6.1: The  $\phi\pi^+$  invariant mass spectrum obtained from DsToPhiPi skim. The fit function is a single Gaussian for each peak, with their widths constrained to be equal on top of an exponential background.

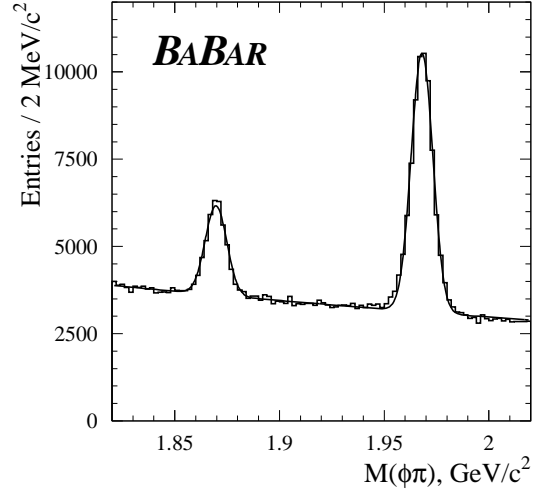


Figure 6.2: The  $\phi\pi^+$  invariant mass spectrum corrected using its momentum dependence. The fit function is a single Gaussian for each peak, with their widths constrained to be equal on top of an exponential background.

is also observed in the Monte Carlo simulation where  $B\bar{B}$  and  $c\bar{c}$  events have been generated. One can parameterize this dependence using the function

$$f(m) = p_1(1 - p_2 e^{-p_3 m}) \quad (6.1)$$

where the three parameters  $p_i$  are free in the fit, and thus correct the data from this effect. The resulting  $\phi\pi^+$  distribution is shown in Fig.6.2. This improves slightly the average resolution ( $\sigma = 5.13 \pm 0.04$  MeV). Fig.6.8 shows the  $\phi\pi^+$  mass resolution as a function of momentum in the  $\Upsilon(4S)$  rest frame both for data and Monte Carlo. It is interesting to note that the mass resolution depends only mildly on the  $D_s^+$  momentum as it increases from 4.5 to 6 MeV for data. One observes a similar dependence in the Monte Carlo events although the absolute resolution is 3.5 to 5 MeV.

The efficiency  $\epsilon$  of the  $D_s^+$  selection is calculated from Monte Carlo using simulated  $B\bar{B}$  and  $c\bar{c}$  events. It varies as a function of the  $D_s^+$  momentum,  $p^*$  in the center-of-mass frame. The efficiency ranges from about 20% when the  $D_s^+$  is at rest in the center-of-mass to about 40% for  $p^* = 5$  GeV/c as shown in Fig.6.11. The difference for the fitted masses and resolution between data and Monte Carlo may lead to some bias in the efficiency determination. In order to verify that the obtained efficiency depends neither on the peak value nor on the resolution, two methods are used. First, the  $D_s^+$  yield is defined by counting the number of events within a large  $\phi\pi^+$  mass

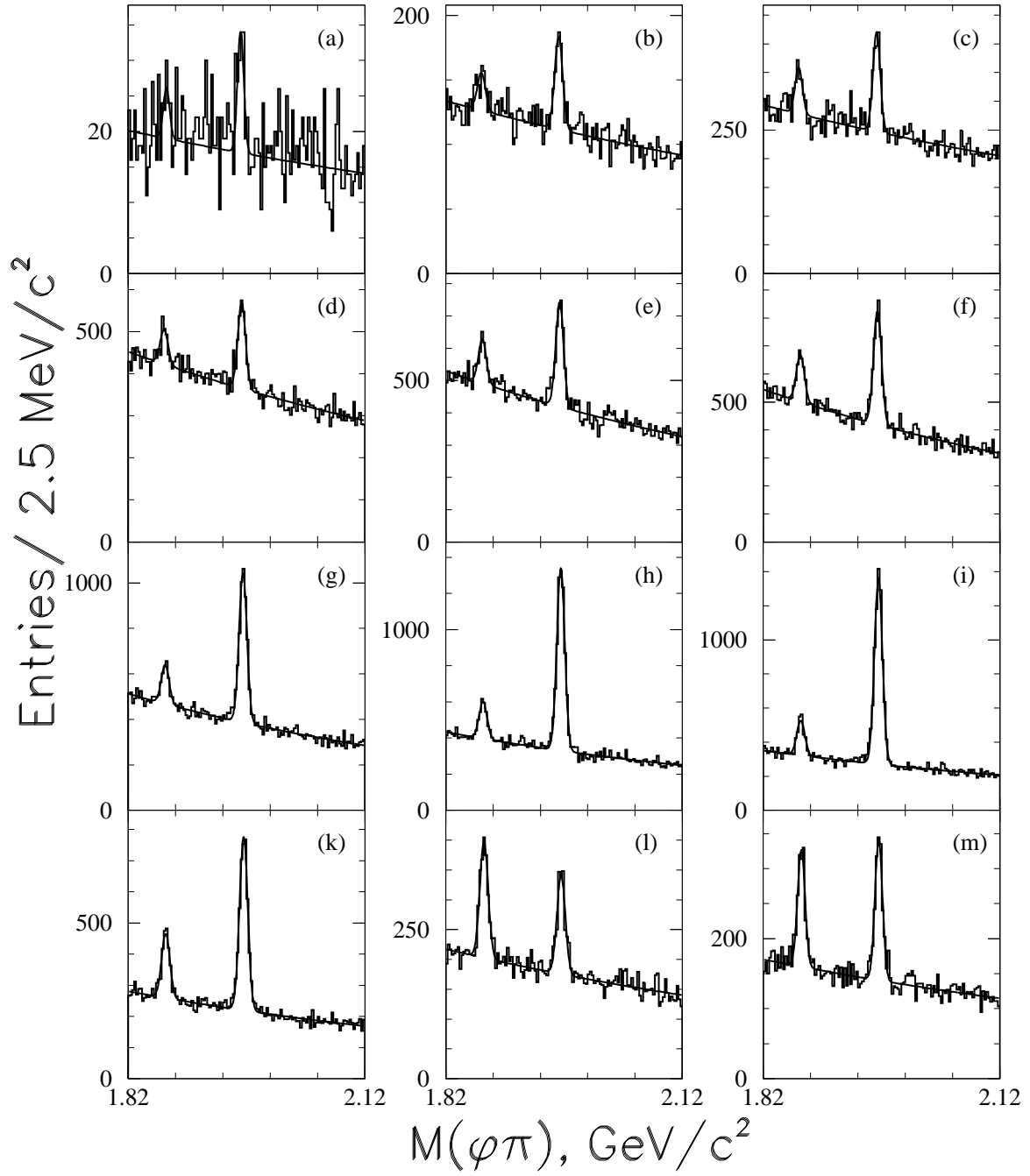


Figure 6.3: The  $\phi\pi^+$  mass distributions for the on-resonance data for 12 different momentum windows (a) 0-0.2, (b) 0.2-0.4, (c) 0.4-0.6, (d) 0.6-0.8, (e) 0.8-1.0, (f) 1.0-1.2, (g) 1.2-1.4, (i) 1.4-1.6, (h) 1.6-1.8, (k) 1.8-2.0, (l) 2.0-2.2, (m) 2.2-2.4  $\text{GeV}/c$ . The result of the fit described in the text is overlaid.

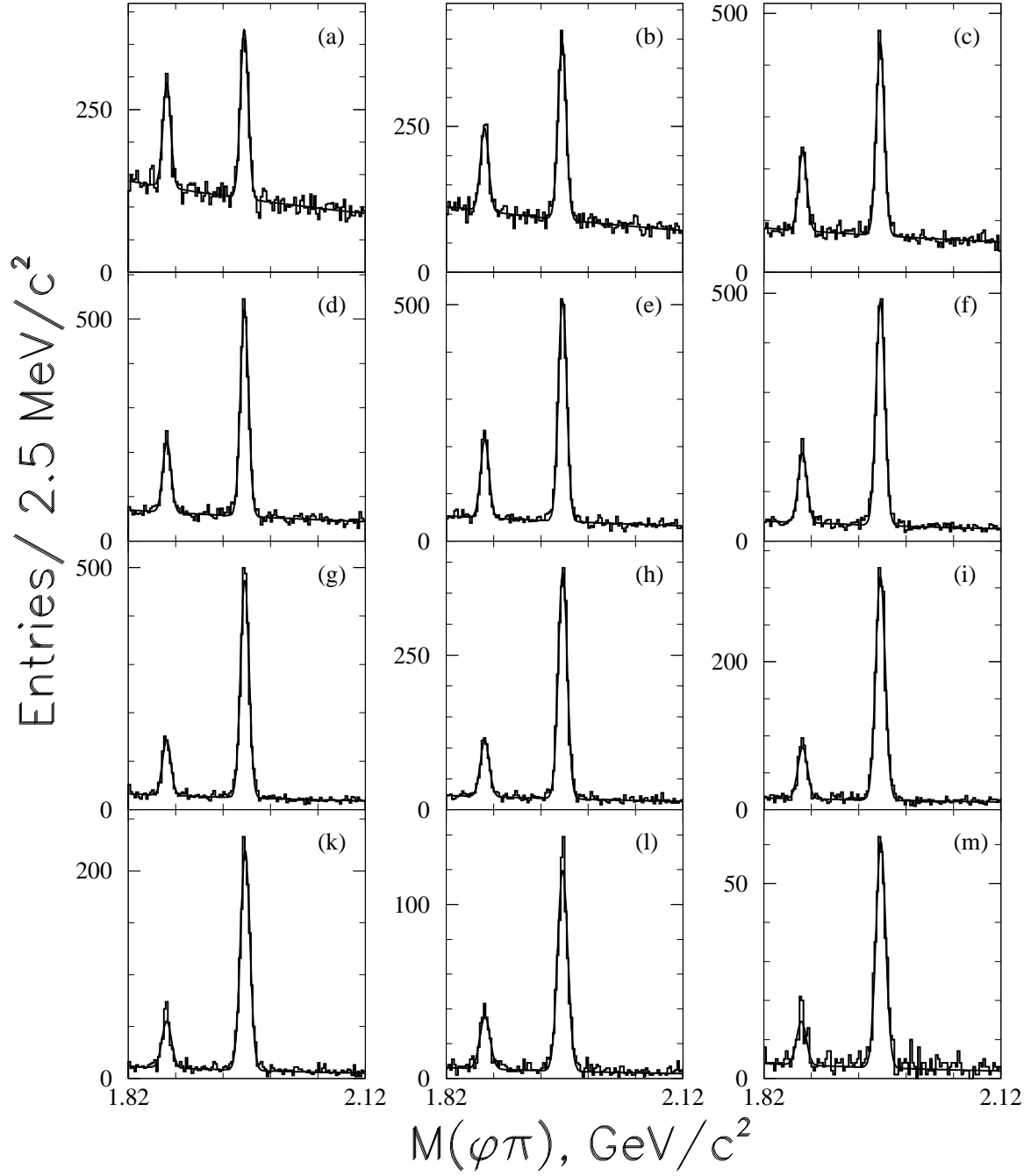


Figure 6.4: The  $\phi\pi^+$  mass distributions for the on-resonance data for 12 different momentum windows (a) 2.4-2.6 GeV/c, (b) 2.6-2.8, (c) 2.8-3.0, (d) 3.0-3.2, (e) 3.2-3.4, (f) 3.4-3.6, (g) 3.6-3.8, (i) 3.8-4.0, (h) 4.0-4.2, (k) 4.2-4.4, (l) 4.4-4.6, (m) 4.6-4.8 GeV/c. The result of the fit described in the text is overlaid.



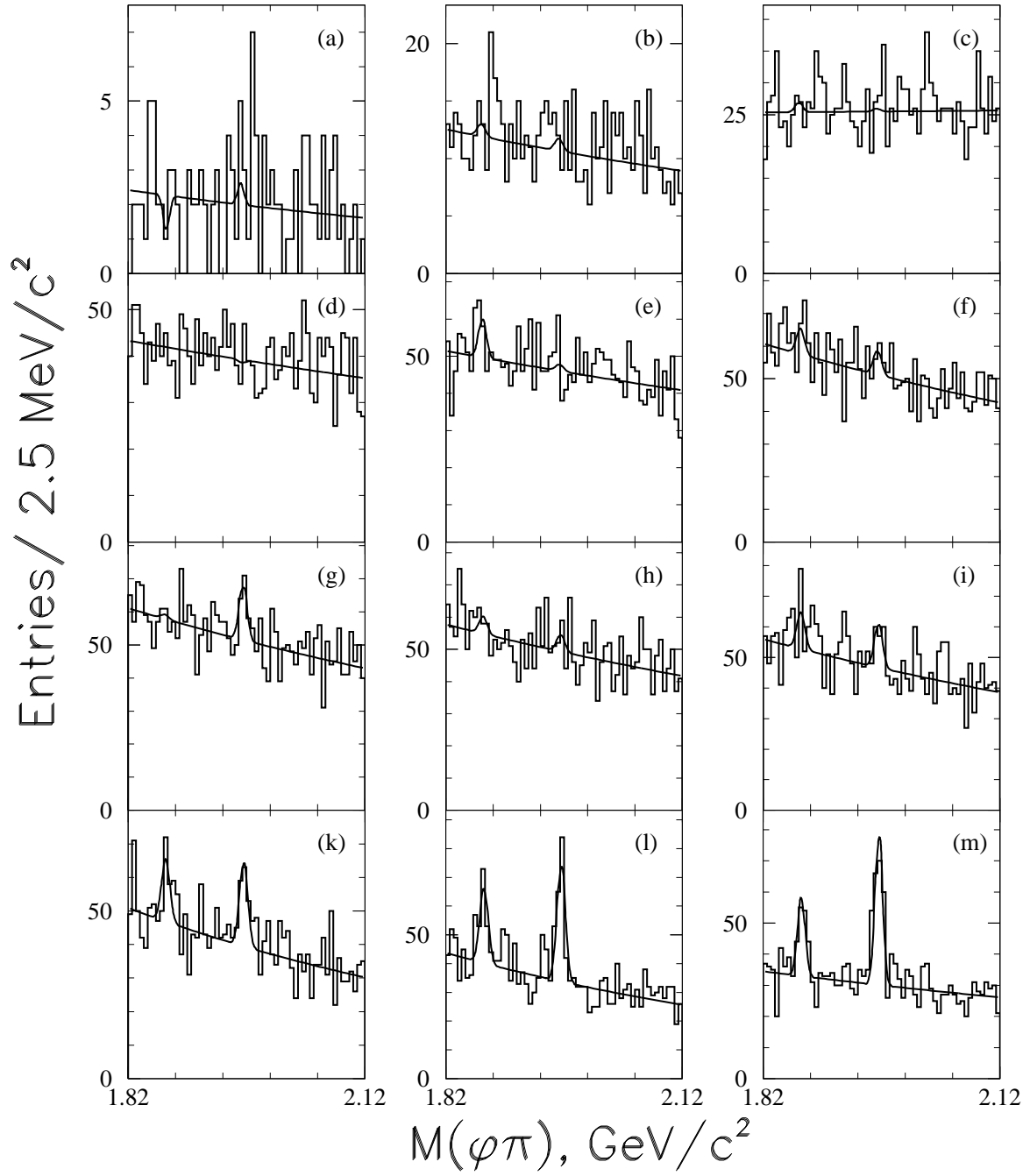


Figure 6.5: The  $\phi\pi^+$  mass distributions for the off-resonance data for 12 different momentum windows (a) 0-0.2, (b) 0.2-0.4, (c) 0.4-0.6, (d) 0.6-0.8, (e) 0.8-1.0, (f) 1.0-1.2, (g) 1.2-1.4, (i) 1.4-1.6, (h) 1.6-1.8, (k) 1.8-2.0, (l) 2.0-2.2, (m) 2.2-2.4  $\text{GeV}/c$ . The result of the fit described in the text is overlaid.

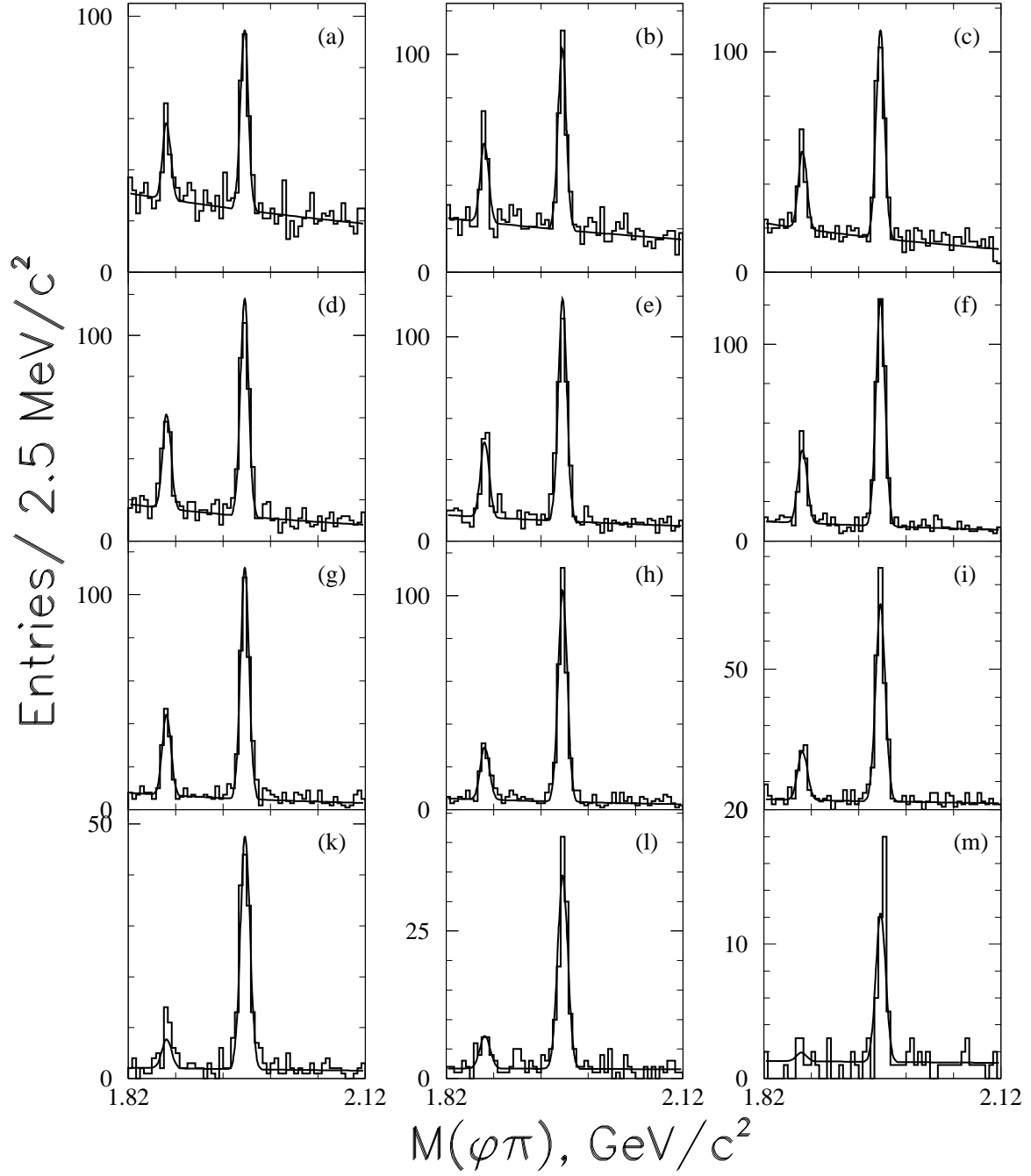


Figure 6.6: The  $\phi\pi^+$  mass distributions for the off-resonance data for 12 different momentum windows (a) 2.4-2.6  $\text{GeV}/c$ , (b) 2.6-2.8, (c) 2.8-3.0, (d) 3.0-3.2, (e) 3.2-3.4, (f) 3.4-3.6, (g) 3.6-3.8, (i) 3.8-4.0, (h) 4.0-4.2, (k) 4.2-4.4, (l) 4.4-4.6, (m) 4.6-4.8  $\text{GeV}/c$ . The result of the fit described in the text is overlaid.

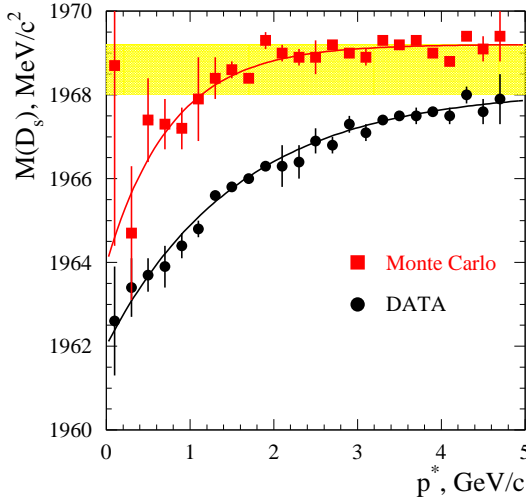


Figure 6.7: The fitted  $D_s^+$  mass as a function of its momentum in the  $\Upsilon(4S)$  rest frame for data and Monte Carlo. The curves show the fit results using the function described in the text. The shaded band shows the PDG value with the error ( $1968.6 \pm 0.6 \text{ MeV}/c^2$ ).

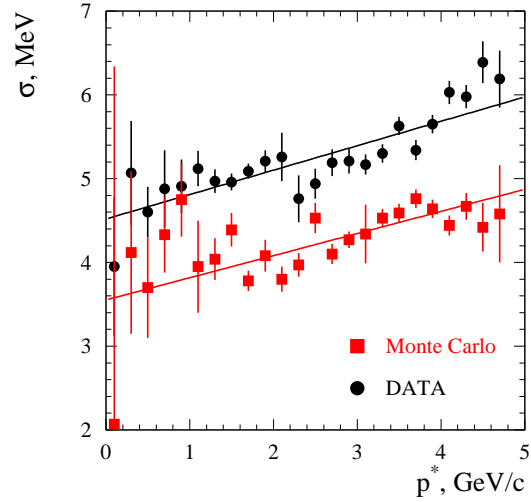


Figure 6.8: The  $\phi\pi^+$  mass resolution as a function of momentum in the  $\Upsilon(4S)$  rest frame for data (black dots) and Monte Carlo (red squares). The points are fitted with a straight line.

window requiring the reconstructed  $D_s^+$  to be a real  $D_s^+$ . This mass range is defined as  $1.952 < M(\phi\pi^+) < 1.985 \text{ GeV}/c^2$ , which corresponds to about 3 standard deviations ( $\sigma$ ) of the  $D_s^+$  mass resolution in the data. For the second method, the number of the reconstructed  $D_s^+$  mesons is extracted from the fit of the  $\phi\pi^+$  invariant mass distribution as in data. Both masses and resolution ( $M(D^+)$ ,  $M(D_s^+)$  and  $\sigma$ ) are free in the fit. One can see from the plot (Fig.6.11) that both methods are in agreement within statistical errors.

The number of reconstructed  $D_s^+$  mesons as a function of their momentum in the center-of-mass frame is shown in Fig.6.9 for off-resonance and in Fig.6.10 for on-resonance data. The efficiency-corrected  $D_s^+$  momentum spectrum is shown in Fig.6.12. The fact that there are no  $D_s^+$  mesons from  $B$  decays with  $p^* > 2.45 \text{ GeV}/c$  is used to derive the  $D_s^+$  momentum spectrum from the continuum with increased statistic. This is done by adding the  $D_s^+$  momentum spectrum from the on-resonance sample after scaling it using the off/on luminosity ratio. The efficiency-corrected  $D_s^+$  yield as a function of its momentum is then fit using an Andersson fragmentation function [47]. As will be shown in Sec.6.4.2 this function reproduces the best this distribution.

In order to obtain the  $D_s^+$  momentum spectrum from  $B$  decays, one needs to subtract

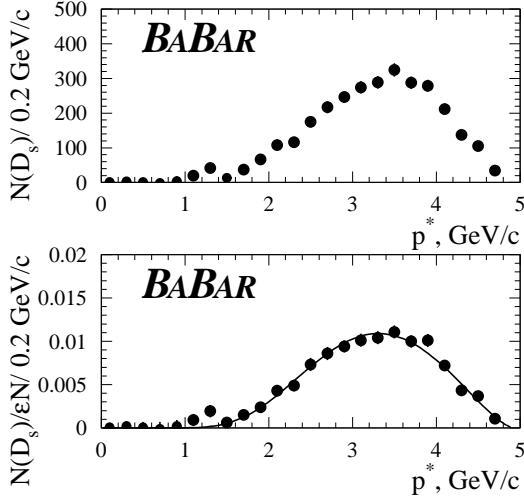


Figure 6.9: The  $D_s^+$  momentum spectrum before (top) and after (bottom) efficiency correction obtained from off-resonance data. The fit uses an Andersson function.

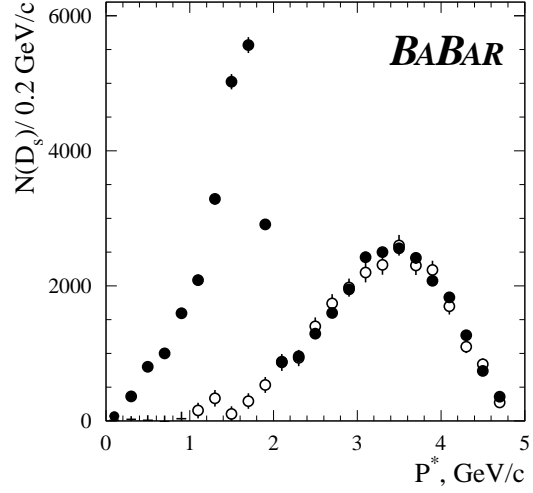


Figure 6.10: The  $D_s^+$  yield from on-resonance (solid circles) and off-resonance (open circles) data scaled according to the luminosity ratio before efficiency correction.

the continuum contribution below  $p^* = 2.45 \text{ GeV}/c$ . There are two possible ways to do so. Either one uses the value of the fit function derived from the on- and off-resonance data and subtracts it bin-by-bin from the on-resonance efficiency corrected data (Fig. 6.13 shows the resulting momentum spectrum). This method has the advantage to minimize the statistical error due to the limited off-resonance statistic, but has the disadvantage of larger systematic error due to the parameterization uncertainty. An alternative method, independent of any assumption regarding the shape of the fragmentation function is also used. The off-resonance data scaled by the on- to off-resonance luminosity ratio are subtracted bin-by-bin from the on-resonance data (i.e., not efficiency-corrected). This increases slightly the statistical error for each point. The resulting efficiency-corrected  $D_s^+$  momentum distribution is shown in Figs. 6.14. Since the final results are not dominated by the statistical errors for the inclusive  $D_s^+$  branching fraction, the last method is used. The first method which assumes the fragmentation parameterization gives then a cross check of the results.

## 6.2 $D_s^{*+}$ Momentum Spectrum

The  $D_s^{*+}$  mesons are reconstructed in the mode  $D_s^{*+} \rightarrow D_s^+ \gamma$ , with the subsequent decay  $D_s^+ \rightarrow \phi \pi^+$ . Fig 6.15 shows the  $\Delta M = M(D_s^+ \gamma) - M(D_s^+)$  distribution for

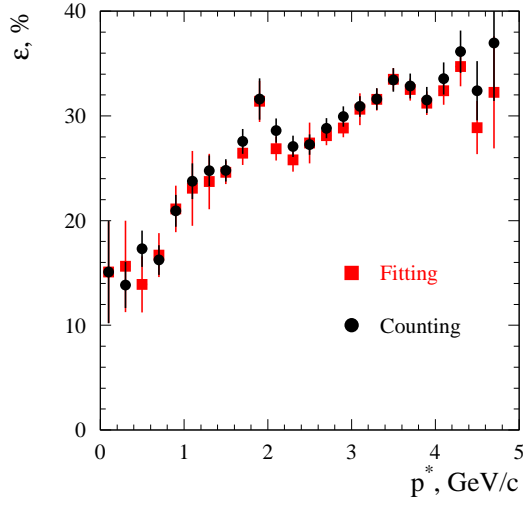


Figure 6.11: The efficiency for  $D_s^{*+} \rightarrow \phi\pi^+$  with consequent  $\phi \rightarrow K^+K^-$  decay as a function of momentum in the center-of-mass frame. Two methods described in the text are used to account the number of reconstructed  $D_s^+$ .

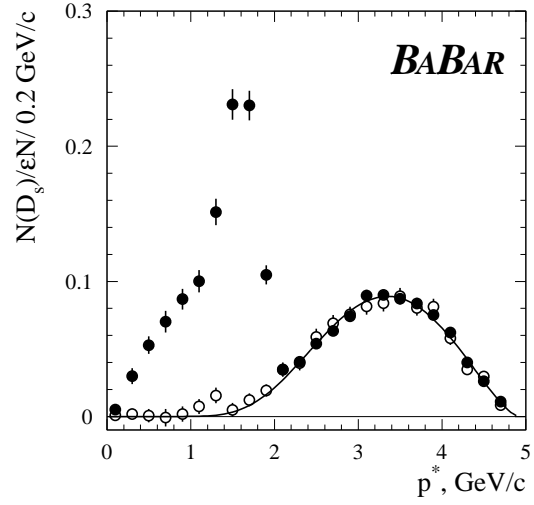


Figure 6.12: The  $D_s^+$  efficiency-corrected momentum spectrum for on-resonance (filled circles) and scaled off-resonance data (open circles). The curve shows the fit with an Andersson function.

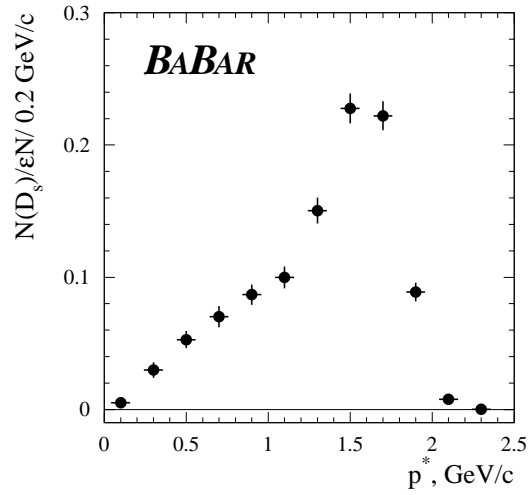
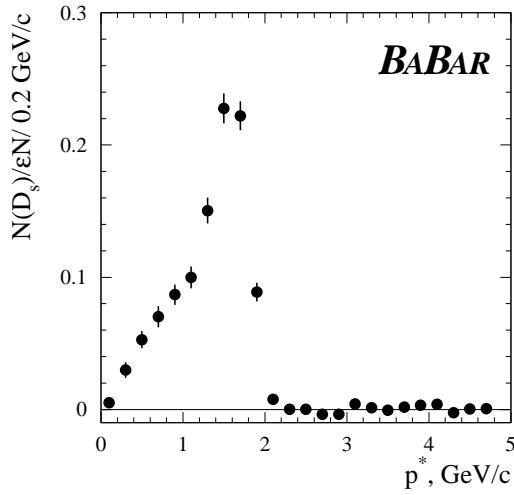


Figure 6.13: The efficiency-corrected  $D_s^{*+}$  momentum spectrum from  $B$  decays. The Andersson fragmentation function is used for the fit of the continuum events. The entire momentum range (left) and below 2.5 GeV/c (right) are shown

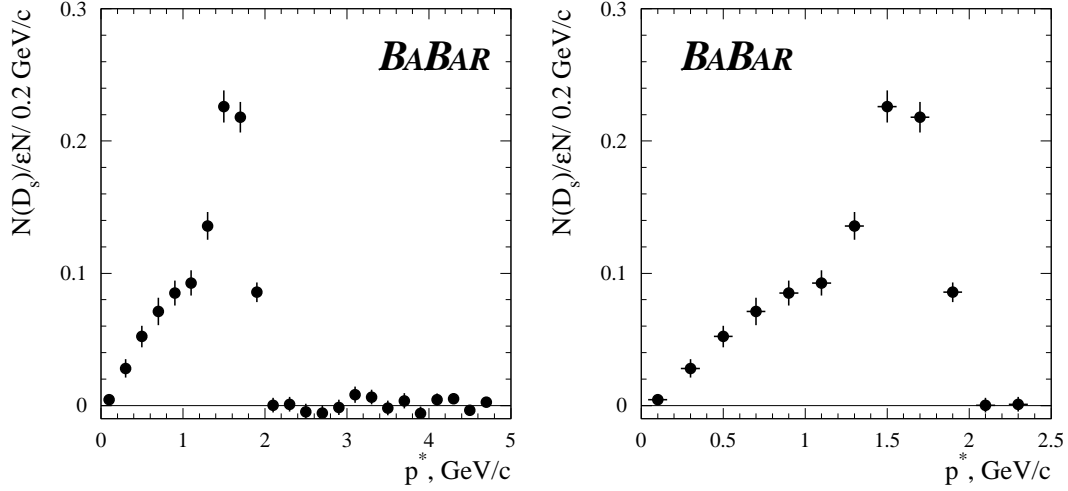


Figure 6.14: The efficiency-corrected  $D_s^+$  momentum spectrum from  $B$  decays. The scaled off-resonance data are subtracted directly from the on-resonance data. The entire momentum range (left) and below 2.5 GeV/c (right) are shown

the analysed statistic. The peak at  $\Delta M = 144.2 \pm 0.2 \text{ MeV}/c^2$  contains  $14392 \pm 376$  reconstructed  $D_s^{*+}$  mesons. Fig. 6.16 shows the signal peak after subtraction of the combinatorial background using the fit result. The average  $\Delta M$  resolution for  $D_s^{*+}$  candidate with the full momentum range is  $6.8 \pm 0.2 \text{ MeV}$ .

The  $D_s^{*+}$  momentum spectrum is extracted by fitting the  $\Delta M$  invariant mass distribution in 250 MeV/c wide momentum bins. The lower yield of  $D_s^{*+}$  mesons compared to  $D_s^+$  is the reason for this larger window. The  $\Delta M$  distribution for the  $D_s^+ \gamma$  signal is fitted with the Crystal Ball function Eq. 5.3. The threshold function in Eq. 5.4 is used to parameterize the background. The four parameters  $p_i$  are free in the fit. After verifying that the point that connect the Gaussian to the power-law tail does not depend on the  $D_s^{*+}$  momentum and agrees with the Monte Carlo, this parameter is fixed to  $0.89\sigma$  in the final fit. The off-resonance data are fitted with the Gaussian parameters ( $\bar{x}$  and  $\sigma$ ) obtained from the fit of the on-resonance data. The  $\Delta M$  distributions for on- and off- resonance data are shown in Figs. 6.17, 6.18, 6.19, 6.20.

Fig. 6.21 shows the  $D_s^{*+}$  peak value as a function of center-of-mass momentum. One can see that the  $D_s^{*+}$  peak value is shifted down at low momentum in data while this effect is not observed in the Monte Carlo simulation. Fig. 6.22 shows the  $\Delta M$  resolution as a function of the  $D_s^{*+}$  momentum in the  $\Upsilon(4S)$  rest frame both for data and for Monte Carlo. One can see that, the  $\Delta M$  resolution depends very mildly on the  $D_s^{*+}$  momentum and is slightly lower in Monte Carlo.

The efficiency of the  $D_s^{*+}$  selection is calculated from the Monte Carlo simulation

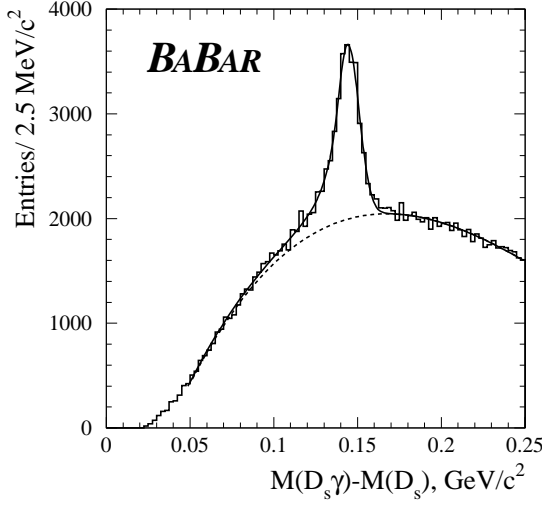


Figure 6.15: The  $\Delta M = M(D_s^+ \gamma) - M(D_s^+)$  mass spectrum for  $D_s^+$  reconstructed in  $\phi\pi^+$  mode. The fit function is described in the text.

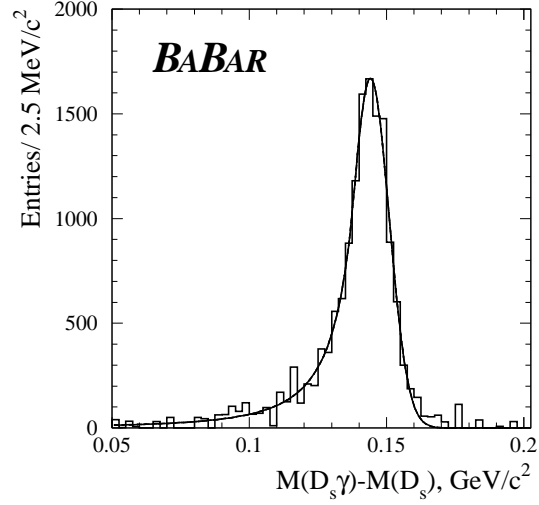


Figure 6.16: The  $D_s^{*+}$  signal after subtraction of background. The curve shows the fit using a Crystal Ball function.

using generated  $B\bar{B}$  and  $c\bar{c}$  events. It varies as a function of the  $D_s^{*+}$  momentum,  $p^*$ . The efficiency rises from 5% when the  $D_s^{*+}$  is at rest in the center-of-mass to 20% for  $p^* = 5 \text{ GeV}/c$  as shown in Fig. 6.25. In a similar way as for  $D_s^+$ , we verified the effect due to different reconstructed mass and resolution in data and Monte Carlo by comparing two methods. In the first method, the number of reconstructed  $D_s^{*+}$  mesons is counted for  $\Delta M < 0.165 \text{ GeV}/c^2$  requiring the reconstructed  $D_s^{*+}$  candidate to be the true  $D_s^{*+}$  meson. In the second method, the number of reconstructed  $D_s^{*+}$  are defined from the fit of  $\Delta M$  distribution as in data. One can see from the plot that both methods are in a good agreement within the statistical errors.

The number of reconstructed  $D_s^{*+}$  as a function of their momentum in the center-of-mass frame is shown in Fig. 6.23 for off-resonance and in Fig. 6.24 for on-resonance data. The efficiency corrected  $D_s^{*+}$  momentum spectrum is shown in Fig. 6.26.

Since the combinatorial background is rather high in the  $\Delta M$  distribution at low momentum region, it is more difficult to extract the number of reconstructed  $D_s^{*+}$  mesons at low  $p^*$ , in particular for the off-resonance data where statistic is limited. Therefore, the systematic error is increased for the first two points of the momentum spectrum. It is obtained by counting the number of events with different background parameterizations and fit ranges. Consequently, the maximum variation between the number of events is used as an additional systematic error. The  $D_s^{*+}$  momentum spectrum is obtained by subtracting bin-by-bin the off-resonance data from the on-resonance data after proper scaling of luminosity. The efficiency-corrected  $D_s^{*+}$  momentum spec-

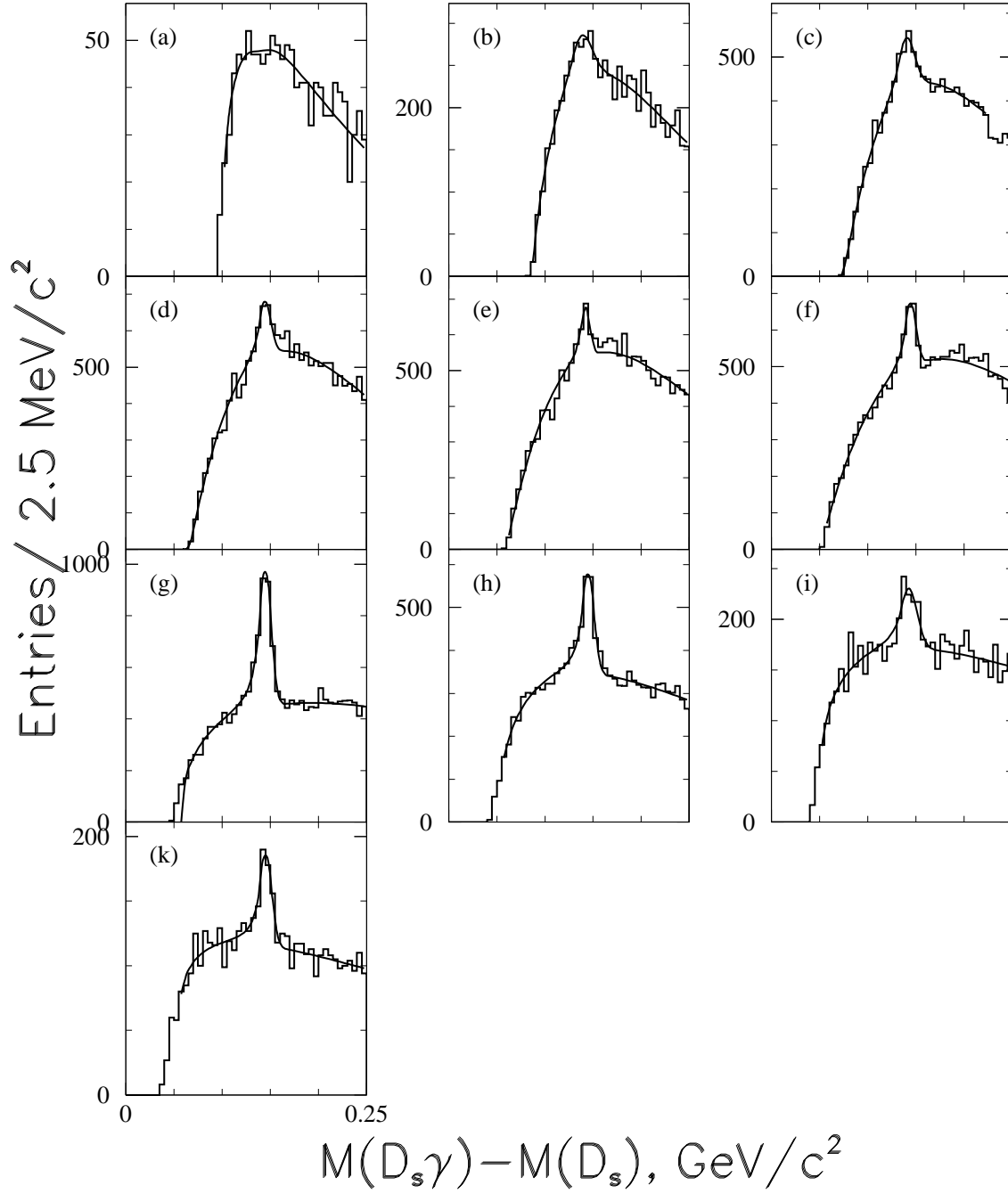


Figure 6.17: The  $\Delta M = M(D_s^{*+}\gamma) - M(D_s^+)$  distributions for the on-resonance data for 10 different momentum windows (a) 0-0.25, (b) 0.25-0.5, (c) 0.5-0.75, (d) 0.75-1.0, (e) 1.0-1.25, (f) 1.25-1.5, (g) 1.5-1.75, (i) 1.75-2.0, (h) 2.0-2.25, (k) 2.25-2.5 GeV/c. The result of the fit described in the text is overlaid.



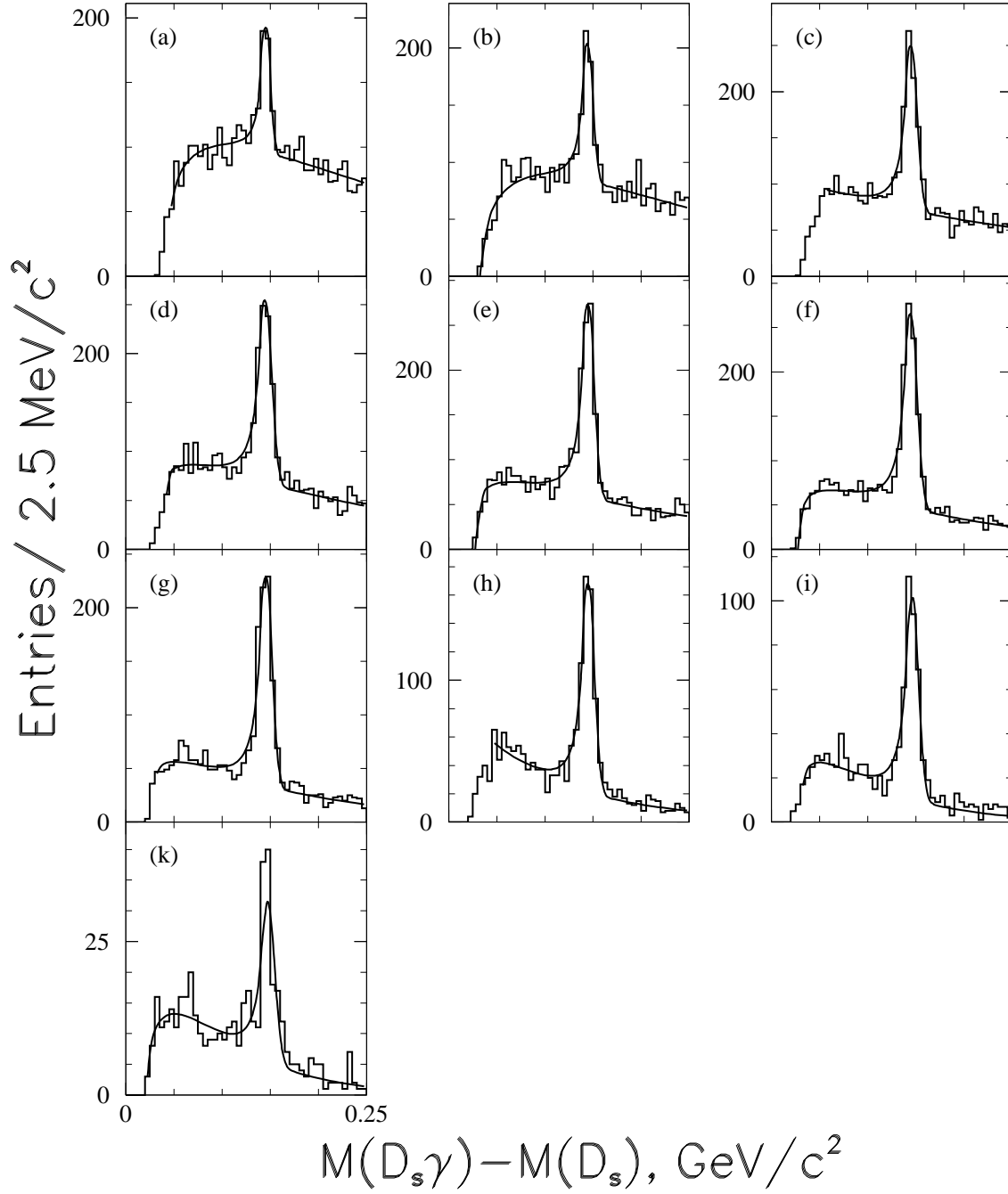


Figure 6.18: The  $\Delta M = M(D_s^{*+}\gamma) - M(D_s^+)$  distributions for the on-resonance data for 10 different momentum windows (a) 2.5-2.75, (b) 2.75-3.0, (c) 3.0-3.25, (d) 3.25-3.5, (e) 3.5-3.75, (f) 3.75-4.0, (g) 4.0-4.25, (i) 4.25-4.5, (h) 4.5-4.75, (k) 4.75-5.0 GeV/c. The result of the fit described in the text is overlaid.

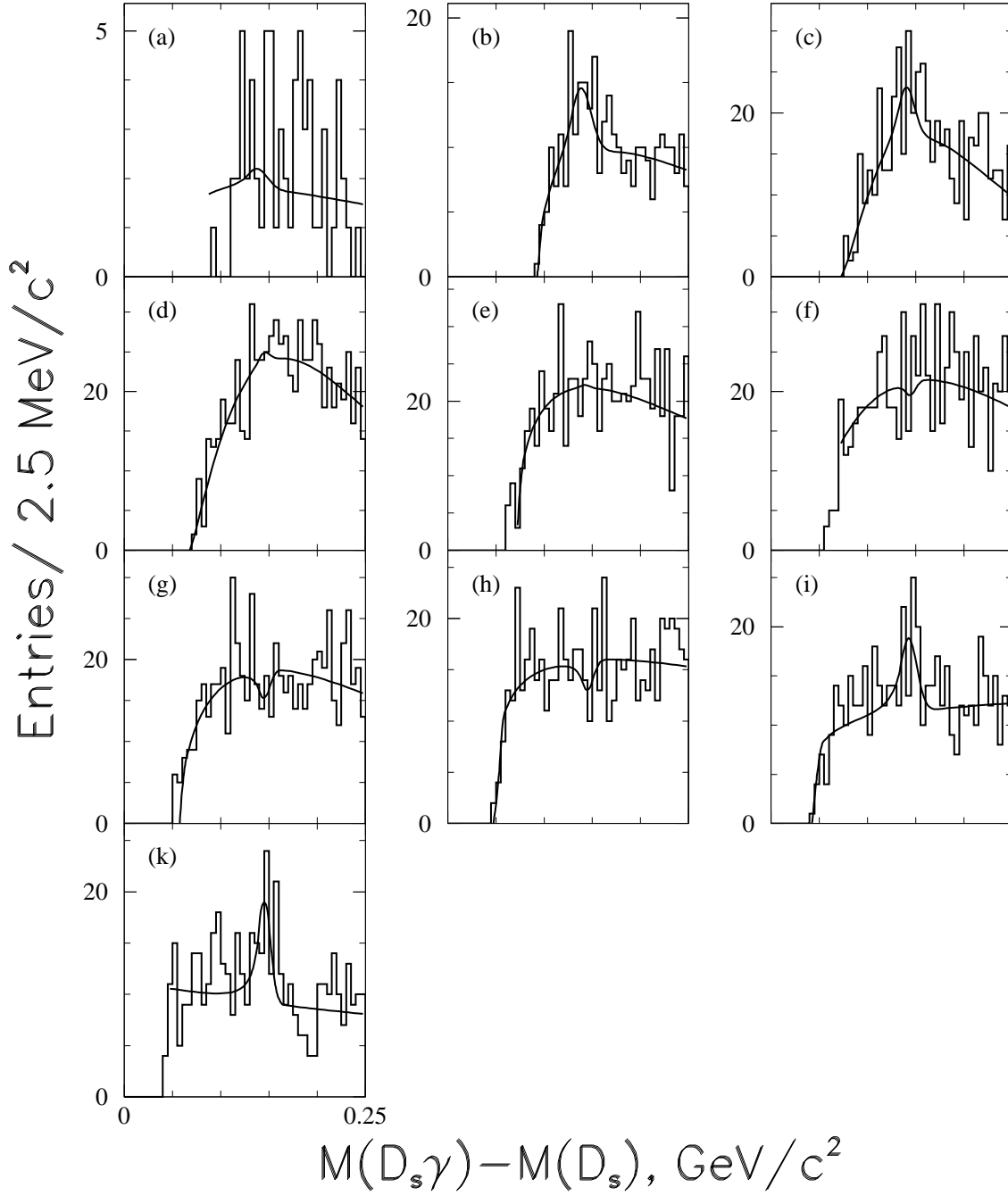


Figure 6.19: The  $\Delta M = M(D_s^{*+}\gamma) - M(D_s^+)$  distributions for the off-resonance data for 10 different momentum windows (a) 0-0.25, (b) 0.25-0.5, (c) 0.5-0.75, (d) 0.75-1.0, (e) 1.0-1.25, (f) 1.25-1.5, (g) 1.5-1.75, (i) 1.75-2.0, (h) 2.0-2.25, (k) 2.25-2.5  $\text{GeV}/c$ . The result of the fit described in the text is overlaid.

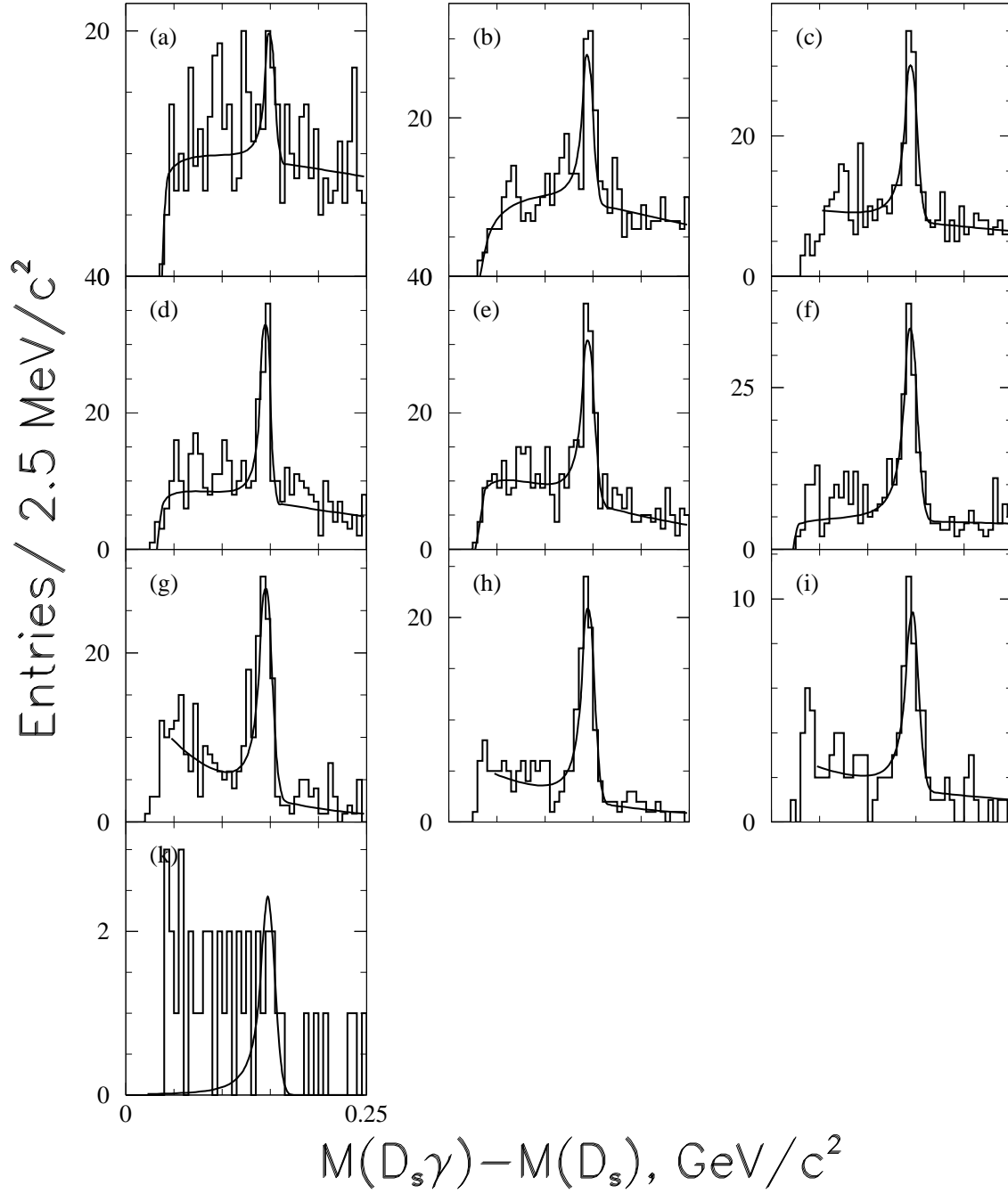


Figure 6.20: The  $\Delta M = M(D_s^{*+} \gamma) - M(D_s^+)$  distributions for the off-resonance data for 10 different momentum windows (a) 2.5-2.75, (b) 2.75-3.0, (c) 3.0-3.25, (d) 3.25-3.5, (e) 3.5-3.75, (f) 3.75-4.0, (g) 4.0-4.25, (i) 4.25-4.5, (h) 4.5-4.75, (k) 4.75-5.0 GeV/c. The result of the fit described in the text is overlaid.

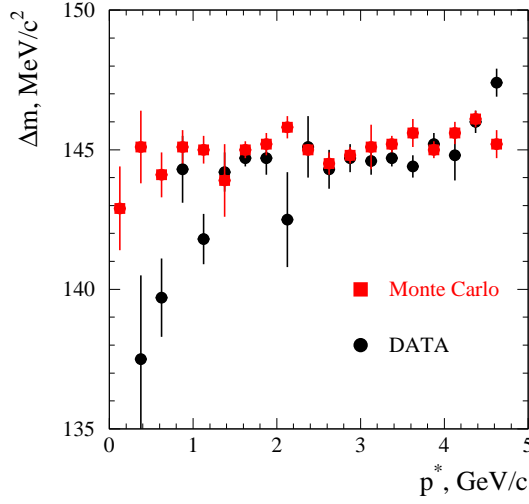


Figure 6.21: The fitted  $\Delta m = m(D_s^{*+}) - m(D_s^+)$  as a function of the  $D_s^{*+}$  momentum in the  $\Upsilon(4S)$  center-of-mass for data and Monte Carlo.

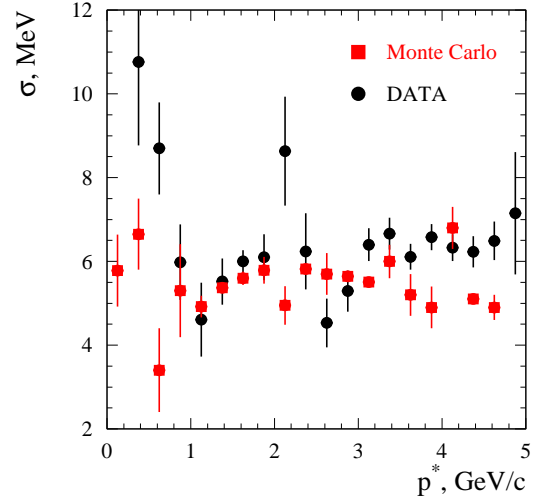


Figure 6.22: The  $\Delta M$  resolution as a function of the  $D_s^{*+}$  momentum in the  $\Upsilon(4S)$  center-of-mass for data and Monte Carlo.

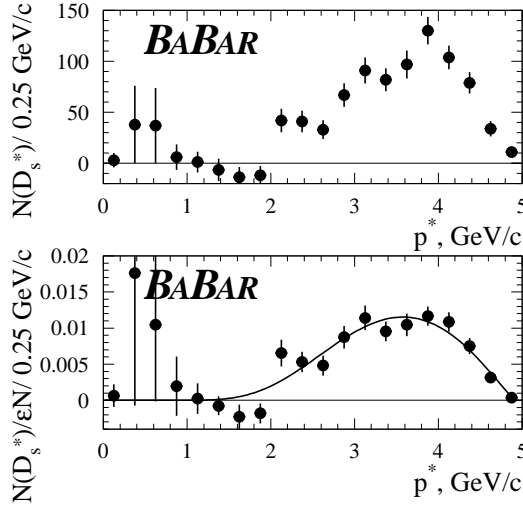


Figure 6.23: The  $D_s^{*+}$  momentum spectrum before (top) and after (bottom) efficiency correction for off-resonance data. The fit uses the Andersson function

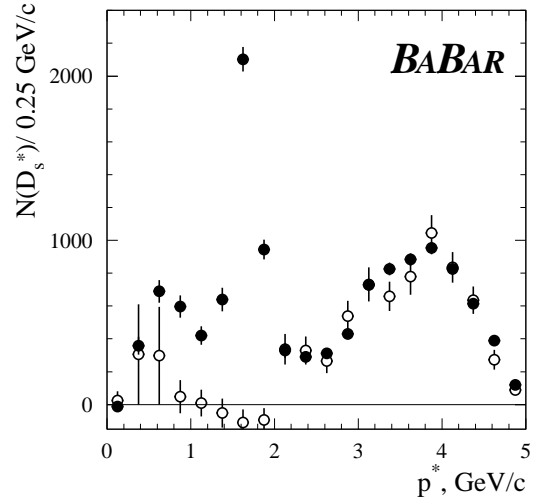


Figure 6.24: The  $D_s^{*+}$  yield from on-resonance (filled circles) and off-resonance data (open circles) scaled according to the corresponding luminosity ratio before efficiency correction.

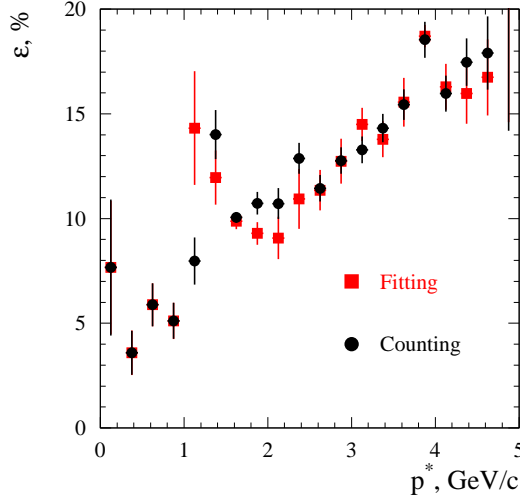


Figure 6.25: The efficiency for  $D_s^{*+} \rightarrow D_s^+ \gamma$  with  $D_s^+ \rightarrow \phi \pi^+$  and  $\phi \rightarrow K^+ K^-$  as a function of the  $D_s^{*+}$  momentum in the center-of-mass rest frame. Two methods described in the text are used to count the number of reconstructed  $D_s^{*+}$ .

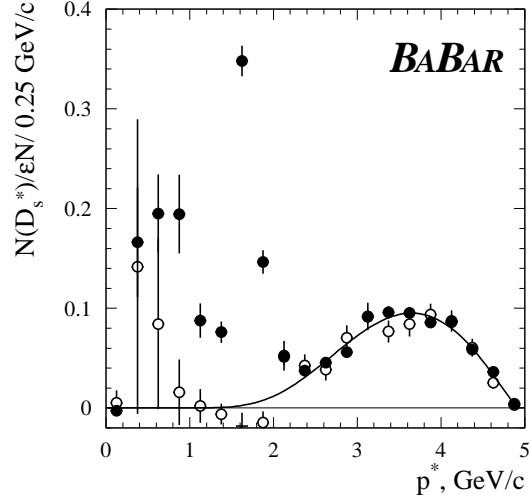


Figure 6.26: The  $D_s^{*+}$  efficiency-corrected momentum spectrum for on-resonance (filled circles) and scaled off-resonance data (open circles). The curve shows the fit using the Andersson function.

trum is shown in Figs. 6.27. It is important to note that the method described for  $D_s^+$  momentum spectrum measurement with the use of the fragmentation function for continuum parameterization, leads to the overestimation of the  $D_s^{*+}$  yield from  $B$  decays. The reason is that the combinatorial background for the  $\Delta M$  distribution peaks at low  $\Delta M$  the low momentum bins ( $< 1$  GeV/c) (see Fig. 6.17). However, this effect partially cancels out by subtracting the off-resonance data while it does not when one uses the parameterization function.

### 6.3 $B \rightarrow D_s^{(*)+} X$ Branching Fraction

Integrating the spectrum after continuum subtraction and efficiency correction gives a total  $D_s^+$  yield from  $B$  meson decays of  $87711 \pm 1485$  events. This corresponds to an inclusive branching fraction of

$$\mathcal{B}(B \rightarrow D_s^+ X) = \left[ (10.93 \pm 0.19 \pm 0.58) \times \frac{(3.6 \pm 0.9)\%}{\mathcal{B}(D_s^+ \rightarrow \phi \pi^+)} \right] \%. \quad (6.2)$$

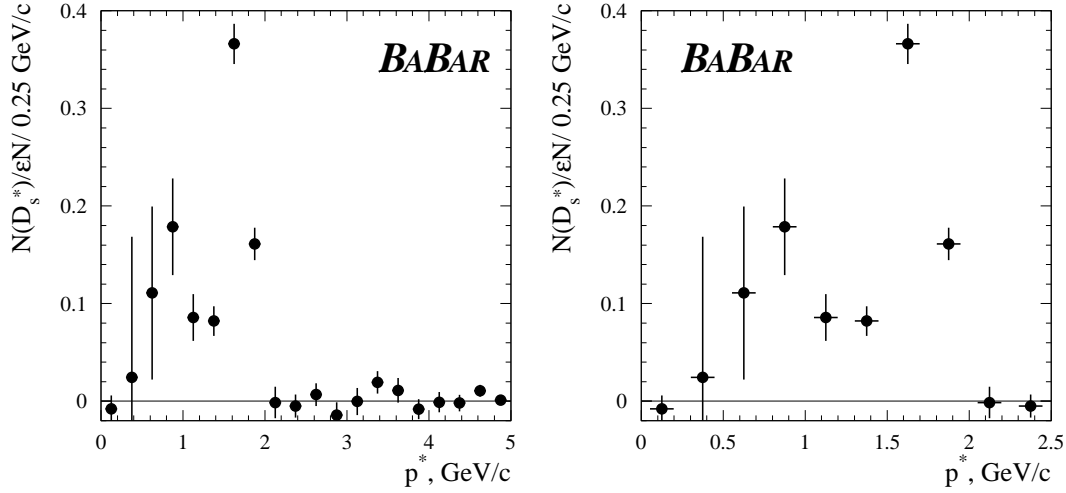


Figure 6.27: The efficiency-corrected  $D_s^{*+}$  momentum spectrum from  $B$  decays. The scaled off-resonance data are subtracted directly from the on-resonance data. All momentum range (left) and below 2.5 GeV/c (right) are shown

The total  $D_s^{*+}$  yield from  $B$  meson decays is  $60047 \pm 6201$  events, leading to the inclusive branching fraction of

$$\mathcal{B}(B \rightarrow D_s^{*+} X) = \left[ (7.94 \pm 0.82 \pm 0.72) \times \frac{(3.6 \pm 0.9)\%}{\mathcal{B}(D_s^+ \rightarrow \phi\pi^+)} \right] \%. \quad (6.3)$$

In the equations above, the first error is statistical, the second is systematic. The dominant error is due to the uncertainty in the  $D_s^+ \rightarrow \phi\pi^+$  branching fraction of  $(3.6 \pm 0.9)\%$  [8] and is shown separately. This allows us to measure the vector to pseudoscalar ratio (Eq. 4.21)

$$\frac{\mathcal{B}(B \rightarrow D_s^{*+} X_q)}{\mathcal{B}(B \rightarrow D_s^+ X_q)} = 0.73 \pm 0.08 \pm 0.06 \quad (6.4)$$

which is in a good agreement with the theoretical prediction 0.68 given in [35]. It is important to note that, with the used method, these results are independent of any assumption regarding the shape of the fragmentation function.

The various contributions to the systematic error are listed in Table 6.1. The following sources are considered for the  $D_s^{(*)+}$  yield:

- Signal shape

The systematic effect due to deviation of the signal peak shape from a single Gaussian (Crystal Barrel asymmetric lineshape) may bias the  $D_s^+$  ( $D_s^{*+}$ ) yield.

Source	Fractional Error on $\mathcal{B}$ (%)	
	$B \rightarrow D_s^+ X$	$B \rightarrow D_s^{*+} X$
Signal shape	0.5	3.0
Background subtraction	0.4	4.2
Monte Carlo statistics	2.5	4.2
Bin width	1.4	2.0
Total for $D_s^+$ yield	2.9	7.0
Number of $B\bar{B}$ events	1.6	1.6
$\mathcal{B}(\phi \rightarrow K^+ K^-)$	1.6	1.6
Particle identification	1.0	1.0
Tracking efficiency	3.6	3.6
$\mathcal{B}(D_s^{*+} \rightarrow D_s^+ \gamma)$		2.7
Photon efficiency		1.3
$\pi^0$ veto		2.7
Total systematic error	5.3	9.0

Table 6.1: Systematic errors for  $\mathcal{B}(B \rightarrow D_s^{(*)+} X)$ 

- Background shape

The ambiguity with the parameterization of the  $\phi\pi^+$  and  $\Delta M$  combinatorial background.

- Monte Carlo statistic

This effect is due to the statistical error in the determination of the  $D_s^{*+}$  efficiency from Monte Carlo simulation.

- Bin width

An uncontrolled variation of the efficiency within one momentum range, i.e. 200 MeV/c for  $D_s^+$  and 250 MeV/c for  $D_s^{*+}$ , biases the  $D_s^{(*)+}$  yield. Defined for each bin these errors are weighted according to the momentum spectrum in order to evaluate the mean value.

A detailed study of the systematic error is presented in Section 6.5

As a cross check, the  $D_s^+$  branching fraction is computed using the momentum spectrum (Fig. 6.13) obtained by subtraction of the value of the fitted curve where the Andersson function is applied. One obtains an inclusive branching fraction of  $\mathcal{B}(B \rightarrow D_s^+ X) = 11.37 \pm 0.14(stat) \pm 0.61(syst)\%$ . Additional systematic error of 1.1% is assumed for this value due to the parameterization function. Considering that the most of systematic errors shown in Table 6.1 are correlated, these values are consistent at the level of  $1.7\sigma$ .

## 6.4 $D_s^{(*)+}$ production from $q\bar{q}$ continuum

### 6.4.1 Cross Sections

The production cross section for  $D_s^{(*)+}$  from continuum events is obtained by integrating the spectrum (counting the number of events) obtained from the off-resonance data. This gives

$$\sigma(e^+e^- \rightarrow D_s^\pm X) \mathcal{B}(D_s^+ \rightarrow \phi\pi^+) = 7.55 \pm 0.20 \pm 0.34 \text{ pb} \quad (6.5)$$

and

$$\sigma(e^+e^- \rightarrow D_s^{*\pm} X) \mathcal{B}(D_s^+ \rightarrow \phi\pi^+) = 5.79 \pm 0.66 \pm 0.50 \text{ pb} \quad (6.6)$$

Table 6.2 summarizes the different sources of the systematic errors for  $\sigma(e^+e^- \rightarrow D_s^{(*)\pm} X) \mathcal{B}(D_s^+ \rightarrow \phi\pi^+)$ . It is important to say, that the contribution of the low momentum range ( $p^* < 2 \text{ GeV}/c$ ) to the statistical error is dominant. Since only off-resonance data present in this region, the use of the continuum spectrum constructed with both on- and off-resonance data sets does not improve the statistical significance of the result.

The vector to pseudoscalar production ratio is usually described using the variable

$$P_V = \frac{V}{V + P} \quad (6.7)$$

where  $P$  and  $V$  represent the number of pseudoscalar and vector mesons directly produced in  $e^+e^-$  annihilation. This quantity can be measured very precisely because many systematic errors cancel out. From the measured cross sections one finds

$$P_V = 0.77 \pm 0.09(stat) \pm 0.05(syst). \quad (6.8)$$

### 6.4.2 Fragmentation Functions

Measurement of fragmentation functions of heavy quarks that describe the process of hadronization, provides information about non-perturbative particle production



Source	Fractional Error on $\mathcal{B}$ (%)	
	$e^+e^- \rightarrow D_s^\pm X$	$e^+e^- \rightarrow D_s^{*\pm} X$
Signal shape	0.5	3.0
Monte Carlo statistic	1.0	4.8
Luminosity	1.5	1.5
Particle identification	1.0	1.0
Tracking efficiency	3.6	3.6
$\mathcal{B}(\phi \rightarrow K^+ K^-)$	1.6	1.6
$\mathcal{B}(D_s^{*+} \rightarrow D_s^+ \gamma)$		2.7
Photon efficiency		1.3
$\pi^0$ veto		2.7
Total systematic error	4.5	8.2

Table 6.2: Systematic errors for  $\sigma(e^+e^- \rightarrow D_s^{(*)\pm} X) \mathcal{B}(D_s^+ \rightarrow \phi \pi^+)$ .

in a variety of experimental environments. The study of the fragmentation functions and the production cross section from continuum events for charm mesons ( $D^{*+}$ ,  $D^{*0}$ ,  $D^0$ ,  $D_s^+$ ,  $\Lambda_c$ ) were reported by *CLEO* in [45, 46].

Many functional forms have been suggested for the momentum spectra of the heavy quarks produced in  $e^+e^-$  annihilation. Most of them are a function of one variable  $z$ , defined for a heavy quark  $Q$ , light-quark  $\bar{q}$  system as the ratio of the energy plus longitudinal momentum of the hadron  $Q\bar{q}$  to the sum of the energy and momentum of the heavy quark after accounting for initial state radiation, gluon bremsstrahlung, and final state radiation:

$$z = \frac{(E + p_{\parallel})_{Q\bar{q}}}{E + p_Q}, \quad (6.9)$$

where  $p_{\parallel}$  is the component of  $p$  along the direction of the heavy quark. The main advantage of this quantity is that it is relativistically invariant with respect to the boost in the direction of the primary quark. Unfortunately, as this variable is not directly measured, experiments typically use other scaling variables, which are close approximations to  $z$ . They are

$$x^+ = \frac{(E + p_{\parallel})_{hadron}}{(E + p)_{max}}, \quad x_p = p/p_{max}, \quad x_E = E_{hadron}/E_{beam}, \quad (6.10)$$

where the maximum momentum of the hadron is defined as

$$p_{max} = \sqrt{E_{beam}^2 - m^2} \quad (6.11)$$

The  $x_p$  parameter is used as an approximation of  $z$  in this work.

Name of function	Analytical expression
Andersson (Lund) [47]:	$f(x_p) = N \frac{(1-x_p)^\beta}{x_p} \exp\{-\frac{\alpha}{x_p}\}$
Peterson <i>et al.</i> [48]:	$f(x_p) = \frac{N}{x_p} \left(1 - \frac{1}{x_p} - \frac{\epsilon}{1-x_p}\right)^{-2}$
Collins and Spiller [49]:	$f(x_p) = N \left(\frac{1-x_p}{x_p} + \frac{2-x_p}{1-x_p}\epsilon\right) (1+x_p^2) \left(1 - \frac{1}{x_p} - \frac{\epsilon}{1-x_p}\right)^{-2}$
Kartvelishvili <i>et al.</i> [50]:	$f(x_p) = N x_p^\alpha (1-x_p)$

Table 6.3: Analytical expressions for the fragmentation functions.

The measured  $D_s^{(*)+}$  momentum spectrum (i.e. efficiency-corrected) from continuum, which uses on-resonance data with momentum above 2.45 GeV/c ( $x_p > 0.5$ ) and off-resonance data scaled according to the luminosity ratio is fitted using 4 different fragmentation functions described in Table 6.3. The result of the fit for  $D_s^+$  mesons is shown in Figs. 6.28, 6.29. The production cross section is obtained by integrating the function of the fit. The extracted cross sections, the shape parameters and  $\chi^2$  of the fit are shown in Table 6.4.

Name of function	Shape parameter	$\sigma$ , pb	$\chi^2 / \text{ndof}$
Andersson(Lund)	$\alpha = 2.93 \pm 0.04,$ $\beta = 1.55 \pm 0.03$	$7.27 \pm 0.09 \pm 0.02$	30.2/33
Peterson <i>et al.</i>	$\epsilon = (11.14 \pm 0.32) \times 10^{-2}$	$8.23 \pm 0.10 \pm 0.22$	68.5/33
Collins and Spiller	$\epsilon = (29.4 \pm 1.3) \times 10^{-2}$	$8.58 \pm 0.11 \pm 0.23$	207.5/33
Kartvelishvili <i>et al.</i>	$\alpha = 2.23 \pm 0.05$	$8.35 \pm 0.31 \pm 0.14$	312.6/33

Table 6.4: The fit results and cross section  $\sigma(e^+e^- \rightarrow D_s^{*+} X) \mathcal{B}(D_s^+ \rightarrow \phi \pi^+)$ , Only the statistical errors (uncorrelated and correlated for the cross sections) are given.

Figs. 6.30, 6.31 show the result of the fit of  $D_s^{*+}$  continuum data with different fragmentation functions. The production cross section for  $D_s^{*+}$  from continuum events with shape parameters and  $\chi^2$  from the fit are shown in Table 6.5.

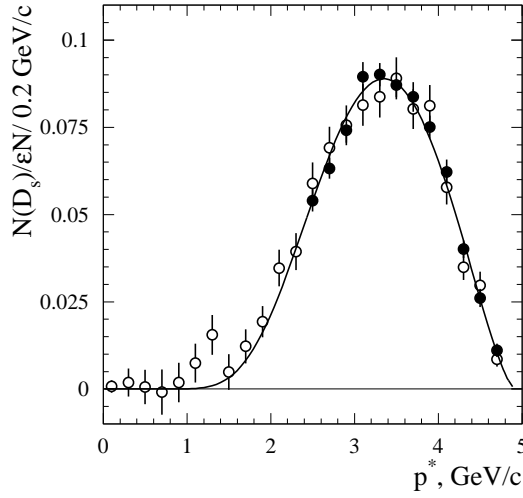


Figure 6.28: The fit with an Andersson function of  $D_s^+$  continuum spectrum.

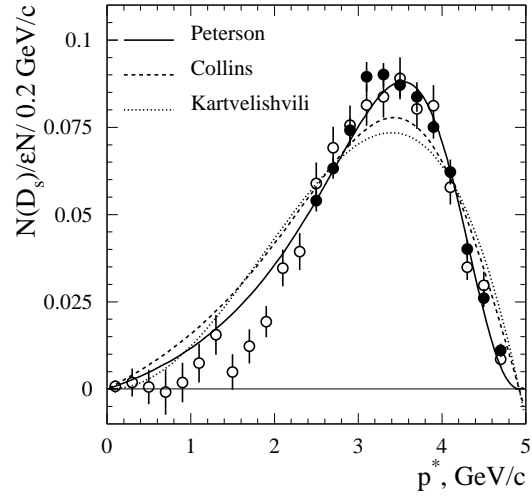


Figure 6.29: The fit with Peterson, Collins and Kartvelishvili functions of  $D_s^+$  continuum spectrum.

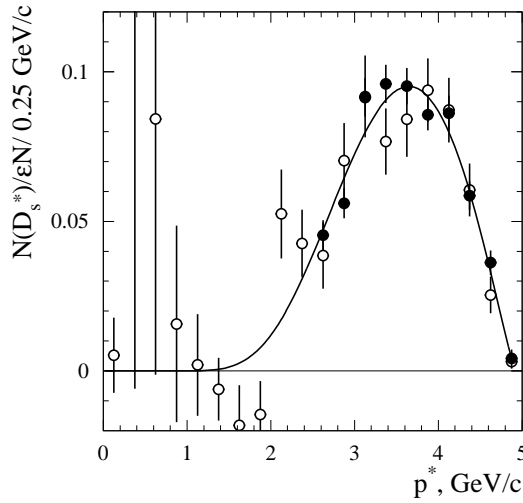


Figure 6.30: The fit with an Andersson function of  $D_s^{*+}$  continuum spectrum.

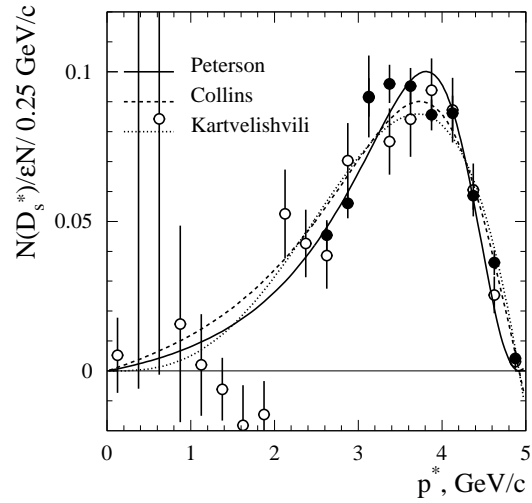


Figure 6.31: The fit with Peterson, Collins and Kartvelishvili functions of  $D_s^{*+}$  continuum spectrum.

As one can see from the fit results, the best parameterization of the hadronization process is the Andersson (Lund) function [47] since the  $\chi^2$  of the fit is the best. Using

Name of function	Parameter	$\sigma$ , pb	$\chi^2/\text{ndof}$
Andersson(Lund)	$\alpha = 3.31 \pm 0.09$ , $\beta = 1.21 \pm 0.05$	$5.49 \pm 0.12 \pm 0.03$	25.2/25
Peterson <i>et al.</i>	$\epsilon = (6.61 \pm 0.36) \times 10^{-2}$	$6.04 \pm 0.13 \pm 0.27$	46.0/25
Collins and Spiller	$\epsilon = (14.6 \pm 1.3) \times 10^{-2}$	$6.50 \pm 0.14 \pm 0.29$	33.4/25
Kartvelishvili <i>et al.</i>	$\alpha = 3.05 \pm 0.12$	$6.18 \pm 0.13 \pm 0.22$	48.3/25

Table 6.5: The fit results and cross section  $\sigma(e^+e^- \rightarrow D_s^{*+} X) \mathcal{B}(D_s^+ \rightarrow \phi \pi^+)$ , Only the statistical errors (uncorrelated and correlated for the cross sections) are given.

this approximation one finds

$$P_V = 0.75 \pm 0.02(stat) \pm 0.05(syst). \quad (6.12)$$

This value is consistent with Eq. 6.8 and the error is dominated by the systematic error. Therefore we conclude that the spin counting model applies to the  $D_s^{*+}$  system similarly as for the  $D^{*+}$  [51]. Indeed, counting the number of spin states available to an L=0 meson leads to the expected value of  $P_V = 0.75$ .

## 6.5 The Systematic Errors

### 6.5.1 Tracking Efficiency

The detection efficiency of the charged tracks can be extracted from the data. The fortunate case of having two devices (the SVT and DCH) allows one to reconstruct tracks independently measuring the efficiency of each device by using the presence of a charged track in the other as a trigger. Since the GTL list, which requires at least 12 hits in the DCH, is used in the present analysis, only the DCH efficiency is important.

The method is to start with an SVT track and measure how often a corresponding drift chamber track is found. The results of the analysis are tables of the efficiencies binned in the  $p_T$ ,  $\theta$ ,  $\phi$  and multiplicity bins [52]. The extraction of these tables is done separately for the runs with low (1900 V) and high (1960 V) voltages on the DCH wires. The efficiency correction procedure of the Monte Carlo events implies that the efficiency of each track has to be weighted according to its performances.

	1900 V	1960 V
Not corrected (NC)	$0.960 \pm 0.005$	$0.985 \pm 0.004$
Corrected (C)	$0.985 \pm 0.005$	$0.995 \pm 0.004$
NC/C	$0.975 \pm 0.007$	$0.990 \pm 0.006$

Table 6.6: The ratio  $\epsilon_{Data}/\epsilon_{MC}$  for the single track integrating on entire momentum. Uncertainty is statistical only.

In addition the ratio of the GTL efficiency to that of GTVL,  $R_\epsilon = \epsilon_{GTL}/\epsilon_{GTVL}$  can be measured using  $D^0 \rightarrow K^-\pi^+\pi^-\pi^+$  ( $K3\pi$ ) decay. The ratio  $R_\epsilon$  is given by the number of reconstructed events for which all four tracks satisfy the GTL criteria over the number of events for which three tracks satisfy the GTL criteria and the fourth track is required to satisfy the GTVL criteria. In order to improve the signal to background ratio only  $D^0$  candidates originating from  $D^{*+} \rightarrow D^0\pi$  are selected. Since the efficiency of tracks satisfying the GTVL criteria in Monte Carlo is consistent with data, the ratio of the data efficiency over that for Monte Carlo can be produced for GTL. Table 6.6 presents this ratio before and after efficiency correction using the tables. A small difference of about 1% between data and Monte Carlo still remains after correction that is added to the systematic error. This effect is explained by the signal shape uncertainty and the background subtraction in the  $K3\pi$  mass distribution. Taking into account that this is a common effect for both corrected and not corrected distributions, their ratio (the last line in Table 6.6) gives the track correction factor used in the present analysis with an associated systematic error of 1.2% per track.

In order to ensure that extracted correction factor can be used for another decay modes and in particularly for  $D_s^{(*)+}$ , i.e. it does not reflect some special topology or multiplicity of the events involving  $D^0 \rightarrow K3\pi$  decays, the correction tables were used for the eight  $B \rightarrow D_s^{(*)}D^{(*)}$  decay channels using a full reconstruction method (Section 4.5.1). The result shows that the track weighted efficiency is consistent within 0.3% with the correction factor obtained with  $D^0 \rightarrow K3\pi$  events. This is significantly smaller than the systematic error associated with one track.

Thus, one can conclude that for the decay chain  $D_s^+ \rightarrow \phi\pi^+$ ,  $\phi \rightarrow K^+K^-$  with three tracks in the final state, the weighted luminosity correction is  $(0.982)^3 = 0.947$  with  $3 \times 1.2\% = 3.6\%$  systematic error per  $D_s^+$  candidate.

### 6.5.2 Neutral Efficiency

The study of the simulation validation of the EMC in terms of reconstruction efficiency of neutral particles ( $\gamma$ ,  $\pi^0$ ) uses the  $e^+e^- \rightarrow \tau^+\tau^-$  decay channel. One of the  $\tau$  leptons

is tagged into  $\tau^- \rightarrow e^- \bar{\nu}_e \nu_\tau$  mode while the second  $\tau$  decays to neutrino plus hadron (mostly  $\pi^\pm$ ) and one or two  $\pi^0$ :  $\tau^- \rightarrow \pi^- (2) \pi^0 \nu_\tau$ . The yields for the  $1\pi^0$  and  $2\pi^0$  are compared. In this case the systematic errors due to tracking efficiency and luminosity cancel in the ratio of the yields. Since the branching fractions are known at the level of 1%, the decay kinematic and the  $\pi^0$  efficiency govern the relative yield. Thus, the  $\pi^0$  efficiency can be measured directly in the data and compared with the Monte Carlo simulation.

The analysis is performed based on a binned  $\pi^0$  energy between 0 and 3.5 GeV [53]. The result shows that additional suppression of 2.5% of all photons in the event is needed in the Monte Carlo. Applying this recipe to the simulation, it was found that the  $\pi^0$  efficiency in data is consistent with the Monte Carlo at the level of 0.5%. An estimated systematic error, mostly defined by the branching fraction knowledge and the uncertainty of the energy calibration, is 1.3% per photon and 2.5% per  $\pi^0$ .

### 6.5.3 Particle Identification

The  $D_s^+$  candidates are required to have two oppositely charged tracks satisfying the “loose” kaon criterium, with at least one of them passing the “tight” criterium. A possible difference of the particle identification efficiency between data and Monte Carlo is a source of systematic error. A study is performed using the  $D^0 \rightarrow (K^- \pi^+)$  channel with  $D^0$  mesons coming from  $D^{*+} \rightarrow D^0 \pi^+ \rightarrow (K^- \pi^+) \pi^+$  decay. The comparison of the  $D^0$  yield with and without positive kaon identification using different criteria allows us to extract the efficiency of the particle identification for a single track.

Fig. 6.32 shows the kaon efficiency as a function of its momentum in the laboratory frame for the two selection criteria: “loose” and “tight”. Integrating over the entire momentum range one gets  $\epsilon_L=0.99$  and  $\epsilon_T=0.93$  for Monte Carlo while  $\epsilon_L=0.98$  and  $\epsilon_T=0.91$  for data.

A total efficiency with one “loose” and one “tight” kaon in the final state can be expressed as

$$\epsilon_{L+T} = 2\epsilon_T\epsilon_L - \epsilon_T^2. \quad (6.13)$$

The ratio

$$r \equiv \frac{\epsilon_{2T}}{\epsilon_{L+T}} = \frac{\epsilon_T}{2\epsilon_L - \epsilon_T} \quad (6.14)$$

is extracted from the  $D_s^+$  yield when the positive identification of one “loose” and one “tight” kaon is compared with that when both kaons satisfy a “tight” criterion. Thus the  $\epsilon_T/\epsilon_L = 2r/(1+r)$  can be measured from both  $D_s^+$  and  $D^0$  decays. The comparison of  $\epsilon_T/\epsilon_L$  with two decay modes ensures the result against possible systematic effects due to different number of kaons in the final state. Table 6.7 shows the comparison of these ratios obtained with data and Monte Carlo.

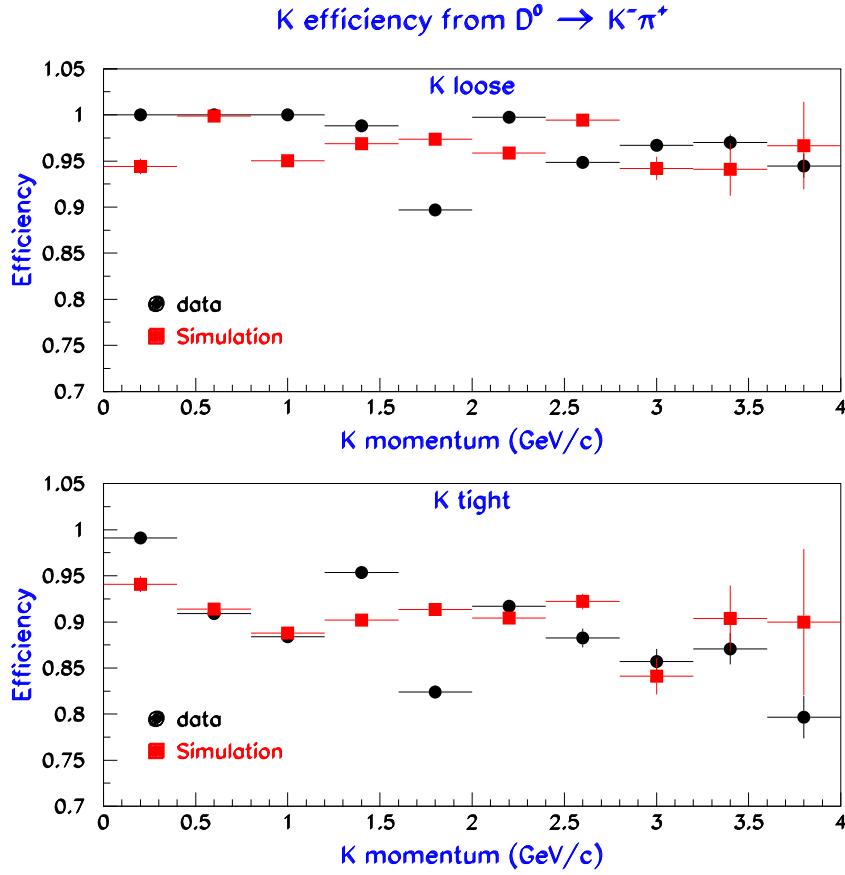


Figure 6.32: Kaon efficiency as a function of momentum for data and Monte Carlo with two identification criteria: “loose” (upper plot) and “tight” kaon (bottom plot).

One can extract from this table  $\epsilon_{L+T}^{Data}/\epsilon_{L+T}^{MC} = 0.979 \pm 0.019$  and an estimated systematic error is about 1%. This is obtained by comparing the signal yield fitting the  $\Delta M$  and  $K^- \pi^+$  mass distributions when no positive kaon identification is required to that where it is required.

#### 6.5.4 $\pi^0$ Overlap

In order to improve the signal to background ratio for  $D_s^{*+}$  candidates, the photon candidate from  $D_s^{*+} \rightarrow D_s^+ \gamma$  decay should not form a  $\pi^0$ , when combined with any other photon in the event. Due to possible difference in the reconstruction efficiency of photons and consequently  $\pi^0$  mesons between data and Monte Carlo, an additional systematic error to the  $D_s^{*+}$  yield has to be taken into account.

	Data	MC
From $D_s^+$		
$r$	$0.839 \pm 0.020$	$0.85 \pm 0.014$
$\epsilon_T/\epsilon_L$	$0.913 \pm 0.012$	$0.924 \pm 0.008$
From $D^*$		
$\epsilon_T/\epsilon_L$	$0.929 \pm 0.004$	$0.939 \pm 0.004$
$\epsilon_{L+T}$	$0.956 \pm 0.013$	$0.977 \pm 0.013$

Table 6.7:  $r$ ,  $\epsilon_T/\epsilon_L$  and  $\epsilon_{L+T}$  for data and Monte Carlo obtained with  $D_s^+$  and  $D^*$  decays.

A possible candidate for a calibration mode in this study is  $D^{*0} \rightarrow D^0 \gamma$ , where the product of the production yield, reconstruction efficiency and signal to background ratio is better than for  $D_s^{*+} \rightarrow D_s^+ \gamma$ . Since the photon energy is relatively small (about 400 MeV maximum), the reconstruction efficiency is very sensitive to energy. Therefore, the best way to study the systematic error due to  $\pi^0$  veto is the  $D_s^{*+} \rightarrow D_s^+ \gamma$  mode itself. The ratio

$$R = \frac{N_{D_s^*}^{\text{veto}} \times \epsilon}{N_{D_s^*} \times \epsilon^{\text{veto}}} \quad (6.15)$$

is calculated for each  $D_s^{*+}$  momentum range using the number of reconstructed events and the efficiency obtained both with and without  $\pi^0$  overlap requirement. Fig 6.33 shows the  $\Delta M$  distribution for data with and without the  $\pi^0$  veto using the  $D_s^{*+}$  candidates in all momentum ranges. The significant improvement of the reconstruction efficiency ( $22027 \pm 615$  events in the peak compared to  $14392 \pm 376$ ) is accompanied by a worser signal to background ratio. The extracted value of  $R$  as a function of the  $D_s^{*+}$  momentum is shown in Fig. 6.34. A straight line fit gives

$$R = 0.956 \pm 0.0257. \quad (6.16)$$

This is used as the correction factor for the  $D_s^{*+}$  yield with an associated systematic error of 2.7%.

### 6.5.5 Signal Shape

Deviation of the  $D_s^+$  ( $D_s^{*+}$ ) signal peak from a single Gaussian (Crystal Barrel line-shape) leads to the systematic uncertainty for the  $D_s^+$  ( $D_s^{*+}$ ) yield. The integral of the fit function used for the signal parameterization gives the number of reconstructed



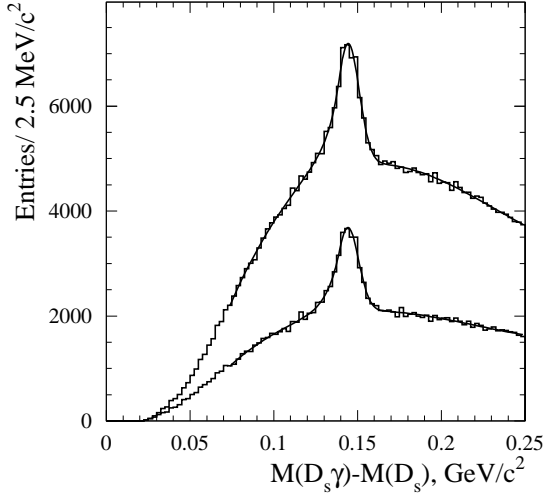


Figure 6.33:  $\Delta M = M_{D_s\gamma} - M_{D_s}$  mass spectra. Upper histogram corresponds to no veto with  $\pi^0$  to be required, while the lower histogram shows the  $\Delta M$  spectrum with  $\pi^0$  veto requirements for the photon candidate.

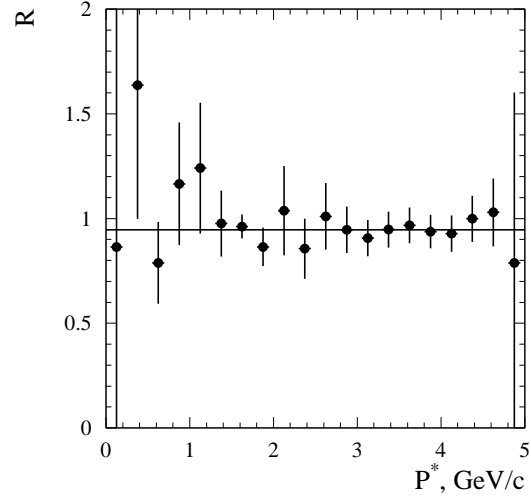


Figure 6.34:  $R$  as a function of  $D_s^{*+}$  center-of-mass momentum. Line shows the fit result described in the text.

events. This number is used as the  $D_s^+$  ( $D_s^{*+}$ ) yield in the present analysis. It can also be found by counting the number of events in the histogram obtained after subtracting bin-by-bin the value of the fitted background function from the  $\phi\pi^+$  ( $\Delta M$ ) mass distribution. No assumption for the extrapolation of the signal peak is assumed with this method. A variation of the signal yield with the procedure mentioned above is accounted as systematic error due to the signal shape.

### 6.5.6 Background Subtraction

The components of the background for the on-resonance data are different from off-resonance. Both  $B\bar{B}$  and  $q\bar{q}$  continuum are sources for the on-resonance data while only the last source is present in the off-resonance data. In general, the parameterization, which describes the background well at relatively high momentum, might not fit the low momentum ranges. Therefore, an uncertainty due to the chosen parameterization of the combinatorial background leads to a systematic error.

In contrast to the  $\phi\pi^+$  distribution where the signal to background ratio is slightly increased with diminishing the  $D_s^+$  candidate momentum, the combinatorial background for the  $\Delta M$  distribution is strongly increasing near the  $D_s^{*+}$  mass at low

momentum ( $< 1 \text{ GeV}/c$ ). Therefore, the uncertainty due to background subtraction is one of the dominant systematic error for the  $D_s^{*+}$  branching fraction in contrast to the  $D_s^+$  (Table 6.1).

The other independent method for extracting the  $D_s^{(*)+}$  yield coming from  $B$  decays is the following. The  $\phi\pi^+$  ( $\Delta M$ ) histograms obtained from the off-resonance data are subtracted bin-by-bin from the corresponding on-resonance histogram after the proper luminosity scaling. Fig. 6.35 shows the resulting distributions for the  $\phi\pi^+$  invariant mass, while the fitted  $\Delta M$  spectra are shown in Fig. 6.36. Part of combinatorial background coming from  $q\bar{q}$  continuum cancels in these distributions. The efficiency-corrected  $D_s^{(*)+}$  momentum spectrum is shown in Figs 6.37 and 6.38. Integrating these spectra gives the inclusive branching fraction of  $\mathcal{B}(B \rightarrow D_s^+ X) = 10.77 \pm 0.23\%$  and  $\mathcal{B}(B \rightarrow D_s^{*+} X) = 7.62 \pm 0.88\%$ . These results are in agreement with Eqs. 6.2, 6.3 within statistical error.

Using a third order polynomial parameterization for the combinatorial background, one obtains the inclusive branching fraction  $\mathcal{B}(B \rightarrow D_s^{*+} X) = 8.36 \pm 0.87 \pm 0.76\%$ , which is also consistent with Eq. 6.3. The corresponding  $D_s^{*+}$  momentum spectrum obtained with this parameterization is shown in Fig. 6.39. The variation of the branching fractions obtained with these methods is included in the systematic error due to background subtraction.

### 6.5.7 Momentum Smearing

As shown above, the reconstructed mass and resolution of the  $D_s^{(*)+}$  mesons in the data are somewhat different from the ones using Monte Carlo simulation. Since the method determining the efficiency is dependent on the mean value of the peak and its resolution, a second method to cross check the efficiency is used. It gives consistent results within the statistical errors. A special feature in Monte Carlo (track momentum smearing) allows us to reproduce better the data. Fig 6.40 shows the  $\phi\pi$  invariant mass distributions obtained with and without the smearing procedure. The generated  $B^0 \rightarrow D_s^{*+} D^{*-}$  decay modes are used for this purpose. The peak parameters of the fit are presented in Table 6.8. The  $D_s^+$  candidates are selected within  $1.6 < p^* < 1.8 \text{ GeV}/c$  center-of-mass momentum range.

One can see from this table that the smearing procedure shifts down the reconstructed  $D_s^+$  mass peak and worsens the resolution, reproducing better the reconstructed parameters in the data. The efficiencies obtained with and without the momentum smearing procedure are consistent within the statistical error about 2%.

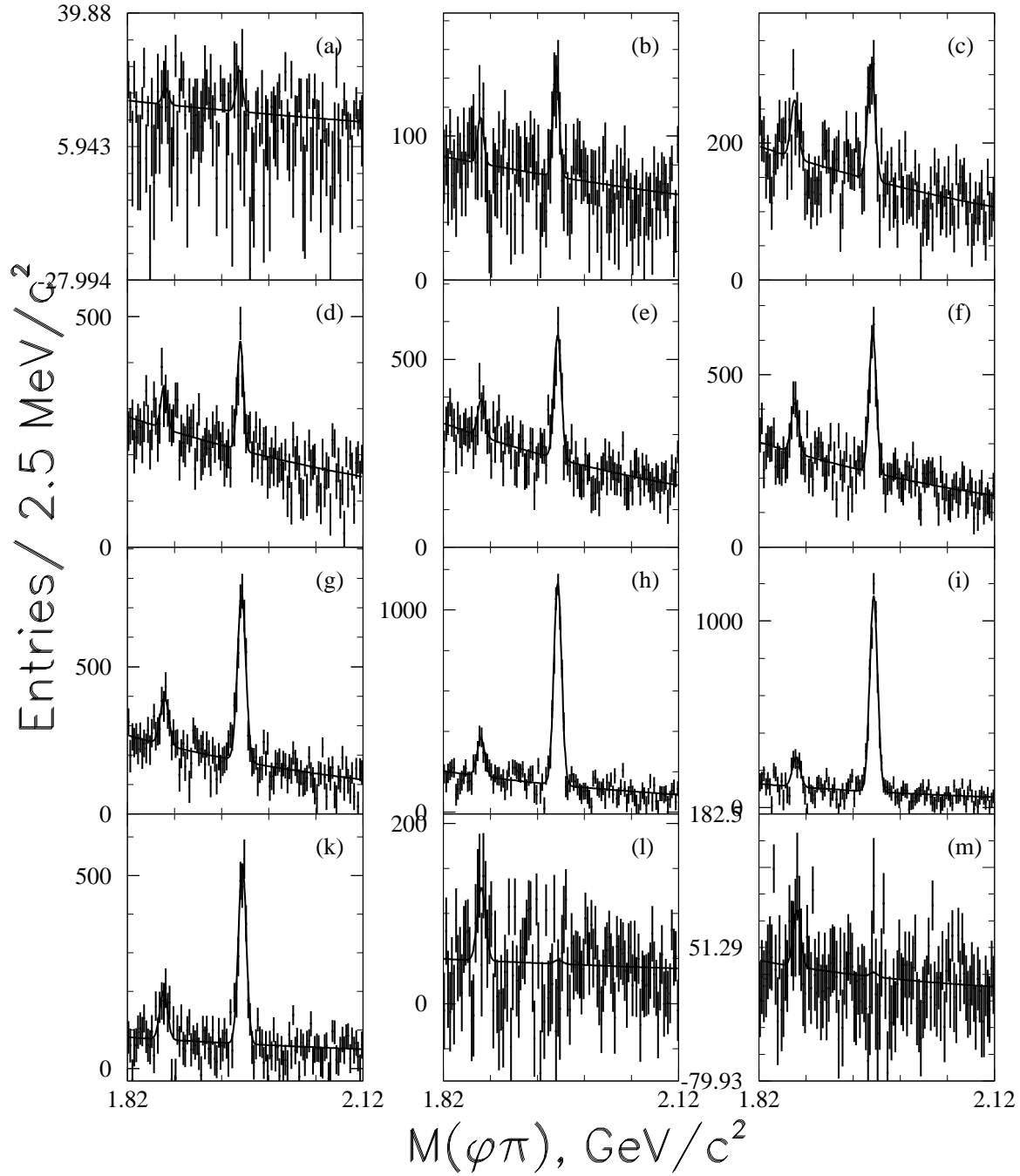


Figure 6.35: The  $\phi\pi^+$  mass distributions obtained by subtracting the off-resonance histogram after luminosity scaling to the corresponding on-resonance histogram. The  $D_s^+$  yield is defined in the 12 momentum windows (a) 0-0.2, (b) 0.2-0.4, (c) 0.4-0.6, (d) 0.6-0.8, (e) 0.8-1.0, (f) 1.0-1.2, (g) 1.2-1.4, (i) 1.4-1.6, (h) 1.6-1.8, (k) 1.8-2.0, (l) 2.0-2.2, (m) 2.2-2.4 GeV/c. The result of the fit described in the text is overlaid.

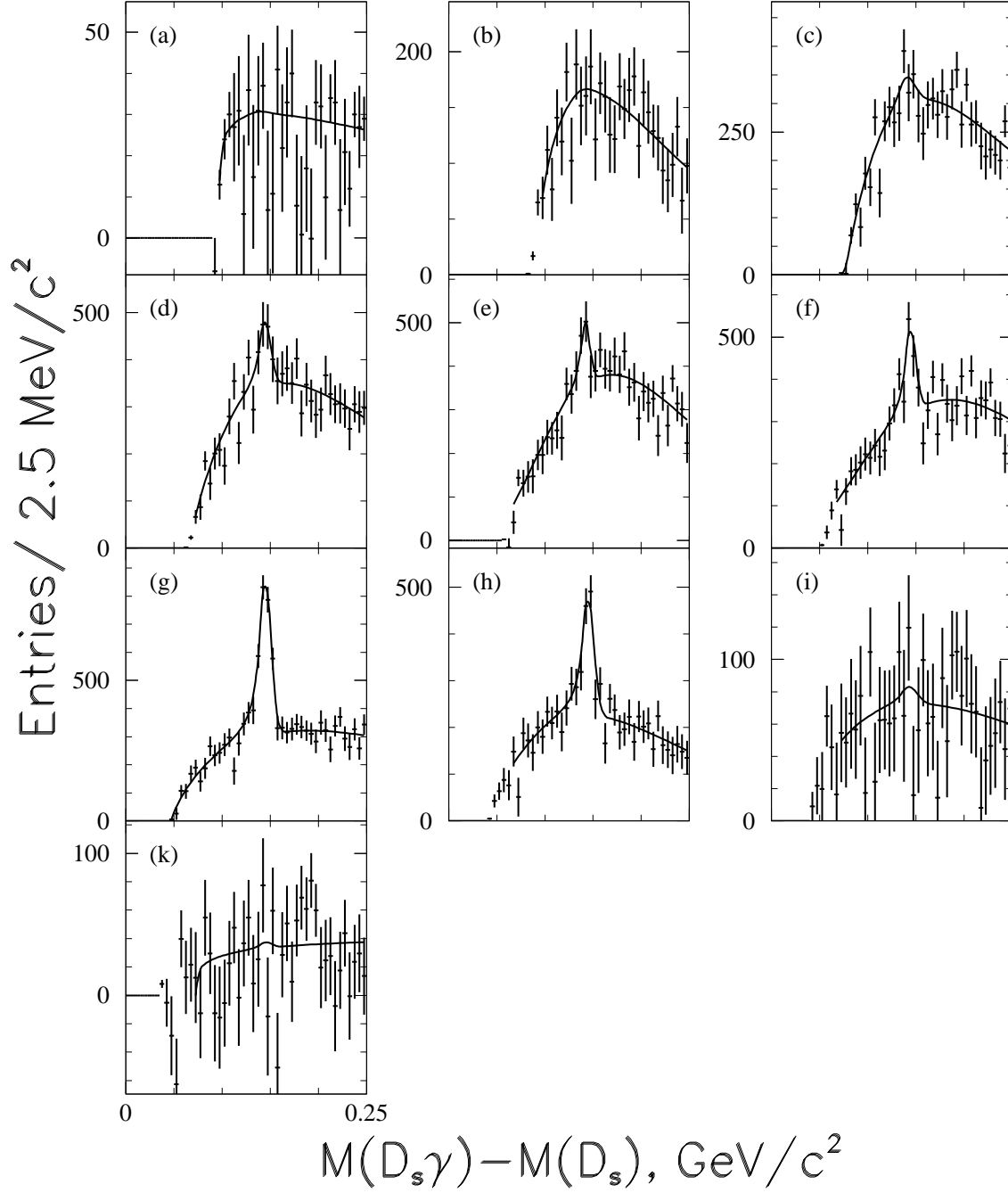


Figure 6.36: The  $\Delta M = M(D_s^{*+} \gamma) - M(D_s^+)$  distributions obtained by subtracting the off-resonance histogram after luminosity scaling to the corresponding on-resonance histogram. The  $D_s^{*+}$  yield is defined in the 10 momentum windows (a) 0-0.25, (b) 0.25-0.5, (c) 0.5-0.75, (d) 0.75-1.0, (e) 1.0-1.25, (f) 1.25-1.5, (g) 1.5-1.75, (i) 1.75-2.0, (h) 2.0-2.25, (k) 2.25-2.5  $\text{GeV}/c$ . The result of the fit described in the text is overlaid.

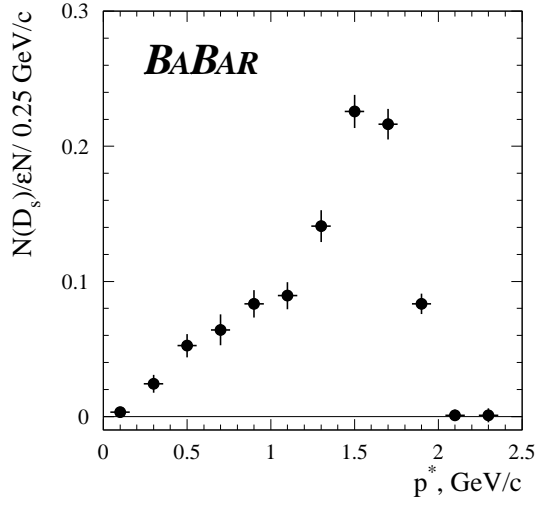


Figure 6.37: The  $D_s^+$  momentum spectrum from  $B$  decays. Scaled off-resonance histograms are subtracted directly from the corresponding on-resonance histograms.

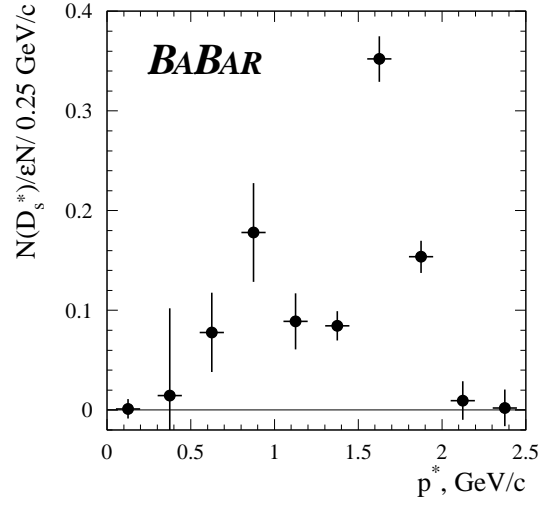


Figure 6.38: The  $D_s^{*+}$  momentum spectrum from  $B$  decays. Scaled off-resonance histograms are subtracted directly from the corresponding on-resonance histograms.

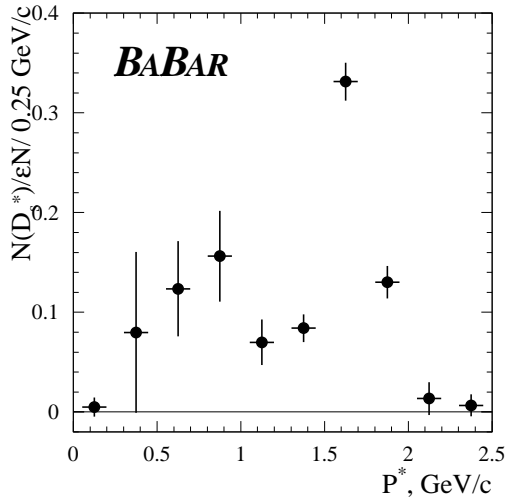


Figure 6.39: The  $D_s^{*+}$  momentum spectrum from  $B$  decays. The third order of polynomial is used for the combinatorial background parameterization.

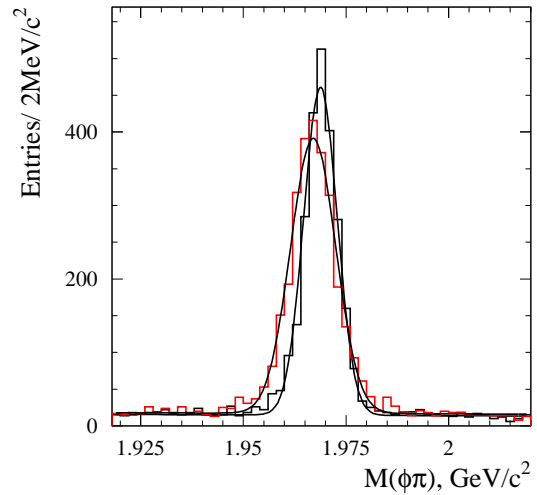


Figure 6.40: The  $\phi\pi^+$  mass spectrum from Monte Carlo obtained with (red histogram) and without (black histogram) smearing procedure.

	No smearing	Smearing	Data
$M_{D_s}$ , MeV	$1968.8 \pm 0.1$	$1967.0 \pm 0.1$	$1966.0 \pm 0.1$
$\sigma$ , MeV	$4.07 \pm 0.09$	$5.50 \pm 0.12$	$5.09 \pm 0.09$
Efficiency, %	$25.08 \pm 0.55$	$25.60 \pm 0.55$	

Table 6.8: The  $D_s^+$  peak parameters with and without smearing. The efficiency is corrected neither for tracking nor for particle identification.

## 6.6 Fits to $D_s^{(*)+}$ Momentum Spectra

### 6.6.1 Components of Momentum Spectrum

By fitting the  $D_s^{(*)+}$  momentum spectrum, the relative branching fractions of  $B$  decays to different final states containing a  $D_s^{(*)+}$  meson are obtained. In the  $\Upsilon(4S)$  rest frame, two-body  $B$  decays produce  $D_s^{(*)+}$  mesons with a  $\sim 300$  MeV/ $c$  wide momentum spectrum. In  $B$  decays, the  $D_s^{(*)+}$  momentum spectrum is essentially governed by the production of direct  $D_s^{(*)+}$ . Other  $c\bar{s}$  states (with  $L=1$ ), such as  $D_{s1}^+(2536)$  and  $D_{s2}^{*+}(2573)$ , primarily decay to  $D^{(*)}K$ . Because  $D_s^{*+}$  decays to  $D_s^+\gamma$  or  $D_s^+\pi^0$ , the  $D_s^+$  momentum distribution is slightly broader and softer compared to the direct production  $B \rightarrow D_s^+ X$ .

Three different sources of  $D_s^{(*)+}$  mesons in  $B$  decays are considered for the momentum spectrum.

- (1)  $B \rightarrow D_s^{(*)+} \bar{D}^{(*)}$  decays. The relative branching fractions of the individual channels can be taken either from the existing measurements [55] or from predictions assuming factorization [28], [29], [31]. Table. 6.9 shows the predictions for the relative branching fraction with respect to the different theoretical models and *CLEO* measurement. The fit is performed for both cases, with the assumption  $f_{D_s^{*+}} = f_{D_s^+}$  for the theoretical models, where  $f_{D_s^{(*)+}}$  are the  $D_s^{(*)+}$  decay constants.
- (2)  $B \rightarrow D_s^{(*)+} \bar{D}^{**}$  decays. Four  $\bar{D}^{**}$  states are considered:  $\bar{D}_0^*(j = 1/2)$ ,  $\bar{D}_1(2420)$ ,  $\bar{D}_1(j = 1/2)$  and  $\bar{D}_2^*(2460)$ . The observation of  $B \rightarrow D_s^{(*)+} \bar{D}^{**}$  decays was recently reported by *CLEO* [54].
- (3) Three-body  $B \rightarrow D_s^{(*)+} \bar{D}^{(*)} \pi / \rho / \omega$  decays. Since little is known about these decays, they are considered with equal weights and the momentum distributions are generated according to phase space.

	$\frac{\Gamma(B \rightarrow D_s^{*+} D)}{\Gamma(B \rightarrow D_s^+ D^*)}$	$\frac{\Gamma(B \rightarrow D_s^+ D)}{\Gamma(B \rightarrow D_s^+ D^*)}$	$\frac{\Gamma(B \rightarrow D_s^{*+} D^*)}{\Gamma(B \rightarrow D_s^{*+} D)}$
BSW [28]	$1.31 \left( \frac{f_{D_s^*}}{f_{D_s}} \right)^2$	2.24	2.77
Rosner [29]	$1.00 \left( \frac{f_{D_s^*}}{f_{D_s}} \right)^2$	1.43	2.59
Neubert [31]	$1.04 \left( \frac{f_{D_s^*}}{f_{D_s}} \right)^2$	1.47	2.56
CLEO [55]	$0.80 \pm 0.24$	$0.99 \pm 0.24$	$2.70 \pm 0.81$

Table 6.9: Predictions and experimental results for the ratios of the width in  $B \rightarrow D_s^{(*)+} \bar{D}^{(*)}$  decays

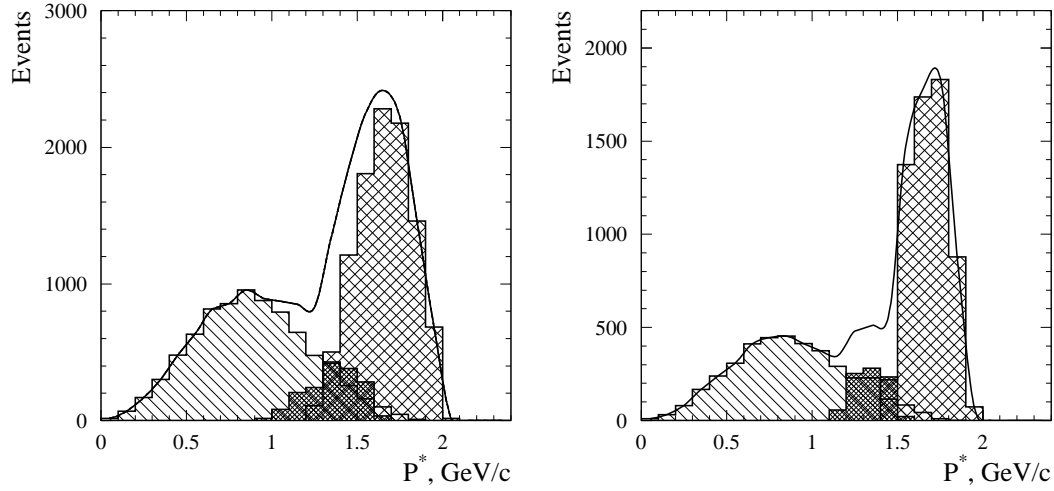


Figure 6.41: The generated  $D_s^+$  (left) and  $D_s^{*+}$  (right) momentum spectra. Type (1),  $B \rightarrow D_s^{(*)+} \bar{D}^{(*)}$  - the slightly cross hatched histogram, Type (2),  $B \rightarrow D_s^{(*)+} \bar{D}^{**}$  - the cross hatched histogram and Type (3),  $B \rightarrow D_s^{(*)+} \bar{D}^{(*)} \pi / \rho / \omega$  - slightly hatched histogram. The smooth line is the sum of the three components.

Fig. 6.41 shows the  $D_s^+$  and  $D_s^{*+}$  momentum spectra generated with respect to the models described above. The individual contributions are also shown.

## 6.6.2 Fit and Systematic Errors

The minimum- $\chi^2$  fits to the  $D_s^{(*)+}$  momentum spectrum is performed leaving the total number of the  $D_s^{(*)+}$  events as a free parameter \*. From the fits to the  $D_s^+$  and  $D_s^{*+}$  spectra, the ratio of two-body modes (1) to the total inclusive rate is determined to be

$$\frac{\Sigma \mathcal{B}(B \rightarrow D_s^{(*)+} \bar{D}^{(*)})}{\mathcal{B}(B \rightarrow D_s^+ X)} = (46.4 \pm 1.3 \pm 1.4 \pm 0.6)\%, \quad (6.17)$$

$$\frac{\Sigma \mathcal{B}(B \rightarrow D_s^{*+} \bar{D}^{(*)})}{\mathcal{B}(B \rightarrow D_s^{*+} X)} = (53.3 \pm 3.7 \pm 3.1 \pm 2.1)\%. \quad (6.18)$$

The first error is statistical. The second error represents the systematic error due to the limited Monte Carlo statistics and the background parameterization. The last error is due to the model uncertainty. It is obtained by varying the individual relative contributions of the modes into each source of  $D_s^{(*)+}$  listed above.

The fit is performed using different assumptions of the relative contributions of the modes in source (1). We take the theoretical predictions and measurements listed in Table 6.9. Different weights of  $B \rightarrow D_s^+ \bar{D}^{**}$  and  $B \rightarrow D_s^{*+} \bar{D}^{**}$  as well as different relative branching fractions of the four modes within source (2) are used for the fit (see Table 6.10 and 6.11). For source (3), two cases are considered: either  $B \rightarrow D_s^{(*)} \bar{D}^{(*)} \pi$  or  $B \rightarrow D_s^{(*)} \bar{D}^{(*)} \rho/\omega$  is assumed to be dominant. The results of the fits to the  $D_s^{(*)+}$  momentum spectra are shown in Fig. 6.42 for the assumption of the equal weights for the individual contributions within sources (2) and (3), and with weights for source (1) taken from [31]. The fit results for the different assumptions of the relative contributions of the modes for all three sources are presented in Tables 6.10, 6.11.

The  $\chi^2$  of the fit for the inclusive  $D_s^{*+}$  momentum spectrum is best when the contribution  $B \rightarrow D_s^{(*)} \bar{D}^{(*)} \rho/\omega$  is dominant compared to  $B \rightarrow D_s^{(*)} \bar{D}^{(*)} \pi$ . Fig 6.43 shows the fit results for these two assumptions.

---

\*A set of  $N$  ( $N = 12$  for  $D_s^+$  and  $N = 10$  for  $D_s^{*+}$ ) measurements at points  $x_i$  are supposed. The  $i$ th measurement  $y_i$  has a variance  $\sigma_i$ . The fit function  $F(x_i)$  consists of the three components of the  $D_s^{(*)+}$  sources  $v_j$ , where  $j = 1, 2, 3$ , respectively. Each component is normalized on unity, i.e.

$$\sum_{i=1}^N v_j(x_i) = 1.$$

The set of parameters  $p_1, p_2, n$  is found minimizing the  $\chi^2$  calculated as

$$\chi^2 = \sum_{i=1}^N \left( \frac{n[p_1 v_1(x_i) + p_2 v_2(x_i) + (1 - p_1 - p_2) v_3(x_i)] - y_i}{\sigma_i} \right)^2,$$

where  $p_1$  is the fraction of type (1),  $p_2$  is the fraction of type (2),  $n$  is the total  $D_s^{(*)+}$  yield.



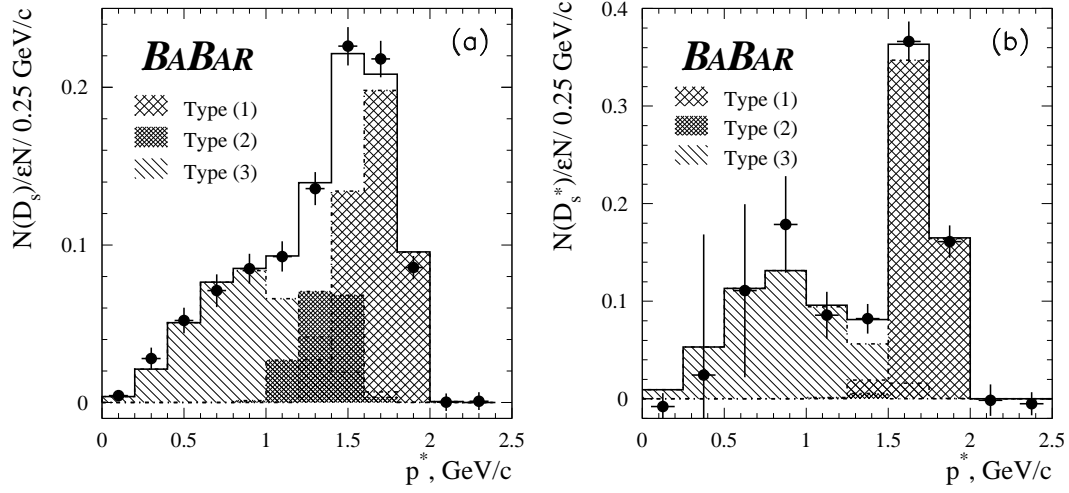


Figure 6.42: The fit result for (a)  $D_s^+$  and (b)  $D_s^{*+}$  momentum spectra. The data are the dots with error bars, and the histograms represent the three components described in the text, i.e. Type (1) is  $B \rightarrow D_s^{(*)+} \bar{D}^{(*)}$ , Type (2) is  $B \rightarrow D_s^{(*)+} \bar{D}^{**}$  and Type (3) is  $B \rightarrow D_s^{(*)+} \bar{D}^{(*)} \pi / \rho / \omega$ . The solid histogram is the sum of the three components.

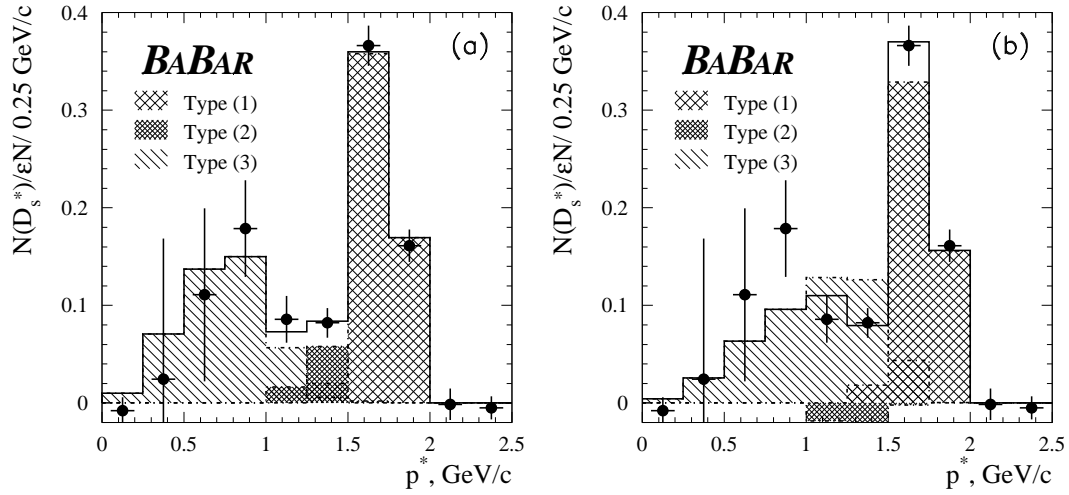


Figure 6.43: The fit result for  $D_s^{*+}$  momentum spectra. (a) The  $B \rightarrow D_s^{(*)} D^{(*)} \rho / \omega$  and (b) the  $B \rightarrow D_s^{(*)} D^{(*)} \pi$  are dominant in source (3). The data are dots with error bars and the histograms represent the three components described in the text. Type (1) is  $B \rightarrow D_s^{(*)+} \bar{D}^{(*)}$ , Type (2) is  $B \rightarrow D_s^{(*)+} \bar{D}^{**}$  and Type (3) is  $B \rightarrow D_s^{(*)+} \bar{D}^{(*)} \pi / \rho / \omega$ . The solid histogram is the sum of the three components.

Model	$\Sigma B \rightarrow D_s^{(*)+} \bar{D}^{(*)}$	$\Sigma \mathcal{B}(B \rightarrow D_s^* D^{(*)})$
Equal $B \rightarrow D_s^{(*)} D^{(*)} \pi / \rho / \omega$		
$D_1(2420), D_2^*(2460)$ $D_s^* D^{**} : D_s D^{**} = 1:1$		
BSW	$46.0 \pm 1.9$	$52.4 \pm 4.6$
Rosner	$45.6 \pm 1.8$	$52.4 \pm 4.6$
Neubert	$45.7 \pm 1.9$	$52.4 \pm 4.5$
<i>CLEO</i>	$45.9 \pm 1.9$	$52.5 \pm 4.6$
$D_1(2420), D_0^*(j = 1/2), D_1(j = 1/2), D_2^*(2460)$ $D_s^* D^{**} : D_s D^{**} = 1:1$		
Neubert	$45.6 \pm 1.9$	$52.4 \pm 4.5$
$D_s^* D^{**} : D_s D^{**} = 2:1$		
BSW	$47.3 \pm 1.8$	$52.5 \pm 4.6$
Rosner	$47.0 \pm 1.8$	$52.4 \pm 4.5$
Neubert	$47.1 \pm 1.8$	$52.4 \pm 4.6$
<i>CLEO</i>	$47.3 \pm 1.8$	$52.5 \pm 4.6$

Table 6.10: The results of the fit for the different assumptions concerning the relative contribution of the modes for each source of  $D_s^+$

In order to evaluate the systematic error for the fraction of the two-body modes (1) the fit of the  $D_s^{(*)+}$  momentum spectrum obtained by two alternative methods described in Section 6.5.6 is done. From the fit of the  $D_s^+$  momentum spectrum obtained by direct background subtraction, the fraction of two-body modes (1) relative to the total inclusive rate is determined to be  $45.7 \pm 1.9\%$  (error includes the Monte Carlo statistics). It is in agreement with the fit regarding the same model assumption of the spectrum obtained with a basic procedure ( $45.7 \pm 1.9\%$ ). Fig 6.44 shows the fit results of  $D_s^{*+}$  momentum spectrum extracted by two methods. The fraction of the two-body modes (1) as obtained from the fit is  $52.7 \pm 4.9\%$  for the first plot (a) and  $50.5 \pm 4.3\%$  for the second one (b). This difference is attributed to a systematic error for the fraction of  $B \rightarrow D_s^{*+} \bar{D}^{(*)}$  modes.

The sum of branching fractions for the two-body  $B \rightarrow D_s^{(*)} \bar{D}^{(*)}$  decays are obtained

Model	$\Sigma B \rightarrow D_s^{(*)+} \bar{D}^{(*)}$	$\Sigma \mathcal{B}(B \rightarrow D_s^* D^{(*)})$
Only $B \rightarrow D_s^{(*)} D^{(*)} \pi$		
$D_1(2420), D_2^*(2460)$ $D_s^* D^{**} : D_s D^{**} = 1:1$		
BSW	$46.5 \pm 1.9$	bad fit
Rosner	$46.1 \pm 1.9$	bad fit
Neubert	$46.2 \pm 1.9$	$55.5 \pm 5.1$ (bad fit)
<i>CLEO</i>	$46.4 \pm 1.9$	bad fit
$D_1(2420), D_0^*(j = 1/2), D_1(j = 1/2), D_2^*(2460)$ $D_s^* D^{**} : D_s D^{**} = 1:1$		
Neubert	$46.2 \pm 1.9$	$55.8 \pm 4.9$ (bad fit)
$D_s^* D^{**} : D_s D^{**} = 2:1$		
Neubert	$46.5 \pm 1.8$	$55.9 \pm 4.8$ (bad fit)
Only $B \rightarrow D_s^{(*)} D^{(*)} \rho/\omega$		
$D_1(2420), D_0^*(j = 1/2), D_1(j = 1/2), D_2^*(2460)$ $D_s^* D^{**} : D_s D^{**} = 2:1$		
BSW	$47.5 \pm 1.8$	$51.8 \pm 4.1$
Rosner	$47.2 \pm 1.8$	$51.8 \pm 4.2$
Neubert	$47.4 \pm 1.8$	$51.9 \pm 4.2$
<i>CLEO</i>	$47.5 \pm 1.8$	$51.8 \pm 4.2$

Table 6.11: The results of the fit for the different assumptions concerning the relative contribution of the modes for each source of  $D_s^+$

from the fits of the  $D_s^{(*)+}$  momentum spectra, where the yield of each source is a free

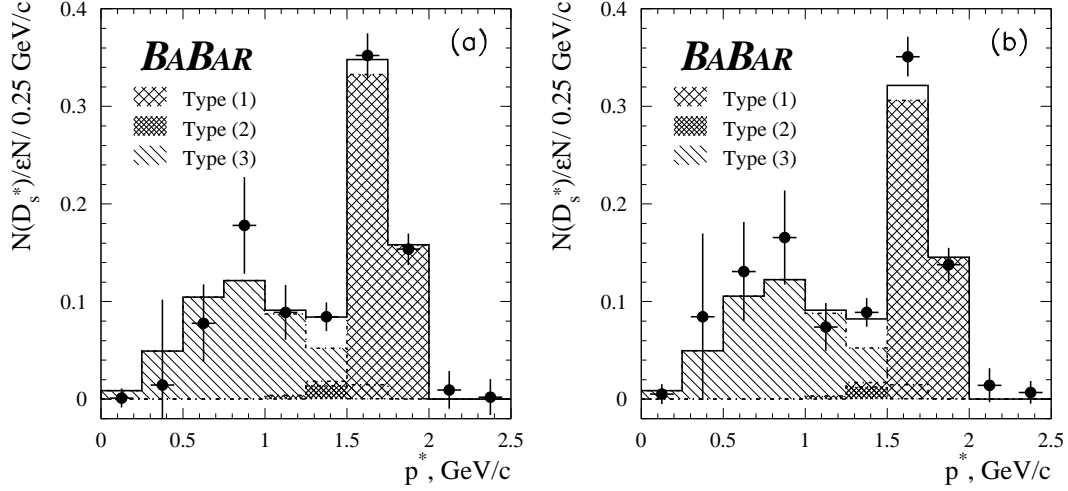


Figure 6.44: The fit result for  $D_s^{*+}$  momentum spectra. (a) Scaled off-resonance histograms are subtracted directly from the corresponding on-resonance histograms. (b) The third order of polynomial is used for the combinatorial background parameterization. The data are the dots with error bars and the histograms represent the three components described in the text. Type (1) is  $B \rightarrow D_s^{(*)+} \bar{D}^{(*)}$ , Type (2) is  $B \rightarrow D_s^{(*)+} \bar{D}^{**}$  and Type (3) is  $B \rightarrow D_s^{(*)+} \bar{D}^{(*)} \pi / \rho / \omega$ . The solid histogram is the sum of the three components.

parameter <sup>†</sup>. We find

$$\Sigma \mathcal{B}(B \rightarrow D_s^{(*)+} \bar{D}^{(*)}) = (5.07 \pm 0.14 \pm 0.30 \pm 1.27)\%, \quad (6.19)$$

$$\Sigma \mathcal{B}(B \rightarrow D_s^{*+} \bar{D}^{(*)}) = (4.1 \pm 0.2 \pm 0.4 \pm 1.0)\%, \quad (6.20)$$

where the first error is statistical, the second is systematic, and the third is due to the  $D_s^+ \rightarrow \phi \pi^+$  branching fraction uncertainty. The systematic error includes the systematic errors of the  $B \rightarrow D_s^{(*)+} X$  branching fractions, the systematic errors of the relative contributions of source (1), and the uncertainty due to model dependence. Two systematic errors due to the limited Monte Carlo statistic and the model uncertainty, are determined separately. The first error is extracted by fitting to the spectrum where the errors from the simulation are not included. The second error is evaluated from the fits for each assumption of the individual contributions of the

<sup>†</sup>The set of parameters  $p_1, p_2, p_3$  is found minimizing the  $\chi^2$  calculated as

$$\chi^2 = \sum_{i=1}^N \left( \frac{[p_1 v_1(x_i) + p_2 v_2(x_i) + p_3 v_3(x_i)] - y_i}{\sigma_i} \right)^2,$$

where  $p_i$  is the yield of type (i).

	Data			Monte Carlo		
	$m(D_s^+)$	$m(D^+)$	$\Delta m$	$m(D_s^+)$	$m(D^+)$	$\Delta m$
$p_1$	$1968.1 \pm 0.1$	$1869.2 \pm 0.2$	$98.9 \pm 0.2$	$1969.2 \pm 0.05$	$1870.2 \pm 0.1$	$99.0 \pm 0.1$
Fit $\Delta m$			$98.4 \pm 0.1$			$99.3 \pm 0.1$
Fit $\phi\pi$	$1966.4 \pm 0.04$	$1868.0 \pm 0.1$	$98.4 \pm 0.1$			
Truth				1968.6	1869.3	99.3

Table 6.12:  $m(D_s^+)$ ,  $m(D^+)$ ,  $\Delta m = m(D_s^+) - m(D^+)$  in  $\text{MeV}/c^2$  obtained with different procedures for data and Monte Carlo. The last line shows the value of the mass used the simulation.

modes into each source of  $D_s^{(*)+}$ . The lower part of the spectrum, especially for  $D_s^{*+}$ , is determined with larger errors. Since the overlap of source (1) with the other two sources is small, only the bins with the maximum yield are relevant for the two-body modes of source (1). Therefore, the relative error of the sum of the two-body modes of source (1) is smaller than the relative error of the  $B \rightarrow D_s^{(*)+} X$  branching fraction or the relative rate of source (1), where the lower part of the spectrum is accounted.

## 6.7 $D_s^+$ and $D^+$ Mass Difference

Together with the  $D_s^+ \rightarrow \phi\pi^+$  channel, a signal for the Cabibbo-suppressed decay mode  $D^+ \rightarrow \phi\pi^+$  is observed. Fig 6.45 shows the reconstructed  $D^+$  mass as a function of the center-of-mass momentum for both data and Monte Carlo. A fit using the function in Eq. 6.1 is done with three free parameters,  $p_i$ . Although the uncertainties on the absolute mass is of the order of several  $\text{MeV}/c^2$  (sec. 6.1), the systematic error in the determination of the  $D_s^+$  and  $D^+$  mass difference is much smaller, since many sources of error cancel. The systematic error is obtained from a study of the mass difference as a function of momentum in both data and Monte Carlo simulation. Fig 6.46 shows the mass difference  $m(D_s^+) - m(D^+)$  as function of momentum obtained with the data and the Monte Carlo. One can see from this plot that it does not depend on the  $D_s^+$  or  $D^+$  momentum.

The values for the  $m(D_s^+)$ ,  $m(D^+)$  and  $\Delta m$  obtained from different methods are presented in Table 6.12. One can conclude the following:

- The value of  $\Delta m = 99.3 \pm 0.1 \text{ MeV}/c^2$  obtained in Monte Carlo is consistent with the generated mass difference of  $99.3 \text{ MeV}/c^2$ . The statistical error of  $0.1 \text{ MeV}/c^2$  obtained in the fit of the Monte Carlo data is associated to the systematic.

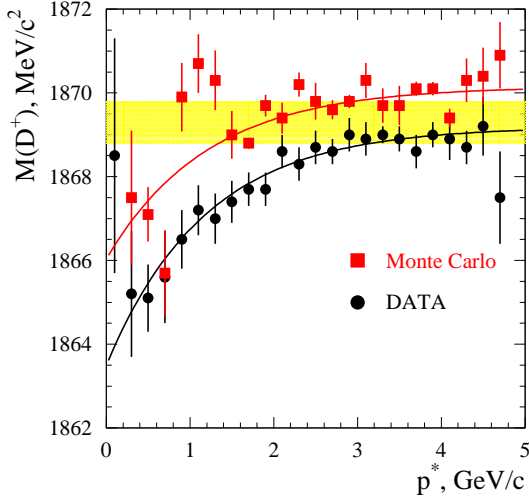


Figure 6.45: The  $D^+$  fitted mass as a function of its momentum in  $\Upsilon(4S)$  rest frame for data and Monte Carlo. The curves show the fit result with a function described in the text. The shaded band shows the PDG value.

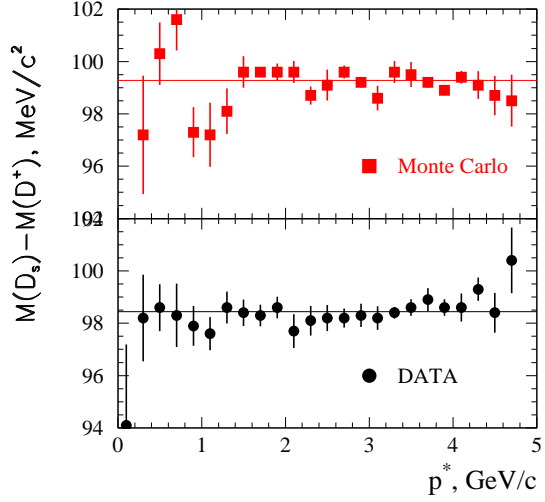


Figure 6.46: The mass difference  $m(D_s^+) - m(D^+)$  as function of center-of-mass momentum obtained with Monte Carlo and data. The  $\chi^2/\text{nDof}$  of the fit with a straight line are 33.4/22 and 15.2/23, respectively.

- The fit of  $\phi\pi$  invariant mass (including all momentum of the candidates) gives  $\Delta m = 98.4 \pm 0.1 \text{ MeV}/c^2$ . This is consistent with  $\Delta m = 98.4 \pm 0.1 \text{ MeV}/c^2$  obtained from the fit  $\Delta m$  as a function of momentum.
- The comparison of mass difference deduced from the value of the fit parameter  $p_1$  is used to determine the systematic uncertainty. The parameters  $p_1^{D_s^+}$  and  $p_1^{D^+}$  are obtained from the fit of the  $D_s^+$  and  $D^+$  mass as a function of the momentum, respectively. We define  $\Delta m(p_1) = p_1^{D_s^+} - p_1^{D^+}$ . It is important to say that this procedure gives a very conservative result, since  $\Delta m^{MC}(p_1)$  gives a wrong value for Monte Carlo. The  $\Delta m$  obtained with data deviates from  $98.4 \pm 0.1$  by  $+0.5 \pm 0.2 \text{ MeV}/c^2$ , while in Monte Carlo it is lower than generated value by  $-0.3 \pm 0.1 \text{ MeV}/c^2$ . Thus the error weighted average of  $0.3 \text{ MeV}/c^2$  is attributed to the systematic uncertainty.

Therefore, the measured mass difference is

$$m(D_s^+) - m(D^+) = 98.4 \pm 0.1 \pm 0.3 \text{ MeV}/c^2. \quad (6.21)$$

The first error is statistical, while the second one accounts for the systematic uncertainties. This result is consistent with PDG value of  $99.2 \pm 0.5 \text{ MeV}/c^2$  [8].

## 6.8 Summary

The branching fractions for the inclusive  $B \rightarrow D_s^{(*)+} X$  production have been determined:

$$\mathcal{B}(B \rightarrow D_s^+ X) = (10.93 \pm 0.19 \pm 0.58 \pm 2.73)\% \quad (6.22)$$

and

$$\mathcal{B}(B \rightarrow D_s^{*+} X) = (7.94 \pm 0.82 \pm 0.72 \pm 1.99)\%. \quad (6.23)$$

The production cross sections for  $D_s^{(*)+}$  from continuum events at center-of-mass energies about 40 MeV below the  $\Upsilon(4S)$  mass are

$$\sigma(e^+e^- \rightarrow D_s^\pm X) \times \mathcal{B}(D_s^+ \rightarrow \phi\pi^+) = 7.55 \pm 0.20 \pm 0.34 \text{ pb} \quad (6.24)$$

and

$$\sigma(e^+e^- \rightarrow D_s^{*\pm} X) \times \mathcal{B}(D_s^+ \rightarrow \phi\pi^+) = 5.79 \pm 0.66 \pm 0.50 \text{ pb}. \quad (6.25)$$

The study of different fragmentation functions was done for the  $D_s^{(*)+}$  momentum spectrum produced from  $q\bar{q}$  continuum events. It was found that the Andersson function provides the best parameterization of the hadronization process. Using this function, the vector to pseudoscalar plus vector production ratio is determined:

$$P_V = \frac{V}{V+P} = 0.75 \pm 0.02 \pm 0.05 \quad (6.26)$$

where the first error is statistical and the second is due to systematics.

The measurements of  $B \rightarrow D_s^{*+} X$  and the  $D_s^{*+}$  production cross section from continuum events are the first of the kind. Our results for  $D_s^+$  are in agreement with previous measurements [55, 56]. However, the precision of the measurements presented here represents a significant improvement. In contrast to previous measurements, the measured values do not rely on any assumptions regarding the shape of the fragmentation function. From the fit of the  $D_s^{(*)+}$  momentum spectrum, the fraction of two-body  $B \rightarrow D_s^{(*)+} \bar{D}^{(*)}$  decays compared to the total production of inclusive  $D_s^+$  is  $(46.4 \pm 1.3 \pm 1.4 \pm 0.6)\%$ . The fraction of  $B \rightarrow D_s^{*+} \bar{D}^{(*)}$  decays compared to the total production of inclusive  $D_s^{*+}$  is  $(53.3 \pm 3.7 \pm 3.1 \pm 2.1)\%$ . The last error on the values quoted above is due to the model dependence. Combining these results, we obtain

$$\Sigma \mathcal{B}(B \rightarrow D_s^{(*)+} \bar{D}^{(*)}) = (5.07 \pm 0.14 \pm 0.30 \pm 1.27)\%, \quad (6.27)$$

$$\Sigma \mathcal{B}(B \rightarrow D_s^{*+} \bar{D}^{(*)}) = (4.1 \pm 0.2 \pm 0.4 \pm 1.0)\%. \quad (6.28)$$

Finally, the mass difference

$$m(D_s^+) - m(D^+) = 98.4 \pm 0.1 \pm 0.3 \text{ MeV}/c^2, \quad (6.29)$$

has been measured. The first error is statistical while the second one accounts for the systematic uncertainties.





## Chapter 7

# The $B^0 \rightarrow D_s^{(*)+} D^{*-}$ Decays

### 7.1 Signal Extraction

The  $B^0 \rightarrow D_s^{(*)+} D^{*-}$  decays are reconstructed partially using the three  $D_s^+$  decay channels:  $D_s^+ \rightarrow \phi\pi^+$ ,  $D_s^+ \rightarrow \bar{K}^{*0}K^+$  and  $D_s^+ \rightarrow \bar{K}^0K^+$ . Fully reconstructed  $D_s^{(*)+}$  candidates satisfying the selection criteria described in section 5.3, are then combined with an oppositely charged soft pion. Finally, to derive the missing mass (section 4.5.2) recoiling against the  $D_s^{(*)+} - \pi$  system is derived assuming both particles are produced from a single  $B$  decay. The  $D_s^+$  ( $D_s^{*+}$ ) candidates are selected requiring the measured invariant mass ( $\Delta M = M_{D_s^+\gamma} - M_{D_s^+}$ ) to be within 3 (2.5) standard deviations ( $\sigma$ ) of the fitted peak value. Since the momentum of the soft pion in the  $\mathcal{T}(4S)$  frame lies in the region between 50 MeV/ $c$  and 210 MeV/ $c$ , there are no specific requirements for the number of hits produced in the drift chamber in order to maximize the reconstruction efficiency.

Due to the high combinatorial background in the  $\Delta M$  distribution, one may find several  $D_s^{*+}$  candidates in one event. Therefore, the following  $\chi^2$

$$\chi^2 = \left( \frac{M_{\phi, K^*, K_s}^{rec} - M_{\phi, K^*, K_s}^{mean}}{\sigma_{\phi, K^*, K_s}} \right)^2 + \left( \frac{M_{D_s}^{rec} - M_{D_s}^{mean}}{\sigma_{D_s}} \right)^2 + \left( \frac{M_{\Delta m}^{rec} - M_{\Delta m}^{mean}}{\sigma_{\Delta m}} \right)^2 \quad (7.1)$$

is calculated for each  $D_s^{*+}$  candidate. Only the candidate with the lowest  $\chi^2$  is accepted. The good discriminant quantity against the continuum is the event shape variable  $R_2 = H_2/H_0$ . It is defined as the ratio of the second to zeroth order Fox-Wolfram moment [57] and is computed using all the charged tracks and neutral clusters in the event. To discriminate the  $B\bar{B}$  events from the  $q\bar{q}$  continuum,  $R_2$  is required to be less than 0.35.

The missing mass distributions for the  $D_s^+ - \pi$  and  $D_s^{*+} - \pi$  combinations obtained from the data are shown in Figs. 7.1–7.6. The distributions for each of the three  $D_s^+$

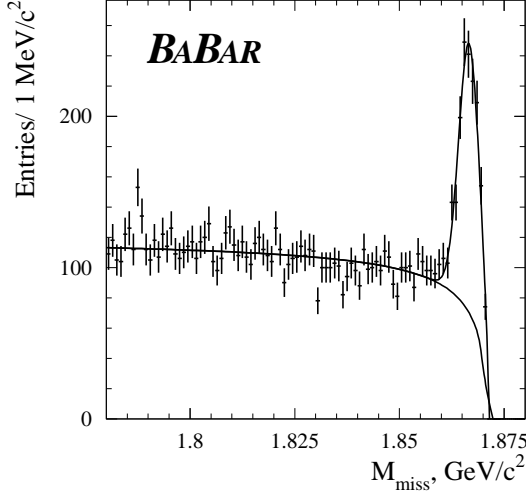


Figure 7.1: The missing mass distribution for  $D_s^+ - \pi$  ( $D_s^+ \rightarrow \phi \pi^+$ ). The result of the fit described in the text is overlaid.

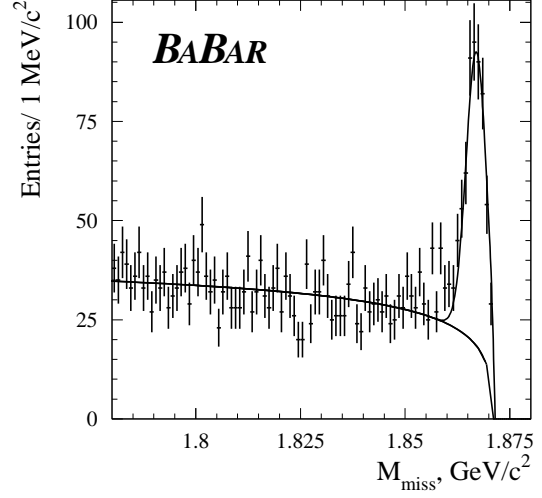


Figure 7.2: The missing mass distribution for  $D_s^{*+} - \pi$  ( $D_s^{*+} \rightarrow \phi \pi^+$ ). The result of the fit described in the text is overlaid.

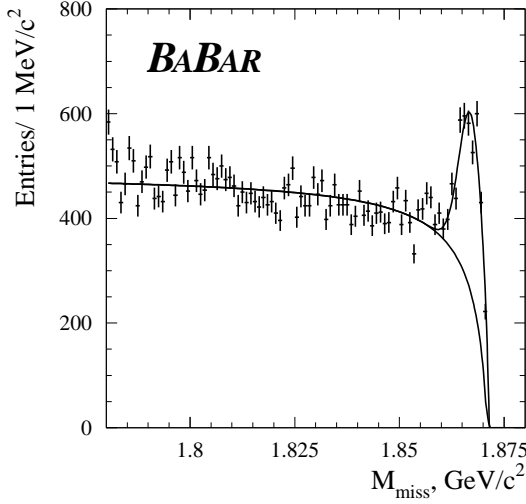


Figure 7.3: The missing mass distribution for  $D_s^+ - \pi$  ( $D_s^+ \rightarrow \bar{K}^{*0} K^+$ ). The result of the fit described in the text is overlaid.

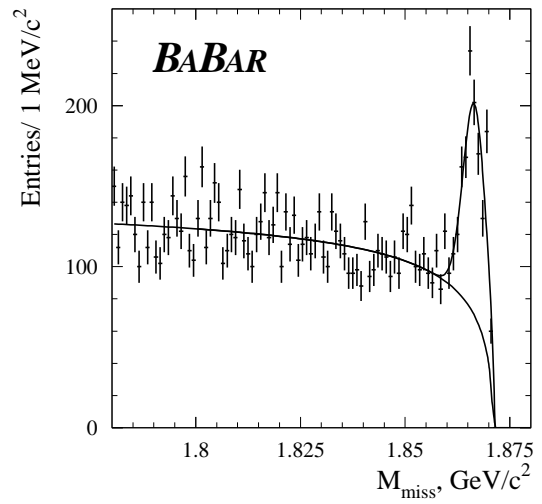


Figure 7.4: The missing mass distribution for  $D_s^{*+} - \pi$  ( $D_s^{*+} \rightarrow \bar{K}^{*0} K^+$ ). The result of the fit described in the text is overlaid.

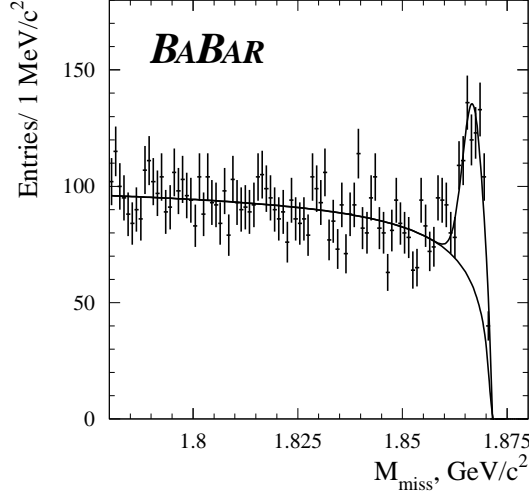


Figure 7.5: The missing mass distribution for the  $D_s^+ - \pi$  ( $D_s^+ \rightarrow \bar{K}^0 K^+$ ). The result of the fit described in the text is overlaid.

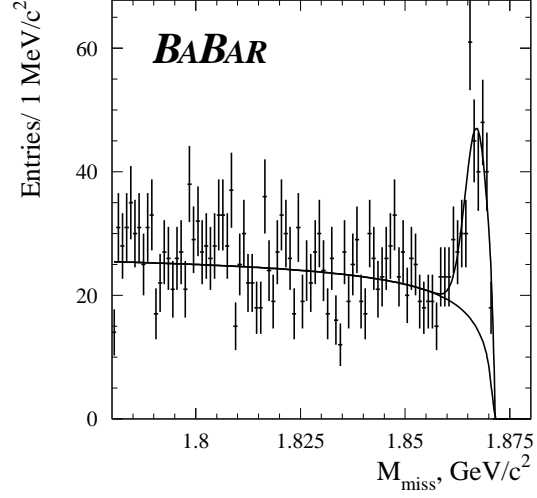


Figure 7.6: The missing mass distribution for the  $D_s^{*+} - \pi$  ( $D_s^{*+} \rightarrow \bar{K}^0 K^+$ ). The result of the fit described in the text is overlaid.

	$D_s^+ \rightarrow \phi\pi^+$	$D_s^+ \rightarrow \bar{K}^{*0}K^+$	$D_s^+ \rightarrow \bar{K}^0K^+$	Sum
$D_s^+ - \pi$	$1057 \pm 80$	$2073 \pm 151$	$509 \pm 80$	$3704 \pm 232$
$D_s^{*+} - \pi$	$390 \pm 48$	$867 \pm 80$	$229 \pm 39$	$1493 \pm 95$

Table 7.1: The Number of signal events observed for the  $D_s^{(*)+} - \pi$  system with  $D_s^+$  identified in three different channels.

decay modes are shown separately. Clear peaks for the recoil  $D^0$  mass are observed. As it will be shown later, no peak is observed in the same distributions for same charge  $D_s^{(*)+} - \pi$  pair combinations. The  $D^0$  signal is fitted with a Gaussian distribution. For the background, a function

$$f_B(x) = \frac{c_1(x_0 - x)^{c_2}}{c_3 + (x_0 - x)^{c_2}} \quad (7.2)$$

is used, where the three parameters  $c_i$  are left free in the fit,  $x$  is the calculated missing mass, and  $x_0$  is the end point defined as  $M_{D^*} - M_\pi = 1.871 \text{ GeV}/c^2$ . The number of signal events obtained from the maximum log likelihood fit of the missing mass distributions are summarized in Table 7.1.

## 7.2 Background Study

### 7.2.1 Peaking Backgrounds

In order to estimate the signal efficiency for a given set of selection criteria, a number of signal  $B^0 \rightarrow D_s^{(*)+} D^{*-}$  events have been generated and passed through the full detector simulation. It is based on the GEANT-3 [58] package which is commonly used for the detector simulations.

Both the slow pion and the soft photon reconstruction efficiency depends on momentum. However, the momentum distributions depend on the polarization. Therefore, the reconstruction efficiency of the  $B^0 \rightarrow D_s^{(*)+} D^{*-}$  decay mode depends on polarization. In particular, the generator code allows one to generate the proper kinematics for pseudoscalar to vector-pseudoscalar and vector-vector decays, with a possibility to select individual helicity amplitudes in the latter case. Three different Monte Carlo samples (with a longitudinal (L), transverse (T) and measured (M) (section 7.5) polarization) were generated in a simulation cycle called Simulation Production #3 (SP3). The reconstruction efficiency of the  $B^0 \rightarrow D_s^{(*)+} D^{*-}$  decay is studied separately for the longitudinal and transverse polarizations and then are propagated to the measured value. The sample with the measured polarization is used as a cross check. The missing mass distributions for the  $B^0 \rightarrow D_s^{(*)+} D^{*-}$  obtained from the Monte Carlo

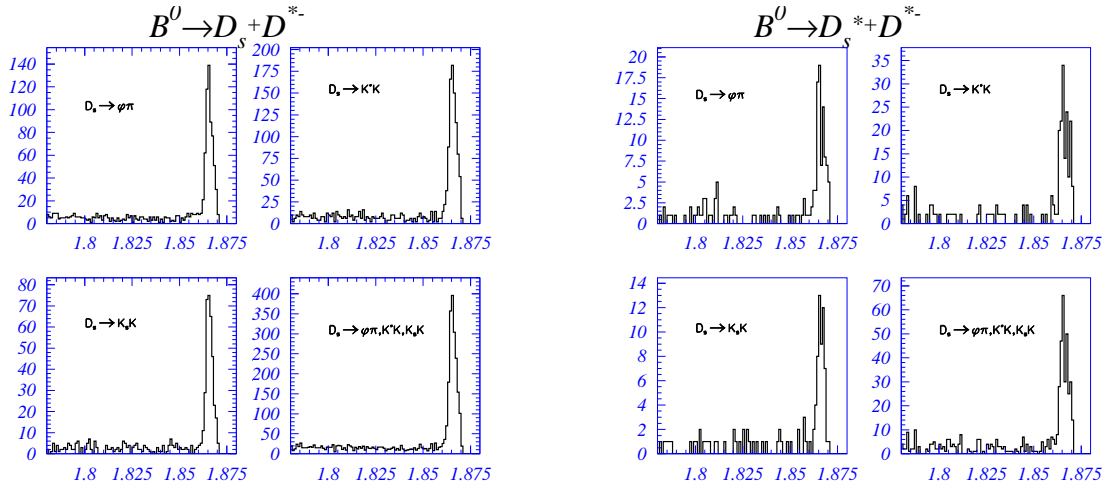


Figure 7.7: The missing mass distribution for the  $D_s^+ - \pi$  (left) and  $D_s^{*+} - \pi$  (right) systems obtained from the Monte Carlo sample. Three different  $D_s^+$  modes are shown separately. The  $B^0 \rightarrow D_s^{(*)+} D^{*-}$  signal is generated according to the measured polarization.

simulation are shown in Fig. 7.7. As expected, these distributions peak at the  $D^0$  mass.

However, there are two sources of background which also peak at the  $D^0$  mass:

- **Cross Feed:** Although the soft photon from  $D_s^{*+} \rightarrow D_s^+ \gamma$  decay is not reconstructed, the  $B^0 \rightarrow D_s^{*+} D^{*-}$  decay mode leads to an enhancement at the end of the missing mass spectrum, when the  $D_s^+ - \pi$  system is considered. Similarly, the  $B^0 \rightarrow D_s^+ D^{*-}$  decay may lead to an enhancement at the  $D^0$  missing mass when the  $D_s^{*+} - \pi$  system is studied. This is due to the accidental addition of a photon to the  $D_s^+$ .
- **Self-Cross Feed:** Wrongly reconstructed  $D_s^{*+}$  obtained by a combination of a true  $D_s^+$  and a fake photon can also produce an enhancement at the missing  $D^0$  mass if the  $B^0 \rightarrow D_s^{*+} D^{*-}$  decay occurs. This type of background takes place only for the  $D_s^{*+} - \pi$  system.

The study of the peaking background is performed using the Monte Carlo signal events. Table 7.2 presents the reconstruction efficiency for the  $B^0 \rightarrow D_s^{*+} D^{*-}$  decay mode and for the  $B^0 \rightarrow D_s^{*+} D^{*-}$  cross feed which contributes in the signal region of

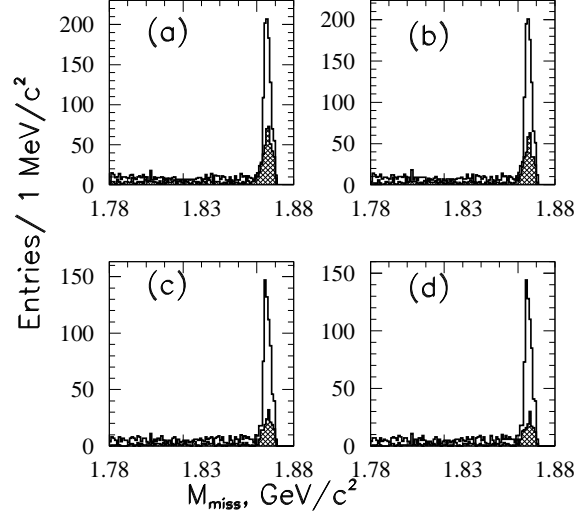


Figure 7.8: The missing mass distribution for  $B^0 \rightarrow D_s^{*+} D^{*-}$  decay mode obtained from Monte Carlo simulation. Different gamma selections are used: (a) all photon candidates, (b)  $E^* > 0.1$  GeV, (c) exclude photons having a  $\pi^0$  overlap, (d) exclude photons having a  $\pi^0$  overlap and  $E^* > 0.1$  GeV cut. The hatched histogram shows the self-cross Feed.

the  $D_s^+ - \pi$  missing mass. The signal region is defined as  $M_{miss} > 1.86 \text{ GeV}/c$ . Fig 7.8 shows the missing mass distribution for the different photon selection criteria. The self-cross feed is shown as a hatched histogram. One can see clearly that the level of the peaking background depends on the selection criteria of the soft photon. Table 7.3 presents the reconstruction efficiencies for the  $B^0 \rightarrow D_s^{*+} D^{*-}$  mode. It also shows the fraction of  $B^0 \rightarrow D_s^+ D^{*-}$  and  $B^0 \rightarrow D_s^{*+} D^{*-}$  events contributing into the signal region either due to cross feed or self-cross feed. One can conclude, that not only the self-cross feed but also the cross feed from the  $B^0 \rightarrow D_s^+ D^{*-}$  mode is diminished when tighter cuts are applied to the photon candidate.

## 7.2.2 Non-Peaking Background

Several types of backgrounds contribute in the signal region:

- (1) Fake  $D_s^{(*)+}$  and a random pion (for example coming from the other  $B$ ).
- (2) Fake  $D_s^{(*)+}$  and a correlated pion (for example coming from the same  $B$ ).
- (3) True  $D_s^{(*)+}$  and a random pion.
- (4) True  $D_s^{(*)+}$  and a correlated pion.

Table 7.4 shows the different types of backgrounds and the method which is used to determine their level. Background types (1)+(3) are obtained by flipping the  $D_s^{(*)+}$  direction. Background types (1)+(2) are extracted using the sidebands of the  $D_s^{(*)+}$  mass distribution. The side-band regions are defined as  $1.89 < M_{D_s^+} < 1.95$  and  $1.985 < M_{D_s^+} < 2.05 \text{ GeV}/c^2$  for the  $D_s^+ - \pi$  system, and  $170 < \Delta M_{D_s^{*+}} < 300 \text{ MeV}/c^2$

Generated mode	$D_s^+ - \pi$	
	$GTL + 2GTVL$	$3GTL$
$B^0 \rightarrow D_s^+ D^{*-}$	$28.0 \pm 1.1\%$	$23.6 \pm 1.0\%$
$B^0 \rightarrow D_s^{*+} D^{*-}$ (M)	$10.9 \pm 0.7\%$	$8.7 \pm 0.6\%$
$B^0 \rightarrow D_s^{*+} D^{*-}$ (L)	$11.1 \pm 0.4\%$	$9.0 \pm 0.3\%$
$B^0 \rightarrow D_s^{*+} D^{*-}$ (T)	$12.8 \pm 0.4\%$	$10.4 \pm 0.3\%$

Table 7.2: The reconstruction efficiency for the  $B^0 \rightarrow D_s^+ D^{*-}$  ( $D_s^+ \rightarrow \phi \pi^+$ ) decay mode. The  $B^0 \rightarrow D_s^{*+} D^{*-}$  cross feed efficiency is shown for the different polarization.

for the  $D_s^{*+} - \pi$  one. By using the side-bands and flipping the  $D_s^{(*)+}$  direction, we find the contribution of the background type (1). Therefore the difference between the distributions for flip and no flip  $D_s^{(*)+}$  direction for the side-bands gives the type (2) and thus it is possible to find the contribution of the background types (1)+(2)+(3). Figs. 7.9, 7.10 show the missing mass distribution for the  $D_s^+ - \pi$  and  $D_s^{*+} - \pi$  systems and the background obtained with the method described above. The remaining part type (4) is very small and extracted from the simulation.

The method with the “flipping” technique is used as a validation test of the simulation. It shows that the Monte Carlo simulation is an appropriate way to study the background, whenever the “flipping” technique is used for the background definition, the contribution of background type (4) is added by using the simulation.

### 7.2.3 Monte Carlo Simulation of the Backgrounds

The generated Monte Carlo sample used for the study of the background, includes  $B\bar{B}$  ( $B^0\bar{B}^0$  and  $B^+B^-$ ) events and continuum  $c\bar{c}$  and  $uds$  events. The number of simulated  $B\bar{B}$  events is normalized according to the recorded data sample using the  $B$ -counting procedure. The  $c\bar{c}$  and  $uds$  events are added according to their cross sections [26]

Generated mode	$D_s^{*+} - \pi$				
	GTL+2GTVL	3 GTL	3 GTL	3 GTL	3 GTL
	$E_\gamma^* > 0$ no $\pi^0$ veto	$E_\gamma^* > 0$ no $\pi^0$ veto	$E_\gamma^* > 0.1$ no $\pi^0$ veto	$E_\gamma^* > 0$ $\pi^0$ veto	$E_\gamma^* > 0.1$ $\pi^0$ veto
$B^0 \rightarrow D_s^+ D^{*-}$	$7.5 \pm 0.6\%$	$5.9 \pm 0.5\%$	$3.5 \pm 0.4\%$	$2.7 \pm 0.4\%$	$1.7 \pm 0.3\%$
$B^0 \rightarrow D_s^{*+} D^{*-}$ (M)	$13.7 \pm 0.8\%$	$11.0 \pm 0.7\%$	$10.5 \pm 0.7\%$	$7.8 \pm 0.6\%$	$7.7 \pm 0.6\%$
SelfCrossFeed	$5.4 \pm 0.5\%$	$4.4 \pm 0.5\%$	$3.5 \pm 0.4\%$	$2.4 \pm 0.3\%$	$1.8 \pm 0.3\%$
$B^0 \rightarrow D_s^{*+} D^{*-}$ (L)	$14.4 \pm 0.4\%$	$11.4 \pm 0.4\%$	$11.0 \pm 0.3\%$	$7.7 \pm 0.3\%$	$7.4 \pm 0.3\%$
SelfCrossFeed	$5.8 \pm 0.3\%$	$4.6 \pm 0.2\%$	$3.6 \pm 0.2\%$	$1.9 \pm 0.1\%$	$1.6 \pm 0.1\%$
$B^0 \rightarrow D_s^{*+} D^{*-}$ (T)	$13.7 \pm 0.4\%$	$11.3 \pm 0.4\%$	$10.1 \pm 0.3\%$	$7.6 \pm 0.3\%$	$6.9 \pm 0.3$
SelfCrossFeed	$5.7 \pm 0.3\%$	$4.4 \pm 0.2\%$	$3.4 \pm 0.2\%$	$1.8 \pm 0.1\%$	$1.4 \pm 0.1\%$

Table 7.3: The reconstruction efficiency for the  $B^0 \rightarrow D_s^{*+} D^{*-}$  ( $D_s^+ \rightarrow \phi\pi^+$ ) decay mode. The self-cross feed as well as the  $B^0 \rightarrow D_s^+ D^{*-}$  cross feed efficiencies are shown for the different polarization.

Background	Flip $D_s^{(*)+}$	Side-bands	Side-bands flip $D_s^{(*)+}$
1. Fake $D_s^{(*)+} + \text{random } \pi$	<b>x</b>	<b>x</b>	<b>x</b>
2. Fake $D_s^{(*)+} + \text{correlated } \pi$		<b>x</b>	
3. True $D_s^{(*)+} + \text{random } \pi$	<b>x</b>		
4. True $D_s^{(*)+} + \text{correlated } \pi$			

Table 7.4: The different data samples which can be used to determine the background in the  $D^0$  signal region.

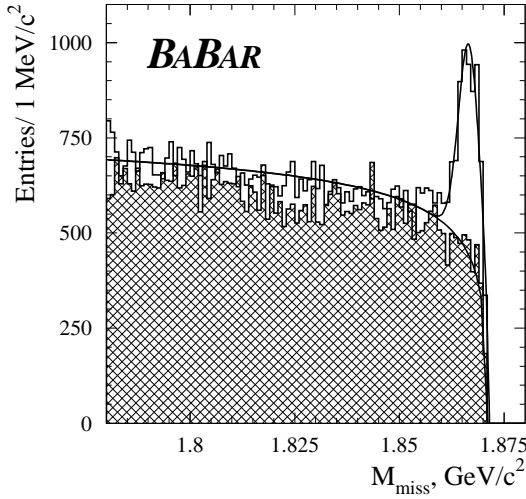


Figure 7.9: The missing mass distribution for the  $D_s^+ - \pi$  system obtained for the sum of three  $D_s^+$  decay channels. The hatched histogram corresponds to the combinatorial background which includes the types (1), (2) and (3) as described in the text.

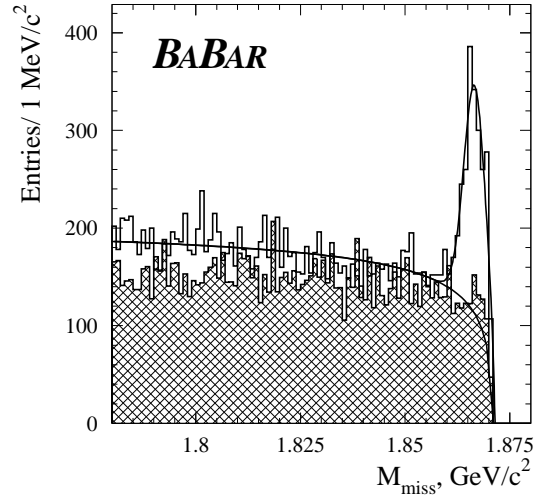


Figure 7.10: The missing mass distribution for the  $D_s^{*+} - \pi$  system obtained for the sum of three  $D_s^+$  decay channels. The hatched histogram corresponds to the combinatorial background which includes the types (1), (2) and (3) as described in the text.

presented in Table 7.5. Fig. 7.11 shows the missing mass distributions for data and Monte Carlo. The tight and loose selection of the soft photon for the  $D_s^{*+} - \pi$  system are shown separately. The different background contributions of the missing mass spectrum are also plotted as hatched histograms. One can see, that the dominant contribution arises from the  $B\bar{B}$  events. The enhancement at the end of the missing mass spectrum for the  $D_s^{*+} - \pi$  system is visible in the background distribution. It



$e^+e^- \rightarrow$	Cross section (nb)
$b\bar{b}$	1.05
$c\bar{c}$	1.30
$s\bar{s}$	0.35
$u\bar{u}$	1.39
$d\bar{d}$	0.35

Table 7.5: Production cross sections at  $\sqrt{s} = M(\Upsilon(4S))$ .

is due to the self-cross feed and the  $B^0 \rightarrow D_s^+ D^{*-}$  cross feed. The contribution from the  $B^0 \rightarrow D_s^{*+} D^{*-}$  cross feed is excluded for the  $D_s^+ - \pi$  spectrum.

The  $D_s^{(*)+} - \pi$  missing mass spectra obtained from the data sample are used as a control sample for the validation of the simulated background. The comparison of the data and the Monte Carlo simulation is performed for different combinations of  $D_s^{(*)+} - \pi$  candidate pairs: the  $D_s^{(*)+}$  signal region, the  $D_s^{(*)+}$  side-band region (SB), the same (wrong) sign  $D_s^{(*)+} - \pi$  combinations (WS) with the  $D_s^{(*)+}$  mass in the signal and side-band region. Figs 7.12- 7.14 show these comparisons.

The combination of a true  $D_s^+$  candidate originated from any of the  $B^0 \rightarrow D_s^{(*)+} D^{*-}$  channels with a fake photon is also present in the side-band region of the  $\Delta M$ . Therefore, the side-band distribution for the  $D_s^{*+} - \pi$  system has a peak in the signal region due to the self-cross feed and the  $B^0 \rightarrow D_s^+ D^{*-}$  cross feed. In order to quantify how well the Monte Carlo represents the data, the ratio (Data-Monte Carlo)/(Monte Carlo) is plotted for each histogram. The resulting histograms are then fitted with a straight line. Table 7.6 shows the values obtained from the fits. The missing mass region from 1.78 to 1.87 GeV/ $c^2$  is fitted for all distributions, except the signal sample, where the fit is performed in the range excluding the signal region (from 1.78 to 1.85 GeV/ $c^2$ ). Since the Monte Carlo simulation reproduces reasonably well both the shape and the absolute level for the missing mass spectra in the various types of combinations, one can conclude that the Monte Carlo describes well the background in the signal region.

A comparison of the background obtained by the combination of the flipped  $D_s^{(*)+}$  and  $D_s^{(*)+}$  side-band distributions with the overall background extracted from the Monte Carlo allows one to estimate the remaining contribution of type (4) (a true  $D_s^{(*)+}$  and a fake pion). We find  $2.1 \pm 2.2\%$  and  $10.8 \pm 2.8\%$  for the  $D_s^+ - \pi$  and  $D_s^{*+} - \pi$  system, respectively. The combinatorial background in the  $\Delta M$  spectrum is biased toward the  $D_s^{*+}$  signal peak due to the selection of the best  $D_s^{*+}$  candidate. It is important to note that since the combinatorial background in the  $\Delta M$  distribution is not flat, it

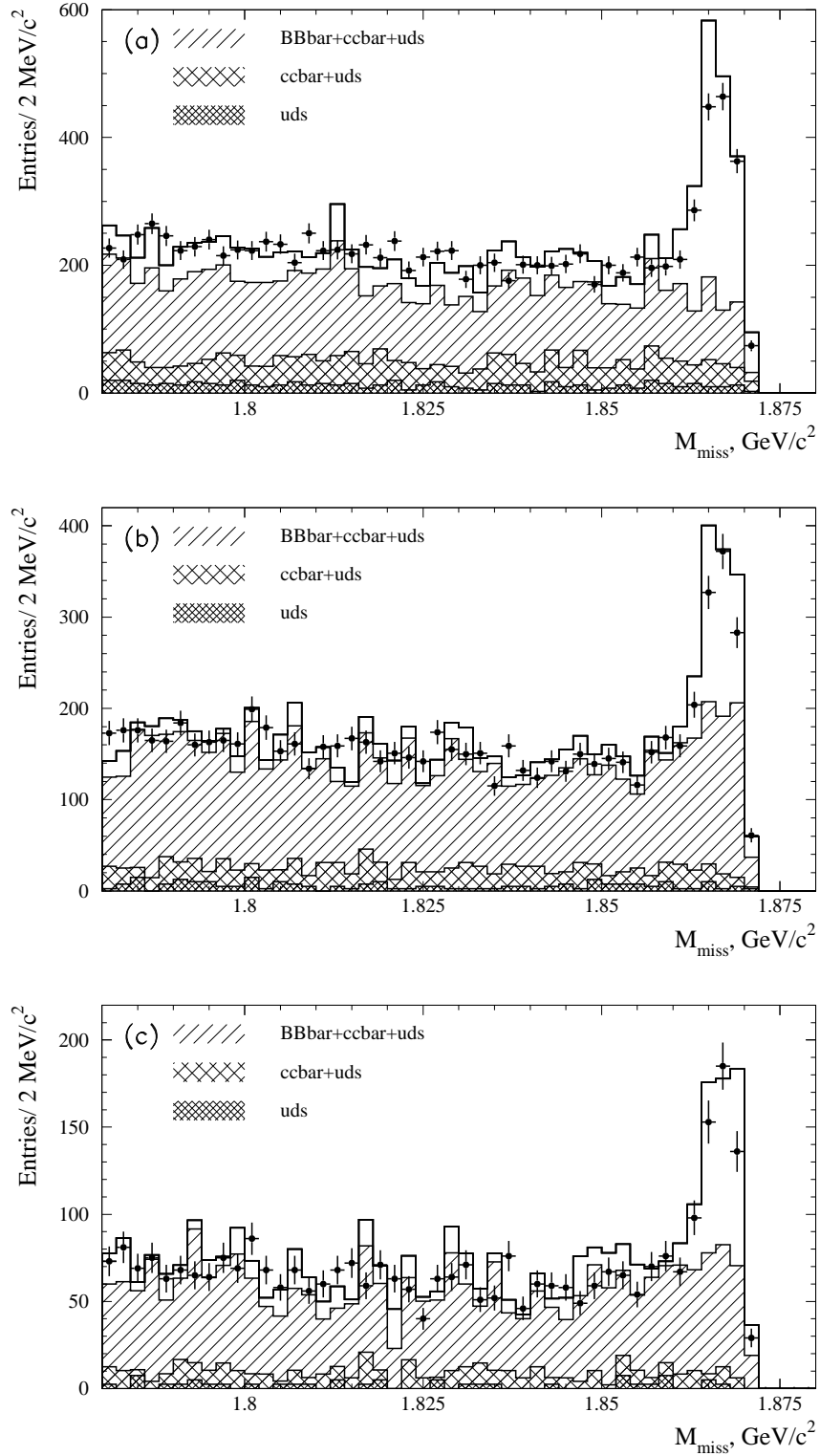


Figure 7.11: The missing mass distribution for the (a)  $D_s^+ - \pi$ , (b)  $D_s^{*+} - \pi$  (no  $\pi^0$  overlap,  $E_\gamma^* > 0$ ) (c)  $D_s^{*+} - \pi$  ( $\pi^0$  overlap,  $E_\gamma^* > 0.1 \text{ GeV}$ ) for data (dots) and Monte Carlo (histogram). The contributions from the  $B\bar{B}$ ,  $c\bar{c}$  and  $uds$  are shown separately.

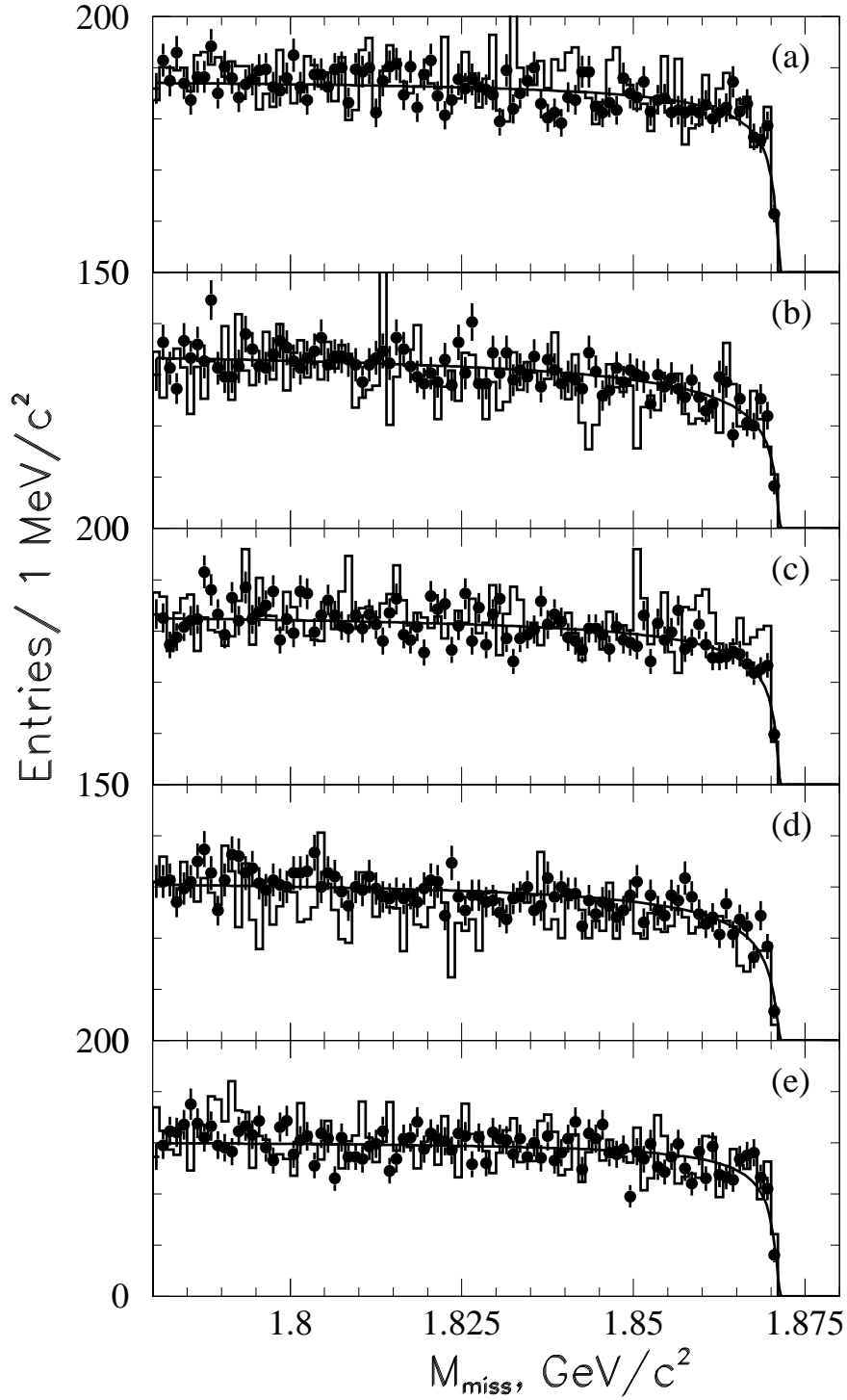


Figure 7.12: The missing mass distribution for the  $D_s^+ - \pi$  system for data (dots) and Monte Carlo (histogram) for five combinations: (a)  $D_s^+$  side-band region, (b) same sign combination for the  $D_s^+$  signal region, (c) same sign combination for the  $D_s^+$  side-band region, (d) flip  $D_s^+$  direction for the  $D_s^+$  signal region, (e) flip  $D_s^+$  direction for the  $D_s^+$  side-band region. The result of the fit using Eq. 7.2 is overlaid.

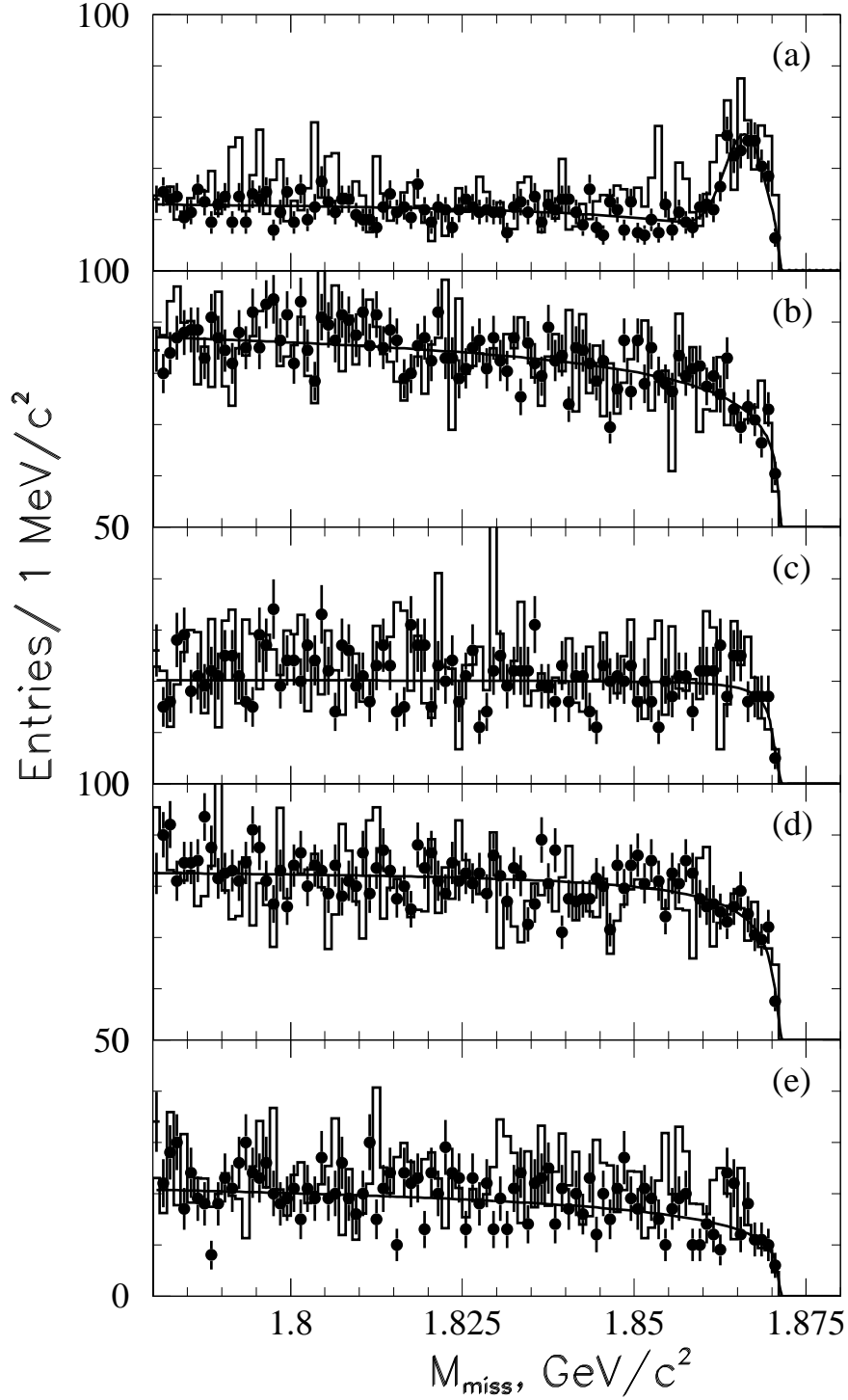


Figure 7.13: The missing mass distribution for the  $D_s^{*+} - \pi$  system for data (dots) and Monte Carlo (histogram) No  $\pi^0$  overlap and  $E_\gamma > 0$  are required. The following five combinations are shown: (a)  $D_s^{*+}$  side-band region, (b) same sign combination for the  $D_s^{*+}$  signal region, (c) same sign combination for the  $D_s^{*+}$  side-band region, (d) flip  $D_s^{*+}$  direction for the  $D_s^{*+}$  signal region, (e) flip  $D_s^{*+}$  direction for the  $D_s^{*+}$  side-band region. The result of the fit using Eq. 7.2 is overlaid.

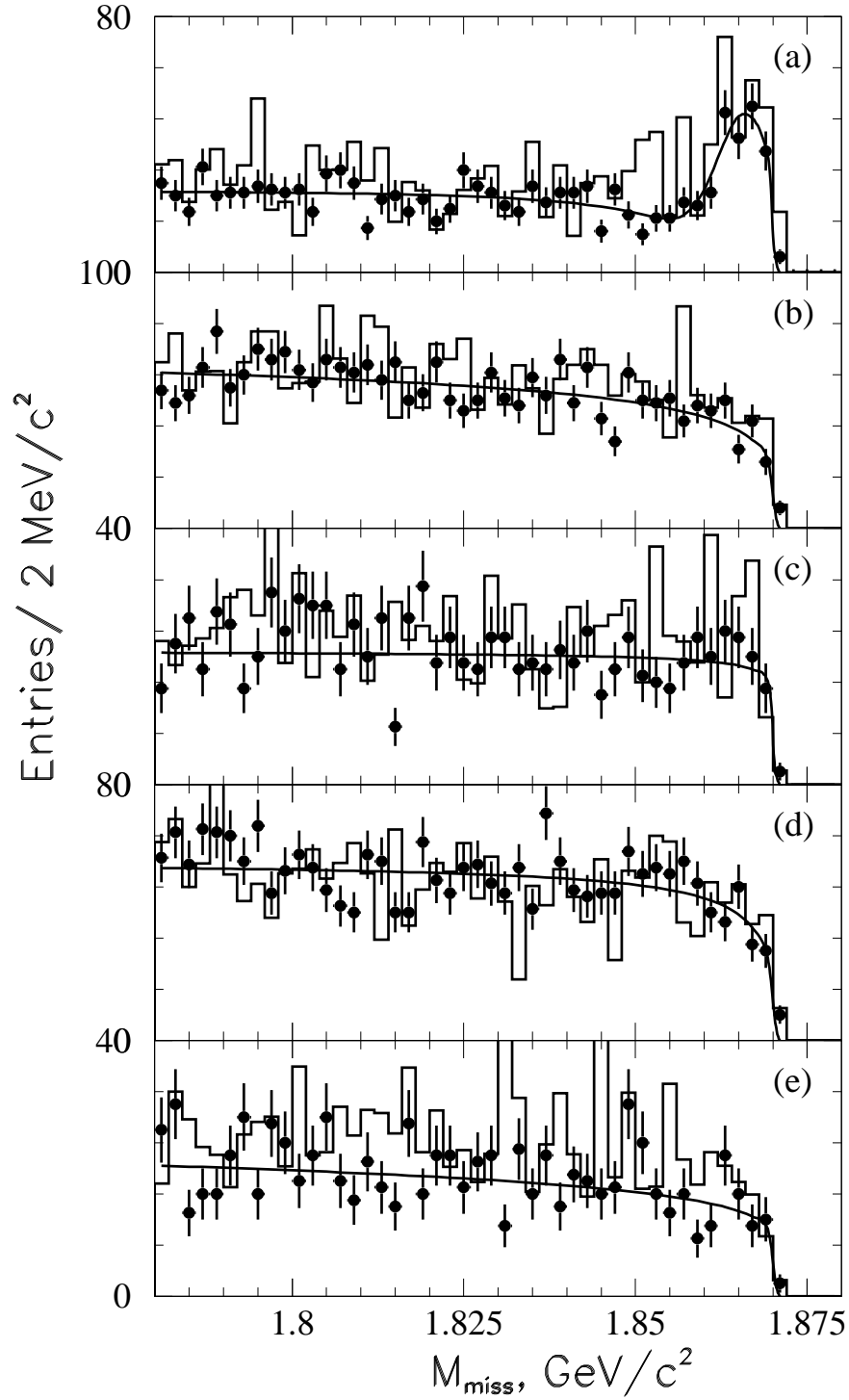


Figure 7.14: The missing mass distribution for the  $D_s^{*+} - \pi$  system for data (dots) and Monte Carlo (histogram) where  $\pi^0$  overlap and  $E_\gamma^* > 0.1$  GeV are required. The following five combinations are shown: (a)  $D_s^{*+}$  side-band region, (b) same sign combination for the  $D_s^{*+}$  signal region, (c) same sign combination for the  $D_s^{*+}$  side-band region, (d) flip  $D_s^{*+}$  direction for the  $D_s^{*+}$  signal region, (e) flip  $D_s^{*+}$  direction for the  $D_s^{*+}$  side-band region. The result of the fit using Eq. 7.2 is overlaid.

Sample type	$D_s^+ - \pi$	$D_s^{*+} - \pi$
$D_s^{(*)+}$ Signal	$-0.032 \pm 0.050$	$-0.031 \pm 0.057$
$D_s^{(*)+}$ SB	$-0.066 \pm 0.039$	$-0.031 \pm 0.074$
$D_s^{(*)+}$ Signal, WS	$0.028 \pm 0.055$	$-0.011 \pm 0.061$
$D_s^{(*)+}$ SB, WS	$-0.086 \pm 0.040$	$-0.179 \pm 0.087$
$D_s^{(*)+}$ Signal, Flip $D_s^{(*)+}$	$0.084 \pm 0.061$	$0.035 \pm 0.066$
SB, Flip $D_s^{(*)+}$	$-0.045 \pm 0.044$	$-0.211 \pm 0.086$
(1)+(2)+(3)	$-0.063 \pm 0.082$	$-0.073 \pm 0.071$
Average	$-0.036 \pm 0.018$	$-0.050 \pm 0.028$

Table 7.6: Average (Data-Monte Carlo)/(Monte Carlo) for the different  $D_s^{(*)+} - \pi$  combinations. The notations WS and SB mean a wrong sign combination and a side-band region, respectively.

is difficult to normalize properly the side-band to the signal distributions. Therefore, the extracted difference for the  $D_s^{*+} - \pi$  missing mass may include the effect due to a wrong normalization, while it should not for the  $D_s^+ - \pi$ . This might explain why the observed difference is consistent with zero for the  $D_s^+ - \pi$  while it is not for the  $D_s^{*+} - \pi$  system.

### 7.3 The $B^0 \rightarrow D_s^{(*)+} D^{*-}$ Decay Rates

In the case of absence of peaking backgrounds due to the (self) cross feed, the branching fractions can be calculated as\*

$$\mathcal{B}(B^0 \rightarrow D_s^{(*)+} D^{*-}) = \frac{1}{N_{B\bar{B}}} \frac{N_{D_s^{(*)+} D^{*-}}}{\mathcal{B}(D^{*-} \rightarrow D^0 \pi^-) \sum \epsilon_i \mathcal{B}_i} \quad (7.3)$$

where  $N_{B\bar{B}}$  is the number of produced  $B\bar{B}$  pairs,  $N_{D_s^{(*)+} D^{*-}}$  is the number of the observed signal events,  $\mathcal{B}_i$  is the branching fraction of the  $i$ th  $D_s^+$  decay mode, and  $\epsilon_i$  is the  $B^0 \rightarrow D_s^{(*)+} D^{*-}$  reconstruction efficiency for the  $i$ th  $D_s^+$  decay channel. In case of peaking background the formula is more complicated. One may write

---

\*Equal production of charged and neutral  $B$  mesons is assumed

$$\begin{cases} N_1 = N_0(\epsilon_{11}\mathcal{B}_1 + \epsilon_{12}\mathcal{B}_2) \\ N_2 = N_0[\epsilon_{21}\mathcal{B}_1 + (\epsilon_{22}\mathcal{B}(D_s^{*+} \rightarrow D_s^+\gamma) + \epsilon')\mathcal{B}_2], \end{cases} \quad (7.4)$$

where  $N_1, N_2$  are the number of the signal events for the  $D_s^+ - \pi$  and  $D_{spstar} - \pi$  systems, respectively,  $\mathcal{B}_1, \mathcal{B}_2$  are the branching fractions of  $B^0 \rightarrow D_s^+ D^{*-}$  and  $B^0 \rightarrow D_s^{*+} D^{*-}$ , respectively,  $\epsilon_{ij}$  are elements of the efficiency matrix where the signal efficiency is diagonal elements while the cross feed efficiency is non-diagonal,  $\epsilon'$  is an efficiency of the self-cross feed, and  $N_0 = N_{B\bar{B}}\mathcal{B}(D^{*-} \rightarrow D^0\pi^-) \sum \bar{\epsilon}_i \mathcal{B}_i$ , where  $\bar{\epsilon}_i$  is the  $D_s^+$  reconstruction efficiency relatively to the  $D_s^+ \rightarrow \phi\pi^+$  decay mode. From the equations above one has

$$\mathcal{B}_1 = \frac{N_2\epsilon_{12} - N_1\tilde{\epsilon}_{22}}{N_0\Delta} \quad (7.5)$$

$$\mathcal{B}_2 = \frac{N_1\epsilon_{21} - N_2\epsilon_{11}}{N_0\Delta} \quad (7.6)$$

where

$$\begin{aligned} \tilde{\epsilon}_{22} &= \epsilon_{22}\mathcal{B}(D_s^{*+} \rightarrow D_s^+\gamma) + \epsilon' \\ \Delta &= \epsilon_{12}\epsilon_{21} - \epsilon_{11}\tilde{\epsilon}_{22} \end{aligned} \quad (7.7)$$

With our selection criteria the efficiency matrix obtained from the Monte Carlo simulation (Table 7.7) is

$$\epsilon = \begin{pmatrix} 23.6 \pm 1.0 & 9.7 \pm 0.4 \\ 1.7 \pm 0.3 & 7.2 \pm 0.4 \end{pmatrix} \quad (7.8)$$

As a cross check of the stability of the result, the branching fractions of the  $B^0 \rightarrow D_s^{(*)+} D^{*-}$  decay modes for different track and photon selection criteria are calculated. They are presented in Table 7.8 using the  $D_s^+ \rightarrow \phi\pi^+$  mode. While the reconstruction efficiency can vary by as much as a factor two, the obtained results are consistent with each other within the statistical errors.

Using three  $D_s^+$  decay channels, the  $B^0 \rightarrow D_s^{(*)+} D^{*-}$  branching fractions corrected for the tracking and particle identification are determined to be

$$\mathcal{B}(B^0 \rightarrow D_s^+ D^{*-}) = (1.03 \pm 0.14 \pm 0.14 \pm 0.26)\%, \quad (7.9)$$

$$\mathcal{B}(B^0 \rightarrow D_s^{*+} D^{*-}) = (1.97 \pm 0.15 \pm 0.28 \pm 0.49)\%, \quad (7.10)$$

$$\Sigma\mathcal{B}(B^0 \rightarrow D_s^{(*)+} D^{*-}) = (3.00 \pm 0.19 \pm 0.38 \pm 0.75)\%, \quad (7.11)$$

where the first error is statistical, the second is systematic and the third error, which is dominant, is due to the  $D_s^+ \rightarrow \phi\pi^+$  branching ratio uncertainty. Table 7.9 presents

Generated mode	Reconstructed mode	
	$D_s^+ - \pi$	$D_s^{*+} - \pi$
$B^0 \rightarrow D_s^+ D^{*-}$	$23.6 \pm 1.0\%$	$1.7 \pm 0.3\%$
$B^0 \rightarrow D_s^{*+} D^{*-}$ (L)	$9.0 \pm 0.3\%$	$7.4 \pm 0.3\%$
Self-Cross Feed		$1.6 \pm 0.1\%$
$B^0 \rightarrow D_s^{*+} D^{*-}$ (T)	$10.4 \pm 0.3\%$	$6.9 \pm 0.3\%$
Self-Cross Feed		$1.4 \pm 0.1\%$

Table 7.7: Efficiencies for the partially reconstructed  $B^0 \rightarrow D_s^{(*)+} D^{*-}$  decay modes. The columns show the contribution of the different modes to the  $D_s^+ - \pi$  and  $D_s^{*+} - \pi$  missing mass distributions in the signal region.

Mode	GTL+2GTVL	3 GTL	3 GTL	3 GTL	3 GTL
	$E_\gamma^* > 0$ no $\pi^0$ veto	$E_\gamma^* > 0$ no $\pi^0$ veto	$E_\gamma^* > 0.1$ no $\pi^0$ veto	$E_\gamma^* > 0$ $\pi^0$ veto	$E_\gamma^* > 0.1$ $\pi^0$ veto
$B^0 \rightarrow D_s^+ D^{*-}$	$1.13 \pm 0.19$	$1.11 \pm 0.17$	$1.07 \pm 0.16$	$1.09 \pm 0.18$	$1.10 \pm 0.18$
$B^0 \rightarrow D_s^{*+} D^{*-}$	$1.76 \pm 0.21$	$1.65 \pm 0.19$	$1.75 \pm 0.15$	$1.79 \pm 0.29$	$1.75 \pm 0.27$

Table 7.8:  $B^0 \rightarrow D_s^{(*)+} D^{*-}$  ( $D_s^+ \rightarrow \phi\pi^+$ ) branching fractions in percent obtained with different track and photon selection criteria. Both tracking and neutral reconstruction as well as particle identification corrections are applied. Only statistical error is shown.

the measured branching fractions for each  $D_s^+$  decay mode and their average. An additional systematic error due to the uncertainty of the branching fraction relative to the  $D_s^+ \rightarrow \phi\pi^+$  mode is shown separately for the  $D_s^+ \rightarrow \bar{K}^{*0} K^+$  and  $D_s^+ \rightarrow \bar{K}^0 K^+$  decay modes.

## 7.4 Systematic Errors

The various contributions to the systematic error are summarized in Table 7.10. In particular, they include:

- The uncertainty due to the non-peaking *background subtraction*. To evaluate



Mode	$D_s^+ \rightarrow \phi\pi^+$	$D_s^+ \rightarrow \bar{K}^{*0}K^+$	$D_s^+ \rightarrow \bar{K}^0K^+$	Average
$B^0 \rightarrow D_s^+ D^{*-}$	$1.10 \pm 0.18$	$1.07 \pm 0.18 \pm 0.11$	$0.68 \pm 0.26 \pm 0.17$	$1.03 \pm 0.14 \pm 0.11$
$B^0 \rightarrow D_s^{*+} D^{*-}$	$1.75 \pm 0.27$	$2.20 \pm 0.24 \pm 0.23$	$1.65 \pm 0.35 \pm 0.41$	$1.97 \pm 0.15 \pm 0.20$

Table 7.9:  $B^0 \rightarrow D_s^{(*)+} D^{*-}$  branching fractions in percent obtained for each  $D_s^+$  mode. Both tracking and neutral reconstruction as well as particle identification corrections are applied. The first error is statistical, the second is due to the relative branching fraction uncertainty.

Source	Error (%)	
	$B^0 \rightarrow D_s^+ D^{*-}$	$B^0 \rightarrow D_s^{*+} D^{*-}$
Background subtraction	3.2	3.2
Monte Carlo statistics	4.2	6.0
Polarization uncertainty	0.8	0.5
Cross Feed	3.2	2.4
Total yield	6.2	7.2
$N_{B\bar{B}}$	1.6	1.6
$\mathcal{B}(\phi \rightarrow K^+ K^-)$	1.6	1.6
Particle identification	1.0	1.0
Tracking efficiency	3.6	3.6
Soft pion efficiency	2.0	2.0
Relative branchings	10.2	10.2
$\mathcal{B}(D_s^{*+} \rightarrow D_s^+ \gamma)$		2.7
Photon efficiency		1.3
$\pi^0$ veto		2.7
Systematic error	11.7	12.3
Total systematic error	13.2	14.3

Table 7.10: Systematic errors for  $\mathcal{B}(B^0 \rightarrow D_s^{(*)+} D^{*-})$ .

this, the number of the signal events is obtained assuming different background definitions. The extracted signal yield from the fit is compared with the one obtained by counting the number of events in the histogram after subtracting bin-by-bin the background determined from the Monte Carlo simulation and from the “flipping” technique. Using this method, the systematic error due to a possible deviation of the signal shape from a Gaussian is included.

- A variation of the detection efficiency of the  $B^0 \rightarrow D_s^{*+} D^{*-}$  mode contributing to both the  $D_s^+ - \pi$  and the  $D_s^{*+} - \pi$  missing mass is determined by varying within  $1\sigma$  the measured polarization. It gives the systematic error due to *polarization uncertainty*.
- The uncertainty of the *cross feed* efficiency due to the limited Monte Carlo statistic. Since the sum of the *self-cross feed* and detection efficiency actually contributes to the calculated branching fraction of the  $B^0 \rightarrow D_s^{*+} D^{*-}$  mode, the systematic error due to this type of background vanishes.
- One of the dominant systematic errors is associated with the uncertainty of the detection efficiency of charged tracks. It is accounted in the following manner. The tracking efficiency error of 1.2% per track is assumed for the decay chain  $D_s^+ \rightarrow \phi \pi^+$ ,  $\phi \rightarrow K^+ K^-$ . An additional 1.6% is added in quadrature for the slow pion from  $D^{*+} \rightarrow D^0 \pi^+$ , bringing the total systematic error for the slow pion to 2%. This arises because the tracking efficiency diminishes sharply at low momentum. The tracking errors are added linearly except for the additional 1.6% for the slow pion.
- The dominant systematic error is due to the  $D_s^+ \rightarrow \bar{K}^{*0} K^+$  and  $D_s^+ \rightarrow \bar{K}^0 K^+$  *branching fractions* uncertainty relative to the  $D_s^+ \rightarrow \phi \pi^+$  mode. In the present analysis the rates  $(0.95 \pm 0.10)\%$  and  $(1.01 \pm 0.25)\%$  are used, respectively [8].

## 7.5 Polarization Measurement

### 7.5.1 $B^0 \rightarrow D_s^{*+} D^{*-}$ Angular Distributions

The angular distribution of  $B^0 \rightarrow D_s^{*+} D^{*-}$  decay can be described by three angles: the helicity angle of the soft photon  $\theta_\gamma$ , the helicity angle of the slow pion  $\theta_\pi$ , and the transversity angle  $\phi_{tr}$ . The  $\theta_\gamma$  is defined as the angle in the  $D_s^+$  rest frame between the direction of the gamma and the  $D^{*-}$  direction. The  $\theta_\pi$  is the angle in the  $D^{*-}$  rest frame between the direction of the pion and the  $D_s^+$  direction. The  $\phi_{tr}$  is the angle between the decay planes of  $D_s^{*+}$  and  $D^{*-}$  in the  $B$  rest frame. Since the  $B$  meson is a spin-zero particle, and its daughters  $D_s^{*+}$  and  $D^{*-}$  are spin-one particles, they must have equal helicities ( $\lambda$ ) in the rest frames. Using the helicity formalism [59],

the final state of the pseudoscalar meson decay into two vector mesons is a coherent superposition of three possible helicity states where both  $D_s^{*+}$  and  $D^{*-}$  are in helicity 0 states (longitudinal polarization), both in helicity +1 state and both in helicity -1 state (transverse polarization). Using the angles defined above the amplitude  $A(B^0 \rightarrow D_s^{*+} D^{*-})$  can be expressed in terms of  $D$ -functions:

$$\sum_{\alpha=\pm 1} |A|^2 = \sum_{\alpha=\pm 1} \left| \sum_{\lambda=\pm 1,0} D_{\lambda,0}^{1*} D_{\lambda,\alpha}^{1*} H_{\lambda} \right|^2 \propto \sum_{\alpha=\pm 1} \left| \sum_{\lambda=\pm 1,0} e^{i\lambda\phi_{tr}} d_{\lambda,0}^1(\theta_{\pi}) d_{\lambda,\alpha}^1(\theta_{\gamma}) H_{\lambda} \right|^2 \quad (7.12)$$

where  $\alpha$  accounts for the allowed helicities of the real photon from  $D_s^{*+}$ . Using the definition of  $d$ -functions the angular distribution can be written as

$$\begin{aligned} & \frac{9}{32\pi} \left| H_0 \cos \theta_{\pi} \sin \theta_{\gamma} + H_+ \sin \theta_{\pi} \frac{1 + \cos \theta_{\gamma}}{2} e^{i\phi_{tr}} + H_- \sin \theta_{\pi} \frac{1 - \cos \theta_{\gamma}}{2} e^{-i\phi_{tr}} \right|^2 \\ & + \frac{9}{32\pi} \left| H_0 \cos \theta_{\pi} \sin \theta_{\gamma} + H_+ \sin \theta_{\pi} \frac{1 - \cos \theta_{\gamma}}{2} e^{i\phi_{tr}} + H_- \sin \theta_{\pi} \frac{1 + \cos \theta_{\gamma}}{2} e^{-i\phi_{tr}} \right|^2 \end{aligned} \quad (7.13)$$

where the complex amplitudes  $H_+$ ,  $H_0$  and  $H_-$  represent the contribution of helicity +1, 0, -1 states. Integrating over the angle  $\phi_{tr}$ , which can take values from 0 to  $2\pi$ , one obtains [26]

$$\frac{d^2\Gamma}{d \cos \theta_{\pi} d \cos \theta_{\gamma}} \propto |H_0|^2 \cos^2 \theta_{\pi} \sin^2 \theta_{\gamma} + (|H_+|^2 + |H_-|^2) \sin^2 \theta_{\pi} \frac{1 + \cos^2 \theta_{\gamma}}{4}. \quad (7.14)$$

The longitudinal and transverse polarizations are defined as

$$R_0 \equiv \frac{\Gamma_L}{\Gamma} = \frac{|H_0|^2}{|H_0|^2 + |H_+|^2 + |H_-|^2}, \quad \Gamma_T = \Gamma - \Gamma_L. \quad (7.15)$$

Thus, two parameters  $\theta_{\pi}$  and  $\theta_{\gamma}$  are sufficient to determine the longitudinal polarization. Integrating Eq. 7.14 over  $\cos \theta_{\gamma}$  on the one hand and over  $\cos \theta_{\pi}$  on the other hand, the angular distributions for two projections are obtained:

$$\frac{1}{\Gamma} \frac{d\Gamma}{d \cos \theta_{\pi}} = A \left( \cos^2 \theta_{\pi} + p \frac{\sin^2 \theta_{\pi}}{2} \right) = A \left( \cos^2 \theta_{\pi} + \frac{1 - R_0}{R_0} \frac{1 - \cos^2 \theta_{\pi}}{2} \right). \quad (7.16)$$

$$\frac{1}{\Gamma} \frac{d\Gamma}{d \cos \theta_{\gamma}} = A \left( \frac{\sin^2 \theta_{\gamma}}{2} + p \frac{1 + \cos^2 \theta_{\gamma}}{4} \right) = \frac{A}{4} \left[ 2(1 - \cos^2 \theta_{\gamma}) + \frac{1 - R_0}{R_0} (1 + \cos^2 \theta_{\gamma}) \right] \quad (7.17)$$

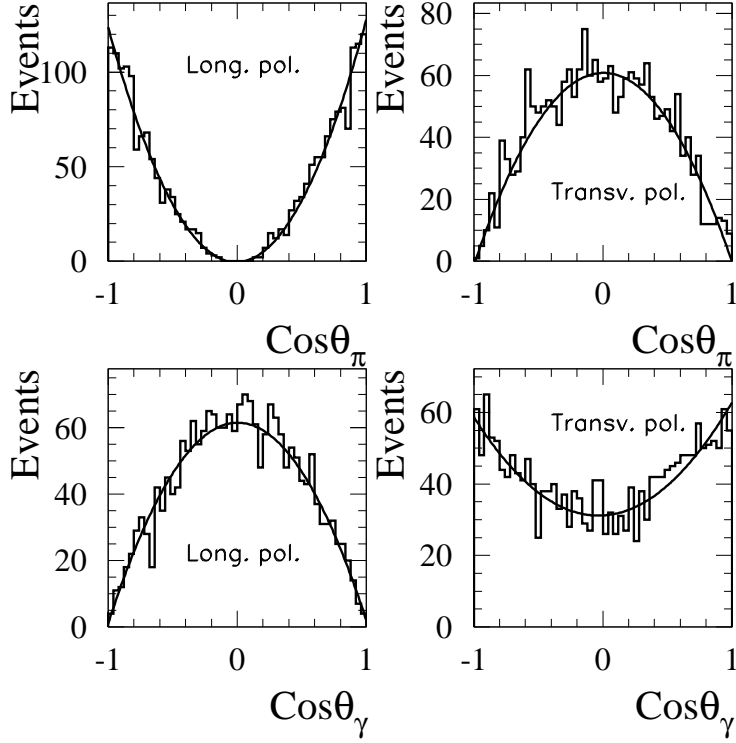


Figure 7.15: Angular distributions for the  $B^0 \rightarrow D_s^{(*)+} D^{*-}$  generated events.

where

$$p = \frac{\Gamma - \Gamma_L}{\Gamma_L} = \frac{1 - R_0}{R_0}. \quad (7.18)$$

Indeed, using the generated  $B^0 \rightarrow D_s^{(*)+} D^{*-}$  signal with longitudinal and transverse polarization, one observes the distributions shown in Fig 7.15 for  $\cos \theta_\gamma$  and  $\cos \theta_\pi$ . Table 7.11 summarizes the functions which describes the helicity angles for these two extreme cases. Thus, weighting this functions according to  $\Gamma_L$  and  $\Gamma_T$  one can obtain the formula given in Eqs. 7.16, 7.17.

### 7.5.2 Extracting Angular Distributions

To reduce the contribution of the self-cross feed and the  $B^0 \rightarrow D_s^+ D^{*-}$  cross feed to the signal peak, the measurement of the polarization in  $B^0 \rightarrow D_s^{(*)+} D^{*-}$  decay is performed by requiring the tight selection for the soft photon: the photon candidate should not form a  $\pi^0$ , when combined with any other photon in the event, and its energy in the center-of-mass  $E_\gamma^* > 0.1$  GeV.

Helicity angle	V polarization	
	Longitudinal	Transverse
$\theta_\pi (V \rightarrow PP)$	$\cos^2 \theta_\pi$	$\frac{1}{2} \sin^2 \theta_\pi$
$\theta_\gamma (V \rightarrow VP)$	$\frac{1}{2} \sin^2 \theta_\gamma$	$\frac{1}{4}(1 + \cos^2 \theta_\gamma)$

Table 7.11: The functions describing the longitudinal and the transverse polarization of the vector meson for the different types of decays.

The  $D_s^{*+} - \pi$  events whose calculated missing mass is in the signal region ( $M_{miss} > 1.86 \text{ GeV}/c^2$ ), are selected for the angular analysis. For each  $D_s^{*+} - \pi$  candidate the helicity angles are calculated. Since the  $D^0$  meson is not reconstructed, the only way to define  $\theta_\gamma$  and  $\theta_\pi$  is to fix its mass at the nominal value [8]. The two dimensional distribution  $(\cos \theta_\gamma, \cos \theta_\pi)$  is divided in five regions in each dimension. The resulting distribution is shown in Fig. 7.16

The same two angles are calculated for each background candidate found in the signal region. For the central value of the polarization, the background is obtained using the Monte Carlo  $B\bar{B}$ ,  $c\bar{c}$ ,  $uds$  events. This allows us to include into the background sample both the self-cross feed and the  $B^0 \rightarrow D_s^+ D^{*-}$  cross feed events. The number of the background events as a function of the helicity angles scaled according to the data/Monte Carlo factor is presented in Table 7.13. As a cross check of the result, the background obtained using the  $D_s^{*+}$  flipping and the side-bands technique is found. This technique also allows us to include into the background sample the self-cross feed and the  $B^0 \rightarrow D_s^+ D^{*-}$  cross feed events. The signal  $B^0 \rightarrow D_s^{*+} D^{*-}$  angular distribution are obtained by subtraction bin-by-bin the background events from the distribution found for all events in the signal region.

Since the detector is not an ideal device, its acceptance is not uniform. Therefore, the observed angular distributions need to be corrected for efficiency, which is a function of the helicity angles. Using the Monte Carlo signal events, generated with the longitudinal and transverse polarization separately, the reconstruction efficiency as a function of the angles  $\theta_\pi$  and  $\theta_\gamma$  is determined. Fig. 7.17 and Table 7.12 show the result for a two-dimensional efficiency mapping. The signal angular distributions are corrected bin-by-bin for the efficiency. The efficiency-corrected signal distribution is shown in Fig. 7.14.

The momentum of the photon in the laboratory frame depends on its helicity angle. The angle  $\theta_\gamma$  close to zero ( $\cos \theta_\gamma \simeq 1$ ) corresponds to the photon direction which is opposite to the  $D_s^{*+}$  boost. Therefore, the energy of the photon is minimal and hence the efficiency is the lowest for this angle.

$\cos \theta_\gamma$					
1.0	18	14	17	15	17
0.6	33	30	25	30	33
0.2	37	48	40	45	46
-0.2	40	37	35	37	39
-0.6	35	33	37	27	22
-1.0	-0.6	-0.2	0.2	0.6	1.0
	$\cos \theta_\pi$				

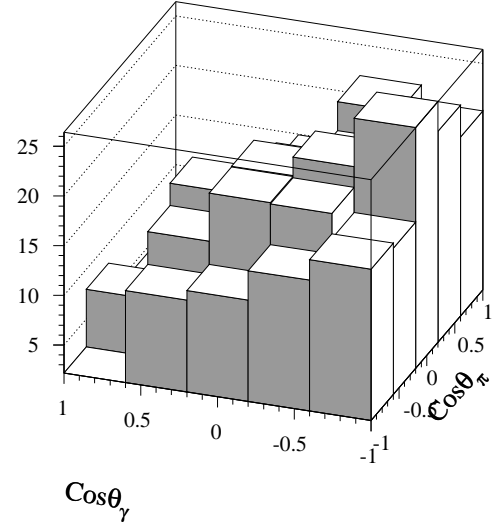


Figure 7.16: Number of events in the signal region as a function of the helicity angles  $\theta_\pi$ ,  $\theta_\gamma$ .

Figure 7.17: Efficiency as a function of the helicity angles  $\theta_\pi$ ,  $\theta_\gamma$ .

$\cos \theta_\gamma$					
1.0	$2.2 \pm 0.8$	$8.0 \pm 1.7$	$4.4 \pm 1.1$	$4.4 \pm 1.1$	$6.1 \pm 1.4$
0.6	$11.4 \pm 1.7$	$14.7 \pm 2.5$	$17.0 \pm 3.4$	$11.2 \pm 1.9$	$8.2 \pm 1.3$
0.2	$12.4 \pm 1.6$	$19.6 \pm 2.9$	$19.7 \pm 3.3$	$16.8 \pm 2.5$	$14.9 \pm 1.9$
-0.2	$15.4 \pm 1.9$	$19.5 \pm 2.7$	$21.5 \pm 3.4$	$19.0 \pm 2.7$	$21.9 \pm 2.5$
-0.6	$17.4 \pm 2.5$	$16.9 \pm 2.5$	$26.4 \pm 3.6$	$23.4 \pm 3.2$	$20.2 \pm 2.8$
-1.0	-0.6	-0.2	0.2	0.6	1.0
	$\cos \theta_\pi$				

Table 7.12: Efficiency in percents as a function of the helicity angles  $\theta_\pi$ ,  $\theta_\gamma$ .

### 7.5.3 Result and Systematic Errors

Once the background level have been determined, a two-dimensional binned minimum- $\chi^2$  fit is applied for the signal distribution using Eq. 7.14. The resulting fit has a  $\chi^2$  of 23.1 for 25 bins with 2 floating parameters. Fig 7.18 shows the data and the result of the fit as projections along  $\cos \theta_\gamma$  and  $\cos \theta_\pi$  axis. The fraction of a longitudinal

$\cos \theta_\gamma$					
1.0	$11.7 \pm 5.2$	$15.7 \pm 6.0$	$13.1 \pm 5.3$	$4.7 \pm 3.3$	$6.4 \pm 3.7$
0.6	$20.7 \pm 6.9$	$4.7 \pm 3.3$	$14.7 \pm 5.6$	$20.1 \pm 6.7$	$12.6 \pm 5.2$
0.2	$11.4 \pm 5.1$	$10.2 \pm 4.6$	$14.6 \pm 5.5$	$28.8 \pm 8.0$	$4.7 \pm 3.3$
-0.2	$10.3 \pm 4.6$	$18.1 \pm 6.4$	$17.7 \pm 6.3$	$10.3 \pm 4.6$	$8.1 \pm 4.0$
-0.6	$12.4 \pm 5.1$	$8.6 \pm 4.3$	$14.9 \pm 5.7$	$6.0 \pm 3.4$	$8.9 \pm 4.5$
-1.0	-0.6	-0.2	0.2	0.6	1.0
	$\cos \theta_\pi$				

Table 7.13: Number of the background events in the signal region as a function of the helicity angles  $\theta_\pi$ ,  $\theta_\gamma$  obtained from the Monte Carlo simulation.

$\cos \theta_\gamma$					
1.0	$289.0 \pm 325.7$	$-21.5 \pm 89.3$	$90.4 \pm 159.6$	$234.1 \pm 130.0$	$174.2 \pm 100.8$
0.6	$107.3 \pm 80.5$	$171.8 \pm 52.3$	$60.3 \pm 46.9$	$88.2 \pm 79.7$	$249.1 \pm 104.3$
0.2	$206.7 \pm 69.7$	$193.0 \pm 51.8$	$129.3 \pm 49.0$	$96.6 \pm 64.9$	$276.9 \pm 61.2$
-0.2	$193.3 \pm 57.2$	$97.4 \pm 47.7$	$80.2 \pm 42.5$	$140.8 \pm 46.0$	$141.6 \pm 38.4$
-0.6	$129.3 \pm 49.6$	$144.1 \pm 48.2$	$83.7 \pm 34.0$	$89.9 \pm 30.0$	$64.6 \pm 33.7$
-1.0	-0.6	-0.2	0.2	0.6	1.0
	$\cos \theta_\pi$				

Table 7.14: Number of signal events as a function of  $\cos \theta_\gamma$ ,  $\cos \theta_\pi$  efficiency-corrected.

polarization is determined to be

$$\Gamma_L/\Gamma = 51.9 \pm 5.0 \pm 2.8\%. \quad (7.19)$$

where the first error is statistical, the second is systematic. The systematic error comes from our level of understanding of the background. To evaluate this error a different procedure for the background subtraction is used. The following procedure is applied to obtain the systematic errors listed in Table 7.15:

- The *background subtraction* error is due to the possible difference between the background level in the data and in the Monte Carlo. The variation of the fit

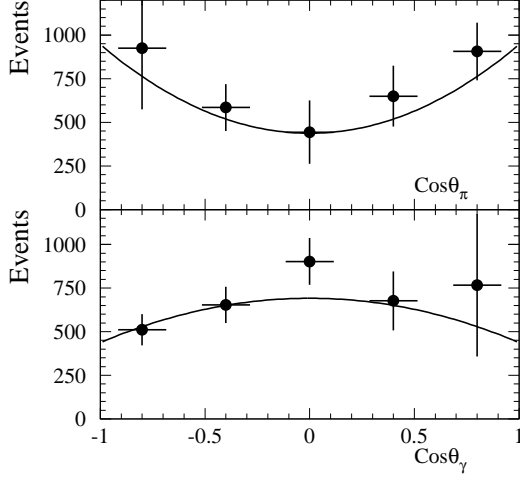


Figure 7.18: Projection of the number of events on the  $\cos \theta_\gamma$  and  $\cos \theta_\pi$  axis. The result of the two-dimensional fit is overlaid. The background is obtained from the Monte Carlo simulation.

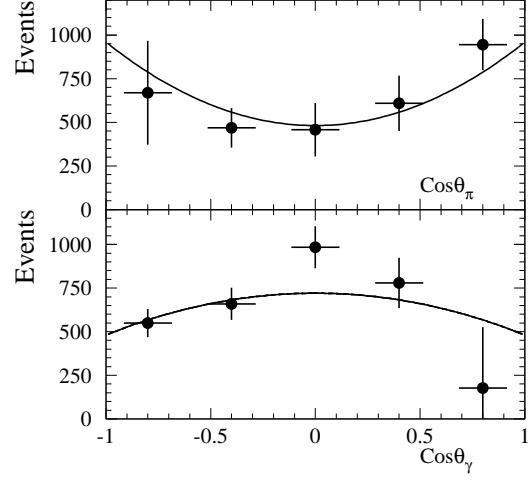


Figure 7.19: Projection of the number of events on the  $\cos \theta_\gamma$  and  $\cos \theta_\pi$  axis. The result of the two-dimensional fit is overlaid. The background is obtained using the  $D_s^{*+}$  flipping and the side-bands technique.

Source	$\sigma(\Gamma_L/\Gamma)$ , %
Background subtraction	0.48
Monte Carlo statistics	2.74
Particle identification	0.10
Tracking efficiency	0.46
Soft pion efficiency	0.16
Photon efficiency	0.12
$\pi^0$ veto	0.26
Total	2.84

Table 7.15: Systematic errors for  $\Gamma_L/\Gamma$ .

result by changing of the background level according to the average difference between data and Monte Carlo (see Table 7.6), is accounted as a systematic



error.

- *Monte Carlo statistics* is the error which accounts the efficiency uncertainty due to limited Monte Carlo statistics.
- Since the background is determined from the Monte Carlo simulation, the uncertainties between the data and the Monte Carlo such as *tracking, photon, particle identification and  $\pi^0$  overlap* efficiencies are the sources of the systematic errors. The variation of the fit result by changing of the background level according to the corresponding errors (see Table 7.10), is assigned as the systematic error.

As a cross check, the fraction of the longitudinal polarization is extracted from the fit where the background is obtained using the  $D_s^{*+}$  flipping and the side-bands technique. One obtains

$$\Gamma_L/\Gamma = 49.9 \pm 4.7 \pm 3.5\%. \quad (7.20)$$

Fig 7.19 shows the result of the fit as projections along  $\cos\theta_\gamma$  and  $\cos\theta_\pi$  axis. Additional systematic error of 2.1% is assumed due to knowledge of true  $D_s^{*+}$  + correlated  $\pi$  background, which can not be extracted with this technique. As shown in section 7.2.3 using the generated  $B\bar{B}$  and  $q\bar{q}$  events, the fraction of this kind of background is determined to be  $10.8 \pm 2.8\%$ . The error is defined from the fit by variation of the background level according to the fraction of the unmeasured type. As conclusion, this result is consistent within error with Eq. 7.19.

## 7.6 Prospect for the $D_s^+ \rightarrow \phi\pi^+$ Branching Fraction Measurement

As shown, the uncertainty in the  $D_s^+ \rightarrow \phi\pi^+$  branching fraction is the dominant systematic error for all measurements of the branching fractions involving  $D_s^{(*)+}$  mesons. The 1994 version of the Particle Data Book [60] lists  $\mathcal{B}(D_s^+ \rightarrow \phi\pi^+) = (3.5 \pm 0.4)\%$ . However, this value is based mainly on measurements of  $\Gamma(D_s^+ \rightarrow \phi\pi^+)/\Gamma(D_s^+ \rightarrow \phi l^+ \nu)$ . This is done by assuming that  $\Gamma(D_s^+ \rightarrow \phi l^+ \nu)$  and  $\Gamma(D^+ \rightarrow K^* l^+ \nu)$  are equal up to a small theoretical corrections. The *CLEO* measurement [61] of the absolute branching fraction ( $\mathcal{B}(D_s^+ \rightarrow \phi\pi^+) = (3.6 \pm 0.9)\%$ ) does not rely on this theoretical assumption. It is done using the partial reconstruction technique for the  $B^0 \rightarrow D_s^{*+} D^{*-}$  decay mode. Indeed, this channel can be reconstructed partially in two different ways:

- (1) The fully reconstructed  $D^{*-}$  is associated with the soft photon from  $D_s^{*+} \rightarrow D_s^+ \gamma$  decay. In this case, the missing mass has to be peaked at  $D_s^+$  mass if the decay  $B^0 \rightarrow D_s^{*+} D^{*-}$  indeed occurred. The measured yield is independent on the  $D_s^+ \rightarrow \phi\pi^+$  branching fraction.

- (2) The fully reconstructed  $D_s^{*+}$  is associated with the soft pion from  $D^{*-} \rightarrow D^0 \pi^-$  decay. The missing mass is peaked at  $D^0$  mass for the signal.

Combining the result from method (1) with the one obtained in the present analysis (2), one is able to extract the  $D_s^+ \rightarrow \phi \pi^+$  branching fraction. One needs to note, that indeed the  $D_s^+ \rightarrow \phi \pi^+$  branching fraction relatively to  $D^0 \rightarrow K^- \pi^+$  is measured, which is much more precise.

## 7.7 Summary

The decays  $B^0 \rightarrow D_s^+ D^{*-}$  and  $B^0 \rightarrow D_s^{*+} D^{*-}$  have been observed using a partial reconstruction technique and the following branching fractions have been determined:

$$\mathcal{B}(B^0 \rightarrow D_s^+ D^{*-}) = (1.03 \pm 0.14 \pm 0.14 \pm 0.26)\% , \quad (7.21)$$

$$\mathcal{B}(B^0 \rightarrow D_s^{*+} D^{*-}) = (1.97 \pm 0.15 \pm 0.28 \pm 0.49)\% , \quad (7.22)$$

$$\Sigma \mathcal{B}(B^0 \rightarrow D_s^{(*)+} D^{*-}) = (3.00 \pm 0.19 \pm 0.38 \pm 0.75)\% , \quad (7.23)$$

These values are consistent with the previous measurement presented in [55, 56]. From the angular analysis, the fraction of the longitudinal polarization in the  $B^0 \rightarrow D_s^{*+} D^{*-}$  decay channel has been measured:

$$\Gamma_L/\Gamma = 51.9 \pm 5.0 \pm 2.8\% . \quad (7.24)$$

This result is consistent with the CLEO [54] measurement of  $50.6 \pm 13.9 \pm 3.6\%$ .

## Chapter 8

# Comparison with Theory and Other Experiments

Let us first summarize the existing measurements of  $B \rightarrow D_s^+ X$  branching fraction since 1987 ([8]) including the preliminary result for  $B \rightarrow D_s^{(*)+} X$  obtained with the *BABAR* detector and presented at the XXX<sup>th</sup> International Conference on High Energy Physics in Osaka [62]. This result was obtained using  $7.7 \text{ fb}^{-1}$  on-resonance and  $1.2 \text{ fb}^{-1}$  off-resonance data samples.

The different measurements are shown in Fig. 8.1 using the same  $D_s^+ \rightarrow \phi\pi^+$  branch-

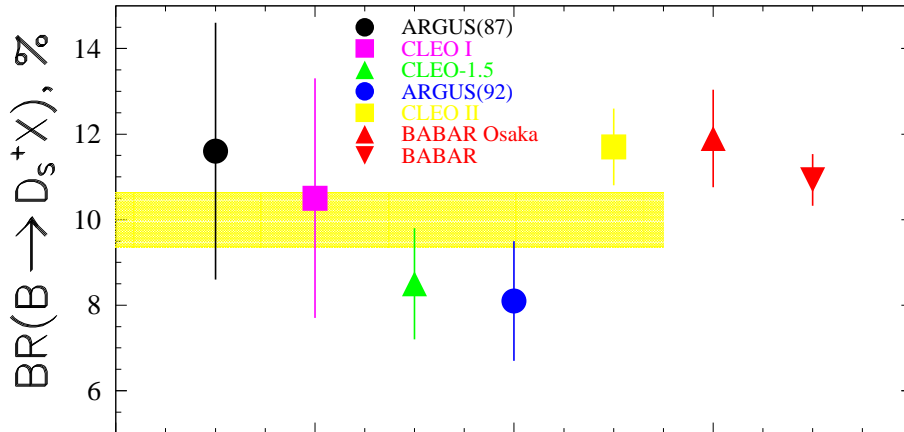


Figure 8.1: The inclusive  $D_s^+$  branching fraction from  $B$  decays obtained by different experiments. All values are normalized using  $\mathcal{B}(D_s^+ \rightarrow \phi\pi^+) = 3.6\%$ .

ing fraction  $(3.6 \pm 0.9)\%$ . The result obtained in this dissertation is consistent with the world average as well as the preliminary *BABAR* measurement. The dominant error in the *CLEO* and the preliminary *BABAR* results is due to the uncertainty in the tracking efficiency which is 2.5% per track. This leads to 7.5% per  $D_s^+$  candidate. In the present measurement not only statistical but also systematic error have been improved. This allowed us significantly increase the overall precision about a factor 2.

The measurement of the  $B \rightarrow D_s^{*+} X$  branching fraction has been obtained for the first time. This allowed us to measure the ratio

$$\frac{\mathcal{B}(B \rightarrow D_s^{*+} X_q)}{\mathcal{B}(B \rightarrow D_s^+ X_q)} = 0.73 \pm 0.08 \pm 0.06 \quad (8.1)$$

which is in a good agreement with the theoretical prediction 0.68 obtained in [35].

The calculation of the relative rate of the sum of two-body modes  $B \rightarrow D_s^{(*)+} \bar{D}^{(*)}$  presents some difficulties due to the uncertainty in the  $b$ -quark mass. Assuming factorization and  $4.4 \leq m_b \leq 5.2 \text{ GeV}/c^2$ , reference [41] predicts

$$\frac{\Sigma \mathcal{B}(B \rightarrow D_s^{(*)+} \bar{D}^{(*)})}{\mathcal{B}(B \rightarrow D_s^+ X)} = (70 \pm 20)\%. \quad (8.2)$$

The measured value  $(46.4 \pm 1.3 \pm 1.4 \pm 0.6)\%$  is consistent with this prediction.

Using the  $D_s^{(*)+}$  momentum spectra produced from continuum events we find that the Andersson fragmentation function offers the best parameterization of the hadronization process. It was shown in [63] by measuring of the  $D_s^{(*)+}$  momentum spectrum above  $x_p > 0.44$ , that the Andersson parameterization was better than the Peterson one. Several measurements of  $P_V$  for charm and bottom mesons are presented in Table 8.1. Since all these results are made using different methodology and center-of-mass energies, it is difficult to make a direct comparison between them. One can note, that the measurements of  $P_V(B)$  are rather consistent with the naive spin-counting expectation (0.75) while the ones for  $P_V(D_{(s)})$  give lower values. Our measurement of  $P_V$  is consistent within errors with experiments at the  $Z^0$  resonance and the spin-counting expectation. The result  $P_V(D_s) = 0.77 \pm 0.09 \pm 0.05$  deviates from the *CLEO* measurement reported in [63] by  $2.9\sigma$ . The *CLEO* result has some model dependence since one needs to extrapolate the result for full momentum range.

Table 8.2 summarizes the theoretical predictions for some ratios of the branching fractions. They are compared with the results obtained in this dissertation. Although some of these ratios differ from the predictions by more than  $2\sigma$ , it is not yet possible

at $Z^0$ resonance	
<i>ALEPH</i> [46]	$P_V(D) = 0.60 \pm 0.05$
<i>OPAL</i> [64]	$P_V(D) = 0.57 \pm 0.06$
<i>SLD</i> [65]	$P_V(D) = 0.57 \pm 0.06$
<i>L3</i> [66]	$P_V(B) = 0.76 \pm 0.10$
<i>OPAL</i> [67]	$P_V(B) = 0.76 \pm 0.09$
<i>ALEPH</i> [46]	$P_V(D_s) = 0.60 \pm 0.19$
at $\Upsilon(4S)$ resonance	
<i>CLEO</i> [63]	$P_V(D_s) = 0.45 \pm 0.05^*$
<i>BABAR</i> (this result)	
No parameterization	$P_V(D_s) = 0.77 \pm 0.09 \pm 0.05$
with Andersson function	$P_V(D_s) = 0.75 \pm 0.02 \pm 0.05$

Table 8.1: Results of previous measurements of  $P_V$  for heavy quark mesons at other experiments. The results obtained in this work are shown too. The *CLEO* result marked \* is model dependent. The  $P_V$  value is measured in the range  $x_p > 0.44$  and than extrapolated to the all momentum range using some theoretical assumption.

to state whether the factorization approach does or does not describe the experimental data. It is important to continue the studies with higher statistics.

The longitudinal polarization as a function of  $q^2$  is plotted in Fig. 8.2. It is compared with the existing measurements for  $D^*\rho$ ,  $D^*\rho'$ , and  $D_s^{*+}D^{*-}$ . The measured fraction of a longitudinal polarization in  $B^0 \rightarrow D_s^{*+}D^{*-}$  decay channel is  $51.9 \pm 5.0 \pm 2.8\%$ . It is in agreement with the *CLEO* measurement presented in [54] ( $50.6 \pm 13.9 \pm 3.6\%$ ). Averaging both experiments one obtains

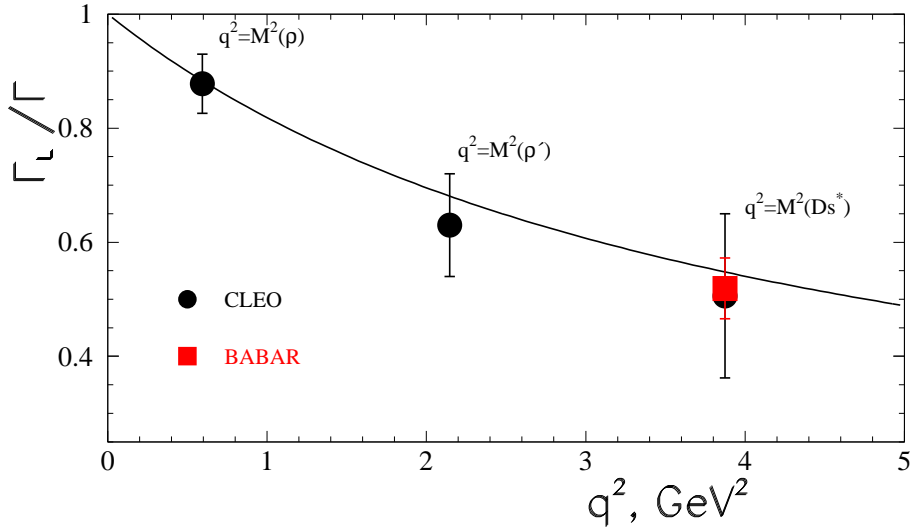
$$\frac{\Gamma_L}{\Gamma} = 51.7 \pm 5.3\% \quad (8.3)$$

where the error represents the quadratic sum of the statistical and the systematic errors. This result is consistent with the theoretical prediction ( $53.5 \pm 3.3\%$ ) assuming factorization, HQET, and the semileptonic form factor measurements [68].

In summary, all obtained results are consistent within errors with existing theoretical predictions and other experiments.

	$\frac{\mathcal{B}(B \rightarrow D_s^{*+} D^*)}{\mathcal{B}(B \rightarrow D_s^+ D^*)}$	$\frac{\mathcal{B}(B \rightarrow D_s^{*+} D^*)}{\Sigma \mathcal{B}(B \rightarrow D_s^{(*)+} D^{(*)})}$	$\frac{\Sigma \mathcal{B}(B \rightarrow D_s^{(*)+} D^*)}{\Sigma \mathcal{B}(B \rightarrow D_s^{(*)+} D^{(*)})}$	$\frac{\Sigma \mathcal{B}(B \rightarrow D_s^{*+} D^{(*)})}{\Sigma \mathcal{B}(B \rightarrow D_s^{(*)+} D^{(*)})}$
$f_{D_s^{*+}} = f_{D_s^+}$				
BSW [28]	3.63	0.44	0.57	0.60
Rosner [29]	2.59	0.43	0.59	0.60
Neubert [31]	2.66	0.43	0.59	0.60
$f_{D_s^{*+}} = 1.2 f_{D_s^+}$				
Neubert [31]	3.83	0.50	0.62	0.69
<i>BABAR</i>	$1.91 \pm 0.36$	$0.39 \pm 0.06$	$0.59 \pm 0.08$	$0.80 \pm 0.08$

Table 8.2: Comparison with theoretical prediction assuming factorization.

Figure 8.2: Factorization prediction for the fraction of the longitudinal polarization for the decays involving two vector mesons as a function of  $q^2$ . Dots are experimental results obtained with the *BABAR* and *CLEO* detectors.

# Chapter 9

## Conclusion

The production of  $D_s^{(*)+}$  at the  $\Upsilon(4S)$  energy (or 40 MeV below) has been studied with the *BABAR* detector. The measurements of the  $D_s^{(*)+}$  inclusive branching fractions and exclusive decays  $B^0 \rightarrow D_s^{*+} D^{*-}$  have been performed. Table 9.1 summarizes the highlights of the studies described in this dissertation.

The following cross sections have been found for the continuum:

$$\sigma(e^+e^- \rightarrow D_s^\pm X) \mathcal{B}(D_s^+ \rightarrow \phi\pi^+) = 7.55 \pm 0.20 \pm 0.34 \text{ pb} , \quad (9.1)$$

$$\sigma(e^+e^- \rightarrow D_s^{*\pm} X) \mathcal{B}(D_s^+ \rightarrow \phi\pi^+) = 5.79 \pm 0.66 \pm 0.50 \text{ pb} . \quad (9.2)$$

Using the on-resonance data, the following inclusive branching fraction for the  $B$  meson decays have been measured:

$$\mathcal{B}(B \rightarrow D_s^+ X) = \left[ (10.93 \pm 0.19 \pm 0.58) \times \frac{3.6 \pm 0.9\%}{\mathcal{B}(D_s^+ \rightarrow \phi\pi^+)} \right] \% , \quad (9.3)$$

$$\mathcal{B}(B \rightarrow D_s^{*+} X) = \left[ (7.9 \pm 0.8 \pm 0.7) \times \frac{3.6 \pm 0.9\%}{\mathcal{B}(D_s^+ \rightarrow \phi\pi^+)} \right] \% , \quad (9.4)$$

From the fit of the momentum spectrum, fraction of two-body modes  $B \rightarrow D_s^{(*)+} \bar{D}^{(*)}$  relative to the total  $D_s^+$  inclusive rate is obtained:

$$\frac{\Sigma \mathcal{B}(B \rightarrow D_s^{(*)+} \bar{D}^{(*)})}{\mathcal{B}(B \rightarrow D_s^+ X)} = (46.4 \pm 1.3 \pm 1.4 \pm 0.6) \% . \quad (9.5)$$

Using the  $D_s^{*+}$  momentum spectrum, we find

$$\frac{\Sigma \mathcal{B}(B \rightarrow D_s^{*+} \bar{D}^{(*)})}{\mathcal{B}(B \rightarrow D_s^{*+} X)} = (53.3 \pm 3.7 \pm 3.1 \pm 2.1) \% . \quad (9.6)$$

Highlights	Figure or Table	Page(s)
$\phi\pi^+$ invariant mass	Fig. 6.1	70
$\Delta M = M(D_s^+\gamma) - M(D_s^+)$ distribution	Fig. 6.15	79
$D_s^+$ efficiency-corrected mom. spec.	Fig. 6.12	77
$D_s^{*+}$ efficiency-corrected mom. spec.	Fig. 6.26	85
Systematic errors for $\mathcal{B}(B \rightarrow D_s^{(*)+}X)$	Fig. 6.1	87
Fit to $D_s^+$ mom. spec. from $q\bar{q}$ continuum	Figs. 6.28, 6.29	91, 91
Res. to $D_s^+$ mom. spec. from $q\bar{q}$ continuum	Table 6.4	90
Fit to $D_s^{*+}$ mom. spec. from $q\bar{q}$ continuum	Figs. 6.30, 6.31	91, 91
Res. $D_s^{*+}$ mom. spec. from $q\bar{q}$ continuum	Table 6.5	92
Fit to $D_s^+$ mom. spec.	Fig. 6.42a	105
Fit to $D_s^{*+}$ mom. spec.	Fig. 6.42b	105
Miss. mass for $D_s^+ - \pi$ system	Figs. 7.1- 7.5	114- 115
Miss. mass for $D_s^{*+} - \pi$ system	Figs. 7.2- 7.6	114- 115
Monte Carlo sim. for $D_s^{(*)+} - \pi$ missing mass	Fig. 7.11	122
Background study for $D_s^{(*)+} - \pi$ missing mass	Figs. 7.12- 7.14	123-125
Systematic errors for $\mathcal{B}(B^0 \rightarrow D_s^{(*)+}D^{*-})$	Table 7.10	129
Projections on $\cos\theta_\gamma$ and $\cos\theta_\pi$	Fig. 7.18	136
Systematic errors for $\Gamma_L/\Gamma$	Table 7.15	136

Table 9.1: A summary of the analysis highlights. The relevant figures or tables with the corresponding pages, are shown.

From the fit of the  $D_s^{(*)+}$  momentum spectrum, the sum of two-body modes is also determined:

$$\Sigma\mathcal{B}(B \rightarrow D_s^{(*)+}\bar{D}^{(*)}) = \left[ (5.07 \pm 0.14 \pm 0.30) \times \frac{3.6 \pm 0.9\%}{\mathcal{B}(D_s^+ \rightarrow \phi\pi^+)} \right] \%, \quad (9.7)$$

$$\Sigma\mathcal{B}(B \rightarrow D_s^{*+}\bar{D}^{(*)}) = \left[ (4.1 \pm 0.2 \pm 0.4) \times \frac{3.6 \pm 0.9\%}{\mathcal{B}(D_s^+ \rightarrow \phi\pi^+)} \right] \%. \quad (9.8)$$



have been measured. The mass difference

$$m(D_s^+) - m(D^+) = 98.4 \pm 0.1 \pm 0.3 \text{ MeV}/c^2, \quad (9.9)$$

where the first error is statistical, and the second is systematic, has been measured.

The decays  $B^0 \rightarrow D_s^+ D^{*-}$  and  $B^0 \rightarrow D_s^{*+} D^{*-}$  have been observed using a partial reconstruction technique and the following branching fractions have been determined:

$$\mathcal{B}(B^0 \rightarrow D_s^+ D^{*-}) = (1.03 \pm 0.14 \pm 0.14 \pm 0.26)\%, \quad (9.10)$$

$$\mathcal{B}(B^0 \rightarrow D_s^{*+} D^{*-}) = (1.97 \pm 0.15 \pm 0.28 \pm 0.49)\%, \quad (9.11)$$

$$\Sigma \mathcal{B}(B^0 \rightarrow D_s^{(*)+} D^{*-}) = (3.00 \pm 0.19 \pm 0.38 \pm 0.75)\%, \quad (9.12)$$

Using the angular analysis, the fraction of the longitudinal polarization in  $B^0 \rightarrow D_s^{*+} D^{*-}$  decay channel has been extracted:

$$\Gamma_L/\Gamma = 51.9 \pm 5.0 \pm 2.8\%. \quad (9.13)$$

This result is in a good agreement with the prediction using factorization ( $53.5 \pm 3.3$ )%.

A comparison of the *BABAR* results reported in this dissertation with the ones from *CLEO* are shown in Table 9.2. Our results are in a good agreement with the existing measurements.

	<i>BABAR</i>	<i>CLEO</i>
$\mathcal{B}(B \rightarrow D_s^+ X), \%$	$10.93 \pm 0.19 \pm 0.58$	$11.77 \pm 0.38 \pm 0.86$
$\mathcal{B}(B \rightarrow D_s^{*+} X), \%$	$7.9 \pm 0.8 \pm 0.7$	—
$\Sigma \mathcal{B}(B \rightarrow D_s^{(*)+} D^{(*)}), \%$	$5.07 \pm 0.14 \pm 0.30$	$5.38 \pm 0.22 \pm 0.54$ $5.37 \pm 0.55 \pm 1.31^*$
Fraction, %	$46.4 \pm 1.3 \pm 1.4 \pm 0.6$	$45.7 \pm 1.9 \pm 3.7 \pm 0.6$
$\Sigma \mathcal{B}(B \rightarrow D_s^{*+} D^{(*)}), \%$	$4.1 \pm 0.2 \pm 0.4$	— $3.30 \pm 0.50 \pm 0.55^*$
Fraction, %	$53.3 \pm 3.7 \pm 3.1 \pm 2.1$	—
$\mathcal{B}(B^0 \rightarrow D_s^+ D^{*-}), \%$	$1.03 \pm 0.14 \pm 0.14$	$1.10 \pm 0.18 \pm 0.10$ $0.90 \pm 0.22 \pm 0.16^*$
$\mathcal{B}(B^0 \rightarrow D_s^{*+} D^{*-}), \%$	$1.97 \pm 0.15 \pm 0.28$	$1.82 \pm 0.37 \pm 0.24$ $1.97 \pm 0.50 \pm 0.36^*$
$\Gamma_L/\Gamma, \%$	$51.9 \pm 5.0 \pm 2.8$	$50.6 \pm 13.9 \pm 3.6$

Table 9.2: Comparison of the *BABAR* and *CLEO* results.  $\mathcal{B}(D_s^+ \rightarrow \phi\pi^+) = 3.6\%$  is used for normalization. The results marked by \* were obtained using full *B* meson reconstruction (see section 4.5.1).

# Bibliography

- [1] V. Jain, Nucl. Phys. B Proc. Suppl. **50**, 96-102 (1996); *CLEO* Collaboration, T. E. Coan *et al.*, Phys. Rev. Lett. **80**, 1150 (1998).
- [2] I. Bigi *et al.*, Phys. Lett. B **323**, 408-416 (1994).
- [3] A. F. Falk, M. B. Wise and I. Dunietz, Phys. Rev. D **51**, 1183-1191 (1995).
- [4] R. Aleksan. "Quark Mixing and *CP* Violation". Techniques and Concepts of High Energy Physics X, 487-596.
- [5] L H. Ryder, Elementary Particles and Symmetries, Gordon and Breach Science Publishers, London, 1975.
- [6] M. Gell-Mann and A. Pais, Phys. Rev. **97**, 1387 (1955).
- [7] J. H. Christenson, J. W. Cronin, V. L. Fitch and R. Turlay, Phys. Rev. Lett. **13**, 138 (1964)
- [8] Particle Data Group, D. E. Groom *et al.*, Eur. Phys. Jour. C **15**, 1 (2000).
- [9] L. Wolfenstein, Phys. Rev. Lett. **13** 562 (1964).
- [10] NA48 Collaboration, A. Lai, Eur. Phys. Jour. C **22** 231 (2001).
- [11] KTeV Collaboration, A. Alavi-Harati, Phys. Rev. Lett. **83** 22 (1999).
- [12] P.Kokkaas, CPLEAR Collaboration, presented at the XXIX ICHEP98, Vancouver, Canada, July 23-29, 1998
- [13] M. Kobayashi and T. Maskawa, Prog. Th. Phys. **42** 652 (1973)
- [14] P. Higgs, Phys. Rev. Lett. **13** 508 (1964).
- [15] L. Wolfenstein, Phys. Rev. Lett. **51** 1945 (1983)
- [16] S. Herrlich and U. Nierste, Phys. Rev. D **52** 6505 (1995)

- [17] T. Inami and C. S. Lim, Prog. Th. Phys. **65** 297 (1981)
- [18] BABAR Collaboration, B. Aubert *et al.*, Phys. Rev. Lett. **87** 091801 (2001).
- [19] BABAR Collaboration, B. Aubert *et al.*, Phys. Rev. Lett. **87** 241801 (2001).
- [20] PEP-II Conceptual Design Report, SLAC-R-418 (1993).
- [21] BABAR Technical Design Report, D. Boutigny *et al.*, SLAC-R-95-457, March 1995.
- [22] BABAR Collaboration, B. Aubert *et al.*, SLAC-PUB-8569, hep-ex/0105044, to appear in Nucl. Instr. and Methods
- [23] The BABAR Silicon Vertex Tracker, C. Bozzi *et al.*, Nucl. Instr. and Methods A **435**, 25 (1999)
- [24] I. Adam *et al.*, Nucl. Instr. and Methods A **453** 301 (2000); I. Adam *et al.*, Nucl. Phys. Proc. Suppl. **93** 340 (2001).
- [25] Simulation and measurement of the fringe field of the 1.5 T BABAR solenoid, E. Antokhin *et al.*, Nucl. Instr. and Methods A **432**, 24 (1999)
- [26] "The BABAR Physics Book", D. Boutigny *et al.*, SLAC-R-504, October 1998, ed. by P. F. Harrison and H. R. Quinn.
- [27] CLEO Collaboration, S. Anderson *et al.*, Report No CLEO CONF 99-6, XIX International Symposium on Lepton and Photon Interactions at High Energies, Stanford, California, 1999 (hep-ex/9908009).
- [28] M. Bauer *et al.*, Z. Phys. C **34**, 103 (1987).
- [29] J. Rosner, Phys. Rev. D **42(11)**, 3732 (1990).
- [30] T. Mannel, W. Roberts, Z. Ryzak, Phys. Lett. B **259**, 485 (1991).
- [31] M. Neubert and V. Rieckert, Nucl. Phys. B **382**, 97 (1992)
- [32] N. Isgur and M. B. Wise, Phys. Lett. B **232**, 113 (1989); Phys. Lett. B **237**, 527 (1990)
- [33] M. K. Gaillard and B. Lee, Phys. Rev. Lett. **33** 108 (1974); G. Altarelli and L. Maiani, Phys. Lett. B **52** 351 (1974)
- [34] R. Aleksan, M. Zito, A. Le Yaouanc, L. Oliver, O. Pène and J.-C. Raynal, Preprint hep-ph/9906504 , also LPT-ORSAY-99-35 and DAPNIA-SPP-99-18 (1999).

- [35] R. Aleksan, M. Zito, A. Le Yaouanc, L. Oliver, O. Pène and J.-C. Raynal, Preprint hep-ph/9906505 , also LPT-ORSAY-99-36 and DAPNIA-SPP-99-19 (1999).
- [36] *CLEO* Collaboration, B. Barish *et al.*, Phys. Rev. Lett. **76** 397 (1996); *ARGUS* Collaboration, H. Albrecht *et al.*, Phys. Lett. B **318** 397 (1993).
- [37] E. Bagan, P. Ball, B. Fiol, and P. Gosdzinsky, Phys. Lett. B **351**, 546 (1995); E. Bagan, P. Ball, V. M. Braun, and P. Gosdzinsky, Phys. Lett. B **342**, 362 (1995); M. V. Voloshin, Phys. Rev. D **51**, 3948 (1995).
- [38] J. D. Richman, Progress in Understanding Heavy Flavor Decays, contribution to the ICHEP'96, Warsaw, Poland (1996).
- [39] *ALEPH* Collaboration, ICHEP pa05-061 (1996).
- [40] *ALEPH* Collaboration, EPS-0404, contribution to the Int'l. Europhysics Conference on High Energy Physics, Brussels, Belgium (1996); *DELPHI* Collaboration, P. Abreu *et al.*, Z. Phys. C **66**, 323 (1995); *L3* Collaboration, CERN-PPE/96-49, submitted to Z. Phys. C , (1996); *OPAL* Collaboration, R. Akers *et al.*, Z. Phys. C **60**, 199 (1993).
- [41] G. Bichalla, I. Dunietz, and H. Yamamoto, Preprint hep-ph/9507437, also FERMILAB-PUB-95/167-T (1995).
- [42] *ARGUS* Collaboration, H. Albrecht *et al.* Z. Phys. C **48**, 543 (1990).
- [43] Hadronic Event Selection and *B*-Counting for Inclusive Charmonium Measurements, *BABAR* Analysis Document #30.
- [44] D. Antreasyan, Crystal Ball Note 321 (1983).
- [45] *CLEO* Collaboration, D. Bortoletto *et al.*, Phys. Rev. D **37**, 1719 (1988).
- [46] *ALEPH* Collaboration, Eur. Phys. Jour. C **16**, 597 (2000).
- [47] B. Andersson *et al.*, Z. Phys. C **20**, 317 (1983)
- [48] C. Peterson *et al.*, Phys. Rev. D **27**, 105 (1983)
- [49] P. Collins and T. Spiller, J. Phys. **G11**, 1289 (1985)
- [50] V.G. Kartvelishvili *et al.*, Phys. Lett. B **78**, 615 (1978) [ Sov. J. Nucl. Phys.38, 952 (1983) ]
- [51] *CLEO* Collaboration, G. Brandenburg *et al.*, Phys. Rev. D **58**, 052003 (1998)

- [52] Measurement of the GoodTrackLoose efficiency using SVT tracks, *BABAR* Analysis Document #157.
- [53] Study of  $\pi^0$  Reconstruction Efficiency in RUN I data using  $\tau\tau$  1-on-1 Decays, *BABAR* Analysis Document #196.
- [54] *CLEO* Collaboration, S. Ahmed *et al.*, Phys. Rev. D **62**, 112003 (2000).
- [55] *CLEO* Collaboration, D. Gibaut *et al.*, Phys. Rev. D **53**, 4734 (1996).
- [56] *ARGUS* Collaboration, H. Albrecht *et al.*, Z. Phys. C **54**, 1 (1992).
- [57] G. C. Fox and S. Wolfram, Phys. Rev. Lett. **41**, 1581 (1978); G. C. Fox and S. Wolfram, Nucl. Phys. B **149** 413 (1979).
- [58] GEANT Detector Description and Simulation Tool, Version 3.21, CERN Program Library W5103 (1995).
- [59] I. Dunietz *et al.*, Phys. Rev. D **43**, 2193 (1991).
- [60] Review of Particle Properties, Phys. Rev. D **50**, Part I (1994).
- [61] *CLEO* Collaboration, M. Artuso *et al.*, Phys. Lett. B **378** 364 (1996).
- [62] *BABAR* Collaboration, Report No *BABAR* CONF-00/13, XXX International Conference on High Energy Physics, Osaka, Japan (hep-ex/0008056).
- [63] *CLEO* Collaboration, R. A. Briere *et al.*, Phys. Rev. D **62**, 072003 (2000).
- [64] *OPAL* Collaboration, K. Ackerstaff *et al.*, Eur. Phys. Jour. C **5** 1 (1998).
- [65] *SLD* Collaboration, K. Abe *et al.*, presented at the International Europhysics Conference on Hight-Energy Physics (HEP97), Jerusalem, Israel, 1997, Report No SLAC-PUB-7574.
- [66] *L3* Collaboration, M. Acciarri *et al.*, Phys. Lett. B **345**, 589 (1995).
- [67] *OPAL* Collaboration, K. Ackerstaff *et al.*, Z. Phys. C **74** 413 (1997).
- [68] J. D. Richman, in Probing the Standard Model of Particle Interactions, edited by R. Gupta, A. Morel, E. de Rafael, and F. David (Elsevier Science, 1999) p. 640.

# List of Tables

3.1	PEP-II parameters. Values are given for the design and average during the first year of operation. The notations HER and LER means the high energy $e^-$ and low energy $e^+$ ring, respectively. $\sigma_x$ , $\sigma_y$ and $\sigma_z$ refer to the horizontal, vertical and longitudinal rms of the bunches. . . . .	29
4.1	Factorization model predictions for the relative branching fractions of $B \rightarrow D_s^{(*)+} \bar{D}^{(*)}$ . Average values for the different form factor parameterization are displayed. . . . .	46
5.1	Luminosity, number of $B\bar{B}$ events $N_{B\bar{B}}$ and the ratio on to off resonance data sets for the different voltages on the drift chamber . . . . .	58
5.2	The skim rates and efficiencies for the four $D_s^+$ decay modes. . . . .	61
5.3	Selection criteria, fit parameters and efficiencies for $D_s^+ \rightarrow \phi\pi^+$ , $D_s^+ \rightarrow \bar{K}^{*0}K^+$ , $D_s^+ \rightarrow \bar{K}^0K^+$ and $D_s^+ \rightarrow \phi\rho^+$ decay modes. The data from the InclDs skim are analyzed. . . . .	64
5.4	The fit results for $\Delta M = M(D_s^+\gamma) - M(D_s^+)$ mass spectrum. The $D_s^+$ mesons are identified in $D_s^+ \rightarrow \bar{K}^0K^+$ , $D_s^+ \rightarrow \bar{K}^{*0}K^+$ , $D_s^+ \rightarrow \bar{K}^0K^+$ modes. The data from the InclDs skim are analysed. . . . .	68
6.1	Systematic errors for $\mathcal{B}(B \rightarrow D_s^{(*)+}X)$ . . . . .	87
6.2	Systematic errors for $\sigma(e^+e^- \rightarrow D_s^{(*)\pm}X)\mathcal{B}(D_s^+ \rightarrow \phi\pi^+)$ . . . . .	89
6.3	Analytical expressions for the fragmentation functions. . . . .	90
6.4	The fit results and cross section $\sigma(e^+e^- \rightarrow D_s^{*+}X)\mathcal{B}(D_s^+ \rightarrow \phi\pi^+)$ , Only the statistical errors (uncorrelated and correlated for the cross sections) are given. . . . .	90
6.5	The fit results and cross section $\sigma(e^+e^- \rightarrow D_s^{*+}X)\mathcal{B}(D_s^+ \rightarrow \phi\pi^+)$ , Only the statistical errors (uncorrelated and correlated for the cross sections) are given. . . . .	92

6.6	The ratio $\epsilon_{Data}/\epsilon_{MC}$ for the single track integrating on entire momentum. Uncertainty is statistical only. . . . .	93
6.7	$r$ , $\epsilon_T/\epsilon_L$ and $\epsilon_{L+T}$ for data and Monte Carlo obtained with $D_s^+$ and $D^*$ decays. . . . .	96
6.8	The $D_s^+$ peak parameters with and without smearing. The efficiency is corrected neither for tracking nor for particle identification. . . . .	102
6.9	Predictions and experimental results for the ratios of the width in $B \rightarrow D_s^{(*)+} \bar{D}^{(*)}$ decays . . . . .	103
6.10	The results of the fit for the different assumptions concerning the relative contribution of the modes for each source of $D_s^+$ . . . . .	106
6.11	The results of the fit for the different assumptions concerning the relative contribution of the modes for each source of $D_s^+$ . . . . .	107
6.12	$m(D_s^+)$ , $m(D^+)$ , $\Delta m = m(D_s^+) - m(D^+)$ in $\text{MeV}/c^2$ obtained with different procedures for data and Monte Carlo. The last line shows the value of the mass used the simulation. . . . .	109
7.1	The Number of signal events observed for the $D_s^{(*)+} - \pi$ system with $D_s^+$ identified in three different channels. . . . .	115
7.2	The reconstruction efficiency for the $B^0 \rightarrow D_s^+ D^{*-}$ ( $D_s^+ \rightarrow \phi \pi^+$ ) decay mode. The $B^0 \rightarrow D_s^{*+} D^{*-}$ cross feed efficiency is shown for the different polarization. . . . .	118
7.3	The reconstruction efficiency for the $B^0 \rightarrow D_s^{*+} D^{*-}$ ( $D_s^+ \rightarrow \phi \pi^+$ ) decay mode. The self-cross feed as well as the $B^0 \rightarrow D_s^+ D^{*-}$ cross feed efficiencies are shown for the different polarization. . . . .	119
7.4	The different data samples which can be used to determine the background in the $D^0$ signal region. . . . .	120
7.5	Production cross sections at $\sqrt{s} = M(\Upsilon(4S))$ . . . . .	121
7.6	Average (Data-Monte Carlo)/(Monte Carlo) for the different $D_s^{(*)+} - \pi$ combinations. The notations WS and SB mean a wrong sign combination and a side-band region, respectively. . . . .	126
7.7	Efficiencies for the partially reconstructed $B^0 \rightarrow D_s^{(*)+} D^{*-}$ decay modes. The columns show the contribution of the different modes to the $D_s^+ - \pi$ and $D_s^{*+} - \pi$ missing mass distributions in the signal region. . . . .	128
7.8	$B^0 \rightarrow D_s^{(*)+} D^{*-}$ ( $D_s^+ \rightarrow \phi \pi^+$ ) branching fractions in percent obtained with different track and photon selection criteria. Both tracking and neutral reconstruction as well as particle identification corrections are applied. Only statistical error is shown. . . . .	128



7.9	$B^0 \rightarrow D_s^{(*)+} D^{*-}$ branching fractions in percent obtained for each $D_s^+$ mode. Both tracking and neutral reconstruction as well as particle identification corrections are applied. The first error is statistical, the second is due to the relative branching fraction uncertainty. . . . .	129
7.10	Systematic errors for $\mathcal{B}(B^0 \rightarrow D_s^{(*)+} D^{*-})$ . . . . .	129
7.11	The functions describing the longitudinal and the transverse polarization of the vector meson for the different types of decays. . . . .	133
7.12	Efficiency in percents as a function of the helicity angles $\theta_\pi$ , $\theta_\gamma$ . . . .	134
7.13	Number of the background events in the signal region as a function of the helicity angles $\theta_\pi$ , $\theta_\gamma$ obtained from the Monte Carlo simulation. . . . .	135
7.14	Number of signal events as a function of $\cos \theta_\gamma$ , $\cos \theta_\pi$ efficiency-corrected. . . . .	135
7.15	Systematic errors for $\Gamma_L/\Gamma$ . . . . .	136
8.1	Results of previous measurements of $P_V$ for heavy quark mesons at other experiments. The results obtained in this work are shown too. The <i>CLEO</i> result marked * is model dependent. The $P_V$ value is measured in the range $x_p > 0.44$ and than extrapolated to the all momentum range using some theoretical assumption. . . . .	141
8.2	Comparison with theoretical prediction assuming factorization. . . . .	142
9.1	A summary of the analysis highlights. The relevant figures or tables with the corresponding pages, are shown. . . . .	144
9.2	Comparison of the <i>BABAR</i> and <i>CLEO</i> results. $\mathcal{B}(D_s^+ \rightarrow \phi \pi^+) = 3.6\%$ is used for normalization. The results marked by * were obtained using full $B$ meson reconstruction (see section 4.5.1). . . . .	146



# List of Figures

2.1	The unitarity triangle. Some $B$ decay modes, which allow one to measure the angles are shown. . . . .	17
2.2	Experimental constraints of the unitarity triangle before observation of $CP$ violation in the $B^0$ system. . . . .	20
2.3	Hadronic cross section in the $\Upsilon$ region. . . . .	21
2.4	A schematic view of an interaction with asymmetric beam energy. . .	22
2.5	a) Distribution of $M_{ES}$ for $B_{CP}$ candidates having a $K_S^0$ in the final state ( $\eta_{CP} = -1$ ); b) distribution of $\Delta E$ for $J/\psi K_L^0$ candidates ( $\eta_{CP} = +1$ ). . . . .	24
2.6	The time dependent asymmetry. Number of candidates having a $K_S^0$ in the final state ( $\eta_{CP} = -1$ ) in the signal region a) with a $B^0$ tag $N_{B^0}$ and b) with a $\bar{B}^0$ tag $N_{\bar{B}^0}$ and c) the asymmetry as a function of $\Delta t$ . The plots d)-f) present the corresponding information for $J/\psi K_L^0$ mode ( $\eta_{CP} = +1$ ). . . . .	24
2.7	Graphical displays of existing $\sin 2\beta$ measurements. . . . .	26
3.1	The PEP-II/ <i>BABAR</i> accelerator complex. . . . .	28
3.2	The PEP-II/ <i>BABAR</i> integrated luminosity in 1999-2000. . . . .	28
3.3	The <i>BABAR</i> Detector. 1. Silicon Vertex Tracker (SVT), 2. Drift Chamber (DCH), 3. Particle Identification Subsystem (DIRC—Detector of Internally Reflected Cherenkov Light, 4. Electromagnetic Calorimeter (EMC), 5. Magnet, 6. Instrumented Flux Return (IFR). . . . .	30
3.4	Schematic view of SVT. . . . .	31
3.5	The SVT resolution in $z$ (left) and $\phi$ (right) coordinates in microns as a function of the angle of incidence of the tracks. . . . .	32
3.6	Schematic view of DCH. The chamber center is offset by 370 mm from the interaction point (IP). . . . .	33

3.7	Average DCH position resolution as a function of the drift distance in layer. . . . .	33
3.8	Measurement of $dE/dx$ in DCH as a function of track momentum. The curves are the Bethe-Bloch functions derived from the different particle masses. . . . .	33
3.9	Schematic view of DIRC quartz radiator bar and the photon detection region. . . . .	35
3.10	The efficiency and misidentification for pion tracks . . . . .	36
3.11	The efficiency and misidentification for kaon tracks . . . . .	36
3.12	Schematic view of EMC. . . . .	37
3.13	The EMC energy resolution as a function of energy, as determined from the observed width of $\pi^0$ and $\eta$ decays to two photons of equal energy and from Bhabha electrons. The shaded band is the best fit to the $\pi^0$ , $\eta$ , and Bhabha data. Also shown is the energy resolution of the 6.13 MeV photons from the radioactive source and from the photons of the transition $\chi_{c1} \rightarrow J/\psi\gamma$ . . . . .	37
3.14	Two gamma invariant mass distribution showing the $\pi^0 \rightarrow \gamma\gamma$ decay. .	38
3.15	The EMC angular resolution as a function of energy. . . . .	38
3.16	Schematic view of IFR resistive plate chambers. . . . .	39
3.17	The difference between the direction of the reconstructed neutral hadron cluster and the missing transverse momentum. . . . .	40
3.18	The muon efficiency and pion misidentification as a function of a track momentum. . . . .	40
4.1	Diagram shows a two-body decay of $B$ mesons. . . . .	43
4.2	Factorization prediction for the fraction of the longitudinal polarization for the decays involving two vector mesons as a function of $q^2$ . The experimental results for $B \rightarrow D^*\rho$ , $B \rightarrow D^*\rho'$ and $B \rightarrow D^*D_s^{*+}$ are shown too. . . . .	45
4.3	Comparison of $n_c$ versus $\mathcal{B}_{SL}$ for measurements at the $\Upsilon(4S)$ and the $Z$ with theoretical prediction from Ref. [41]. . . . .	50
4.4	The main spectator diagram leading to the production of $D_s^{(*)+}$ mesons in $B$ decays. . . . .	51
4.5	Additional diagrams leading to the production of $D_s^{(*)+}$ mesons from the $c\bar{c}$ continuum or from $B$ decays. . . . .	52

4.6	The $M_{ES}$ distribution for the reconstructed $B$ mesons. . . . .	53
4.7	Definition of the $B$ cone angle $\theta_B$ and arbitrary angle $\phi$ . . . . .	55
5.1	The $\phi\pi^+$ invariant mass spectrum from the InclDs skim . . . . .	62
5.2	The $\overline{K}^{*0}K^+$ invariant mass spectrum from the InclDs skim. . . . .	62
5.3	The $K_s^0K^+$ invariant mass spectrum from the InclDs skim. . . . .	62
5.4	The $\phi\pi^+\pi^0$ invariant mass spectrum from the InclDs skim. . . . .	62
5.5	$D_s^+$ momentum resolution from SP3 Monte Carlo. (a) - $D_s^+ \rightarrow \phi\pi^+$ , (b) - $D_s^+ \rightarrow \overline{K}^{*0}K^+$ , (c) - $D_s^+ \rightarrow \overline{K}^0K^+$ , (d) - $D_s^+ \rightarrow \phi\rho^+$ . . . . .	65
5.6	Distribution of the $\Delta M = M_{D_s\gamma} - M_{D_s}$ with $D_s^+$ identified in $D_s^+ \rightarrow \phi\pi^+$ mode from the InclDs skim. The fit function is a Crystal Ball function for the signal plus a threshold function. . . . .	66
5.7	Distribution of the $\Delta M = M_{D_s\gamma} - M_{D_s}$ with $D_s^+$ identified in $D_s^+ \rightarrow \overline{K}^{*0}K^+$ mode from the InclDs skim. The fit function is a Crystal Ball function for the signal plus a threshold function. . . . .	66
5.8	Distribution of the $\Delta M = M_{D_s\gamma} - M_{D_s}$ with $D_s^+$ identified in $D_s^+ \rightarrow \overline{K}^0K^+$ mode from the InclDs skim. The fit function is a Crystal Ball function for the signal plus a threshold function. . . . .	67
5.9	Distribution of the $\Delta M = M_{D_s\gamma} - M_{D_s}$ with $D_s^+$ identified in $D_s^+ \rightarrow \phi\pi^+$ , $D_s^+ \rightarrow \overline{K}^{*0}K^+$ and $D_s^+ \rightarrow \overline{K}^0K^+$ modes from the InclDs skim. . . . .	67
6.1	The $\phi\pi^+$ invariant mass spectrum obtained from DsToPhiPi skim. The fit function is a single Gaussian for each peak, with their widths constrained to be equal on top of an exponential background. . . . .	70
6.2	The $\phi\pi^+$ invariant mass spectrum corrected using its momentum dependence. The fit function is a single Gaussian for each peak, with their widths constrained to be equal on top of an exponential background. . . . .	70
6.3	The $\phi\pi^+$ mass distributions for the on-resonance data for 12 different momentum windows (a) 0-0.2, (b) 0.2-0.4, (c) 0.4-0.6, (d) 0.6-0.8, (e) 0.8-1.0, (f) 1.0-1.2, (g) 1.2-1.4, (i) 1.4-1.6, (h) 1.6-1.8, (k) 1.8-2.0, (l) 2.0-2.2, (m) 2.2-2.4 GeV/c. The result of the fit described in the text is overlaid. . . . .	71
6.4	The $\phi\pi^+$ mass distributions for the on-resonance data for 12 different momentum windows (a) 2.4-2.6 GeV/c, (b) 2.6-2.8, (c) 2.8-3.0, (d) 3.0-3.2, (e) 3.2-3.4, (f) 3.4-3.6, (g) 3.6-3.8, (i) 3.8-4.0, (h) 4.0-4.2, (k) 4.2-4.4, (l) 4.4-4.6, (m) 4.6-4.8 GeV/c. The result of the fit described in the text is overlaid. . . . .	72

6.5	The $\phi\pi^+$ mass distributions for the off-resonance data for 12 different momentum windows (a) 0-0.2, (b) 0.2-0.4, (c) 0.4-0.6, (d) 0.6-0.8, (e) 0.8-1.0, (f) 1.0-1.2, (g) 1.2-1.4, (i) 1.4-1.6, (h) 1.6-1.8, (k) 1.8-2.0, (l) 2.0-2.2, (m) 2.2-2.4 GeV/c. The result of the fit described in the text is overlaid. . . . .	73
6.6	The $\phi\pi^+$ mass distributions for the off-resonance data for 12 different momentum windows (a) 2.4-2.6 GeV/c, (b) 2.6-2.8, (c) 2.8-3.0, (d) 3.0-3.2, (e) 3.2-3.4, (f) 3.4-3.6, (g) 3.6-3.8, (i) 3.8-4.0, (h) 4.0-4.2, (k) 4.2-4.4, (l) 4.4-4.6, (m) 4.6-4.8 GeV/c. The result of the fit described in the text is overlaid. . . . .	74
6.7	The fitted $D_s^+$ mass as a function of its momentum in the $\Upsilon(4S)$ rest frame for data and Monte Carlo. The curves show the fit results using the function described in the text. The shaded band shows the PDG value with the error ( $1968.6 \pm 0.6$ MeV/c <sup>2</sup> ). . . . .	75
6.8	The $\phi\pi^+$ mass resolution as a function of momentum in the $\Upsilon(4S)$ rest frame for data (black dots) and Monte Carlo (red squares). The points are fitted with a straight line. . . . .	75
6.9	The $D_s^+$ momentum spectrum before (top) and after (bottom) efficiency correction obtained from off-resonance data. The fit uses an Andersson function. . . . .	76
6.10	The $D_s^+$ yield from on-resonance (solid circles) and off-resonance (open circles) data scaled according to the luminosity ratio before efficiency correction. . . . .	76
6.11	The efficiency for $D_s^+ \rightarrow \phi\pi^+$ with consequent $\phi \rightarrow K^+K^-$ decay as a function of momentum in the center-of-mass frame. Two methods described in the text are used to account the number of reconstructed $D_s^+$ . . . . .	77
6.12	The $D_s^+$ efficiency-corrected momentum spectrum for on-resonance (filled circles) and scaled off-resonance data (open circles). The curve shows the fit with an Andersson function. . . . .	77
6.13	The efficiency-corrected $D_s^+$ momentum spectrum from $B$ decays. The Andersson fragmentation function is used for the fit of the continuum events. The entire momentum range (left) and below 2.5 GeV/c (right) are shown . . . . .	77
6.14	The efficiency-corrected $D_s^+$ momentum spectrum from $B$ decays. The scaled off-resonance data are subtracted directly from the on-resonance data. The entire momentum range (left) and below 2.5 GeV/c (right) are shown . . . . .	78

6.15	The $\Delta M = M(D_s^+ \gamma) - M(D_s^+)$ mass spectrum for $D_s^+$ reconstructed in $\phi\pi^+$ mode. The fit function is described in the text. . . . .	79
6.16	The $D_s^{*+}$ signal after subtraction of background. The curve shows the fit using a Crystal Ball function. . . . .	79
6.17	The $\Delta M = M(D_s^{*+} \gamma) - M(D_s^+)$ distributions for the on-resonance data for 10 different momentum windows (a) 0-0.25, (b) 0.25-0.5, (c) 0.5-0.75, (d) 0.75-1.0, (e) 1.0-1.25, (f) 1.25-1.5, (g) 1.5-1.75, (i) 1.75-2.0, (h) 2.0-2.25, (k) 2.25-2.5 GeV/c. The result of the fit described in the text is overlaid. . . . .	80
6.18	The $\Delta M = M(D_s^{*+} \gamma) - M(D_s^+)$ distributions for the on-resonance data for 10 different momentum windows (a) 2.5-2.75, (b) 2.75-3.0, (c) 3.0-3.25, (d) 3.25-3.5, (e) 3.5-3.75, (f) 3.75-4.0, (g) 4.0-4.25, (i) 4.25-4.5, (h) 4.5-4.75, (k) 4.75-5.0 GeV/c. The result of the fit described in the text is overlaid. . . . .	81
6.19	The $\Delta M = M(D_s^{*+} \gamma) - M(D_s^+)$ distributions for the off-resonance data for 10 different momentum windows (a) 0-0.25, (b) 0.25-0.5, (c) 0.5-0.75, (d) 0.75-1.0, (e) 1.0-1.25, (f) 1.25-1.5, (g) 1.5-1.75, (i) 1.75-2.0, (h) 2.0-2.25, (k) 2.25-2.5 GeV/c. The result of the fit described in the text is overlaid. . . . .	82
6.20	The $\Delta M = M(D_s^{*+} \gamma) - M(D_s^+)$ distributions for the off-resonance data for 10 different momentum windows (a) 2.5-2.75, (b) 2.75-3.0, (c) 3.0-3.25, (d) 3.25-3.5, (e) 3.5-3.75, (f) 3.75-4.0, (g) 4.0-4.25, (i) 4.25-4.5, (h) 4.5-4.75, (k) 4.75-5.0 GeV/c. The result of the fit described in the text is overlaid. . . . .	83
6.21	The fitted $\Delta m = m(D_s^{*+}) - m(D_s^+)$ as a function of the $D_s^{*+}$ momentum in the $\Upsilon(4S)$ center-of-mass for data and Monte Carlo. . . . .	84
6.22	The $\Delta M$ resolution as a function of the $D_s^{*+}$ momentum in the $\Upsilon(4S)$ center-of-mass for data and Monte Carlo. . . . .	84
6.23	The $D_s^{*+}$ momentum spectrum before (top) and after (bottom) efficiency correction for off-resonance data. The fit uses the Andersson function . . . . .	84
6.24	The $D_s^{*+}$ yield from on-resonance (filled circles) and off-resonance data (open circles) scaled according to the corresponding luminosity ratio before efficiency correction. . . . .	84
6.25	The efficiency for $D_s^{*+} \rightarrow D_s^+ \gamma$ with $D_s^+ \rightarrow \phi\pi^+$ and $\phi \rightarrow K^+ K^-$ as a function of the $D_s^{*+}$ momentum in the center-of-mass rest frame. Two methods described in the text are used to count the number of reconstructed $D_s^{*+}$ . . . . .	85

6.26	The $D_s^{*+}$ efficiency-corrected momentum spectrum for on-resonance (filled circles) and scaled off-resonance data (open circles). The curve shows the fit using the Andersson function. . . . .	85
6.27	The efficiency-corrected $D_s^{*+}$ momentum spectrum from $B$ decays. The scaled off-resonance data are subtracted directly from the on-resonance data. All momentum range (left) and below 2.5 GeV/c (right) are shown	86
6.28	The fit with an Andersson function of $D_s^+$ continuum spectrum. . . .	91
6.29	The fit with Peterson, Collins and Kartvelishvili functions of $D_s^+$ continuum spectrum. . . . .	91
6.30	The fit with an Andersson function of $D_s^{*+}$ continuum spectrum. . . .	91
6.31	The fit with Peterson, Collins and Kartvelishvili functions of $D_s^{*+}$ continuum spectrum. . . . .	91
6.32	Kaon efficiency as a function of momentum for data and Monte Carlo with two identification criteria: “loose” (upper plot) and “tight” kaon (bottom plot). . . . .	95
6.33	$\Delta M = M_{D_s \gamma} - M_{D_s}$ mass spectra. Upper histogram corresponds to no veto with $\pi^0$ to be required, while the lower histogram shows the $\Delta M$ spectrum with $\pi^0$ veto requirements for the photon candidate. . . . .	97
6.34	$R$ as a function of $D_s^{*+}$ center-of-mass momentum. Line shows the fit result described in the text. . . . .	97
6.35	The $\phi\pi^+$ mass distributions obtained by subtracting the off-resonance histogram after luminosity scaling to the corresponding on-resonance histogram. The $D_s^+$ yield is defined in the 12 momentum windows (a) 0-0.2, (b) 0.2-0.4, (c) 0.4-0.6, (d) 0.6-0.8, (e) 0.8-1.0, (f) 1.0-1.2, (g) 1.2-1.4, (i) 1.4-1.6, (h) 1.6-1.8, (k) 1.8-2.0, (l) 2.0-2.2, (m) 2.2-2.4 GeV/c. The result of the fit described in the text is overlaid. . . . .	99
6.36	The $\Delta M = M(D_s^{*+}\gamma) - M(D_s^+)$ distributions obtained by subtracting the off-resonance histogram after luminosity scaling to the corresponding on-resonance histogram. The $D_s^{*+}$ yield is defined in the 10 momentum windows (a) 0-0.25, (b) 0.25-0.5, (c) 0.5-0.75, (d) 0.75-1.0, (e) 1.0-1.25, (f) 1.25-1.5, (g) 1.5-1.75, (i) 1.75-2.0, (h) 2.0-2.25, (k) 2.25-2.5 GeV/c. The result of the fit described in the text is overlaid. . . . .	100
6.37	The $D_s^+$ momentum spectrum from $B$ decays. Scaled off-resonance histograms are subtracted directly from the corresponding on-resonance histograms. . . . .	101



- 6.38 The  $D_s^{*+}$  momentum spectrum from  $B$  decays. Scaled off-resonance histograms are subtracted directly from the corresponding on-resonance histograms. . . . . 101
- 6.39 The  $D_s^{*+}$  momentum spectrum from  $B$  decays. The third order of polynomial is used for the combinatorial background parameterization. . . 101
- 6.40 The  $\phi\pi^+$  mass spectrum from Monte Carlo obtained with (red histogram) and without (black histogram) smearing procedure. . . . . 101
- 6.41 The generated  $D_s^+$  (left) and  $D_s^{*+}$  (right) momentum spectra. Type (1),  $B \rightarrow D_s^{(*)+}\bar{D}^{(*)}$  - the slightly cross hatched histogram, Type (2),  $B \rightarrow D_s^{(*)+}\bar{D}^{**}$  - the cross hatched histogram and Type (3),  $B \rightarrow D_s^{(*)+}\bar{D}^{(*)}\pi/\rho/\omega$  - slightly hatched histogram. The smooth line is the sum of the three components. . . . . 103
- 6.42 The fit result for (a)  $D_s^+$  and (b)  $D_s^{*+}$  momentum spectra. The data are the dots with error bars, and the histograms represent the three components described in the text, i.e. Type (1) is  $B \rightarrow D_s^{(*)+}\bar{D}^{(*)}$ , Type (2) is  $B \rightarrow D_s^{(*)+}\bar{D}^{**}$  and Type (3) is  $B \rightarrow D_s^{(*)+}\bar{D}^{(*)}\pi/\rho/\omega$ . The solid histogram is the sum of the three components. . . . . 105
- 6.43 The fit result for  $D_s^{*+}$  momentum spectra. (a) The  $B \rightarrow D_s^{(*)}D^{(*)}\rho/\omega$  and (b) the  $B \rightarrow D_s^{(*)}D^{(*)}\pi$  are dominant in source (3). The data are dots with error bars and the histograms represent the three components described in the text. Type (1) is  $B \rightarrow D_s^{(*)+}\bar{D}^{(*)}$ , Type (2) is  $B \rightarrow D_s^{(*)+}\bar{D}^{**}$  and Type (3) is  $B \rightarrow D_s^{(*)+}\bar{D}^{(*)}\pi/\rho/\omega$ . The solid histogram is the sum of the three components. . . . . 105
- 6.44 The fit result for  $D_s^{*+}$  momentum spectra. (a) Scaled off-resonance histograms are subtracted directly from the corresponding on-resonance histograms. (b) The third order of polynomial is used for the combinatorial background parameterization. The data are the dots with error bars and the histograms represent the three components described in the text. Type (1) is  $B \rightarrow D_s^{(*)+}\bar{D}^{(*)}$ , Type (2) is  $B \rightarrow D_s^{(*)+}\bar{D}^{**}$  and Type (3) is  $B \rightarrow D_s^{(*)+}\bar{D}^{(*)}\pi/\rho/\omega$ . The solid histogram is the sum of the three components. . . . . 108
- 6.45 The  $D^+$  fitted mass as a function of its momentum in  $\Upsilon(4S)$  rest frame for data and Monte Carlo. The curves show the fit result with a function described in the text. The shaded band shows the PDG value. . . . . 110
- 6.46 The mass difference  $m(D_s^+) - m(D^+)$  as function of center-of-mass momentum obtained with Monte Carlo and data. The  $\chi^2/\text{nDof}$  of the fit with a straight line are 33.4/22 and 15.2/23, respectively. . . . . 110

7.1	The missing mass distribution for $D_s^+-\pi$ ( $D_s^+ \rightarrow \phi\pi^+$ ). The result of the fit described in the text is overlaid. . . . .	114
7.2	The missing mass distribution for $D_s^{*+}-\pi$ ( $D_s^+ \rightarrow \phi\pi^+$ ). The result of the fit described in the text is overlaid. . . . .	114
7.3	The missing mass distribution for $D_s^+-\pi$ ( $D_s^+ \rightarrow \bar{K}^{*0}K^+$ ). The result of the fit described in the text is overlaid. . . . .	114
7.4	The missing mass distribution for $D_s^{*+}-\pi$ ( $D_s^+ \rightarrow \bar{K}^{*0}K^+$ ). The result of the fit described in the text is overlaid. . . . .	114
7.5	The missing mass distribution for the $D_s^+-\pi$ ( $D_s^+ \rightarrow \bar{K}^0K^+$ ). The result of the fit described in the text is overlaid. . . . .	115
7.6	The missing mass distribution for the $D_s^{*+}-\pi$ ( $D_s^+ \rightarrow \bar{K}^0K^+$ ). The result of the fit described in the text is overlaid. . . . .	115
7.7	The missing mass distribution for the $D_s^+-\pi$ (left) and $D_s^{*+}-\pi$ (right) systems obtained from the Monte Carlo sample. Three different $D_s^+$ modes are shown separately. The $B^0 \rightarrow D_s^{*+}D^{*-}$ signal is generated according to the measured polarization. . . . .	116
7.8	The missing mass distribution for $B^0 \rightarrow D_s^{*+}D^{*-}$ decay mode obtained from Monte Carlo simulation. Different gamma selections are used: (a) all photon candidates, (b) $E^* > 0.1$ GeV, (c) exclude photons having a $\pi^0$ overlap, (d) exclude photons having a $\pi^0$ overlap and $E^* > 0.1$ GeV cut. The hatched histogram shows the self-cross Feed. . . . .	117
7.9	The missing mass distribution for the $D_s^+-\pi$ system obtained for the sum of three $D_s^+$ decay channels. The hatched histogram corresponds to the combinatorial background which includes the types (1), (2) and (3) as described in the text. . . . .	120
7.10	The missing mass distribution for the $D_s^{*+}-\pi$ system obtained for the sum of three $D_s^+$ decay channels. The hatched histogram corresponds to the combinatorial background which includes the types (1), (2) and (3) as described in the text. . . . .	120
7.11	The missing mass distribution for the (a) $D_s^+-\pi$ , (b) $D_s^{*+}-\pi$ (no $\pi^0$ overlap, $E_\gamma^* > 0$ ) (c) $D_s^{*+}-\pi$ ( $\pi^0$ overlap, $E_\gamma^* > 0.1$ GeV) for data (dots) and Monte Carlo (histogram). The contributions from the $B\bar{B}$ , $c\bar{c}$ and $uds$ are shown separately. . . . .	122

7.12	The missing mass distribution for the $D_s^+ - \pi$ system for data (dots) and Monte Carlo (histogram) for five combinations: (a) $D_s^+$ side-band region, (b) same sign combination for the $D_s^+$ signal region, (c) same sign combination for the $D_s^+$ side-band region, (d) flip $D_s^+$ direction for the $D_s^+$ signal region, (e) flip $D_s^+$ direction for the $D_s^+$ side-band region. The result of the fit using Eq.7.2 is overlaid. . . . .	123
7.13	The missing mass distribution for the $D_s^{*+} - \pi$ system for data (dots) and Monte Carlo (histogram) No $\pi^0$ overlap and $E_\gamma^* > 0$ are required. The following five combinations are shown: (a) $D_s^{*+}$ side-band region, (b) same sign combination for the $D_s^{*+}$ signal region, (c) same sign combination for the $D_s^{*+}$ side-band region, (d) flip $D_s^{*+}$ direction for the $D_s^{*+}$ signal region, (e) flip $D_s^{*+}$ direction for the $D_s^{*+}$ side-band region. The result of the fit using Eq.7.2 is overlaid. . . . .	124
7.14	The missing mass distribution for the $D_s^{*+} - \pi$ system for data (dots) and Monte Carlo (histogram) where $\pi^0$ overlap and $E_\gamma^* > 0.1$ GeV are required. The following five combinations are shown: (a) $D_s^{*+}$ side-band region, (b) same sign combination for the $D_s^{*+}$ signal region, (c) same sign combination for the $D_s^{*+}$ side-band region, (d) flip $D_s^{*+}$ direction for the $D_s^{*+}$ signal region, (e) flip $D_s^{*+}$ direction for the $D_s^{*+}$ side-band region. The result of the fit using Eq.7.2 is overlaid. . . . .	125
7.15	Angular distributions for the $B^0 \rightarrow D_s^{*+} D^{*-}$ generated events. . . . .	132
7.16	Number of events in the signal region as a function of the helicity angles $\theta_\pi, \theta_\gamma$ . . . . .	134
7.17	Efficiency as a function of the helicity angles $\theta_\pi, \theta_\gamma$ . . . . .	134
7.18	Projection of the number of events on the $\cos\theta_\gamma$ and $\cos\theta_\pi$ axis. The result of the two-dimensional fit is overlaid. The background is obtained from the Monte Carlo simulation. . . . .	136
7.19	Projection of the number of events on the $\cos\theta_\gamma$ and $\cos\theta_\pi$ axis. The result of the two-dimensional fit is overlaid. The background is obtained using the $D_s^{*+}$ flipping and the side-bands technique. . . . .	136
8.1	The inclusive $D_s^+$ branching fraction from $B$ decays obtained by different experiments. All values are normalized using $\mathcal{B}(D_s^+ \rightarrow \phi\pi^+) = 3.6\%$ . . . . .	139
8.2	Factorization prediction for the fraction of the longitudinal polarization for the decays involving two vector mesons as a function of $q^2$ . Dots are experimental results obtained with the <i>BABAR</i> and <i>CLEO</i> detectors. . . . .	142



# Acknowledgments

I would like to thank Roy Aleksan who was my thesis advisor since May 1999. I consider myself very fortunate that I had an opportunity to work with Roy. In any situation, no matter how complicated or even hopeless, concerning physics or anything else I knew that I could get help, advice and kind encouragement.

I am very grateful to Helmut Koch who was also my thesis advisor during the last year. I would particularly like to thank Helmut for his constant support, which I have always felt in any situation.

I would also like to thank the *BABAR* group of *CEA – SACLAY* where I worked from May 1999 till December 2000 and who helped me over these years in my work. In particular, I would like to express my deepest gratitude to my friend and colleague Andre Gaidot for offering a big support both physics and life in general. I am very grateful to Georges London with whom I worked very close together being in *BABAR* collaboration since 1996 and got a lot of experience as physicist. I would like to say special thanks to Gautier Hamel de Monchenault who first introduced me to the *BABAR* software and was providing great help concerning physics despite his own extremely busy schedule.

I would also like to express my gratitude to the *BABAR* group of Bochum University where I have already worked one year. In particular, I would like to thank Klaus Peters and Marcel Kunze who always found time to discuss different kind of problems and helped me to improve both the content and the style as well as the grammar of the entire dissertation. I would like to express special thanks to Matthias Steinke and Bernd Lewandowski for the permanent help and support concerning computing.

I would also like to express my gratitude to professor A. Onuchin with whom I worked from 1993 till 1999 being in the stuff of Budker Institute of Nuclear Physics.

Last but not least, I would like to express special thanks and deepest gratitude to my Wife for offering unconditional support of all my professional endeavors.



# Lebenslauf

<i>Persönliche Daten</i>	Name:	Serguei Ganjour
	Anschrift:	Auf dem Aspei 59, 44801 Bochum
	Geboren:	01.11.1971 in Gomel, Weißrußland, UdSSR
	Nationalität:	russisch
	Familienstand:	verheiratet, 1 Kind (geb. 1997)
<i>Schullaufbahn:</i>	1978-1988	Besuch der Grundschule und Hochschule in Petropavlovsk-Kamtschatski, Rußland Abschluß: Abitur
<i>Studium:</i>	1988-1993	Fakultät für Physik der Staatl. Universität Novosibirsk Abschluß: Diplom in Physik
	1993-1995	Fakultät für Physik der Staatl. Universität Novosibirsk Abschluß: Master of Science
<i>Berufstätigkeit:</i>	1995-1999	Wissenschaftlicher Mitarbeiter am Budker Institute of Nuclear Physics, Novosibirsk
	1999-2000	Wissenschaftlicher Mitarbeiter am CEA - Centre d'Etude de Saclay, Frankreich
	seit 2001	Wissenschaftlicher Mitarbeiter am Institut für Experimentalphysik I der Ruhr-Universität Bochum